TIDAL INTERACTIONS OF SHORT-PERIOD EXTRASOLAR TRANSIT PLANETS WITH THEIR HOST STARS: CONSTRAINING THE ELUSIVE STELLAR TIDAL DISSIPATION FACTOR

Inaugural-Dissertation

zur

Erlangung des Doktorgrades

der Mathematisch-Naturwissenschaftlichen Fakultät

der Universität zu Köln

vorgelegt von

Ludmila Carone

aus Bukarest

Abstract

The orbital and stellar rotation evolution of CoRoT planetary systems due to tides raised by the planet on the star (stellar tidal friction) and by tides raised by the star on the planet (planetary tidal friction, for $e > 0$) is investigated. The evolution time scale depends on the stellar tidal dissipation factor over stellar Love number $Q_*/k_{2,*}$ which is not very well constrained. Tidal energy dissipation models yield $Q_*/k_{2,*} = 10^5 - 10^9$.

Many CoRoT planets may migrate towards their star because the stellar rotation rate Ω_* is smaller than the planetary mean revolution rate n. To guarantee long-term stability of the CoRoT-planets, $\frac{Q_*}{k_{2,*}} \geq 10^7 - 10^8$ is derived as a common stability limit. As the planet migrates towards the star, the stellar rotation is spun-up efficiently. For most CoRoT stars no sign of tidal spin up is found, therefore $\frac{Q_*}{k_{2,*}} > 10^6$ is derived by requiring tidal friction to be weaker than magnetic braking. CoRoT-17 apparently is experiencing moderate tidal spin-up which requires $4 \times 10^7 \leq \frac{Q_*}{k_{2,*}} < 10^9$.

For planets with $e \geq 0.5$, like CoRoT-10b and CoRoT-20b, planetary and stellar tidal friction may act on similar timescales. This may lead to a positive feedback effect, decreasing the semi major axis/increasing the stellar rotation rapidly. To avoid this, $\frac{Q_*}{k_{2,*}} > 10^6$ is required.

The CoRoT-3 and CoRoT-15 system may be tidal equilibrium states, where $\Omega_* = n$. To achieve this state and to maintain it in the presence of magnetic braking $\frac{Q_*}{k_{2,*}} \leq 10^7 - 10^8$ is required. Even then, the double synchronous orbit may decay because magnetic braking removes angular momentum from the system. Therefore, only F stars are capable to maintain a double synchronous state with a massive companion, because these stars are not strongly affected by magnetic braking.

The $\frac{Q_*}{k_{2,*}}$ values required for double synchronous rotation are comparatively low although $\frac{Q_*}{k_{2,*}}$ is expected to grow as $\Omega_* \to n$. This discrepancy is explained by the on-set of dynamical tides as stellar eigenfrequencies are exited, leading to a more efficient tidal energy dissipation and reducing $\frac{Q_*}{k_{2,*}}$. The other CoRoT-systems are assumed not to excite dynamical tides.

Kurzzusammenfassung

Die Entwicklung des Orbits und der Sternrotation von CoRoT Planetensystemen aufgrund von stellarer Gezeitenreibung und planetarer Gezeitenreibung wird untersucht. Die Entwicklungszeiträume hängen vom stellaren Gezeitendissipationsfactor über stellare Love-Zahl $Q_*/k_{2,*}$ ab, deren Grösse nicht genau bekannt ist. Aus Gezeitenenergie-Dissipations-Modelle ergeben sich: $Q_*/k_{2,*} = 10^5 - 10^9$.

Viele CoRoT-Planeten könnten zum Stern wandern, da $\Omega_* < n$. Um das Überleben der CoRoT-Planeten zu garantieren, ergibt sich $\frac{Q_*}{k_{2,*}} \geq 10^7 - 10^8$ als Stabilitätslimit. Wenn der Planet zum Stern wandert, wird die Sternrotation stark beschleunigt. Die meisten CoRoT-Sterne zeigen kein Zeichen einer Gezeitenbeschleunigung, daher ergibt sich $\frac{Q_*}{k_{2,*}} > 10^6$, wenn angenommen wird, dass Gezeitenreibung schwächer ist als 'magnetic braking'. Die Rotation von CoRoT-17 scheint moderat durch Gezeitenreibung beschleunigt zu werden, woraus sich $4 \times 10^7 \leq \frac{Q_*}{k_{2,*}} < 10^9$ ergibt.

Planeten mit $e \geq 0.5$, wie CoRoT-10b und CoRoT-20b, sind gleichzeitig planetarer und stellarer Gezeitenreibung unterworfen. Das führt zu einer positiven Rückkopplung, wobei sich die große Halbachse stark verringert bzw. die Sternrotation stark beschleunigt. Um dies zu verhindern, ist $\frac{Q_*}{k_{2,*}} > 10^6$ erforderlich.

Das CoRoT-3 und CoRoT-15-System könnte in einem Gleichgewichtszustand sein, so dass $\Omega_* = n$. Um diesen Zustand trotz 'magnetic braking' aufrechtzuerhalten, ist $\frac{Q_*}{k_{2,*}} \leq 10^7 - 10^8$ erforderlich. Selbst dann könnte der doppelt-synchrone Orbit aufgrund von 'magnetic braking' zerfallen. Daher können nur F-Sterne einen doppelt-synchronen Zustand mit einem schweren Begleiter aufrechterhalten, weil diese Sterne reduziertem 'magnetic braking' unterworfen sind.

Die $\frac{Q_*}{k_{2,*}}$-Werte für den doppelt-synchronen Zustand sind verhältnismässig klein, obwohl erwartet wird, dass $\frac{Q_*}{k_{2,*}}$ wächst, wenn $\Omega_* \to n$. Das kann durch dynamische Gezeiten erklärt werden, wenn stellare Eigenfrequenzen angeregt werden. Das führt zu einer effizienten Gezeitenenergie-Dissipation und einem kleineren $\frac{Q_*}{k_{2,*}}$. Es wird angenommen, dass die anderen CoRoT-Systeme keine dynamischen Gezeiten anregen.

Table of Contents

List of Tables

List of Figures

x

Variables and constants

Constants	description
$G = 6.673 \times 10^{-11} \text{m}^3 \text{kg}^{-1} \text{s}^{-2}$	gravitational constant
$AU = 1.496 \times 10^{11}$ m	astronomical unit
$c = 2.9979 \times 10^8 \text{ms}^{-1}$	velocity of light (vacuum)
$M_{Jup} = 1.8986 \times 10^{27}$ kg	Jovian mass
$R_{Jup} = 69.911 \times 10^6$ m	volumetric mean radius of Jupiter
$M_{Sun} = 1.989 \times 10^{30}$ kg	Solar mass
$R_{Sun} = 6.96 \times 10^8$ m	Solar radius
$R_{Earth} = 6.378 \times 10^6$ m	Earth radius
$M_{Earth} = 5.973 \times 10^{24}$ kg	Earth mass
Variables	description
Q_P	primary dissipation factor
Q_S	secondary dissipation factor
$k_{2,P}$	primary Love number
$k_{2,S}$	secondary Love number
Q_*	stellar dissipation factor
Q_{pl}	planetary dissipation factor
$k_{2,*}$	stellar Love number
$k_{2,Pl}$	planetary Love number
M_P	primary mass
M_S	secondary mass
R_P	primary radius

R_S	secondary radius
Ω_P	primary rotation rate
Ω_S	secondary rotation rate
ω	tidal frequency
a	semi major axis of an orbit
e	orbital eccentricity
a_{equiv}	equivalent semi major axis of the corresponding circular orbit
ρ	bulk density
g_P	gravitational acceleration at the surface of a primary
$\tilde{\mu}$	effective rigidity
ζ_P	amplitude of the equilibrium tide on a primary
τ_P	tidal lag time on the primary
τ_d	damping time scale
T_P	tidal time scale
n	orbital revolution rate
M_*	stellar mass
M_{Pl}	planetary mass
Ω_*	stellar rotation rate
Ω_{Pl}	planetary rotation rate
P_*	stellar rotation period
C_P	moment of inertia of the primary
I_P	normalized moment of inertia of the primary
P_{orb}	orbital period
P_{Pl}	planetary rotation period
L	angular momentum
L_{tot}	total angular momentum

L_{orb}	orbital angular momentum
$L_{rot,*}$	stellar rotation angular momentum
$L_{rot,Pl}$	planetary rotation angular momentum
E	energy
E_{orb}	orbital energy
I_*	stellar normalized moment of inertia
I_{Pl}	planetary normalized moment of inertia
C_*	stellar moment of inertia
τ_{synchr}	synchronization time scale
τ_{Roche}	time scale to reach Roche limit
Do	planetary Doodson constant
PF	tidal property factor

Introduction

> While I'm still confused and uncertain, it's on a much higher plane, d'you
> see, and at least I know I'm bewildered about the really fundamental and
> important facts of the universe.
>
> *Terry Pratchett, humorist & writer (Equal Rites)*

In 1995, something was discovered that took many planetary scientists by surprise: Michel Mayor and Didier Queloz found a 0.46 Jupiter mass object that orbits the main sequence star 51 Pegasi every 4.2 days (*Mayor and Queloz*, 1995). This period corresponds to an orbit with a semi major axis of 0.05 astronomical units (AU). For comparison, Mercury, the innermost planet in our Solar System, has an orbit with a semi major axis of 0.39 AU. 51 Pegasi b, as the planet is called now, is the first extrasolar planet found around a Sun-like star and it is a strange planet when compared to the planets in our Solar System.

Not only is the very close orbit a surprise, but also the fact that such a short-period orbit is occupied by a gas giant and not by a terrestrial planet. Before the discovery of 51 Pegasi b, it was regarded as self-evident that the innermost region of planetary systems can only harbor planets of terrestrial composition and that gas giants can only form beyond the 'snow line. The 'snow line' marks the distance from a star where volatile materials like helium and hydrogen, the building blocks of gas

giants, can exist in a primordial gas-dust disc without being dispersed by stellar wind and irradiation (*Hayashi*, 1981; *Sasselov and Lecar*, 2000). This idea was challenged by 51 Pegasi b's very existence.

Today, more than 600 extrasolar planets[1] have been discovered and, yet, it remains controversial if the formation theory of planetary systems requires 'just' small corrections by allowing gas giants to migrate towards their stars (*Lin et al.*, 1996; *Weidenschilling and Marzari*, 1996) or if the formation theory itself needs to be modified to allow for in-situ formation in close proximity to the star (*Wuchterl*, 1999; *Broeg and Wuchterl*, 2007). In any case, extrasolar planets continue to challenge and broaden our conceptions of how planetary systems form and evolve over time.

This work focuses on another aspect of extrasolar planetary system evolution: Tidal interactions between a close-in planet and its star. More specifically, tidal friction is investigated where torques due to the tidal bulge on the star and on the planet lead to changes in the planet's orbit and the rotation rates of the star and planet; this is a research field that holds surprises as well.

Tidal friction raised by a massive close-in planet on the star may have an influence on the stellar rotation evolution. It is one of the rare examples of direct star-planet interactions. Furthermore, tidal friction may destabilize the orbit of a planet and spin up the stellar rotation. The timescale on which these effects take place depends on how much energy is dissipated within the star as the tidal bulge plows over the stellar surface. These dissipation processes depend on the inner structure of the star. Therefore, tidal friction between close-in extrasolar planets and their star may allow to 'probe' the stellar interior or, at least, the stellar outer layer. In the case of main

---

[1]As listed in the exoplanet catalogue: http://www.exoplanet.eu/catalog-all.php as of 14th October 2011.

sequence stars, which are investigated in this work, the outer layer is the convective envelope; a turbulent plasma environment.

Compared to the Solar System, this is an unparalleled situation. The Solar System planets are too far away and the innermost planets not very massive. Consequently, the resulting planetary tidal forces are too small to produce an observable effect (*Goldreich and Soter*, 1966).

The goal of this work is to investigate the evolution of planets discovered by the CoRoT mission (*Baglin*, 2003) due to the influence of tidal torques. From the evolution scenarios, the timescale on which tidal friction acts on the planetary systems can be constrained. This in turn sheds light upon the stellar energy dissipation mechanisms, currently not very well constrained.

The CoRoT planets are selected because they provide a variety of interesting scenarios:

- Planets on circular orbits around slowly rotating low-mass stars.

- Planets on circular orbits around slowly rotating F-stars.

- Planets on eccentric orbits.

- Planets around fast-rotating stars.

- Possible double synchronous systems.

In addition, the stellar and planetary parameters of the CoRoT systems are very well determined (See Tables 1.3, 1.2, and Appendix A).

In Chapter 1, extrasolar planets and brown dwarfs are defined, a brief detection history is given and extrasolar planet detection methods are discussed. The CoRoT

space mission is presented because the planets found by CoRoT provide the basis of this work. Furthermore, a quick overview over the properties of the planetary systems discovered so far is given.

Subsequently (Chapter 2), the theoretical foundations of this work is laid out. Tidal potentials, tidal forces and tidal torques are developed. The influence of tidal torques on planetary systems with circular and eccentric orbits is calculated. The tidal dissipation factor Q, describing the amount of tidal energy dissipated within a body, and the Love number k_2, from which the tidal deformation can be derived, are introduced. Several Q/k_2 values derived for Solar System and extrasolar objects are discussed. The angular momentum and energy criteria for the stability of double synchronous states are presented. Furthermore, the magnetic braking effect in main sequence stars is discussed. Several moments of inertia are calculated for ideal bodies, Solar System planets and the Sun. The solar moment of inertia is derived from a Solar model. Finally, the Roche zone is presented where a planet may be tidally disrupted as it approaches its star.

In Chapter 3, the constant Q assumption is critically investigated, which is the basis of the tidal friction model used in this work. It will be shown that the majority of the CoRoT planets are tidally locked. Furthermore, the angular momenta and energies of a typical planetary system consisting of a 'hot Jupiter' and a Sun-like star are calculated, showing that the majority of the angular momentum is stored in the planet's orbit. Furthermore, it will be shown that the Roche zone may be under-or overestimated if the planetary density is not known.

In Chapter 4, the CoRoT planets are identified that may reach the Roche zone for $\frac{Q_*}{k_{2,*}} = 10^5 - 10^9$ within the stellar lifetime, and that exert strong tidal forces on

the star. It will be shown that the majority of the CoRoT planets are potentially unstable due to tidal friction.

In Chapter 5, the tidal evolution of planets around slowly rotating stars is investigated and an orbital stability limit for $\frac{Q_*}{k_{2,*}}$ is derived. Chapter 6 presents the stellar rotation evolution of their host stars and shows that tidal friction may lead to an acceleration of the stellar rotation. From this a spin-up limit for $\frac{Q_*}{k_{2,*}}$ is derived. In both Chapters, it will be shown that for planets on orbits with large eccentricities ($e \geq 0.5$), planetary and stellar tidal friction may lead to an accelerated tidal evolution.

Chapter 7 presents the tidal evolution for fast rotating stars of spectral type F for different magnetic braking scenarios. It will be investigated which magnetic braking and tidal friction scenario is compatible with the observed stellar rotation periods of CoRoT spectral type F stars. Furthermore, an orbital stability limit for $\frac{Q_*}{k_{2,*}}$ is derived again.

In Chapter 8, it will be investigated which CoRoT systems may be 'true' double synchronous states. A spin-up limit for $\frac{Q_*}{k_{2,*}}$ is derived required to force the star into corotation with the planet's revolution. An evolution limit for $\frac{Q_*}{k_{2,*}}$ is derived, if it is assumed that the planet migrated towards the double synchronous state. It will be investigated how the double synchronous orbit evolves in the presence of magnetic braking and how this can be described mathematically. It will be investigated for which magnetic braking scenarios, the CoRoT-3 and CoRoT-15 system may still be stable within the systems' lifetime. It will be shown why the evolution of the CoRoT-20 system depends on the initial stellar rotation period and why the system may be forced into a double synchronous state for certain conditions but can not maintain it

in the presence of magnetic braking.

Finally, the results are summarized, compared and discussed in Chapter 9.

Chapter 1

Extrasolar planets and Brown Dwarfs

Since their discovery in 1995, extrasolar planets have become an important branch of modern astronomy. In this chapter, an overview of extrasolar planets and the methods used so far to detect them is given. Sometimes, it is not easy to ascertain the true nature of a stellar companion. Therefore, first of all, a consistent definition is needed to distinguish planets from other objects.

1.1 Definition of extrasolar planets and brown dwarfs

In 2003, the Working Group on Extrasolar Planets (WGESP) of the International Astronomical Union (IAU) developed the following working definitions commonly used by astronomers today:

1: Objects with true masses below the limiting mass for thermonuclear fusion of deuterium (currently calculated to be 13 Jupiter masses for objects of solar metallicity) that orbit stars or stellar remnants are "planets" (no matter how they formed). The

minimum mass/size required for an extrasolar object to be considered a planet should be the same as that used in our Solar System.[1]

2: Substellar objects with true masses above the limiting mass for thermonuclear fusion of deuterium are "brown dwarfs", no matter how they formed nor where they are located.

3: Free-floating objects in young star clusters with masses below the limiting mass for thermonuclear fusion of deuterium are not "planets", but are "sub-brown dwarfs" (or whatever name is most appropriate).[2]

Planets and stars not only differ by mass, which would be a quantitative difference only, they also differ qualitatively and hierarchically according to the standard theory of planetary formation: Stars form by cloud-collapse, whereas planets form around a star by matter accretion. It has to be emphasized that planets always require a central star, whereas a star does by no mean require a planet. That is the reason why free floating objects in young star clusters - although similar in mass to planets - are not regarded as 'true' planets.

Brown dwarfs with masses[3] between 13 and 80 $M_{Jupiter}$ appear to represent a transitional stage between Jupiter-like gas giants and bona-fide stars. On the one hand, they are not massive enough to reach the stage of hydrogen burning in thermal equilibrium. On the other hand, they are massive enough to ignite deuterium fusion processes which are, however, inefficient nuclear reactions that are not capable to compensate the radiative heat loss. Therefore, unlike stars, brown dwarfs gradually

---

[1] Resolution B5, the IAU's definition of a planet in the Solar System can be found at: http://www.iau.org/public/pluto/.

[2] http://www.dtm.ciw.edu/boss/definition.html

[3] This mass range is valid for substellar objects with solar metallically and may be corrected for individual cases. As a rough estimate, however, it is sufficient.
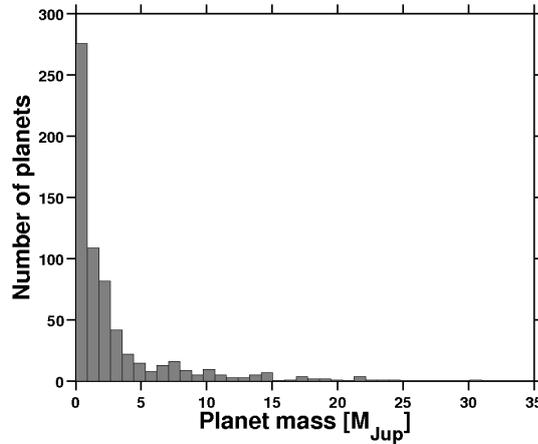
Figure 1.1: Histogram of the masses of all detected exoplanets. The data were taken from the exoplanet catalogue: http://www.exoplanet.eu/catalog-all.php as of 14th October 2011.

cool down with time (see for example *Unsoeld and Baschek* (2001)).

To date, it is controversial if brown dwarfs form either by cloud collapse or matter accretion. There may even be two classes of brown dwarfs: light brown dwarfs that are more or less overweight planets formed by matter accretion, and very massive brown dwarfs that may be regarded as failed stars and have formed by cloud collapse (*Deleuil et al.* (2008) among others).

That there are maybe two classes of brown dwarfs, light ones at the higher end of the exoplanet's mass regime and heavy ones at the low end of the stellar mass regime, may explain the mysterious 'brown dwarf desert' (*Marcy and Butler*, 2000; *Halbwachs et al.*, 2000): There is a deficiency in numbers of objects between masses of 13-80 Jupiter masses which can not be explained by an observation bias (Figure 1.1)[4]. As will be shown in Section 1.3, the more massive an object is, the easier it is to discover. Not only are brown dwarfs that orbit main sequence stars rare objects, free floating

---

[4]The data were taken from the exoplanet catalogue: http://www.exoplanet.eu/catalog-all.php as of 14th October 2011.

brown dwarfs are found far more often although they are more difficult to detect (*Marcy and Butler*, 2000)[5]. Some of these rare brown dwarfs around main sequence stars, CoRoT-3b (*Deleuil et al.*, 2008) and CoRoT-15b (*Bouchy et al.*, 2011), will play an important role in subsequent chapters.

This work focuses on tidal interactions of companions around main sequence stars where the formation of the system is completed. In the context of tidal interaction, it is only important that the mass of the stellar companion is orders of magnitude smaller than the mass of the star. Therefore, brown dwarfs and their less massive counterparts are regarded as 'planetary objects', regardless of their formation history.

1.2   History of extrasolar planet detection

In the following, a short - but on no account exhaustive - summary of historical events in the course of extrasolar planet detection is given.

- In 1989, using the radial velocity method (Section 1.3.1), a substellar object was discovered around the Sun-like star HD 114762, which was identified as a Brown Dwarf with 11 Jupiter masses (*Latham et al.*, 1989).

- In 1992, the existence of two planets with masses of at least 2.8 M_{Earth} and 3.4 M_{Earth} around the pulsar PSR1257 + 12 was inferred using the pulsar timing method (Section 1.3.1, *Wolszczan and Frail* (1992)). This was confirmed in 1994 (*Wolszczan*, 1994).

---

[5]The latter can only be observed directly by their faint infrared radiation, whereas the existence of the former can be inferred more easily by their influence on the host star.

- In 1995, the first Jupiter-mass companion around a solar type star was discovered using radial velocity measurements (*Mayor and Queloz*, 1995). The gas giant 51 Pegasi b with a minimum mass of 0.5 M_{Jup} orbits its host star at only 0.05 AU.

- In 2002, a free floating planetary mass object of mass $3^{+5}_{-1}M_{Jup}$ in the σ *Orionis* cluster was reported. It was discovered by direct imaging (section 1.3.2) during a near-infrared survey (*Zapatero Osorio et al.*, 2002).

- In December 2006, the European space mission CoRoT was launched. It is the first space mission dedicated to the search of extrasolar planets. To date, CoRoT discovered more than 20 planets. Chapters 5, 6, 7 and 8 will investigate the tidal evolution of 21 CoRoT planets in more detail.

- In 2009, CoRoT announced the discovery of CoRoT-7b, the first **definitely** terrestrial extrasolar planet (*Léger et al.*, 2009). Objects with a few Earth masses have been discovered previously, but CoRoT-7b is the first planet for which both, its mass $(4.8 \pm 0.8\, M_{Earth})$ and radius $(1.68 \pm 0.09\, R_{Earth})$, could be determined (*Queloz et al.*, 2009). A bulk density consistent with that of a terrestrial planet was derived: $\rho = 5.6 \pm 1.3 \mathrm{g/cm^3}$. Recently, *Hatzes et al.* (2011) revised the mass of CoRoT-7b $(7.42 \pm 1.21\, M_{Earth})$ which yields with improved stellar parameters of CoRoT-7 (*Bruntt et al.*, 2010) and therefore improved radius of CoRoT-7b $(1.58 \pm 0.10\, R_{Earth})$ a density of $\rho = 10.4 \pm 1.8 \mathrm{g/cm^3}$, still consistent with a terrestrial planet.

- In March 2009, the NASA space telescope Kepler was launched. It is the second space mission dedicated to the search of extrasolar planets. To date, Kepler

confirmed 35 planetary systems.

- In 2010, *Holman et al.* (2010) announced the discovery of the first multiple transiting planetary system consisting of two Saturn-size planets by Kepler.

- In 2011, *Batalha et al.* (2011) announced the discovery of Kepler's first rocky planet, Kepler-10b, which – apart from its greater age – is a CoRoT-7b analogue ($4.56^{+1.17}_{-1.29}\,M_{Earth}$, $1.416^{+0.033}_{-0.036}\,R_{Earth}$, and $\rho = 8.8^{+2.1}_{-2.9}\mathrm{g/cm^3}$).

To date, 759 extrasolar planets in 609 planetary systems have been discovered [6].

1.3 Extrasolar planets detection methods

Various detection methods are used to discover extrasolar planets. A brief overview of the different methods is given, discussing advantages and disadvantages of each technique with special emphasis put on requirements for the investigation of tidal interactions between stars and planets.

1.3.1 Indirect detection methods

Some detection methods monitor the motion of the star which may be influenced gravitationally by an otherwise invisible companion. Both, the companion **and** the star, revolve around a common point: the common center of gravity or barycenter (Figure 1.2). The center of gravity of a star-planet system is defined:

$$\frac{a_*}{a_{Pl}} = \frac{M_{Pl}}{M_*}, \tag{1.3.1}$$

where a_* and a_P are the semi major axis of the star's and the planet's orbit around the barycenter and M_*, M_P are the stellar and planetary mass, respectively.

---

[6]As listed by the Exoplanet catalog http://www.exoplanet.eu/catalog.php maintained by Jean Schneider from the Observatoire de Paris by 11th February 2012
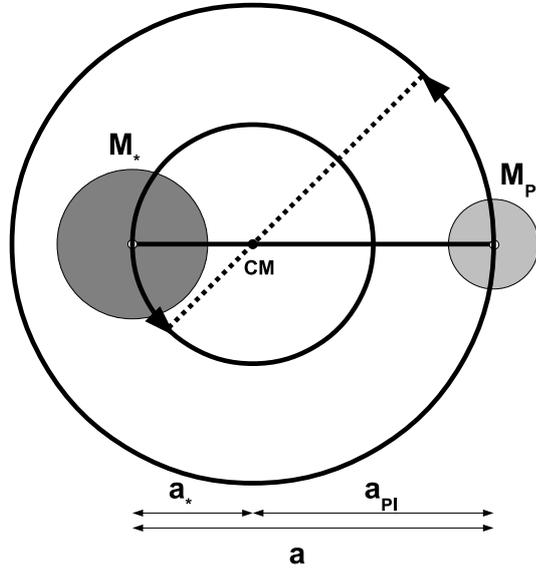
Figure 1.2: The motion of a star and a planet with masses M_* and M_{Pl} and semi major axes a_* and a_{Pl}, respectively, around their common center of mass (CM).

The stellar as well as the planetary orbit obey Kepler's third law, therefore:

$$\frac{(a_* + a_P)^3}{P_{orb}^2} = \frac{G(M_* + M_P)}{4\pi^2}, \quad (1.3.2)$$

where P_{orb} is the orbital period.

If $M_* \gg M_{Pl}$ and $a_* \ll a_{Pl}$, a_{Pl}, equation (1.3.2) can be approximated by:

$$a_{Pl}^3 \approx \frac{GM_*P_{orb}^2}{4\pi^2}. \quad (1.3.3)$$

The indirect exoplanet detection methods observe the revolution of the star around the common center of mass which yields P_{orb} and a_*. The stellar mass M_* is determined by spectral classification. Therefore, a_{Pl} can be derived from equation 1.3.3, and M_{Pl} can be derived from equation (1.3.1).

This is, however, only valid if the orbital plane is parallel to the line-of-sight. If the orbital plane is inclined, indirect methods yield the projection of a_* onto the
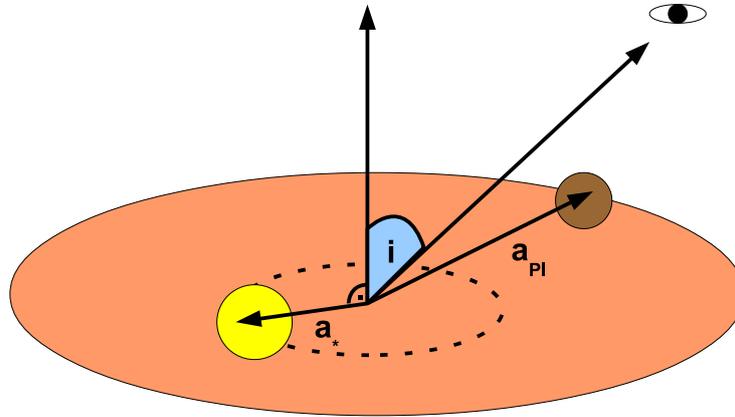
Figure 1.3: The orbital plane of a planetary system which is inclined by the angle i with respect to the line-of-sight. The system consists of a star and a planet with masses M_* and M_{Pl}, revolving with semi major axes a_* and a_{Pl}, respectively, around their common center of mass.

observation plane. Therefore, the orbital inclination i has to be taken into account as well when determining planetary parameters. The orbital inclination of exoplanets is defined as the angle between a vector perpendicular to the orbital plane and the line-of-sight (Figure 1.3).

Pulsar timing method

In 1992, planetary objects were discovered around pulsars. A pulsar is a neutron star formed out of the remnants of a massive star after a supernova explosion. It emits regular radio pulses, hence its name. The arrival time t_a of such a pulse is:

$$t_a = \frac{D}{c},\tag{1.3.4}$$

where D is the distance between the star and observer and c the velocity of light. If a pulsar is orbited by a planet, the motion around the barycenter yields periodic variations in the distance between the observer on Earth and the star. If the system is seen 'edge on', D oscillates between $d + a_*$ and $d - a_*$, where d is the distance between the planetary system's barycenter and the Earth and a_* is the semi major axis of the Keplerian orbit of the star.

The maximum delay time δt from the expected arrival time t_a is:

$$\delta t = \frac{a_*}{c} \tag{1.3.5}$$

Inserting equation (1.3.1) yields the following relation:

$$\delta t = \frac{a_{Pl} M_{Pl}}{M_* c}. \tag{1.3.6}$$

If the orbital plane is inclined with respect to the line-of-sight, then δt is:

$$\delta t = \frac{\sin i \cdot a_{Pl} M_{Pl}}{M_* c}, \tag{1.3.7}$$

where i is the orbital inclination. The pulsar timing method is sensitive to planets with large semi major axes. Planetary systems that are seen 'face on' ($i = 0°$) are 'invisible' to this method.

Because the pulsar intervals can be measured to great precision, even terrestrial planets can be detected by this method. The extrasolar planets discovered in 1992, for example, have only about 2.8 and 3.4 Earth masses (*Wolszczan and Frail*, 1992).

Pulsars are rare objects and planets around pulsars are thought to be even rarer. Indeed, only eight extrasolar planet systems with twelve planets around pulsar stars have been discovered to date [7].

---

[7]As listed by the Exoplanet catalog http://www.exoplanet.eu/catalog.php maintained by Jean Schneider from the Observatoire de Paris by 17th October 2011
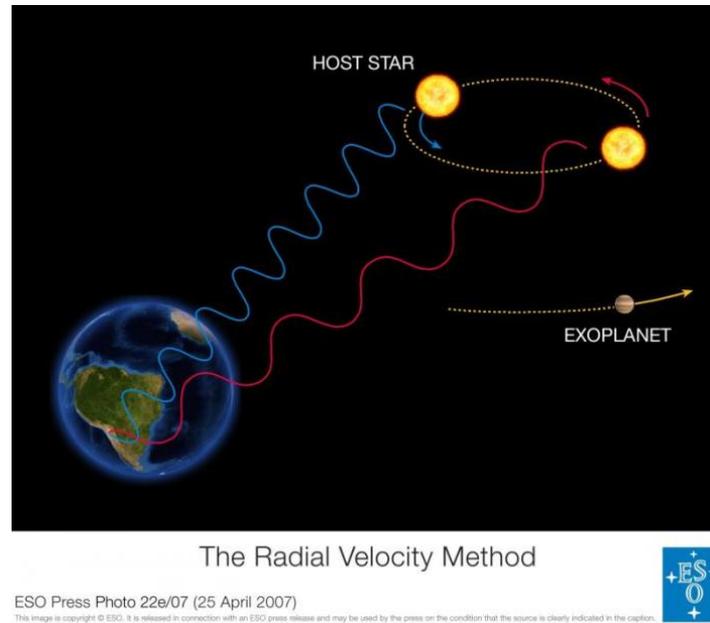
Figure 1.4: As the star moves around the barycenter, emitted light is Doppler shifted (Credit: ESO).

Radial velocity method

The first extrasolar planet around a sun-like host star, *51 Pegasi b*, was discovered by radial velocity measurements (*Mayor and Queloz*, 1995). This method also makes use of the Keplerian motion of the star around the system's barycenter. This motion results in a Doppler shift of the emitted light alternatively toward the bluer (shorter) wavelengths, when the star is moving toward the observer, and toward the redder (longer) wavelengths, when the star is moving away (Figure 1.4).

During one orbital period P_{orb}, the star completes one revolution; therefore, the following relation holds for the stellar velocity v_*:

$$P_{orb}v_* = 2\pi a_*,\tag{1.3.8}$$

where a_* is the semi major axis of the stellar orbit.

Inserting equation (1.3.1), the planet's mass can be determined:

$$M_{Pl} = \frac{M_*}{a_{Pl}} \cdot \frac{v_*}{2\pi} \cdot P_{orb}, \qquad (1.3.9)$$

where a_{Pl} is the semi major axis of the planet's orbit and M_* is the stellar mass.

From the Earth, however, only the Doppler shift due to the velocity component v_r along the line-of-sight can be observed:

$$\Delta\lambda \approx v_r \lambda / c, \qquad (1.3.10)$$

where $\Delta\lambda$ is the Doppler shift, c is the velocity of light, λ is the wavelength of the emitted stellar light, and v_r is:

$$v_r = v_* \sin i. \qquad (1.3.11)$$

i is again the orbital inclination.

The planetary mass can be determined from the observed Doppler shift by:

$$M_{Pl} \sin i = \frac{M_*}{a_{Pl}} \cdot \frac{c \cdot \Delta\lambda}{\lambda 2\pi} \cdot P_{orb}. \qquad (1.3.12)$$

The amplitude of the oscillating stellar radial velocity, caused by the star's motion around the barycenter of the planetary system, is in general very small. Jupiter, for example, induces a solar radial velocity modulation with an amplitude of 12 m/s, Saturn with an amplitude of 2.7 m/s and Earth induces only a solar radial velocity modulation of amplitude 0.04 m/s. *51 Pegasi b*, on the other hand, induces a stellar radial velocity modulation with an amplitude of $\approx$ 50 m/s (Figure 1.5, *Mayor and Queloz* (1995)), which is comparatively large because *51 Pegasi b*'s semi major axis ($a = 0.05$ AU) is very small compared to the semi major axes of Jupiter, Saturn and Earth (5.2 AU, 9.5 AU, and 1 AU, respectively). For comparison, the Super-Earth CoRoT-7b causes a radial velocity modulation with 3.3 m/s amplitude (*Queloz et al.*,
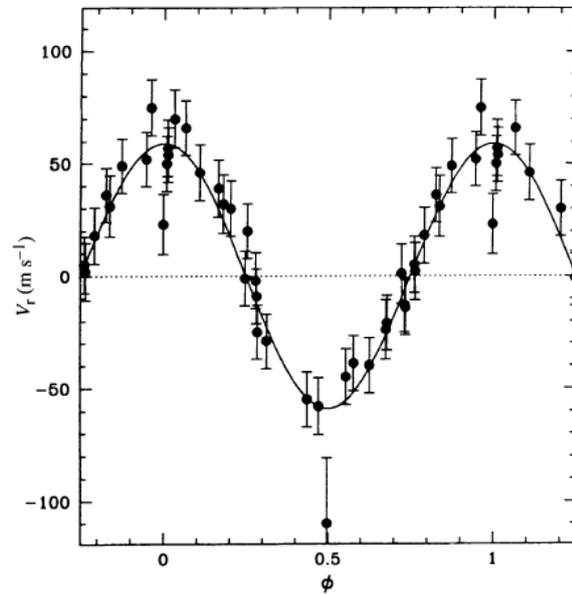
Figure 1.5: Radial velocity curve of 51 Pegasi b. The planet induces a radial velocity modulation of about 50 m/s (*Mayor and Queloz*, 1995).

2009). The radial velocity method is sensitive to massive planets in close proximity to their star. Such planets are ideal for the investigation of tidal interactions between the planet and its star.

A great disadvantage of this method is, especially in terms of tidal interaction investigation, that 'only' the minimum planetary mass $M_P \cdot \sin i$ can be determined. If $i = 0°$, when the system is seen 'face on', the planet is even 'invisible' to this detection method. To obtain the true mass, the measurements have to be complemented by another method that also yields the orbital inclination i: The transit method (see Section 1.3.2).

Another disadvantage of the radial velocity method is, that such measurements are time-consuming and can only be applied to individual stars. The method becomes

even more time consuming, the less massive the companion is. For example, more than 70 hours of observations had been gathered to determine the mass of CoRoT-7b (*Queloz et al.*, 2009).

Still, it is the best detection method to constrain the mass of a substellar companion which is crucial in determining its nature (*Bonfils et al.*, 2011; *Delfosse et al.*, 2012).

To date, 643 planetary systems have been discovered or confirmed by radial velocity measurements[8].

Astrometry method

The astrometry method makes use of the Keplerian stellar motion. This very motion itself may be observed directly by monitoring the proper motion of the star in the night sky.

If the system is seen 'face on' ($i = 0°$), the apparent parallax of the star δa_* is

$$\delta a_* = \frac{a_*}{D}, \tag{1.3.13}$$

where a_* is the star's semi major axis and D is the distance between the observer on Earth and the planetary system.

Inserting equation (1.3.1) yields:

$$\delta a_* = \frac{a_{Pl}}{D} \cdot \frac{M_{Pl}}{M_*}, \tag{1.3.14}$$

a_{Pl} is the planet's semi major axis, M_* and M_{Pl} are the star's and planet's mass, respectively.

---

[8]As listed by the Exoplanet catalog http://www.exoplanet.eu/catalog.php maintained by Jean Schneider from the Observatoire de Paris by 17th October 2011

The astrometry method requires accurate star position measurements which are hard to achieve. Although astrometry is the oldest method to search for extrasolar planets, so far no planet has undoubtedly been discovered by astrometry - despite decades of meticulous observations and claims to the contrary.

- In 1943, Kaj Strand claimed that he found a planet orbiting the widely separated binary star 61 Cygni via astrometric measurements (*Strand*, 1943). Although the announcement was greeted with enthusiasm at that time, the claim remained unsupported. In 1978, the astrometric measurements were reexamined by W.D. Heintz who concluded that *"there is no evidence for any companion of substellar mass"* (*Heintz*, 1978).

- In 1960, Sarah Lippincott claimed that the star Lalande 21185 is orbited by a planet of approximately ten Jupiter masses (*Lippincott*, 1960).

- In 1963, Peter Van de Kamp claimed the discovery of a 1.6 Jupiter mass planet orbiting Barnard's Star at 4.4 AU (*van de Kamp*, 1963). That detection was discounted in 1973 by Gatewood and Eichhorn (*Gatewood and Eichhorn*, 1973). The 'apparent' wobble of the star in the night sky turned out to be a false detection due to systematic effects (*Hershey*, 1973).

- In 2009, *Pravdo and Shaklan* (2009) claimed the discovery of a 6.4 Jupiter mass companion to VB 10 which promptly was rejected by *Bean et al.* (2010).

Maybe astrometry space missions like GAIA, foreseen to launch in 2013, will probably overcome the limitations in accuracy that trouble ground based astrometry measurements (*Perryman*, 2002).

Astrometry method is foreseen to be complementary to other detection methods because it is sensitive to planetary systems with orbital inclination $i \approx 0°$, which are all but invisible to most other detection methods.

Although the astrometry method failed so far to yield extrasolar planet detections, it was used in some cases to constrain the orbital inclination and, therefore, the mass of planets discovered by the radial velocity method (*Reffert and Quirrenbach*, 2011). For tidal interaction investigations, however, the planets found by astrometry will probably be of limited use because this method is sensitive to planets with large semi major axes.

1.3.2 Direct detection methods

In the following, some detection methods are presented that infer the existence of an extrasolar planet by more direct means.[9]

Microlensing method

The microlensing method is a practical application of general relativity. When a star harboring a planet moves through the line of sight between Earth and a background light source (usually another star located further away), the gravitational field of the star and its planet can act as a gravitational binary lens to amplify the luminosity of the source star.

Consequently, the photometric light curve of a star whose light is subjected to microlensing by a star-planet system shows a characteristic double peak (Figure 1.6), where the highest peak is the lensing event due the star and the second smaller peak is the lensing event due to the planet.

---

[9]From now on $a_{Pl} \approx a$ is used.
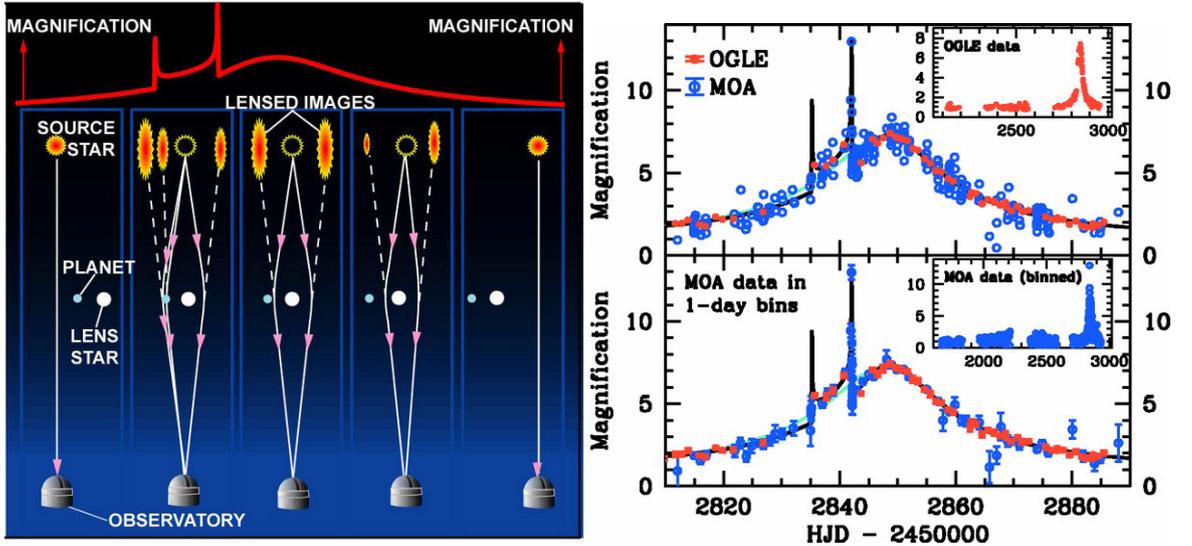
Figure 1.6: Left panel: Schema of the microlensing effect (Credit: OGLE).
Right panel: Photometric curve with best-fitting double-lens models of OGLE 2003-BLG-235/MOA 2003-BLG-53 b (*Bond et al.*, 2004).

The mass of a gravitational lens M can be deduced by determining the Einstein radius R_E of the ring image obtained when the source, lens and observer are collinear. The relation between Einstein radius and mass of a lensing object is:

$$R_E = 2\sqrt{\frac{GMD}{c^2}}, \tag{1.3.15}$$

where D is the reduced distance defined by $1/D = 1/D_{ol} + 1/D_{ls}$. D_{ol} and D_{ls} are the distances from the observer to the lens and from the lens to the source, respectively, and c is the speed of light.

This method is sensitive to planets on very wide orbits because a wide separation between star and planet is needed to resolve the lensing effect of each individual object (*Cassan et al.*, 2012). It is even possible to find planets of a few Earth masses (*Bennett et al.*, 2008).

One major drawback of this method is, that a planet is only observable during the

lensing event. One may reobserve the host star to refine stellar parameters, but the planet becomes 'invisible' after the lensing event. Furthermore, because lensing events are rare and unpredictable, microlensing surveys like OGLE require an observational network that constantly monitors a large number of stars.

Due to the weak constraints on the planetary parameters and the large separation between star and planet, microlensing planets are unsuitable for tidal investigations.

To date, thirteen planets in twelve planetary systems have been discovered by this method[10].

Direct imaging

This method aims at obtaining a direct image of an extrasolar planet. In visible light, however, only stellar light scattered by the planet can be observed.

The luminosity L_{Pl} of a planet due to scattered light is:

$$L_{Pl} \propto \left(\frac{R_{Pl}}{a}\right)^2 L_*, \qquad (1.3.16)$$

where L_* is the luminosity of the star, R_{Pl} is the planet's radius and a the semi major axis of the orbit (*Brown and Burrows*, 1990). *Brown and Burrows* (1990) estimated a brightness ratio $L_{Pl}/L_* = 10^{-8}$ for a cloudy planet with $R_{Pl} = 0.13\, R_{Jup}$ and a semi major axis of 1 AU.

In the infrared, the contrast is much higher, especially for young hot planets. For example, the 5 Jupiter mass giant planet 2M1207b is 0.025 as bright in the infrared (L' band) as the 25 Jupiter mass brown dwarf it orbits (Figure 1.7, *Chauvin et al.* (2004)).

---

[10]As listed by the Exoplanet catalog http://www.exoplanet.eu/catalog.php maintained by Jean Schneider from the Observatoire de Paris by 11th February 2012
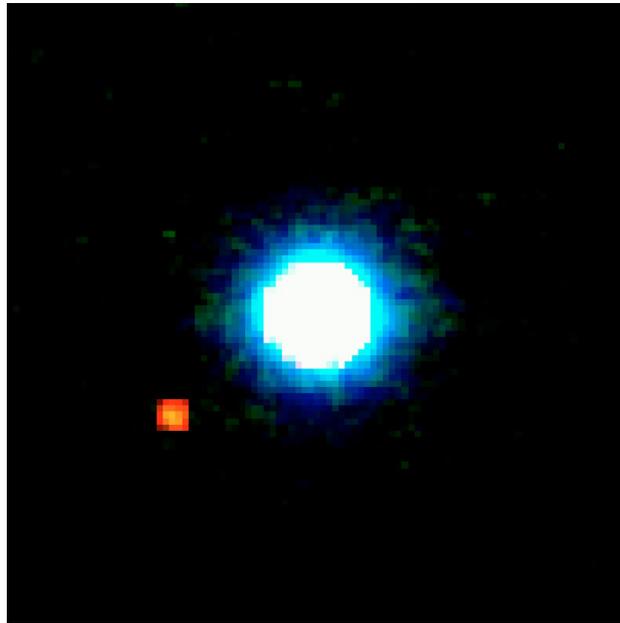
Figure 1.7: Composite image of the brown dwarf 2M1207 and its gas giant companion in the infrared (*Chauvin et al.*, 2004).

This detection method is sensitive to young hot planets (a few tens of million years old) around faint stellar or substellar objects. This work, however, focuses on older systems whose stars have settled on the main sequence. Furthermore, the planets found by direct imaging are so far away from their star that tidal interactions between them are negligible.

To date, 31 planets in 27 planetary systems have been discovered by direct imaging[11].

Transit method

The transit method aims for the detection of the shallow dip in a photometric lightcurve of a star caused by the transit of a planet (Figure 1.8). The depth of

---

[11]As listed by the Exoplanet catalog http://www.exoplanet.eu/catalog.php maintained by Jean
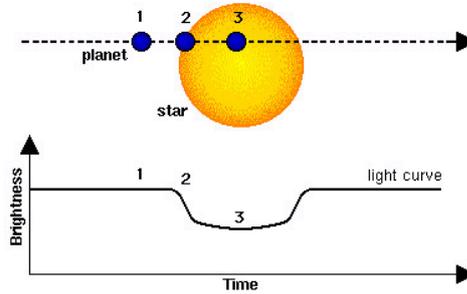
Figure 1.8: As the planet passes in front of its star, the apparent brightness of the star decreases by ΔF (Credit: Hans Deeg, ESA).

a transit $D_{Transit}$ is determined by the following ratio:

$$D_{Transit} = \frac{\Delta F}{F} = \left(\frac{R_{Pl}}{R_*} \right)^2 , \tag{1.3.17}$$

where F is the observed mean flux before and after the transit, ΔF is the flux difference during transit and R_{Pl} and R_* are the planet's and star's radius, respectively. When the spectral type of the star is known, the planet's radius can be inferred immediately. This is the only method that yields the radius of a planet so far.

The transit detection requires accurate star flux monitoring, as can be shown by calculating the transit depth $D_{Transit}$ for Solar System planets: The Jupiter transit leads to a $\approx 1\%$ reduction of the solar flux, the Neptune transit reduces the solar flux by 0.13% and the Earth transit by 0.0084%.

A transit, however, is only visible if the line-of-sight is parallel or nearly parallel to the orbital plane of the planet ($i \approx 90°$) (Figure 1.9). Let γ be the angle between two rays from the top of the star and the bottom of the star of radius R_* that meet the planet at semi major axis a_{Pl}. The same rays span a sphere segment S at distance $a_{Pl} + y$ between star and observer on Earth.

Schneider from the Observatoire de Paris by 11th February 2012
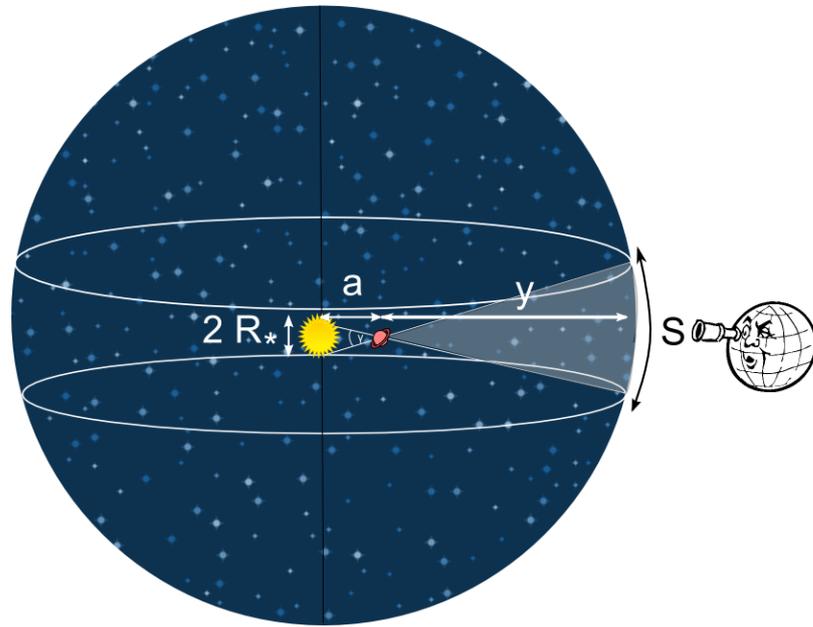
Figure 1.9: Probability to observe a transit from Earth.

The probability $P_{Transit}$ to observe a transit is the ratio of the small segment $2\pi(y+a_{Pl})S$, within which the transit is visible, over the whole sphere surface $4\pi(y+a_{Pl})^2$. Because $y \gg a_{Pl}$ and with the relations $S = \gamma y$ and $2R_* = \gamma a_{Pl}$, the following equation is derived for $P_{Transit}$:

$$P_{Transit} = \frac{R_*}{a_{Pl}}. \tag{1.3.18}$$

The Earth has a 0.42% probability to be observed by a transit by a distant observer, for Jupiter the probability is even less: $P_{Transit} \approx 0.1\%$. For planets like 51 Pegasi b with $a_{Pl} \approx 0.05$ AU and a host star of radius $R_* \approx R_{Sun}$, the probability is about 10%. Therefore, the transit method predominantly finds large planets in close orbits. These represent 10% of the total planet population, assuming that planetary orbits can assume any inclination with respect to the line-of-sight.

The probability to observe a transit event is relatively small. Therefore, observation programs that use the transit method, like the CoRoT and Kepler space missions, monitor a large number of stars to maximize their yields of transiting planets. CoRoT, for example, observes $\approx 10\,000$ stars per star field every six months (*Carone et al.* (2011) among others).

Every transit detection has to be confirmed by radial velocity measurements (Section 1.3.1), because the mass of the planet can not be determined by the transit method. A combination of both methods yields the full parameter set of the system: true planetary mass M_{Pl}, planetary radius R_{Pl}, semi major axis a, eccentricity e, and even the density of a planet which is important to determine its composition.

The full set of planetary parameters and a good knowledge of stellar parameters like the age of the system and the stellar rotation period are very important for the investigations of tidal interactions between extrasolar planets and their host stars discussed in this work. The parameters of planetary systems detected by the transit method, especially those found by the space mission CoRoT, are very well determined and therefore this work focuses on these planets. The space mission Kepler also provided several exoplanets suitable for tidal interaction investigations, but at the time of the writing, the parameters of many Kepler.planets and their host stars were still under investigation. CoRoT-planets benefit from the fact that the CoRoT mission was launched several years earlier.

To date, 230 transiting planets have been found in 196 planetary systems[12].

---

[12]As listed by the Exoplanet catalog http://www.exoplanet.eu/catalog.php maintained by Jean Schneider from the Observatoire de Paris by 11th February 2012

1.4 CoRoT

The space telescope CoRoT (COnvection ROtation and planetary Transits) was launched on 27th December 2006 (*Baglin*, 2003). It orbits the Earth in a polar orbit and is the first space telescope dedicated to the search for extrasolar planets (Figure 1.10). CoRoT is observing several star fields in the galaxy since May 2007

© CNES - Octobre 2005/Illus. D. Ducros
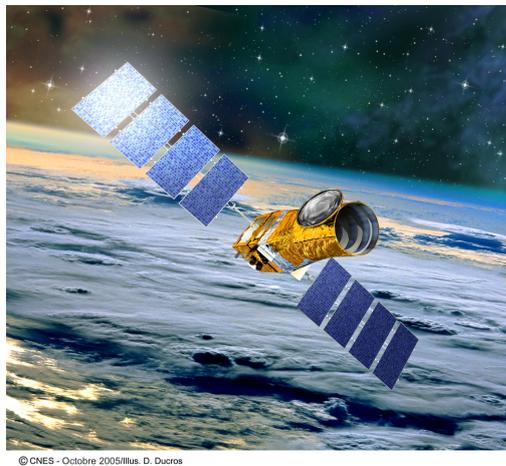
Figure 1.10: Artistic view of the satellite CoRoT in polar orbit around Earth (CNES, D.Ducros).

(see *Carpano et al.* (2009), *Cabrera et al.* (2009), and *Carone et al.* (2011), Figure 1.11). The transit method used by CoRoT is complemented with ground based follow up measurements using the radial velocity method. The CoRoT mission is particularly well endowed in terms of manpower and telescope time. This allows to fully characterize the planetary system to great precision. Even the stellar rotation rate is known for all CoRoT systems. In contrast to that, the stellar rotation rates for many other extrasolar planet systems are not constrained at all. As will be shown in Sections 2.6, 2.7 and 3.1.2, the knowledge of the stellar rotation is indispensable
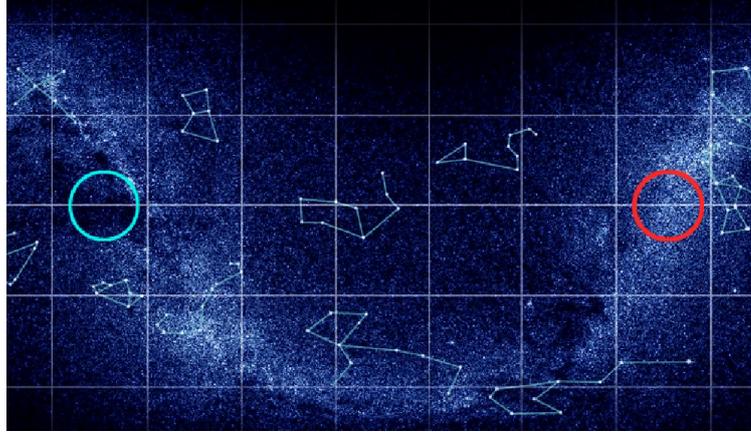
Figure 1.11: The CoRoT 'eyes' in the night sky (diameter:10°). The 'red' circle is observed in summer and contains the Aquila constellation. The 'blue' circle is observed in winter and lies in the Monoceros constellation (CNES).

Planet type	CoRoT planet
Gas Giant	CoRoT-1b, CoRoT-2b, CoRoT-4b, CoRoT-5b, CoRoT-6b, CoRoT-8b, CoRoT-9b, CoRoT-10b, CoRoT-11b, CoRoT-12b, CoRoT-13b, CoRoT-14b, CoRoT-16b, CoRoT-17b, CoRoT-18b, CoRoT-19b, CoRoT-20b, CoRoT-21b
Brown Dwarf	CoRoT-3b, CoRoT-15b
Super Earth	CoRoT-7b

Table 1.1: Planet types discovered by the CoRoT space mission.

for the investigation of tidal interactions. At the time of writing, the full parameter set of twenty-one CoRoT planetary systems is known. Table 1.1 lists the gas giant planets, brown dwarfs and terrestrial planets found by the CoRoT space mission. The stellar and planetary parameters are given in Tables 1.2 and 1.3, respectively. The stellar rotation period and planetary revolution period are listed in Table 1.4. The references for each system are listed in the Appendix (Table A.1).

As can be seen from Table 1.1, many CoRoT planets are massive companions like gas giants and brown dwarfs with small semi major axes. Even one Super Earth,

CoRoT-7b, with an extremely close orbit was discovered. Therefore, the CoRoT planets provide an interesting test field for the investigation of tidal interactions with very well determined parameters.

Furthermore, the author's working group is directly involved in the CoRoT mission and therefore the author had access to data in the proprietary phase (see *Grziwa et al.* (2012) for a description of the analysis of CoRoT data). The data for the CoRoT planets CoRoT-19b-21b were, for example, not public at the time of writing. In addition, the CoRoT planets present several interesting tidal interaction scenarios, as will be shown in Chapter 4, that allow a consistent comparative analysis of tidal interactions in planetary systems from a single data source.

Systems	Spectral type	Stellar Mass $[M_{Sun}]$	Stellar Radius $[R_{Sun}]$	Stellar Rotation Period $[days]$	Stellar Age $[Gyrs]$
CoRoT-1	G0V	0.95 ± 0.15	1.11 ± 0.05	$10.8^{+2.6}_{-1.8}$	-
CoRoT-2	G7V	0.97 ± 0.06	0.902 ± 0.018	3.85 ± 0.17	$0.5^{+3.5}_{-0.3}$
CoRoT-3	F3V	1.37 ± 0.09	1.56 ± 0.09	3.85 ± 0.17	$1.6 - 2.8$
CoRoT-4	F8V	1.1 ± 0.03	1.15 ± 0.03	$9.2^{+1.7}_{-1.3}$	$0.7 - 2$
CoRoT-5	F9V	1 ± 0.2	1.19 ± 0.04	> 30	$5.5 - 8.3$
CoRoT-6	F9V	1.05 ± 0.05	1.025 ± 0.026	7 ± 1	$2.5 - 4$
CoRoT-7	G9V	0.91 ± 0.03	0.82 ± 0.04	$22^{+66}_{-9.4}$	$1.2 - 2.3$
CoRoT-8	K1V	0.88 ± 0.04	0.77 ± 0.02	$19.5^{+19.5}_{-6.5}$	$1.7^{+0.6}_{-0.5}$
CoRoT-9	G3V	0.99 ± 0.04	0.94 ± 0.04	≥ 13.6	$0.15 - 8$
CoRoT-10	K1V	0.89 ± 0.05	0.79 ± 0.05	$20^{+6.6}_{-4}$	$1 - 3$
CoRoT-11	F6V	1.27 ± 0.05	1.37 ± 0.03	1.4 ± 0.3	$1 - 3$
CoRoT-12	G2V	1.08 ± 0.08	1.12 ± 0.1	$57^{+\infty}_{-28}$	$3 - 9$
CoRoT-13	G0V	1.09 ± 0.02	1.01 ± 0.03	$12.8^{+4.3}_{-2.6}$	$0.12 - 3$
CoRoT-14	F9V	1.13 ± 0.09	1.21 ± 0.08	$12.8^{+4.3}_{-2.6}$	$0.4 - 0.8$
CoRoT-15	F7V	1.32 ± 0.12	$1.46^{+0.3}_{-0.14}$	3.9 ± 0.4	$1 - 3$
CoRoT-16	G5V	1.1 ± 0.08	1.19 ± 0.14	≥ 60	6.7 ± 2.8
CoRoT-17	G2V	1.04 ± 0.10	1.59 ± 0.07	18 ± 2	10.7 ± 1.0
CoRoT-18	G9V	0.95 ± 0.15	1.03 ± 0.10	5.4 ± 0.4	0.6 ± 0.4
CoRoT-19	F9V	1.21 ± 0.06	1.65 ± 0.04	14.0 ± 2.4	5 ± 1
CoRoT-20	G2V	1.14 ± 0.08	1.02 ± 0.05	11.5 ± 2.6	$0.1^{+0.8}_{-0.04}$
CoRoT-21	F8IV	1.29 ± 0.09	1.95 ± 0.21	9.0 ± 2.8	4.1 ± 0.5

Table 1.2: Stellar parameters of CoRoT-1 to -21.

Planet	Planetary Mass [M_J]	Planetary Radius [R_J]	Semi Major Axis [AU]	Orbit Ecc.
CoRoT-1b	1.03 ± 0.12	1.49 ± 0.08	0.0254 ± 0.0004	0
CoRoT-2b	3.31 ± 0.16	1.465 ± 0.029	0.0281 ± 0.0009	0
CoRoT-3b	21.66 ± 1	1.01 ± 0.07	0.057 ± 0.003	0
CoRoT-4b	0.72 ± 0.08	1.19 ± 0.06	0.090 ± 0.001	$0 - 0.1$
CoRoT-5b	$0.467^{+0.047}_{-0.024}$	1.39 ± 0.05	0.0495 ± 0.0003	0
CoRoT-6b	2.96 ± 0.34	1.166 ± 0.035	0.0855 ± 0.0015	< 0.1
CoRoT-7b	0.024 ± 0.004	$0.0172 \pm 2 \times 10^{-4}$	0.0172 ± 0.0002	0
CoRoT-8b	0.22 ± 0.03	0.57 ± 0.02	0.063 ± 0.001	0
CoRoT-9b	0.84 ± 0.07	1.05 ± 0.04	0.407 ± 0.005	0.11 ± 0.04
CoRoT-10b	2.75 ± 0.16	0.97 ± 0.07	0.1055 ± 0.0021	0.53 ± 0.04
CoRoT-11b	2.33 ± 0.34	1.43 ± 0.03	0.044 ± 0.005	0
CoRoT-12b	0.92 ± 0.07	1.44 ± 0.13	0.04016 ± 0.0009	$0.07^{+0.06}_{-0.04}$
CoRoT-13b	1.308 ± 0.066	0.885 ± 0.014	0.051 ± 0.003	0
CoRoT-14b	7.6 ± 0.6	1.09 ± 0.07	0.027 ± 0.002	0
CoRoT-15b	63.3 ± 4.1	$1.12^{+0.3}_{-0.15}$	0.045 ± 0.01	0
CoRoT-16b	0.535 ± 0.085	1.17 ± 0.16	0.0618 ± 0.0015	0.3 ± 0.1
CoRoT-17b	2.45 ± 0.16	1.02 ± 0.07	0.0461 ± 0.0080	0
CoRoT-18b	3.47 ± 0.38	1.31 ± 0.18	0.0295 ± 0.016	< 0.08
CoRoT-19b	1.14 ± 0.05	1.45 ± 0.05	0.0518 ± 0.0008	0.047 ± 0.045
CoRoT-20b	4.24 ± 0.23	0.84 ± 0.04	0.092 ± 0.021	0.562 ± 0.013
CoRoT-21b	2.53 ± 0.37	1.30 ± 0.04	0.0417 ± 0.011	0

Table 1.3: Planetary parameters of CoRoT-1b to -21b.

System	Stellar Rotation Period	Planetary Revolution Period
	[days]	[days]
CoRoT-1	$10.8^{+2.6}_{-1.8}$	$1.5089557 \pm 6.4 \cdot \times 10^{-6}$
CoRoT-2	3.85 ± 0.17	$1.7429964 \pm 1.7 \times 10^{-6}$
CoRoT-3	3.85 ± 0.17	$4.2568 \pm 5 \times 10^{-6}$
CoRoT-4	$9.2^{+1.7}_{-1.3}$	9.20205 ± 0.00037
CoRoT-5	$60^{+\infty}_{-30}$	$4.037896 \pm 1 \times 10^{-6}$
CoRoT-6	7 ± 1	$8.886593 \pm 4 \times 10^{-6}$
CoRoT-7	$22^{+66}_{-9.4}$	0.85359 ± 0.00059
CoRoT-8	$19.5^{+19.5}_{-6.5}$	$6.21229 \pm 3 \times 10^{-5}$
CoRoT-9	≥ 13.6	95.2738 ± 0.0014
CoRoT-10	$20^{+6.6}_{-4}$	13.2406 ± 0.0002
CoRoT-11	1.4 ± 0.3	$2.99433 \pm 1 \times 10^{-5}$
CoRoT-12	$57^{+\infty}_{-28}$	$2.82805 \pm 5 \times 10^{-4}$
CoRoT-13	$12.8^{+4.3}_{-2.6}$	$4.03519 \pm 3 \times 10^{-5}$
CoRoT-14	$12.8^{+4.3}_{-2.6}$	$1.51214 \pm 1.3 \times 10^{-4}$
CoRoT-15	3.9 ± 0.4	$3.06036 \pm 3 \times 10^{-5}$
CoRoT-16	≥ 60	5.35227 ± 0.00020
CoRoT-17	18 ± 2	3.76813 ± 0.00026
CoRoT-18	5.4 ± 0.4	$1.9 \pm 2.8 \times 10^{-6}$
CoRoT-19	14.0 ± 2.4	$3.89713 \pm 1 \times 10^{-5}$
CoRoT-20	11.5 ± 2.6	9.244 ± 0.001
CoRoT-21	9.0 ± 2.8	2.72474 ± 0.00014

Table 1.4: Stellar rotation period of CoRoT-1 to -21 and planetary revolution of CoRoT-1b to -21b.

1.5 Overview of exoplanet properties

An overview of the extrasolar planet systems discovered so far and their properties are presented. Special emphasis is put on the relevance of the systems' properties for tidal interactions between the planets and their host stars[13].

Figure 1.1 shows the mass distribution of all known extrasolar planets. The existence of the brown dwarf desert is apparent: There is a deficiency of substellar companions more massive than thirteen Jupiter masses although they are much easier to detect. There is no shortage, on the other hand, of Jupiter mass planets, which are ideal candidates to test their influence on their host stars due to tidal forces. Figure 1.12 contains the distribution of the exoplanets' mass on logarithmic scale.
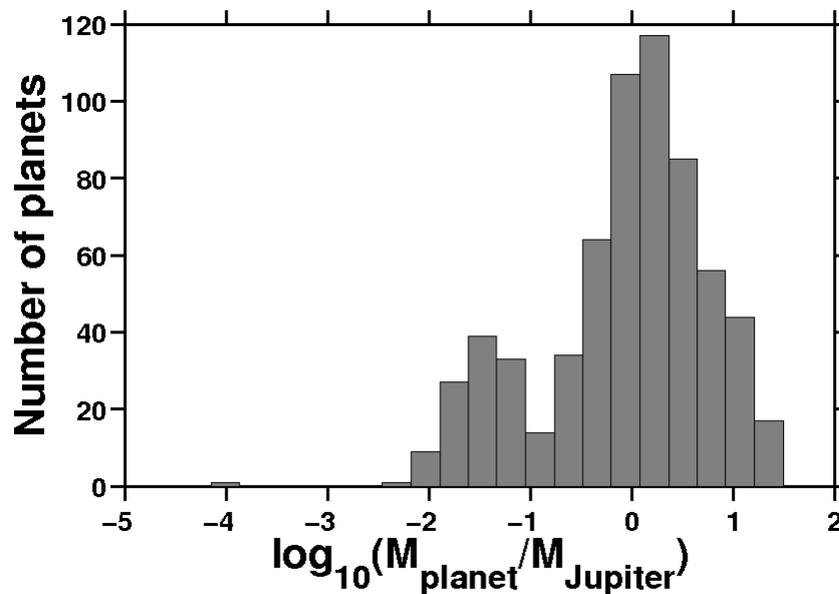
Figure 1.12: Histogram of the masses of all detected exoplanets in logarithmic scale.

---

[13]The parameters were taken once again from the Exoplanet catalog http://www.exoplanet.eu/catalog.php maintained by Jean Schneider from the Observatoire de Paris.

It reveals another interesting feature: a lack of Neptune planets with ≈ 0.1 Jupiter mass which can no longer be explained by detection bias. Indeed, *Carone et al.* (2011) discuss this point in terms of detection efficiency of CoRoT. CoRoT has the full capacity of finding short-period planets down to Super-Earth size but failed to detect Neptune planets in the first two observation years. The deficiency in short period Neptune planets found by Kepler (*Borucki et al.*, 2011) further supports the conclusion that such 'hot Neptunes', i.e., Neptune planets on close orbits are rare objects (*Mazeh et al.*, 2005). Either they do not form in such close proximity of the star or they are eroded by stellar irradiation (*Baraffe et al.*, 2004). The latter may explain the origin of the Super-Earths Kepler-10b and CoRoT-7b as core remnants of eroded Neptune planets. All of this, however, is still speculative. The left panel of
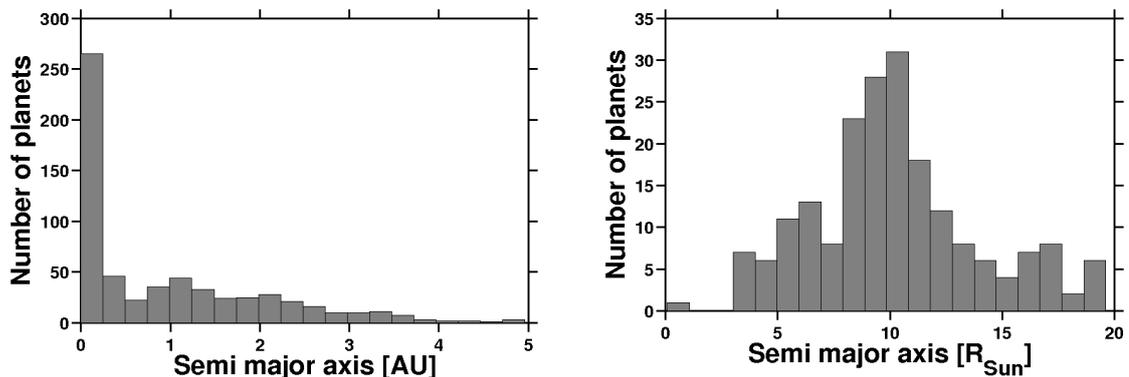
Figure 1.13: Left panel: Histogram of the semi major axis of all detected exoplanets. Right panel: Histogram of the semi major axis of exoplanets in close proximity to their star in units of solar radii.

Figure 1.13 shows the semi major axis distribution of all exoplanets. Most extrasolar planets were found in close proximity to their stars because the most successful exoplanet detection methods, transit detection and radial velocity, are sensitive to planets on close orbits.
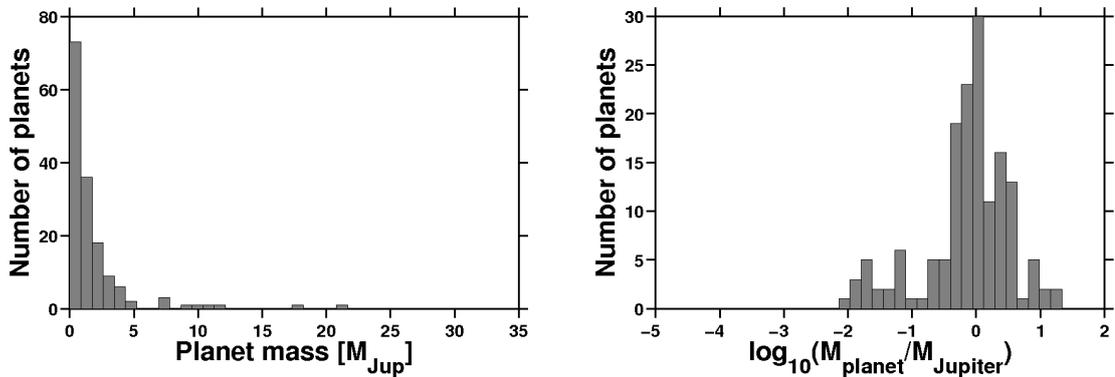
Figure 1.14: Left panel: Histogram of the masses of all detected transiting exoplanets. Right panel: Histogram of the masses of all detected transiting exoplanets in logarithmic scale.

It will be shown in the next chapter that the smaller the semi major axis and the greater the mass of the planet, the stronger the tidal forces acting on the planet and on the star. The distribution of the semi major axes of the exoplanets in very close proximity to their star (Figure 1.13, left panel) is not flat but peaks at 10 solar radii. The slope between 1 and 10 solar radii may hint at an erosion of such very massive extrasolar planets due to tidal forces.

This work focuses on transiting planets because for these the stellar and planetary parameters, particularly the planet's mass, are known to a better degree than for planets discovered by other methods. Figure 1.14 shows their mass distribution and Figure 1.15 shows their semi major axes distribution. Again, the majority of the transit planets are Jupiter-like with a deficiency of Neptune planets. About two hundred transiting planets orbit in very close proximity to their star, making them an ideal target for the investigations of tidal interactions.

The fact that so many close-in extrasolar planets proves the relevance of the investigation of orbital stability due to tidal interactions.
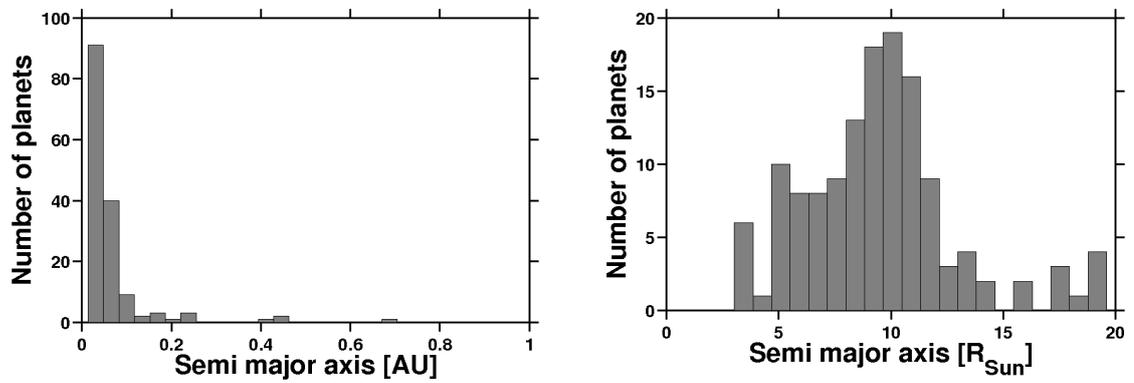
Figure 1.15: Left panel: Histogram of the semi major axis of all detected transiting exoplanets. Right panel: Histogram of the semi major axis of transiting exoplanets in units of solar radii.

Chapter 2

Theory of tidal interaction

The theoretical framework necessary to describe tidal forces will be presented. Special emphasis will be put on potential theory and the mathematical description of radial symmetric potentials in polar coordinates. It will be shown that extended bodies are deformed by tidal forces and that energy is dissipated within them. This leads to tidal friction which may change a planet's orbit and a star's rotation in secular time scales. The relevant equations will be derived for circular as well as for eccentric orbits.

A quick overview will be given on the timescales on which tidal friction acts in the Solar System and on the uncertainties of tidal friction timescales in exoplanet systems. The special case of the equilibrium state under tidal friction will be presented and its stability will be discussed. Furthermore, the angular momentum evolution of main sequence stars and their moment of inertia will be presented, as both are needed to model stellar rotation evolution. Finally, the Roche limit is discussed. This is the distance at which a planet is tidally disrupted.

2.1   The gravitational potential

The gravitational potential for a point mass and an extended uniform sphere will be calculated (according to *Kertz* (1969)) to prepare the calculation of an extended body with an arbitrary mass distribution.

For a point mass M, the gravitational force at a distance r' is described by Newton's law of gravity:

$$\vec{F}_{\text{Gravity}}(r) = \frac{GM}{r'^2}\vec{\hat{r}},\tag{2.1.1}$$

where $G = 6.673 \times 10^{-11}\,\frac{\text{m}^3}{\text{kgs}^2}$ is the gravitational constant and $\vec{\hat{r}}$ is the unit vector of the position vector $\vec{r'}$ of the reference point in a coordinate system with the point mass as its origin.

The corresponding gravitational potential is:

$$\Phi(r) = -\frac{GM}{r'}.\tag{2.1.2}$$

For an extended body, a mass distribution $\int \mathrm{d}m$ needs to be considered.

In the following, the coordinates of a potential reference point in polar coordinates are r', θ', ϕ', the coordinates of a mass element $\mathrm{d}m$ are r, θ, ϕ.

2.1.1   The outer gravitational potential

The easiest case to consider is that of the gravitational potential of a homogeneous sphere of total mass M with radius R and constant density ρ as seen from a reference point P' at distance $r' \geq R$ is (r' is measured from the center of mass):

$$\Phi_{\text{Gravity}}(r') = -\int_M \frac{G\,\mathrm{d}m}{\Delta},\tag{2.1.3}$$
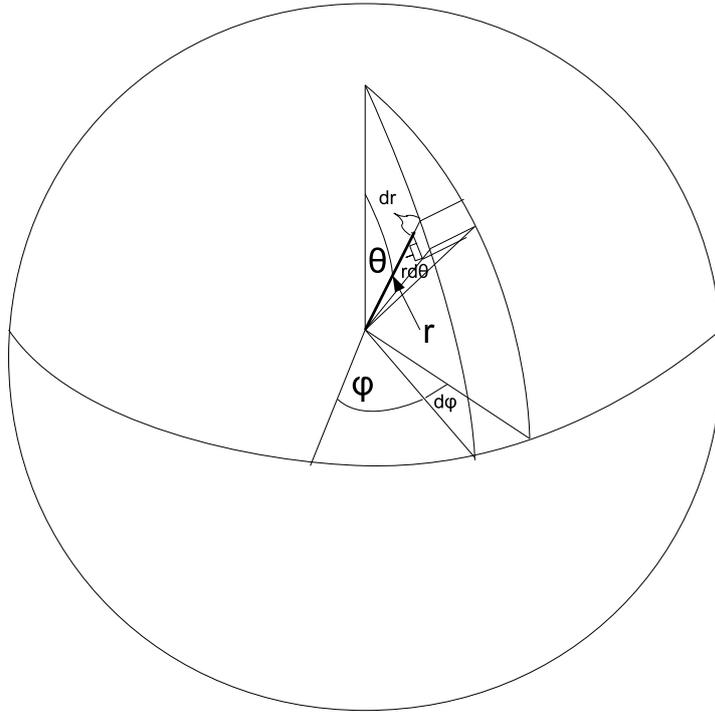
Figure 2.1: The parameters of the mass element $\mathrm{d}m$ in polar coordinates.

where $\mathrm{d}m$ is a mass element at distance $r \leq R$ from the center of mass and Δ is the distance between the mass element $\mathrm{d}m$ and the reference point.

For the mass element $\mathrm{d}m$ at position P the following holds in polar coordinates:

$$\mathrm{d}m = \rho\mathrm{d}V = \rho \cdot \mathrm{d}r \cdot r\,\mathrm{d}\theta \cdot r\sin\theta\,\mathrm{d}\phi, \qquad (2.1.4)$$

where r is the radial distance from the center of mass, θ is the colatitude measured from the polar axis and ϕ is the longitude (Figure 2.1).
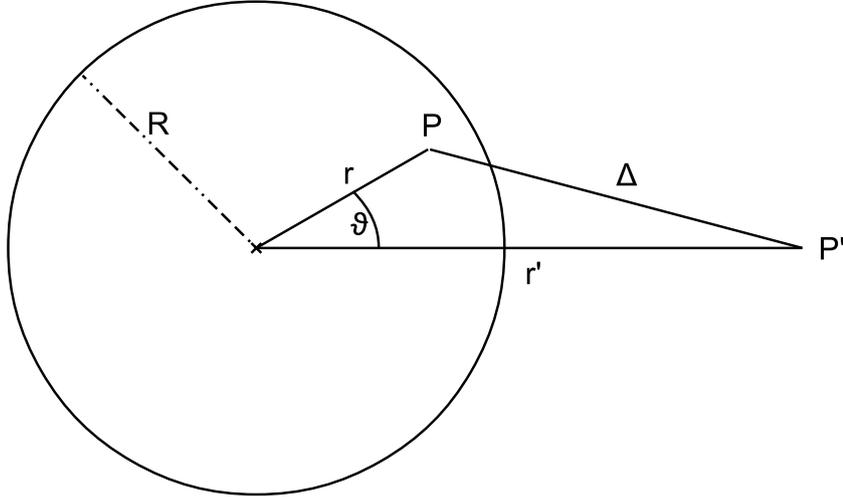
Figure 2.2: The distance Δ between P, the position of the mass element $\mathrm{d}m$, and the reference point P' in polar coordinates

For the distance Δ the following holds (Figure 2.2):

$$\Delta^2 = r'^2 + r^2 - 2r'r\cos\theta. \tag{2.1.5}$$

According to this, $\mathrm{d}\theta$ can be substituted by $\mathrm{d}\Delta$:

$$2\Delta\,\mathrm{d}\Delta = 2rr'\sin\theta\,\mathrm{d}\theta. \tag{2.1.6}$$

The outer gravitational potential is now:

$$\Phi_{\text{Gravity}}(r') = -G\rho \int_0^R \int_0^\pi \int_0^{2\pi} \frac{r^2\sin\theta}{\Delta}\,\mathrm{d}r\,\mathrm{d}\theta\,\mathrm{d}\phi \tag{2.1.7}$$

$$= -G\frac{2\pi\rho}{r'} \int_0^R r \left(\int_{r'-r}^{r'+r} \mathrm{d}\Delta \right) \mathrm{d}r$$

$$= -G\rho\frac{4\pi R^3}{3r'},$$

which is equal to the potential of a point mass M at the center of mass of the extended body because $\rho \frac{4\pi R^3}{3} = \rho \cdot V_{\text{Sphere}} = M$.

2.1.2 Inner gravity potential

The inner potential of a homogeneous sphere of radius R, mass M and density ρ is derived as seen from a reference point P' at distance $r' < R$ from the center of mass (again according to *Kertz* (1969)). It is useful to decompose the inner potential by considering the gravity potential of an inner homogeneous sphere of radius r and the remaining gravity potential of a spherical shell of thickness $R - r'$.

For the potential $\Phi_I(r')$ of the inner sphere the result of (2.1.7) is used. Here, the reference point lies on the surface of the inner sphere ($R_I = r'$) and therefore the potential is:

$$\Phi_I(r') = -G\rho \frac{4\pi r'^2}{3} = -\frac{GMr'^2}{R^3}, \tag{2.1.8}$$

where ρ was substituted by $\frac{3M}{4\pi R^3}$.

For the second part of the inner gravitational potential $\Phi_R(r')$, the potential of a homogeneous spherical shell, the following holds:

$$\begin{aligned}
\Phi_R(r') &= -G\rho \int_{r'}^{R} \int_{0}^{\pi} \int_{0}^{2\pi} \frac{r^2 \sin\theta}{\Delta} \, dr \, d\theta \, d\phi \\
&= -G\frac{2\pi\rho}{r'} \int_{r'}^{R} r \left(\int_{r-r'}^{r+r'} d\Delta \right) dr \\
&= -G2\pi\rho \left(R^2 - r'^2 \right).
\end{aligned} \tag{2.1.9}$$

Consequently, the total internal gravitational potential of a homogeneous sphere is:

$$\Phi_{int}(r) = \Phi_I(r') + \Phi_R(r') = -\frac{2}{3}\pi\rho G(3R^2 - r'^2) \tag{2.1.10}$$

The homogeneous spherical sphere is a very special case. It is, however, useful as a first approximation.

2.2   The role of Legendre polynomials in axial symmetric gravity potentials

In general, the gravitational potential of an extended body of arbitrary shape with inhomogeneous density distribution as seen from a point P' is the sum over the potential of all point masses m_i (the derivation was adapted from *Murray and Dermott* (1999)):

$$\Phi_{\text{gravity,body}}(r') = G \sum_i \frac{m_i}{\Delta} \tag{2.2.1}$$

or

$$\Phi_{\text{gravity,body}}(r') = G \int_V \frac{\rho(P_i)}{\Delta} \, dV_i, \tag{2.2.2}$$

where $\rho(P_i)$ is the density of the volume element dV_i at a point P_i inside the body with the coordinates $(\vec{r_i} = r_i, \theta_i, \phi_i)$. Δ is the distance between the mass element $dm_i = \rho(P_i) \, dV_i$ and the point of reference P' with the coordinates $(\vec{r'} = r', \theta', \phi')$(Figure 2.3). Δ can be described in terms of r_i and r' as:

$$\Delta^2 = r_i^2 + r'^2 - 2r'r_i \cos(\chi), \tag{2.2.3}$$

where χ is the angle between the vectors $\vec{r}$ and $\vec{r_i}$. The term $1/\Delta$ can be expanded binomially either with respect to r' or with respect to r_i:

$$\frac{1}{\Delta} = \begin{cases} \dfrac{1}{r'} \displaystyle\sum_{l=0}^{\infty} P_l(\cos \chi) \left(\dfrac{r_i}{r'}\right)^l & \text{if } r_i \leq r' \\[4mm] \dfrac{1}{r_i} \displaystyle\sum_{l=0}^{\infty} P_l(\cos \chi) \left(\dfrac{r'}{r_i}\right)^l & \text{if } r_i \geq r', \end{cases} \tag{2.2.4}$$
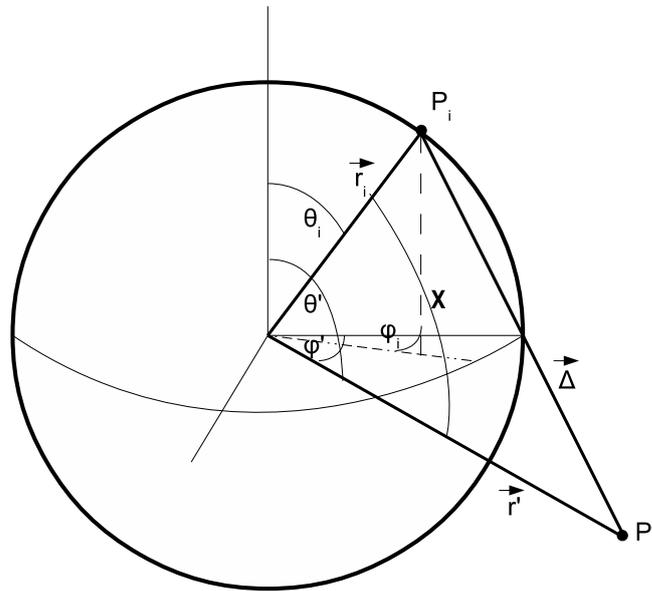
Figure 2.3: The potential of mass element at P_i as seen from an outer reference point P' in a spherical coordinate system.

where $P_l(\cos\chi)$ are the Legendre polynomials. They can be calculated using Rodrigues' formula (see *Murray and Dermott* (1999) among others):

$$P_l(x) = \frac{1}{2^l l!} \frac{\mathrm{d}^l (x^2 - l)^l}{\mathrm{d}x^l}. \tag{2.2.5}$$

The Legendre polynomials play an important role in the solution of potentials that satisfy the Laplace equation. This will be explained in more detail in the following section and follows the treatment given in *Murray and Dermott* (1999) and *Kertz* (1969).

2.2.1 Potential theory

Laplace's equation is:

$$\nabla^2 V = 0. \tag{2.2.6}$$

Transformed into spherical coordinates (r, θ, ϕ), this becomes:

$$\frac{\partial}{\partial r}\left(r^2 \frac{\partial V}{\partial r}\right) + \frac{\partial}{\partial \mu}\left((1 - \mu^2)\frac{\partial V}{\partial \mu}\right) + \frac{1}{1 - \mu^2}\frac{\partial^2 V}{\partial \phi^2} = 0, \tag{2.2.7}$$

where $\mu = \cos\theta$.

Any function V that satisfies the equation above can be decomposed into three functions, each of which depends only on either r, θ or ϕ, respectively. V is called a spherical solid harmonic. The solution of Laplace's equation can be derived by setting $V = r^n S_n(\mu, \phi)$, which contains two functions, one dependent only on r and the other dependent only on μ and ϕ. In the end, $S_n(\mu, \phi)$ has to factorize into two separate functions each dependent on μ and θ, respectively, for V to be a spherical solid harmonic.

Inserting $V = r^n S_n(\mu, \phi)$ into Laplace's equation yields:

$$\frac{\partial}{\partial \mu}\left((1 - \mu^2)\frac{\partial S_n}{\partial \mu}\right) + \frac{1}{1 - \mu^2}\frac{\partial^2 S_n}{\partial \phi^2} + n(n + 1)S_n = 0. \tag{2.2.8}$$

This is Legendre's equation and the function S_n is called a spherical surface harmonic of degree n. Legendre's equation can also be derived from Laplace's equation with the trial function $V = r^{-(n+1)} S_n(\mu, \phi)$. Therefore, the general solution of Laplace's equation (the spherical solid harmonic) is:

$$V = \sum_{n=0}^{\infty} \left(A_n r^n + B_n r^{-(n+1)} \right) S_n(\mu, \phi), \qquad (2.2.9)$$

where A_n and B_n are constants.

A more detailed treatment of the general solution can be found in *Kertz* (1969). In this work, however, axial symmetry is assumed: The situations discussed in the following do not depend on ϕ and consequently $(\partial^2 S_n)/(\partial \phi^2) = 0$. Therefore, Legendre's equation reduces to:

$$(1 - \mu^2) \frac{\partial^2 P_n(\mu)}{\partial \mu^2} - 2\mu \frac{\partial P_n(\mu)}{\partial \mu} + n(n+1) P_n(\mu) = 0. \qquad (2.2.10)$$

The Legendre polynomials $P_n(\mu)$ satisfy Laplace's equation under axial symmetry and are called zonal surface harmonics.

Surface harmonics have the important property that they are orthonormal and satisfy the following relation:

$$\int_0^{2\pi} \int_{-1}^{+1} Y_m(\mu, \phi) S_n(\mu, \phi) \mathrm{d}\mu \phi = 0 \qquad \text{if } m \neq n, \qquad (2.2.11)$$
$$= \frac{4\pi}{2n+1} \qquad \text{if } m = n,$$

where $Y_m(\mu, \phi)$ and $S_n(\mu, \phi)$ are two spherical surface harmonics of degree m and n, respectively. Here, the Schmidt or Gram-Schmidt orthonormalization over a unit sphere is used. A very useful property of this normalization is described in the following: Let P and P' be two points on a unit sphere with the angular coordinates
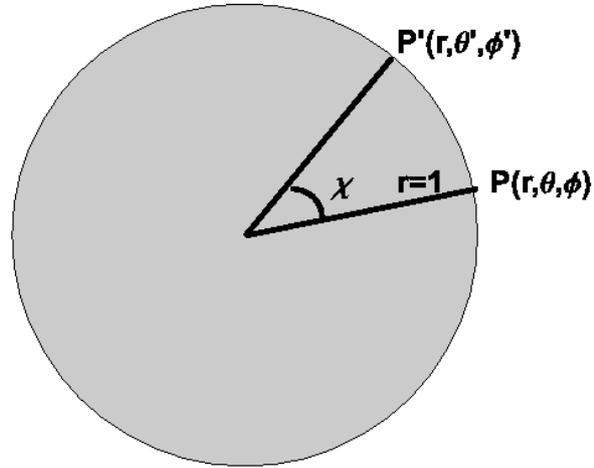
Figure 2.4: The location of two points P and P' on a unit sphere.

(θ, ϕ) and (θ', ϕ'), respectively, and let χ be the angle between the vectors $(r = 1, \theta, \phi)$ and $(r = 1, \theta', \phi')$ (Figure 2.4). Then:

$$\int_0^{2\pi} \int_{-1}^{+1} S_n(\mu', \phi') P_n(\cos \chi) \mathrm{d}\mu' \mathrm{d}\phi' = \frac{4\pi}{2n+1} S_n(\mu, \phi), \qquad (2.2.12)$$

where $\mu' = \cos \theta'$ and $\mu = \cos \theta$.

Applying this to the gravitational potential of an extended inhomogeneous body of arbitrary form and choosing a coordinate system such that its origin coincides with the center of mass, the gravitational potential at a reference point $P(r, \mu = \cos \theta, \phi)$ can be described as (see *Kertz* (1969) and *Murray and Dermott* (1999) for the derivation):

$$\Phi_{\text{gravity,body}}(P) = -\frac{GM}{r} \left[1 - \sum_{n=2}^{\infty} \sum_{m=0}^{n} \left(\frac{R}{r} \right)^n P_n^m(\cos \theta)(C_n^m \cos(m\phi) + S_n^m \sin(m\phi)) \right],$$

$$(2.2.13)$$

where

$$C_n^m = -\frac{1}{R^n M} \int_0^R \mathrm{d}r_i \int_{-1}^1 \mathrm{d}\mu_i \int_0^{2\pi} \mathrm{d}\phi_i \; \rho(P_i) r_i^{n+2} P_n^m(\mu_i) \cos(m\phi_i) \qquad (2.2.14)$$

$$S_n^m = -\frac{1}{R^n M} \int_0^R \mathrm{d}r_i \int_{-1}^1 \mathrm{d}\mu_i \int_0^{2\pi} \mathrm{d}\phi_i \; \rho(P_i) r_i^{n+2} P_n^m(\mu_i) \sin(m\phi_i), \qquad (2.2.15)$$

are integrated over a mass element $\mathrm{d}m_i$ at a point $P_i(r_i, \cos\theta_i = \mu_i, \phi_i)$ with density $\rho(P_i)$ and reflect the mass distribution within an extended body. The associated Legendre polynomials P_n^m are derived from the ordinary Legendre polynomials by:

$$P_n^m(\mu) = (-1)^m (1 - \mu^2)^{\frac{m}{2}} \frac{\mathrm{d}^m P_n(\mu)}{\mathrm{d}\mu^m}, \qquad (2.2.16)$$

with $m = 0, 1, 2, ...n$.

If the potential is axial symmetric with respect to ϕ, then m equals zero. In this case, the associated Legendre polynomials are equal to the ordinary Legendre polynomials ($P_n^0 = P_n$).

This is the theoretical framework - in terms of potential theory - that is needed as a basis for describing the tidal interaction between two bodies.

2.3   Tidal force and potential

The following is derived from *Murray and Dermott* (1999) and *Kertz* (1969). A situation is considered where a celestial object experiences tides due to the gravitational attraction of another body. The first object will be called from now on the primary and its parameters are denoted by the subscript P. The second object will be referred to as the secondary and its parameters are denoted by the subscript S. Furthermore, the mass of the primary is assumed to be much greater than the mass of the secondary: $M_P \gg M_S$. Both shall orbit a common center of mass that lies within the
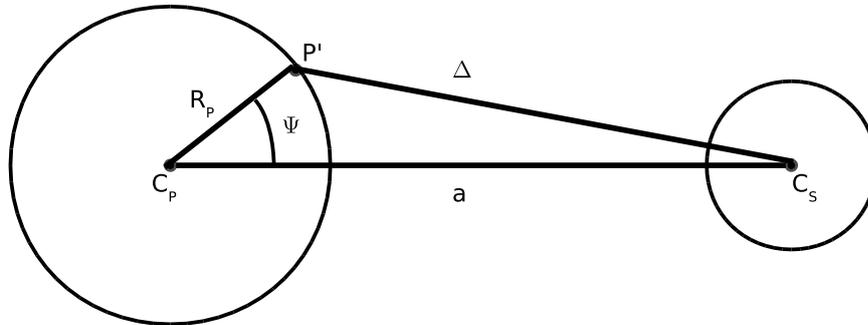
Figure 2.5: The relationships between the radius of the primary, R_P, the radius of the orbit of the secondary, a, and the distance Δ from a point P on the surface of the primary to the center of mass of the secondary.

primary. The orbit shall be circular with a radius a. In addition, a is much greater than the respective radii R_P and R_S of the primary and the secondary: $a \gg R_P$ and $a \gg R_S$. A coordinate system is chosen with its origin at the center of mass of the primary and the latitude Ψ is measured from the axis that points towards the secondary (Figure 2.5).

The gravitational field of the secondary at any position P' on the surface and within the primary is indistinguishable from that of a point mass M_S. The primary on the other hand is considered as extended: Mass elements $\mathrm{d}m$ at position P' within the primary have different distances Δ to the origin of the gravitational force, the center of mass of the secondary. Therefore, the gravitational field as seen from a reference point P' at the surface of the primary with the coordinates $(\vec{r'} = R_P, \Psi)$ is described by:

$$\Phi_{gravity,S}(P') = \frac{GM_S}{\Delta},$$

(2.3.1)

where Δ is:

$$\Delta = R_P^2 + a^2 - 2R_P^2 a \cos \Psi \quad \text{and } R_P \ll a. \tag{2.3.2}$$

Δ is expanded according to equation (2.2.4). Therefore, the gravity potential that is felt at the surface of the primary can be described by:

$$\Phi_{gravity,S}(P') = -\frac{GM_S}{a} \sum_{l=0}^{\infty} \left(\frac{R_P}{a}\right)^l P_l(\cos \Psi) \tag{2.3.3}$$

$$= -\frac{GM_S}{a} \left[1 + \left(\frac{R_P}{a}\right) \cos \Psi + \frac{1}{2} \left(\frac{R_P}{a}\right)^2 (3 \cos^2 \Psi - 1) + ...\right]$$

$$\approx V_1 + V_2 + V_3.$$

Only the leading three terms of the gravitational field are further considered. The corresponding force of this potential is derived by applying the gradient operator:

$$\frac{\vec{F}_{gravity,S}}{M_P} = -\nabla \Phi_{gravity,S}(P') \tag{2.3.4}$$

$$\approx -\nabla V_1 - \nabla V_2 - \nabla V_3.$$

The gradient of the first term of the potential, $-\nabla V_1$, is 0, because V_1 contains only constants [1]. Only V_2 and V_3 remain.

At the same time, $V_2 = -\frac{GM_S}{a^2} R_P \cos \Psi$ according to equation (2.3.3). Because the coordinate system was selected such that one of the axes is pointing along a (Figure 2.5), the gradient of the potential in the direction $R_P \cos \Psi$ is parallel to a, pointing towards the secondary. This gradient applied to V_2 yields:

$$-\frac{\partial V_2}{\partial R_P \cos \Psi} = \frac{GM_S}{a^2}. \tag{2.3.5}$$

---

[1]Note that this is the viewpoint as seen from a reference point P' at any point at the surface of the primary. When the position of the reference point changes, Δ changes as well, but the semi major axis a is constant in this context.
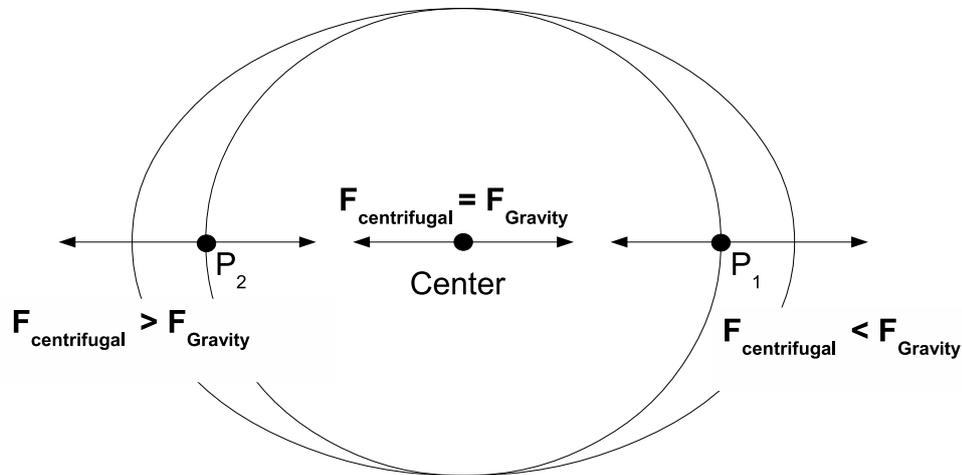
Figure 2.6: Centrifugal versus gravitational force at different points within the primary.

Gravity, however, is not the only force that needs to be considered. Because the primary and the secondary orbit around a common center of mass, a centrifugal force due to this motion arises as well. The difference between the centrifugal and the gravitational force is the tidal force (Figure 2.6).

The properties of the centrifugal force due to the motion of the primary on a gravitationally bound orbit is illustrated by Figure 2.7: All particles within the primary move on congruent circles if rotation is neglected. The corresponding centrifugal force is acting in the direction of the secondary parallel to a and is the same for every point within the primary in magnitude and direction. The magnitude of the centrifugal force is known for one point at least: For the center of mass it has to be equal to GM_PM_S/a^2, the gravitational force between the two point masses M_S and M_P.
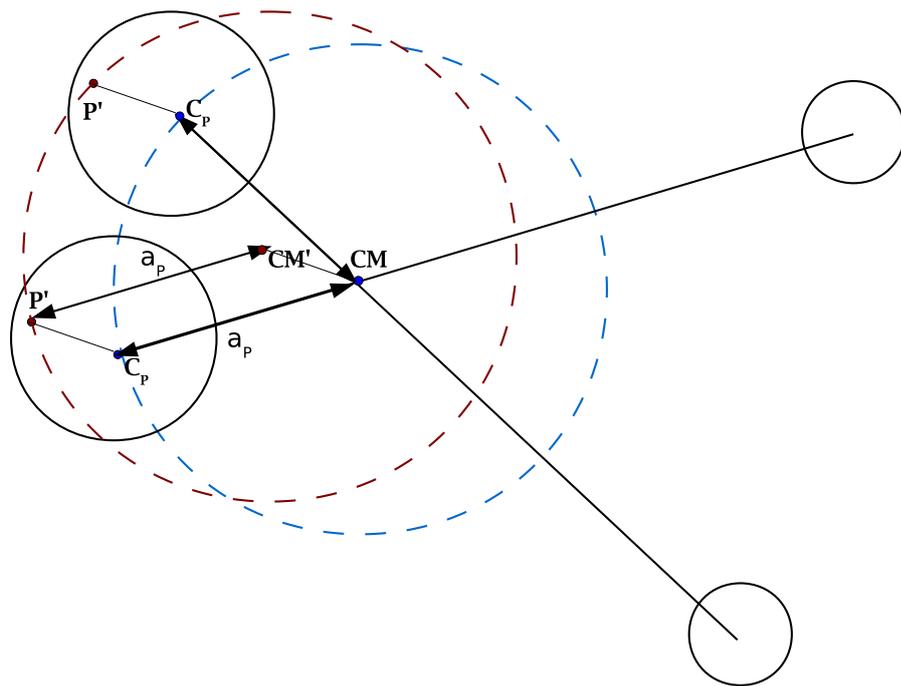
Figure 2.7: The particles in a primary move on circles of identical radii a_P, which is the distance from the primary's center of mass to the common center of gravity CM. This is illustrated by the movement of P' about the point CM' and the center of the primary C_P about CM. In this picture the rotation of the primary about its polar axis is neglected.

Therefore the force arising due to the potential V_2 is compensated by the centrifugal force at any point within the primary.

When the centrifugal force is subtracted from (2.3.3) only the force arising from the potential V_3 remains. This is the tidal force and V_3 is identical to the tidal potential V_{tide}:

$$V_{tide}(P') = \Phi_{gravity,S} - \Phi_{centrifugal} \tag{2.3.6}$$

$$\approx (V_1 + V_2 + V_3) - \Phi_{centrifugal}$$

$$= (\underbrace{V_1}_{\nabla V_1 = 0} + \underbrace{V_2}_{=\Phi_{centrifugal}} + V_3) - \Phi_{centrifugal}$$

$$= V_3$$

$$= -\frac{GM_S}{a}\left(\frac{r}{a}\right)^2 P_2(\cos\Psi).$$

The tidal force acting on any mass m within the primary at a reference point P' with coordinates $\vec{r'} = (r', \Psi)$ is:

$$\vec{F}_{tide}/m = -\nabla V_{tide}$$

$$= -\frac{\partial V_{tide}}{\partial r'}\hat{\vec{r'}} - \frac{1}{r'}\frac{\partial V_{tide}}{\partial \Psi}\hat{\vec{\Psi}}$$

$$= 2\frac{GM_S}{a^3}r'P_2(\cos\Psi)\hat{\vec{r'}} - 2\frac{GM_S}{a^3}r'\frac{3}{4}\sin(2\Psi)\hat{\vec{\Psi}}, \tag{2.3.7}$$

where $\hat{\vec{r'}}$ and $\hat{\vec{\Psi}}$ are the unit vectors in the direction of the r' and Ψ-axis of the coordinate system.

At the surface of the primary $(r' = R_P)$ the tidal potential is:

$$V_{tide}(R_P) = -\frac{GM_S R_P^2}{a^3}P_2(\cos\Psi) = -\zeta_P g_P P_2(\cos\Psi), \tag{2.3.8}$$

where

$$\frac{1}{2}\left(3\cos^2\Psi - 1\right) \tag{2.3.9}$$

is the Legendre Polynomial of degree $n = 2$ with respect to $\cos \Psi'$,

$$g_P = \frac{GM_P}{R_P^2} \tag{2.3.10}$$

is the gravitational acceleration on the surface of the primary, and the remaining terms are combined in ζ_P:

$$\zeta_P = \frac{M_P}{M_S} \left(\frac{R_P}{a} \right)^3 \cdot R_p \,. \tag{2.3.11}$$

$\zeta_P P_2(\cos \Psi)$ is the amplitude of the equilibrium tide for any angle Ψ on the surface of the primary. It reaches its maximum for $\Psi = 0, \pi$ and its minimum for $\Psi = \pi/2, 3\pi/2$. This explains why the tidal force produces two high tides and two low tides per rotation cycle.

2.4 Deformation of celestial bodies

2.4.1 Tidal deformation

Up to now, the primary was considered as spherical throughout the whole evaluation of the potential and forces. The shape of the primary, however, only assumes a spherical form if homogenous density is assumed and if the primary is only subjected to self-gravity. As was shown in the previous section, the mass elements of the primary are not only subjected to the gravitational but also to the tidal potential V_{tide}. This leads to a deformation of the primary, which will be elaborated in the following. The derivation according *Murray and Dermott* (1999) is given.

The mass elements of the surface are assumed to change their position until all the forces acting on them are in equilibrium. Therefore, the surface forms an equipotential surface. In the literature and also in this work, these outermost mass elements are
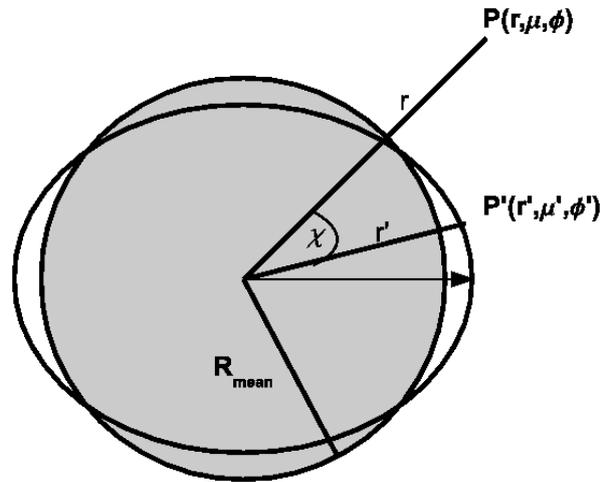
Figure 2.8: The deformation of a homogenous sphere due to the tidal potential.

sometimes called an 'ocean' because in this context they are assumed to behave like a fluid.

The total potential at the surface $(r' = R_P)$ of the primary is:

$$V_{total}(R_P, \Psi) = -\frac{GM_p}{R_P} - \zeta g P_2(\cos \Psi) + gh(\Psi), \qquad (2.4.1)$$

where $h(\Psi)$ is the height of the equipotential surface dependent on Ψ. It accounts for the deformation of the primary due to tides. For the surface to be an equipotential plane, $V_{total}(R_P, \Psi)$ has to be constant and, consequently, $h(\psi) \propto P_2(\cos \Psi)$ has to cancel out the ψ-dependency. Therefore, the primary takes the form of a prolate ellipsoid (like a rugby ball) with its elongated axis pointing towards the secondary (Figure 2.8).

If the primary would be an inflexible sphere covered by a shallow, zero-density fluid, then the surface would be equal to the equilibrium tide $h(\psi) = \zeta P_2(\cos \Psi)$. In

reality, however, the deformation $h(\psi)$ is not the equilibrium tide but deviates from this ideal form due to the self-gravity of the tidal bulge and the flexibility of the inner structures of the primary.

In general, the shape of a tidally deformed body is described by:

$$R(\Psi) = R_P \left[1 + \epsilon P_2(\cos \Psi)\right], \tag{2.4.2}$$

where $\epsilon \ll 1$ is a constant and $\epsilon P_2(\cos \Psi)$ is the true amplitude of the tidal bulge.

In addition, a flexible primary will change its mass distribution due to the tidal deformation. Therefore, its gravitational potential at the surface can no longer be described by $V_{gravity,undisturbed} = GM_P/R_P$.

To calculate the new gravitational potential as seen from point P (Figure 2.8) with the coordinates $(r, \mu = \cos \theta, \phi)$, the deviation from the sphere with radius $R_{mean} = R_P$ (the 'old' surface) is considered. The point $P'(r', \mu' = \cos \theta', \phi')$ on the tidally deformed surface can lie beneath or above the surface of this sphere. The colatitudes θ, θ' are this time measured from the axis of symmetry of the tidal bulge which points towards the secondary (Figure 2.8).

Let χ be the angle between the position vectors to P and P'. The total gravitational potential at point P can therefore be decomposed into several parts. First, into the internal and external gravity potential of a spherical body of radius R_{mean} (equations 2.1.7 and 2.1.10). Second, into the potential of the non-centric part of a thin layer of matter between the surface of the deformed body and the mean sphere, which needs to be added, when this layer lies above the mean radius, and which needs to be subtracted, when the layer lies below the mean radius.

At P', the radial thickness of this thin layer is according to equation (2.4.2) $dr' = \epsilon R_{mean} P_2(\mu')$ and $r' = R_{mean}$. The element of volume at this point is $r'^2\, dr'\, d\mu'\, d\phi' =$

$\epsilon R_{mean}^3 P_2(\mu')\,\mathrm{d}\mu'\,\mathrm{d}\phi'$. The distance between the points P and P' is Δ which again can be expanded binomially (see equation 2.2.4).

Because the height of the tidal bulge can lie either beneath or above R_{mean}, two cases are considered.

Case 1: Here, the internal potential of the non-central deformed mass distribution is derived. Because $r < R_{mean}$ holds, $\Delta = PP'$ can expanded as:

$$\frac{1}{\Delta} = \left(R_{mean}^2 + r^2 - 2R_{mean}r\cos\chi\right)^{-1/2} \tag{2.4.3}$$

$$= \frac{1}{R_{mean}}\sum_{n=0}^{\infty}\left(\frac{r}{R_{mean}}\right)^n P_n(\cos\chi).$$

Therefore, the internal gravitational potential due to the tidal bulge is:

$$V_{int,bulge} = -\frac{Gdm}{\Delta} \tag{2.4.4}$$

$$= -G\rho R_{mean}^2\epsilon\sum_{n=0}^{\infty}\left(\frac{r}{R_{mean}}\right)^n \int\int P_2(\mu')P_n(\cos\chi)\,\mathrm{d}\mu'\,\mathrm{d}\phi'$$

$$= -G\rho R_{mean}^2\epsilon\left(\frac{r}{R_{mean}}\right)^2\frac{4\pi}{5}P_2(\cos\theta)$$

$$= -\frac{4\pi}{5}\rho G r^2\epsilon P_2(\cos\theta).$$

The second last step in the calculations above follows from the special properties of the spherical harmonics given by equations (2.2.11) and (2.2.12).

The total internal potential of a roughly spherical but tidally deformed body is:

$$V_{int,total}(r,\theta) = V_{int,bulge}(r,\theta) + \Phi_{int}(r) \tag{2.4.5}$$

$$= -\frac{4}{3}\pi R_{mean}^3\rho G\left[\frac{3R_{mean}^2 - r^2}{2R_{mean}^3} + \frac{3r^2\epsilon P_2(\cos\theta)}{5R_{mean}^3}\right]$$

Case 2: Equivalently, the outer potential is derived ($r > R_{mean}$). $\Delta = PP'$ can then be expanded as follows:

$$\frac{1}{\Delta} = \frac{1}{r}\sum_{n=0}^{\infty}\left(\frac{R_{mean}}{r}\right)^n P_n(\cos\chi), \tag{2.4.6}$$
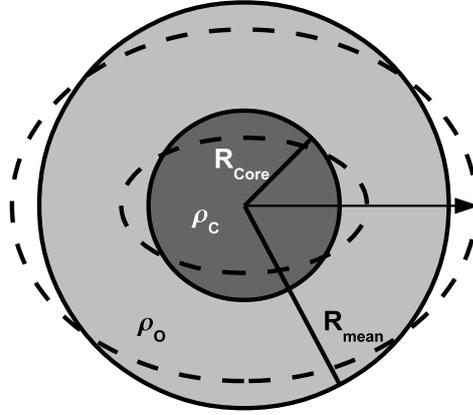
Figure 2.9: The tidal deformation of a two-component model planet of radius R_{mean} and density ρ_o and a core of radius R_{Core} and density ρ_c.

and the total external potential is:

$$V_{ext,total}(r,\theta) = -\frac{4}{3}\pi R_{mean}^3 \rho G \left[\frac{1}{r} + \frac{3R_{mean}^2}{5r^3}\epsilon P_2(\cos\theta)\right]. \qquad (2.4.7)$$

From the internal and external gravitational potential of a tidally deformed body, the true height $h(\psi)$ of the equipotential plane can be derived for a two-component planet of mean radius R_{mean} that consists of a homogenous, incompressible, fluid ocean of density ρ_O, and a homogeneous core of radius R_{Core} with density ρ_C. The core is assumed to be a solid body (Figure 2.9). To form equipotential planes, the shape of the core boundary and the ocean surface must have the following forms, where Ψ is measured again from the axis pointing towards the secondary:

$$R_{CB}(\Psi) = R_{Core}\left[1 + S_2 P_2(\cos\Psi)\right] \qquad (2.4.8)$$

$$R_{OS}(\Psi) = R_{mean}\left[1 + T_2 P_2(\cos\Psi)\right], \qquad (2.4.9)$$

where $S_2 \ll 1$ and $T_2 \ll 1$ are constants. Furthermore, ζ_C is the amplitude of the equilibrium tide at the core boundary:

$$\zeta_C = \frac{M_S}{M_C}\left(\frac{R_{Core}}{a}\right)^3 R_{Core}, \qquad (2.4.10)$$

where M_C is the mass of the tidally deformed core of the primary. The gravity acceleration g_C at the core boundary is:

$$g_C = \frac{GM_C}{R_{Core}^2} \qquad (2.4.11)$$

and $\tilde{\mu}$, the effective rigidity, is a dimensionless constant defined as:

$$\tilde{\mu} = \frac{19\mu}{2\rho_C g_C R_{Core}}, \qquad (2.4.12)$$

where μ is the modulus of rigidity which is defined as the ratio of shear stress to shear strain. If $\tilde{\mu} \ll 1$, the core acts like a liquid, if $\tilde{\mu} \gg 1$ the core hardly deforms at all under tidal deformation because elastic forces put up too much resistance.

The complete calculations of the tidal deformation of a two-component planet can be found in *Murray and Dermott* (1999).

In this two component model, the amplitudes of the tides in the core and in an outer ocean are:

$$R_{Core}S_2 = F\frac{(5/2)\zeta_C}{1+\tilde{\mu}} \qquad (2.4.13)$$

$$R_{mean}T_2 = H\frac{5\zeta}{2}, \qquad (2.4.14)$$

where F is a dimensionless number which quantifies the effect of the ocean on the amplitude of the core tide. H is the effect of the internal structure (elastic forces, gravitational forces) on the external shape of the whole body.

F and H are in general:

$$F = \frac{(1+\tilde{\mu})(1-\rho_O/\rho_C)(1+\frac{3}{2\alpha})}{1+\tilde{\mu}-\rho_O/\rho_C+(3\rho_O/2\rho_C)(1-\rho_O/\rho_C)-\frac{9}{4\alpha}(R_{Core}/R_{mean})^5(1-\rho_O/\rho_C)^2}$$

$$(2.4.15)$$

$$H = \frac{2\langle\rho\rangle}{5\rho_C}\left(\frac{1+\tilde{\mu}+\frac{3}{2}\left(\frac{R_{Core}}{R_{mean}}\right)^2 F\delta}{(1+\tilde{\mu})(\delta+2\rho_O/5\rho_C)}\right),$$

$$(2.4.16)$$

where $<\rho> = M_P/(4/3\pi R_{mean}^3)$ is the mean density,

$\alpha = 1+(5\rho_C)/(2\rho_O)\left(R_{Core}/R_{mean}\right)^3\left(1-\rho_O/\rho_C\right)^3$ and $\delta = \left(R_{Core}/R_{mean}\right)^3\left(1-\rho_O/\rho_C\right)$

(*Murray and Dermott*, 1999).

With this general relation, several special cases can be calculated. For example, when the core and the shallow ocean have the same density ($\rho_C = \rho_O$) then $F = 0$ and $H = 1$. The ocean tide is maximal, 2.5 times the amplitude of the equilibrium tide:

$$R_{mean}(T_2 - S_2) = \frac{5}{2}\zeta,$$

$$(2.4.17)$$

and the core is undeformed ($S_2 = 0$).

If a primary has a large solid core and a shallow ocean ($R_{core} \approx R_{mean}$, $\zeta_c \approx \zeta$), then the following can derived from the two-component model.

The amplitude of the ocean tide is:

$$R_{mean}(T_2 - S_2) = \frac{\tilde{\mu}\zeta}{1-\frac{\rho_O}{\rho_C}+\tilde{\mu}\left(1-\frac{3}{5}\frac{\rho_O}{\rho_C}\right)}.$$

$$(2.4.18)$$

Furthermore, if $\tilde{\mu} \to 0$ then the amplitude of the ocean tide approaches zero as well. The core is maximally deformed and the ocean just follows the form of the core.

The amplitude of the solid body tide, on the other hand, is $R_{Core}S_2$. In the case of a shallow ocean ($R_{core} \approx R_{mean}$), this is:

$$R_{mean}S_2 = \frac{5}{2}\zeta \left[\frac{1 - \frac{\rho_O}{\rho_C}}{1 - \frac{\rho_O}{\rho_C} + \tilde{\mu}\left(1 - \frac{3\rho_O}{5\rho_C}\right)} \right]. \qquad (2.4.19)$$

If the planet is ocean-free, then $\rho_O = 0$ and the solid body tide is:

$$R_{mean}S_2 = \frac{5}{2}\frac{\zeta}{1 + \tilde{\mu}}, \qquad (2.4.20)$$

which agrees with the expression derived by Lord Kelvin (*Thomson*, 1863*a,b*).

2.4.2 Rotational Deformation

The mathematical framework for describing tidal deformation is also useful for describing rotational deformation. Here again the description in *Murray and Dermott* (1999) is used. It is assumed that the tidal as well as the rotational deformations are small, such that they can be calculated independently and added to each other linearly (*Dermott*, 1979*a*).

At first, a spherical rigid body rotating with angular rotation rate Ω about the polar axis is investigated (Figure 2.10). Again, axial symmetry with respect to ϕ is assumed. Consequently, the centrifugal potential depends on r and θ only, where θ is measured from the polar axis of rotation this time. Note that this coordinate system differs from the one previously used where θ was measured from an axis pointing towards the secondary.

The centrifugal potential $V_{cf}(r,\theta)$ at a point $P(r,\theta)$ is:

$$V_{cf}(r,\theta) = -\frac{1}{2}\Omega^2 r^2 \sin^2\theta. \qquad (2.4.21)$$
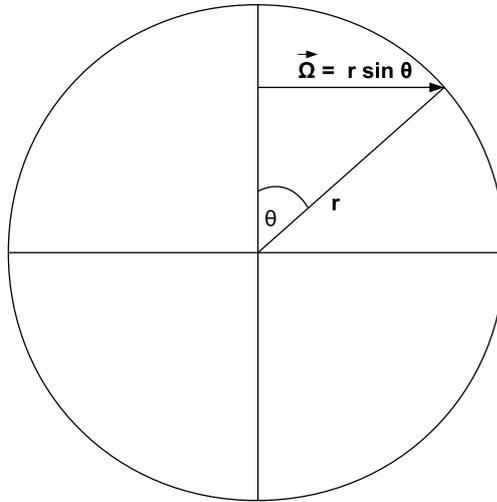
Figure 2.10: Centrifugal force in a primary rotating about its polar axis with the rotation rate Ω in a coordinate system where the angle θ is measured from the rotation axis.

This can also be written as:

$$V_{cf} = \frac{1}{3}\Omega^2 r^2 \left[P_2(\cos\theta) - 1\right].\qquad(2.4.22)$$

A rigid core with a shallow, zero density ocean is assumed as a simple approach to the potential solution. The total potential the fluid experiences at the surface is:

$$V_{total}(R_P, \theta) = -\frac{GM_P}{R_P} + V_{cf}(R_P, \theta),\qquad(2.4.23)$$

where M_P and R_P are the mass and mean radius of the rotating body.

The distortion of the ocean from the surface δr is small and its surface can be described by:

$$r_{surface} = R_P + \delta r(\theta).\qquad(2.4.24)$$

The equipotential on the ocean surface can be derived by inserting $r_{surface}$ into

equation (2.4.23) and using a Taylor approximation for terms depending on $R_P + \delta r$:

$$V_{total}(surface) \approx -\frac{GM_P}{R_P} + \frac{GM_P}{R_P^2}\delta r(\theta) - \frac{1}{2}\Omega^2 R_P^2 \sin^2\theta - \Omega^2 R_P \sin^2\theta\,\delta r(\theta). \quad (2.4.25)$$

If $\Omega^2 R_P \ll GM_P/R_P^2$, the last term can be neglected and the equation above solved for δr yields:

$$\delta r \approx \text{const} + \frac{\Omega^2 R_P^4}{2GM_P}\sin^2\theta. \quad (2.4.26)$$

It is obvious that the rotation of a spherical body about its polar axis will deform it to an oblate ellipsoid. The flattening of such an ellipsoid is defined as:

$$f = \frac{r_{eq} - r_{pole}}{r_{eq}}, \quad (2.4.27)$$

where the equatorial radius is

$$r_{eq} \approx R_P + \delta r(\theta = \pi/2, 3\pi/2) + \text{const} = R_P + \frac{\Omega^2 R_P^4}{2GM_P} + \text{const} \quad (2.4.28)$$

and the polar radius is

$$r_{pole} \approx R_P + \delta r(\theta = 0, \pi) + \text{const} = R_P + \text{const}. \quad (2.4.29)$$

Therefore, the flattening is approximately:

$$f \approx q/2 \quad (2.4.30)$$

where

$$q = \frac{\Omega^2 R_P^3}{GM_P} \quad (2.4.31)$$

is the dimensionless ratio of the centrifugal to the gravitational acceleration at the equator. The upper limit of the rotation rate of a planet is derived when $q \to 1$. Then equation (2.4.31) yields:

$$\Omega_{Max} \approx \left(\frac{GM_P}{R_P^3}\right)^{1/2} \approx 2 \cdot (G\langle\rho\rangle)^{1/2}, \qquad (2.4.32)$$

where $< \rho >$ is the mean density of the planet.

Up to now, the gravitational potential at the surface of the rotating planet was set equal to that of a rigid sphere. This approach neglects feedback effects on the gravitational potential due to the rotational deformation. Now, an improved model of the gravitational potential will be derived taking into account the oblate ellipsoidal form.

The external gravitational potential of such an axially symmetric ellipsoid is (equation 2.2.13 with $m = 0$):

$$\Phi_{rot}(r, \theta) = -\frac{GM_P}{r}\left[1 - \sum_{n=2}^{\infty} J_n \left(\frac{R_P}{r}\right)^n P_n(\cos\theta)\right] \qquad (2.4.33)$$

where M_P is the total mass, R_P is the radius and J_n are dimensionless constants that describe the mass distribution within the body. $P_n(\cos\theta)$ is the Legendre polynomial of degree n.

In general, values for J_n are calculated by:

$$J_n = \frac{1}{R_P^n M_P} \int_0^{R_P} \int_{-1}^{+1} r^n P_n(\mu = \cos\theta)\rho(r, \mu)2\pi r^2 \, d\mu \, dr, \qquad (2.4.34)$$

where $\rho(r, \mu)$ describes the internal density distribution. For roughly spherical bodies like stars and planets several simplifications can be made: If the northern and southern hemispheres are symmetric, then $J_3 = 0, J_5 = 0, J_7 = 0....$ J_2 is the leading term of the J_n-terms,. Indeed, if q is small, $J_n \propto q^{n/2}$ and higher order terms of J_n can be neglected.

Also, for a planet of uniform density, $J_2 = q/2$, and for a body of arbitrary density

according to MacCullaugh's theorem (*Mayor and Queloz*, 1995):

$$J_2 = \frac{C - 1/2(A+B)}{M_P R_P^2} \approx \frac{C - A}{M_P R_P^2},$$ (2.4.35)

where A, B, C are the three moments of inertia about the principal axes and $A = B$ under axial symmetry.

The total potential experienced by the ocean surface of a rotationally deformed planet is:

$$V_{total}(r, \theta) \approx -\frac{GM_P}{r} + \left[\frac{GM_P R^2}{r^3} J_2 + \frac{1}{3}\Omega^2 r^2 \right] P_2(\mu).$$ (2.4.36)

Inserting $r_{surface} = R_P + \delta r(\theta)$ into equation (2.4.36) and taking into account that $\delta r / R_P \ll 1$ yields:

$$\delta r = \text{const} - \left[J_2 + \frac{1}{3}q \right] R_P P_2(\mu).$$ (2.4.37)

This can be inserted into equation (2.4.27) to derive the flattening of a rotating planet with $P_2(\mu) = 1$ for $\theta = \pi/2$ and $P_2(\mu) = -1/2$ for $\theta = 0$:

$$f = \frac{3}{2}J_2 + \frac{q}{2}.$$ (2.4.38)

This is a more accurate description of the flattening f than $f \approx q/2$, as derived previously. Indeed, a good agreement is found when comparing observed versus calculated f for Earth and Jupiter: $f_{Earth,calculated} = 0.003349 \approx f_{Earth,observed} = 0.003353$ and $f_{Jupiter,calculated} = 0.0667 \approx f_{Jupiter,observed} = 0.0649$ (*Murray and Dermott*, 1999).

Now, the special case is considered of a secondary rotating with Ω_S and revolving around a primary of mass M_P in a circular and equatorial orbit with semi major axis a and mean revolution rate n. The rotation of the secondary shall by synchronized with the revolution $\Omega_S = n$. The centrifugal potential within the secondary at a point $P(r, \theta)$ according to equation (2.4.22) is:

$$V_{cf}(P) = \frac{1}{3}\Omega_S^2 r^2 P_2(\cos\theta),$$ (2.4.39)

where θ is the angle between the radius vector and the vertical rotation axis.

The tidal potential acting acting on the secondary is according to (2.3.6):

$$V_{tide}(P) = -\frac{GM_P}{a^3}r^2P_2(\cos\chi),\qquad(2.4.40)$$

where χ is the angle between the radius vector and the axis orientated along the line joining the centers of the primary and the secondary. In general, the angles θ and χ are completely independent of each other because the centrifugal and tidal potential have different axes of symmetry (Figure 2.11).
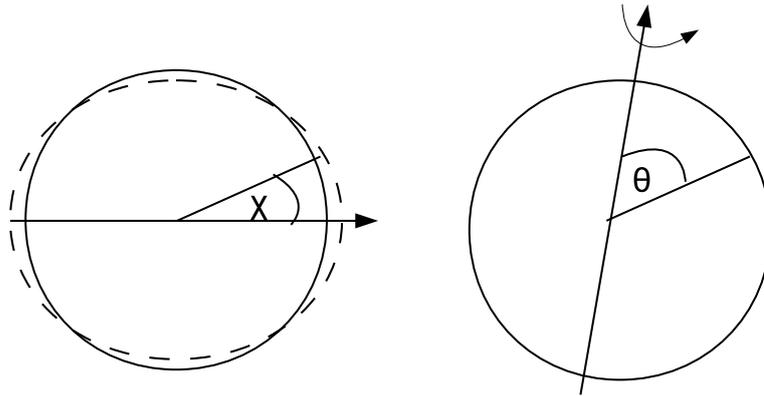
Figure 2.11: Left: Symmetry axis with respect to the tidal deformation. Right: Symmetry axis with respect to the rotation of the body.

It is assumed now that the symmetry axes are perpendicular to each other: $\theta \approx \pi/2 - \chi$. According to Kepler's third law because $\Omega_S = n$: $\Omega_S^2 = GM_P/a^3$. In that case, the tidal potential is:

$$V_{tide} = -\Omega_S^2 r^2 P_2(\cos\phi).\qquad(2.4.41)$$

As can be seen when comparing V_{tide} in this special case with Eq. 2.4.22, the amplitudes of V_{tide} and V_{cf} only differ by a factor of $\frac{1}{3}$. It will be shown in Section 3.2 that the rotation of short-period extrasolar planets is probably tidally locked with their revolution period. Therefore, the rotational deformation is only one third of the tidal deformation. Furthermore, because the revolution period is on the order of several days, the rotational flattening of a close-in extrasolar planet is in any case smaller than that of Jupiter which rotates relatively fast: $f_{Jupiter,observed} = 0.0649$ with a 10 hour rotation period. Consequently, the rotational flattening of the planets is neglected throughout this work.

The main sequence stars investigated in this work usually rotate with rotation periods in the order of ten days. Consequently, their rotational flattening is small and can be neglected as well.

2.5 Tidal waves in the forced damped oscillator framework

The following situation is considered: A tidal wave is raised on the primary by a secondary in a circular, equatorial orbit with orbital mean motion n. The primary, on the other hand, rotates with the angular speed Ω_P. If $\Omega_P \neq n$, the tide moves across the surface of the primary: It experiences tidal oscillations.

This corresponds to a situation of a forced damped harmonic oscillator whose equation of motion is:

$$m\frac{\mathrm{d}^2 x}{\mathrm{d}t^2} = -kx - \beta\frac{\mathrm{d}x}{\mathrm{d}t} + F_0\cos(\omega t), \qquad (2.5.1)$$

where x is the displacement from equilibrium, m is the mass, β is the damping

coefficient, k is the stiffness parameter, kx is the restoring force, F_0/m is the amplitude of the external driving force, and ω the frequency of the driving force.

The equation of motion may also be written as:

$$\frac{\mathrm{d}^2 x}{\mathrm{d}t^2} = -\omega_0^2 x - \frac{1}{\tau_d}\frac{\mathrm{d}x}{\mathrm{d}t} + \frac{F_0}{m}\cos(\omega t), \tag{2.5.2}$$

where ω_0 is the resonance frequency of the oscillator, and τ_d is the damping timescale.

When the oscillator is underdamped, after an initial transient phase, the steady-state solution of the oscillation is:

$$x = A\cos(\omega t + \delta) \tag{2.5.3}$$

with

$$A = \frac{F_0}{m}\left[(\omega_0^2 - \omega^2)^2 + (\omega/\tau_d)^2\right]^{-1/2} \tag{2.5.4}$$

and

$$\tan\delta = -\frac{\omega/\tau_d}{\omega^2 - \omega_0^2}. \tag{2.5.5}$$

The phase shift δ of the forced oscillation with regard to the driving force F_0/m is always negative because the damping force opposes the driving force; more specific $-\pi < \delta \le 0$. In general, the phase shift δ depends on the frequency ω of the driving force but not on the amplitude F_0/m.

The phase shift δ can also be described via the specific dissipation function Q_P, defined by:

$$Q_P = \frac{2\pi E_0}{\Delta E}, \tag{2.5.6}$$

where ΔE is the energy dissipated per cycle and E_0 is the peak energy stored during once cycle. According to *Efroimsky and Williams* (2009) for tidal waves this is

$$Q_P = \frac{|\omega_0^2 - \omega^2|}{\omega/\tau_d}. \tag{2.5.7}$$

Therefore δ and Q_P are related to each other via:

$$\tan|\delta| = \frac{1}{Q_P}.$$ (2.5.8)

If $\omega_0^2 \gg \omega^2 \gg (\omega/\tau_d)^2$, that is, if the system is not close to resonance

$$Q_P^{-1} = \frac{\omega/\tau_d}{\omega_0^2|1 - \frac{\omega^2}{\omega_0^2}|} \approx \frac{\omega/\tau_d}{\omega_0^2}.$$ (2.5.9)

In this 'weak friction' case, the tidal dissipation factor Q_P is inversely proportional to the external driving frequency ω.

In the following, it is argued that a primary of mass M_P, on which tides are raised by the secondary of mass M_S, behaves like a damped oscillator where the driving force is the tidal force and the driving frequency ω is the tidal frequency $2|\Omega_P - n|$. This is twice the difference between the rotation rate of the primary and the revolution rate of the secondary on a Keplerian orbit. In this damped oscillator scenario the response of the oscillator to the external driving frequency, the formation of the tidal bulge, takes some time.

If $\Omega_P > n$, the tidal bulge is carried ahead of the secondary. If $\Omega_P < n$, the tidal bulge lags behind. In both cases, the angle ϵ between the symmetry axis of the tidal bulge and the line connecting the primary and the secondary is very small (Figure 2.12). This tidal lag corresponds to the phase shift in the forced oscillator framework for small angles: $2\epsilon = \delta \approx \tan\delta$. Therefore the tidal lag angle is connected by the following relation with the tidal dissipation factor:

$$2|\epsilon| = Q_P^{-1}.$$ (2.5.10)

2.6 Tidal torques

Due to the tidal lag, the tidal bulge is not symmetric around the line connecting the primary and the secondary's center (Figure 2.12). Therefore, the external gravity potential V_{ext} of the primary at the position $\vec{r}$ of the secondary gives rise to a torque acting on the secondary's revolution rate n that is (*Murray and Dermott*, 1999):

$$\vec{\Gamma} = \vec{r} \times \vec{F}_{ext}, \tag{2.6.1}$$

where

$$\vec{F}_{ext} = -m\nabla V_{ext} \tag{2.6.2}$$

and m is the mass the perturbing force $\vec{F}_{ext}$ acts upon. In this case, it is the mass of the secondary $m = M_S$.

Furthermore, only the component of the force $\vec{F}_{ext}$ perpendicular to the line connecting the centers of the primary and the secondary contributes to the torque:

$$F_\Psi = -\frac{M_S}{r}\frac{\partial V_{ext}}{\partial \Psi}, \tag{2.6.3}$$

where the angle Ψ is measured from the axis that is pointing towards the secondary. Furthermore, only the non-central gravitational potential part due to the tidal bulge $V_{nc,ext}$ contributes:

$$\Gamma = -M_S\frac{\partial V_{nc,ext}}{\partial \Psi}. \tag{2.6.4}$$

According to equation (2.4.7), $V_{nc,ext}$ is:

$$V_{nc,ext} = -\frac{3}{5}g_P\left(\frac{R_P}{r}\right)^3 R_P\epsilon_t P_2(\cos\Psi), \tag{2.6.5}$$

where R_P is the radius of the primary, $g_P = GM_P/R_P^2$ is the gravitational acceleration at the surface and ϵ_t is the tidal distortion (Eq. 2.4.2).

In Section 2.4.1, it was shown that the tidal deformation depends on the inner structure and that the tidal deformation can be described by:

$$R_P \epsilon_t = h_{2,P} \zeta_P,$$ (2.6.6)

where $h_{2,P}$ is a structure constant and $\zeta_P = M_S/M_P \left(R_P/a\right)^3 R_P$ is the amplitude of the equilibrium tide. Inserting into the non-central potential above and setting $k_{2,P} = 3/5 \cdot h_{2,P}$ yields:

$$V_{nc,ext} = -k_{2,P} \zeta g \left(\frac{R_P}{r}\right)^3 P_2(\cos \Psi).$$ (2.6.7)

The coefficients $k_{2,P}$ and $h_{2,P}$ were first introduced by A.E.H. Love and are called 'Love numbers'. *Murray and Dermott* (1999) state that '*They are mostly used as a convenient way to cloak our ignorance of a body's internal structure*'. If sufficient information about the inner structure is available, the Love numbers can be calculated or at least approximated.

If the outer surface of the tidally deformed primary is in hydrostatic equilibrium, then the total potential is constant at the surface: It is an equipotential plane.

The total potential on the surface is the sum over the central gravity potential at the deformed surface, the non-central gravity potential with $r = R_P$ and the already known tidal potential at the surface:

$$-\frac{GM_P}{r} - k_{2,P} \zeta g P_2(\cos \Psi) - \zeta g P_2(\cos \Psi) = \text{const.}$$ (2.6.8)

Substituting r with $r = R_P(1 + \epsilon_t)P_2 \cos \Psi$, the radius of a tidally deformed body, using a Taylor approximation and setting the sum over all $P_2(\cos \Psi)$-dependent terms equal zero to get a constant potential, yields:

$$k_{2,P} = \frac{R_P \epsilon_t}{\zeta} - 1.$$ (2.6.9)

For a two-component model as introduced by *Murray and Dermott* (1999) and outlined in section 2.4.1, $R_P \epsilon_t / \zeta = 5/2H$ and $k_{2,P} = 5/2H - 1$, where H can range between $2/5$ and 1 (eq. 2.4.14). For a homogenous solid body, on the other hand, are $h_{2,P} = 5/2 \cdot 1/(1+\tilde{\mu})$ and $k_{2,P} = 3/5 h_2 = 3/2 \cdot 1/(1+\tilde{\mu})$, where $\tilde{\mu}$, the effective rigidity, is the ratio of gravitational forces over elastic forces determining the tidal deformation. In any case, for the Love number $k_{2,P}$ the following is true: $0 \le k_{2,P} \le 3/2$.

From this, the torque Γ arising from the primary's non-central gravity potential at the position of the secondary $(r = a)$ can be derived:

$$
\begin{aligned}
\Gamma &= -M_S \frac{\partial V_{nc,ext}}{\partial \Psi} \\
&= k_{2,P} \frac{G M_S^2}{a^6} R_P^5 \frac{\partial P_2(\cos \Psi)}{\partial \Psi} \\
&= \frac{3}{2} k_{2,P} \frac{G M_S^2}{a^6} R_P^5 \sin(2\epsilon) \\
&= \frac{3}{2} k_{2,P} \frac{G M_S^2}{a^6} R_P^5 2\epsilon
\end{aligned}
\tag{2.6.10}
$$

In the last two steps, two facts are used: Firstly, the tidal bulge is displaced by the angle ϵ with respect to the line between the centers of masses. Secondly, ϵ is small so that $\sin(2\epsilon) \approx 2\epsilon$, which according to (2.5.10) equals Q_P^{-1}, where Q_P is the primary's tidal dissipation factor introduced in the forced damped oscillator framework.

This torque acts at a rate Γn on the secondary and an opposite torque acts at a rate $\Gamma \Omega_P$ on the primary, where n is the revolution rate of the secondary and Ω_P is the rotation rate of the primary. This effect is called tidal friction and if $\Omega_P \ne n$, angular momentum will be transferred between the orbit and the primary's rotation. At the same time, the total angular momentum L of the system is conserved i.e.

$\dot{L} = 0$:

$$\dot{L} = \frac{\mathrm{d}}{\mathrm{d}t} \left(C_P \Omega_P + \frac{M_P M_S}{M_p + M_S} a^2 n \right) = 0, \qquad (2.6.11)$$

where $C_P = I_P M_P R_P^2$ is the moment of inertia of the rotating primary and the normalized angular momentum I_P reflects the inner mass distribution.

From conservation of angular momentum, the following relation is derived:

$$C_P \dot{\Omega}_P = -\frac{M_P M_S}{2(M_P + M_S)} n a \dot{a}. \qquad (2.6.12)$$

Therefore, a change in the primary's rotation results in a change of semi major axis and the following conclusions can be drawn (Figure 2.12):

- If the primary is rotating faster than the secondary revolves, $\Omega_P > n$, the torque Γ decreases the rotation of the primary at a rate $\Gamma\Omega_P$ ($\dot{\Omega}_P < 0$). An equal and opposite torque increases the orbital revolution of the secondary at a rate Γn. Therefore, the semi major axis a increases ($\dot{a} > 0$). This is the case for the Earth-Moon-system.

- If the primary is rotating slower than the secondary revolves, $\Omega_P < n$, the torque Γ increases the rotation at a rate $\Gamma\Omega_P$ ($\dot{\Omega}_P > 0$). An equal and opposite torque decreases the orbital revolution at a rate Γn and the semi major axis decreases($\dot{a} < 0$). This is the case for the Mars-Phobos-system.

- If the secondary is in a retrograde revolution, the tidal bulge is always lagging behind the line joining the centers. Therefore, the torque Γ decreases the rotation of the primary at a rate $-\Gamma\Omega_P$, therefore $\dot{\Omega}_P < 0$). An equal and opposite torque decreases the orbital revolution at a rate $-\Gamma n$, and $\dot{a} < 0$. The semi major axis of the orbit decreases. This is the case in the Neptune-Triton-system.
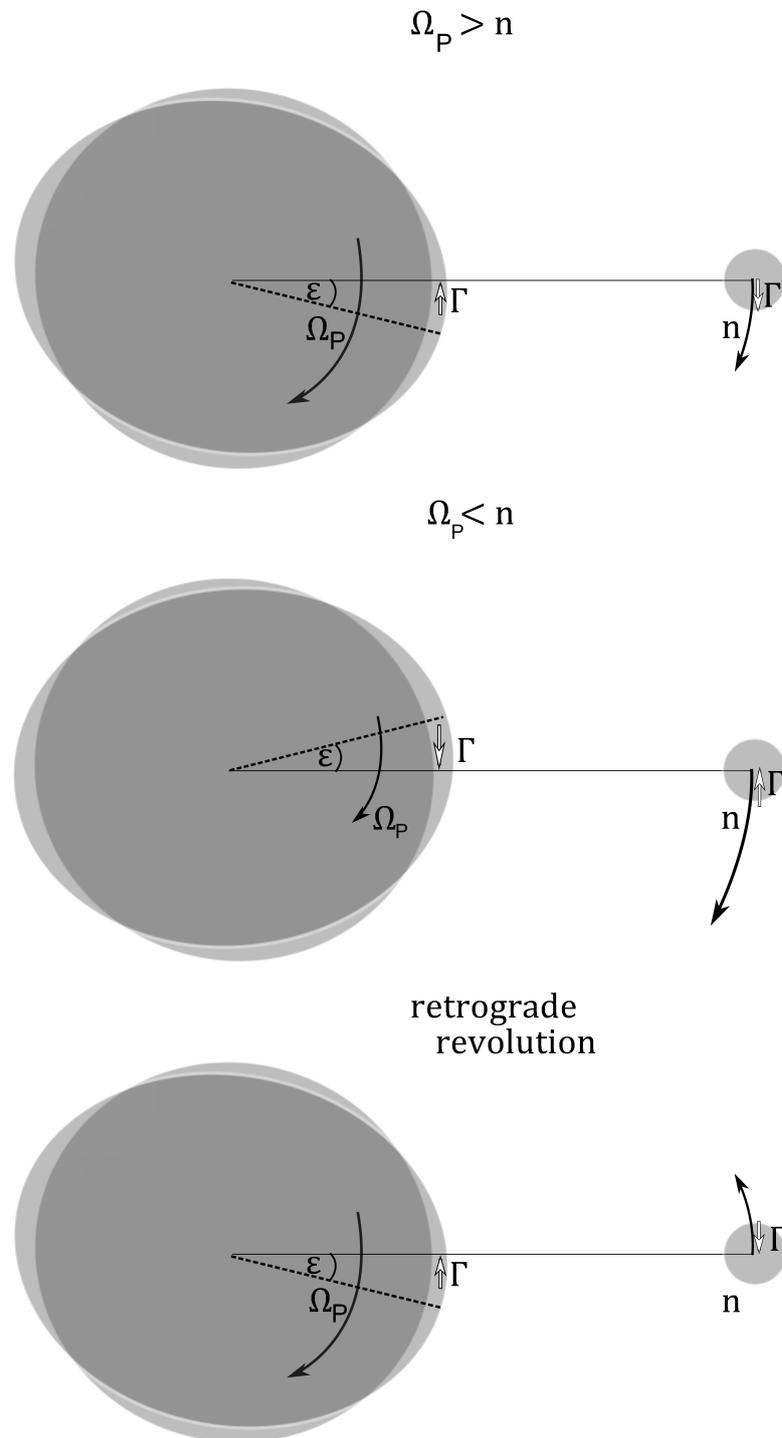
Figure 2.12: Upper panel: If the primary's rotation is faster than the secondary's revolution ($\Omega_P > n$), the tidal bulge is carried ahead the line connecting the two center of masses. The tidal torques decrease Ω_P and increase n.

Middle panel: If the primary's rotation is slower than the secondary's revolution ($\Omega_P < n$), the tidal bulge is lagging behind the line connecting the two center of masses. The tidal torques increase Ω_P and decrease n.

Lower panel: If the system is in retrograde revolution, the tidal torques decrease Ω_P and n.

While the total angular momentum is conserved, if $\Omega_P \neq n$, the total dynamical energy of the system decreases at a rate:

$$\dot{E} = -\text{sign}(\Omega_P - n)\Gamma(\Omega_P - n). \tag{2.6.13}$$

This energy is dissipated within the primary as frictional heat. The rate of energy dissipation depends on the structure and the energy dissipation mechanisms within. *Murray and Dermott* (1999) point out that *'...it is the rate of energy dissipation that determines the rate of orbital evolution'.* Consequently, the orbital evolution is intricately linked with the inner structure of the primary. It should be noted that the model described in this Section, keeps the tidal dissipation factor Q_P constant with time.

The total dynamical energy of the system affected by the tidal torques is the sum of the rotational energy of the primary and the orbital energy of the system. The rate of change of total energy is therefore:

$$\dot{E} = \frac{\mathrm{d}}{\mathrm{d}t}\left(\frac{1}{2}C_P\Omega_P^2 - \frac{GM_PM_S}{2a}\right) = C_P\Omega_P\dot{\Omega}_P + \frac{GM_PM_S}{2a^2}\dot{a}. \tag{2.6.14}$$

By inserting Kepler's third law $G(M_P + M_S) = n^2a^3$, the equation above can be expressed as:

$$\dot{E} = C_P\Omega_P\dot{\Omega}_P + \frac{M_PM_S}{2(M_P + M_S)}n^2a\dot{a}. \tag{2.6.15}$$

Now equation (2.6.12) is inserted:

$$\dot{E} = -\frac{M_PM_S}{2(M_P + M_S)}na\dot{a}(\Omega_P - n). \tag{2.6.16}$$

Combined with equations (2.5.10), (2.6.10), (2.6.13), (2.6.16), and Kepler's third law, the rate of change in the semi major axis a is derived:

$$\dot{a} = \text{sign}(\Omega_P - n)\frac{3k_{2,P}M_S}{Q_PM_P}\left(\frac{R_P}{a}\right)^5 na. \tag{2.6.17}$$

Inserting equation (2.6.17) into equation (2.6.12) yields the rate of change of angular velocity:

$$\dot{\Omega}_P = -\text{sign}(\Omega_P - n)\frac{3k_{2,P}}{2I_PQ_P}\frac{M_S^2}{M_P(M_P + M_S)}\left(\frac{R_P}{a}\right)^3 n^2. \qquad (2.6.18)$$

Tidal torques due to tides raised by the secondary on the primary are not the only torques affecting such a system. There are also tidal torques due to tides raised by the primary on the secondary that need to be considered. These result in angular momentum transfer between the secondary's rotation and the orbit and in energy dissipation within the secondary whose rate is scaled by Q_S.

The relevant equations describing the semi major axis and secondary's rotation evolution are:

$$\dot{a}_S = \text{sign}(\Omega_S - n)\frac{3k_{2,S}M_P}{M_S}\left(\frac{R_S}{a}\right)^5 na \qquad (2.6.19)$$

$$\dot{\Omega}_S = -\text{sign}(\Omega_S - n)\frac{3k_{2,S}}{2I_SQ_S}\frac{M_P^2}{M_S(M_P + M_S)}\left(\frac{R_S}{a}\right)^3 n^2. \qquad (2.6.20)$$

Therefore, the complete tidal evolution of the system due to the displacement of the tidal bulges on the primary and the secondary from the line connecting the centers of masses can be found by adding equations (2.6.19, 2.6.17) and combining them with (2.6.20) and (2.6.18). In the next chapter, however, it will be found that for most planetary systems discovered in this work, $\Omega_S \approx n$ is a good assumption. Therefore, $\dot{a}_S \approx 0$ and $\dot{\Omega}_S \approx 0$.

As a consequence, the long-term evolution of the semi major axis can be calculated by integrating Eq. (2.6.17) at first order. This yields for evolution in the past:

$$\frac{2}{13}a_0^{13/2}\left[1 - \left(\frac{a_i}{a_0}\right)^{13/2}\right] = \text{sign}\left(\Omega_P - n\right)\frac{3k_{2,P}}{Q_P}\left(\frac{G}{M_P}\right)^{1/2}R_P^5 M_S\Delta t_{past} \qquad (2.6.21)$$

where a_i is the initial, a_0 is the current semi major axis and $\Delta t_{past} > 0$ is the elapsed time; assuming that the orbit was approximately circular during Δt_{past}, that $M_S \ll M_P$ and that either $\Omega_P > n$ or $\Omega_P < n$ during the whole integration time.

For evolution in the future this yields:

$$\frac{2}{13}a_0^{13/2}\left[\left(\frac{a_e}{a_0}\right)^{13/2} - 1\right] = \text{sign}\,(\Omega_P - n)\frac{3k_{2,P}}{Q_P}\left(\frac{G}{M_P}\right)^{1/2} R_P^5 M_S \Delta t_{future}, \quad (2.6.22)$$

where a_0 is the current, a_e is the future semi major axis and Δt_{future} is the time needed to achieve the future position. This relation is used in this work to estimate tidal evolution time scales for circular orbits (Section 4.1 and Section 8.4.2).

2.7 Tidal evolution of eccentric orbits

Up to now, the orbit was assumed to be circular which is a good approximation for many planets and moons in our Solar System. In the past years, extrasolar planets on short-period orbits with large eccentricities were found. The orbit of CoRoT-10b, for example, has $e = 0.5$. Therefore, the equations derived in the previous section for circular orbits no longer hold. *Hut* (1981) calculates the force arising due to the non-central gravity potential of the tidal bulge for a secondary on an eccentric orbit using a different derivation than the one in the previous section following *Murray and Dermott* (1999). *Hut* (1981) calculates the perturbed gravitational force between the primary and the secondary due to two point masses at the surface of the primary which represent the two tidal bulges. For $e = 0$, the tidal torques derived by *Murray and Dermott* (1999) and *Hut* (1981) are the same. This will be shown by comparing the Ψ-component of the force acting perpendicular to the line connecting the centers of masses which is the only relevant force-component when the orbit is circular.

Hut (1981) derives:

$$F_\Psi = 3G\frac{M_S^2}{r^2}\left(\frac{R_P}{r}\right)^5 k_{2,P}\tau_P\left(\Omega_P - \dot{\Psi}\right), \tag{2.7.1}$$

where $\dot{\Psi}$ is the instantaneous revolution rate, Ψ is the true anomaly of the orbit, τ_P is a small time lag for the tidal bulge to form on the primary. Furthermore, r is the distance between the primary's and secondary's center of mass, which can vary between $a(1 \pm e)$ for eccentric orbits, $k_{2,P}$ is the Love number[2]. F_Ψ creates a torque $\Gamma = rF_\Psi$ on the secondary.

Comparing this torque Γ with the torque calculated in the previous section shows that the equations (2.6.10) and (2.7.1) are equal for $e = 0$, $r = a$, and $\dot{\Psi} = n$. For a circular orbit

$$\tau_P(\Omega_P - n) = \epsilon, \tag{2.7.2}$$

where ϵ is again the tidal lag angle introduced in the forced oscillator framework, $2|\epsilon| = Q_P^{-1}$ (see eq. (2.5.10)). If the system is not close to resonance and weakly damped, i.e., if the damping time scale τ_d is large, then equation (2.5.7) holds:

$$Q_P^{-1} = \frac{|\omega|/\tau_d}{\omega_0^2}, \tag{2.7.3}$$

where ω_0 is the resonance frequency which is a constant property of the primary and $\omega = 2|\Omega_P - n|$ is the frequency of the tidal waves. Consequently, the time lag $\tau_P = 1/(\tau_d\omega_0^2)$ is indeed small and constant as required by *Hut* (1981). τ_P and Q_P are connected for circular orbits via the following relation:

$$Q_P^{-1} = 2|\Omega_P - n|\tau_P. \tag{2.7.4}$$

---

[2] *Hut* (1981) calls $k_{2,P}$ the apsidal motion constant.

This relation describes one factor that causes much confusion when comparing literature on tidal interactions from the planetary science and the astronomy community. Whereas the first group often uses the tidal dissipation Q_P to quantify the strength of tidal friction and keeps this parameter constant over time, the latter group often uses the time lag τ_P to quantify the strength of tidal friction and keeps this parameter constant over time. As long as $\Omega_P - n \approx$ const, both approaches yield similar results. Care has to be taken when $\Omega_P - n$ is not constant over time. This will be discussed in more detail in subsequent chapters when applying the relevant equations.

The effect of the force component F_Ψ on the orbital parameters for the general case of eccentric orbits can be found by calculating the energy loss during one orbit under conservation of angular momentum. The sum of orbital angular momentum L_{orb} and rotational angular momentum of the primary $L_{rot,P}$ needs to be conserved under force F_Ψ, where the orbital angular momentum is:

$$L_{orb} = \frac{M_P M_S}{M_P + M_S} n a^2 \sqrt{1 - e^2},$$
(2.7.5)

and the rotational angular momentum is:

$$L_{rot,P} = I_P M_P R_P^2 \Omega_P.$$
(2.7.6)

The rate of change in orbital angular momentum is:

$$\dot{L}_{orb} = \frac{1}{2} \frac{M_P M_S}{M_P + M_S} n a \dot{a} \sqrt{1 - e^2} - \frac{M_P M_S}{M_P + M_S} n a^2 \frac{e \dot{e}}{\sqrt{1 - e^2}}.$$
(2.7.7)

The orbital energy is

$$E_{orb} = -G \frac{M_P M_S}{2a},$$
(2.7.8)

and its rate of change is:

$$\dot{E}_{orb} = \frac{\mathrm{d}}{\mathrm{d}t} \left(-G \frac{M_P M_S}{2a} \right) = G \frac{M_P M_S}{2a^2} \dot{a}.$$
(2.7.9)

The angular momentum of a barycentric orbit is connected to the position vector r and the mean anomaly Ψ by

$$L_{orb} = \frac{M_P M_S}{M_P + M_S} h, \tag{2.7.10}$$

where the constant h is

$$h = r^2 \dot{\Psi}, \tag{2.7.11}$$

and the position vector r in polar coordinates is:

$$r = a \frac{1 - e^2}{1 + e \cos \Psi}. \tag{2.7.12}$$

As was already stated, F_Ψ creates a torque $\Gamma = r F_\Psi$ on the secondary by the tides raised on the primary. The corresponding orbital energy loss is:

$$\Delta E_\Psi = \int_0^{2\pi} \Gamma \mathrm{d}\Psi = 3 G M_S^2 R_P^5 k_{2,P} \tau_P \int_0^{2\pi} \frac{\Omega_P - \dot{\Psi}}{r^6} \mathrm{d}\Psi. \tag{2.7.13}$$

Using the equations (2.7.5),(2.7.10), (2.7.12), integrating over Ψ, inserting the mean motion $n = \sqrt{G(M_P + M_S)} a^{-3/2}$ and dividing by the orbital period P_{orb} – which according to Kepler's third law is ($P_{orb} = 2\pi a^{3/2}/\sqrt{G(M_P + M_S)}$) – gives

$$\dot{E}_\Psi = -3 \frac{k_{2,P}}{T_P} G(M_P + M_S) \frac{M_S^2}{M_P} \left(\frac{R_P}{a} \right)^8 \frac{(1 - e^2)^{-15/2}}{a} f_2(e), \tag{2.7.14}$$

where T_P is the typical tidal time scale defined by *Hut* (1981) as $T_P = \frac{R_P^3}{G M_P \tau_P}$ and $f_2(e)$ is a function depending on e:

$$f_2(e) = \left(1 + 14 e^2 + \frac{105}{4} e^4 + \frac{35}{4} e^6 + \frac{35}{128} e^8 \right) \tag{2.7.15}$$
$$- \frac{\Omega_P}{n} (1 - e^2)^{3/2} \left(1 + \frac{15}{2} e^2 + \frac{45}{8} e^4 + \frac{5}{16} e^6 \right).$$

The corresponding change in semi major axis due to the loss of orbital energy is derived by using (2.7.9) and solving for $\dot{a}$:

$$\dot{a} = -6 \frac{k_{2,P}}{T_P} q(1 + q) \left(\frac{R_P}{a} \right)^8 a (1 - e^2)^{-15/2} f_2(e), \tag{2.7.16}$$

where the mass ratio $q = M_S/M_P$ is introduced.

The amount of orbital angular momentum transferred to the primary's rotation per orbit is calculated by:

$$\Delta L_{orb} = \int_{orbit} \Gamma \mathrm{d}t = \int_0^{2\pi} \Gamma \frac{\mathrm{d}\Psi}{\dot\Psi}. \tag{2.7.17}$$

It follows by integrating over Ψ and dividing by P_{orb}:

$$\frac{\mathrm{d}L_{orb}}{\mathrm{d}t} = -3\frac{k_{2,P}}{T}\sqrt{G(M_P + M_S)}\frac{M_S^2}{M_P}R_P^8 a^{-15/2}(1 - e^2)^{-6}f_3(e) \tag{2.7.18}$$

with

$$f_3(e) = \left(1 + \frac{15}{2}e^2 + \frac{45}{8}e^4 + \frac{5}{16}e^6\right) - \frac{\Omega_P}{n}(1 - e^2)^{3/2}\left(1 + 3e^2 + \frac{3}{8}e^4\right). \tag{2.7.19}$$

The change in eccentricity $\dot e$ is derived by using equation (2.7.7) and inserting $\dot a$ and $\dot L_{orb}$ as determined above:

$$\dot e = -\frac{3}{2}\frac{k_{2,P}}{T_P}q(1 + q)\left(\frac{R_P}{a}\right)^8(1 - e^2)^{-13/2}ef_4(e), \tag{2.7.20}$$

with

$$f_4(e) = \left(15 + \frac{225}{4}e^2 + \frac{225}{8}e^4 + \frac{75}{64}e^6\right) \tag{2.7.21}$$
$$- \frac{\Omega_P}{n}(1 - e^2)^{3/2}\left(11 + \frac{33}{2}e^2 + \frac{11}{8}e^4\right).$$

$\dot L_{orb}$ is transferred to the primary. The angular momentum of the primary is $I_P M_P R_P^2 \Omega_P$. I_P is the normalized moment of inertia. Therefore, the angular momentum transfer results in a change of the primary's rotation rate Ω_P which is derived by setting (2.7.18) equal to

$$\frac{\mathrm{d}L_{orb}}{\mathrm{d}t} = I_P M_P R_P^2 \frac{\mathrm{d}\Omega_P}{\mathrm{d}t} \tag{2.7.22}$$

and solving for $\dot{\Omega}_P$. This yields

$$\dot{\Omega}_P = 3\frac{k_{2,P}}{T}\frac{q^2}{I_P}\left(\frac{R_P}{a}\right)^6(1-e^2)^{-6}nf_3(e). \qquad (2.7.23)$$

In addition to F_Ψ, a radial force component arises due to the non-central gravity potential when the orbit is eccentric. The distance r between the primary and the secondary is not constant anymore.

As a reminder, the potential is (eq. 2.6.7):

$$V_{nc,ext}(r(t)) = -k_{2,P}\zeta_P g_P\left(\frac{R_P}{r(t-\tau_P)}\right)^3 P_2(\cos\Psi), \qquad (2.7.24)$$

where $k_{2,P}$ is the Love number, g_P and ζ_P are the surface gravity acceleration and the amplitude of the equilibrium tide on the primary. The tidal potential of the secondary acted at a time $t-\tau_P$ to form the tidal bulge, where τ_P is the tidal time lag, when the secondary was at a distance $r(t-\tau_P)$. At time t, when the displacement of the tidal bulge gives rise to a force acting on the secondary, this secondary is at distance $r(t)$. The distance $r(t-\tau_P)$ with respect to $r(t)$ is $r(t-\tau_P) \approx r(t) - \dot{r}\tau_P = r(t)(1-\frac{\dot{r}}{r}\tau_P)$. Inserting this into the potential and using Taylor approximation yields:

$$V_{nc,ext}(r) = -k_{2,P}\zeta_P g_P\left(\frac{R_P}{r(1-\frac{\dot{r}}{r}\tau_P)}\right)^3 P_2(\cos\Psi)$$

$$\approx -k_2\zeta_P g_P\left(\frac{R_P}{r}\right)^3(1+3\frac{\dot{r}}{r}\tau_P)P_2(\cos\Psi). \qquad (2.7.25)$$

Note that ζ_P, the amplitude of the equilibrium tidal bulge at the time of the tidal bulge formation due to the tidal potential of the secondary, is constant in this context. It does not change when the tidal bulge is displaced with respect to the line connecting the centers of masses. This is equivalent to stating that the height of the tidal bulge does not change between $t-\tau_P$ and t. Therefore, the radial force component F_r

due to the displacement of the tidal bulge acting on the secondary at distance $r(t)$ is derived from:

$$
\begin{aligned}
F_r &= -M_S \frac{\partial V_{nc,ext}(r)}{\partial r} \\
&\approx -3k_{2,P} M_S \zeta_P g_P \left(\frac{R_P}{r}\right)^3 \frac{(1 + 3\frac{\dot{r}}{r}\tau_P)}{r} \\
&= -3k_{2,P} G \frac{M_S^2}{r^2} \left(\frac{R_P}{r}\right)^5 (1 + 3\frac{\dot{r}}{r}\tau_P),
\end{aligned}
\qquad (2.7.26)
$$

where the boundary condition $\Psi(t) = \epsilon$ was used. $P_2(\cos \epsilon) \approx 1$ because the tidal lag angle is small: $\epsilon \ll 1$. In the last step $\zeta_P = \frac{M_S}{M_P} \left(\frac{R_P}{r}\right)^3$ and $g_P = \frac{GM_P}{R_P^2}$ were inserted. While ζ_P was constant during the tidal lag time τ_P, it is not constant over the whole orbit when this orbit is eccentric. ζ_P varies over time because the tidal force of the secondary, that forms the tidal bulge, varies over one orbit as the distance r between the primary and secondary alternatively grows and shrinks.

The corresponding energy loss ΔE due to the radial force F_r is computed by:

$$
\Delta E_{radial} = \int_{orbit} F_r \mathrm{d}r = \int_0^{2\pi} F_r \frac{\mathrm{d}r}{\mathrm{d}\Psi} \mathrm{d}\Psi.
\qquad (2.7.27)
$$

The radial force does not change the orbital angular momentum and therefore $\dot{L}_{orb} = 0$. (Note that for a circular orbit $\frac{\mathrm{d}r}{\mathrm{d}\Psi} = 0$ and $\Delta E_{radial} = 0$.) Using the equations (2.7.5), (2.7.10), (2.7.12) and integrating over Ψ yields:

$$
\Delta E_{radial} = -9\pi G^{3/2}(M_P + M_S)^{1/2} M_S^2 R_P^5 k_{2,P} \tau_P a^{-15/2}(1 - e^2)^{-15/2} f(e),
\qquad (2.7.28)
$$

where $f(e)$ is:

$$
f(e) = e^2 \left[1 + \frac{15}{4}e^2 + \frac{15}{8}e^4 + \frac{5}{64}e^6\right].
\qquad (2.7.29)
$$

ΔE_{radial} is negative as expected for a dissipative process. To derive the mean orbital energy loss $\dot{E}_{orb}$, ΔE_{radial} is divided by the orbital period P.

Consequently, $\dot{E}_{radial}$ is:

$$\dot{E}_{radial} = -\frac{9}{2}G^2(M_P + M_S)M_S^2 R_P^5 k_{2,P}\tau_P a^{-9}(1-e^2)^{-15/2}f(e). \qquad (2.7.30)$$

The change in the semi major axis $\dot{a}$ as a consequence of F_r acting on the orbit is derived by setting $\dot{E}_{radial} = \dot{E}_{orb}$ (equation 2.7.9) and solving for $\dot{a}$:

$$\dot{a} = -9\frac{k_{2,P}}{T_P}q(1+q)\left(\frac{R_P}{a}\right)^8 a(1-e^2)^{-15/2}f(e). \qquad (2.7.31)$$

The change in eccentricity $\dot{e}$ is derived by using the relation (2.7.5) and $\dot{L}_{orb} = 0$ (2.7.7) and solving for $\dot{e}$:

$$\dot{e} = -\frac{9}{2}\frac{k}{T}q(1+q)\left(\frac{R}{a}\right)^8 (1-e^2)^{-13/2}\frac{f(e)}{e}. \qquad (2.7.32)$$

The total change in the semi major axis $\dot{a}$ and eccentricity $\dot{e}$ due to F_r and F_Ψ is derived by adding (2.7.31) to (2.7.16) and adding (2.7.32) to (2.7.20).

This results in the following set of equations for the tidal evolution of the system due to the lag of the tidal bulge on the primary:

$$\dot{a}_P = -6\frac{k_{2,P}}{T_P}q(1+q)\left(\frac{R_P}{a}\right)^8 an^{-1}(1-e^2)^{-15/2}\left[nf_1(e) - (1-e^2)^{3/2}f_2(e)\Omega_P\right]$$
$$(2.7.33)$$

$$\dot{e}_P = -27\frac{k_{2,P}}{T_P}q(1+q)\left(\frac{R_P}{a}\right)^8 en^{-1}(1-e^2)^{-13/2}\left[nf_3(e) - \frac{11}{8}(1-e^2)^{3/2}f_4(e)\Omega_P\right]$$
$$(2.7.34)$$

and

$$\dot{\Omega}_P = -3\frac{k_{2,P}}{T_P}\frac{q^2}{I_P}\left(\frac{R_P}{a}\right)^6 (1-e^2)^{-6}\left[nf_2(e) - (1-e^2)^{-3/2}f_5\Omega_P\right], \qquad (2.7.35)$$

where

$$f_1(e) = 1 + \frac{31}{2}e^2 + \frac{225}{8}e^4 + \frac{185}{16}e^6 + \frac{25}{64}e^8$$

$$f_2(e) = 1 + \frac{15}{2}e^2 + \frac{45}{8}e^4 + \frac{5}{16}e^6$$

$$f_3(e) = 1 + \frac{15}{4}e^2 + \frac{15}{8}e^4 + \frac{5}{64}e^6 \qquad (2.7.36)$$

$$f_4(e) = 1 + \frac{3}{2}e^2 + \frac{1}{8}e^4$$

$$f_5(e) = 1 + 3e^2 + \frac{3}{8}e^4.$$

Up to now, tidal evolution due to tides raised by the secondary on the primary was calculated. As was stated in the previous section, the tidal evolution due to tides raised by the primary on the secondary needs to be taken into account as well. This results in a set of equation similar to the ones above safe for the fact that the subscripts P and S are exchanged and $q = M_S/M_P$ needs to be replaced by $1/q$. The complete tidal friction evolution is described by adding $\dot{a}_P$ and $\dot{a}_S$ and $\dot{e}_P$ and $\dot{e}_S$ and complementing them with the equations describing the evolution of the primary's and secondary's rotation evolution $\dot{\Omega}_P$ and $\dot{\Omega}_S$.

The equations used in this section use the typical tidal time scale T_P which contains the tidal lag time τ_P to determine the rate of change of the orbital elements. This quantity is defined as:

$$T_P = \frac{R_P^3}{GM_P\tau_P}. \qquad (2.7.37)$$

This is connected to the tidal dissipation factor Q_P by:

$$\tau_P = \frac{1}{2Q_P|\Omega_P - n|}. \qquad (2.7.38)$$

Therefore, inserting into the equations above

$$T_P = \frac{2R_P^3 Q_P|\Omega_P - \dot{\Psi}|}{GM_P} \qquad (2.7.39)$$

yields equations dependent on Q_P which are used by other authors (see the next Section).

The difference between a tidal friction model parameterized with $\frac{Q_P}{k_{2,P}}$ and a model parameterized with τ_P will be discussed in more detail in subsequent chapters.

2.8 The tidal dissipation factor and the Love number

In the previous sections, the importance of the tidal dissipation factor Q and the Love number k_2 for describing tidal friction became apparent. The quantity Q describes the energy loss of a damped externally driven oscillator. Q is inversely proportional to the amount of energy dissipated per cycle (see section 2.5, equation (2.5.6)). The larger Q, the less energy is dissipated, the smaller Q the more energy is dissipated. The Love number k_2, on the other hand, describes the feedback effect on the tidal deformation due to the self-gravity on the tidal bulge. If $k_2 = 0$, there is no feedback effect and the tidal deformation has the same amplitude as the tidal equilibrium tide ζ. If $k_2 = 1.5$, the feedback effect is maximal and the tidal deformation is 2.5 times as large as ζ (see Section 2.4.1). Both quantities are dimensionless parameters that contain the knowledge (or lack thereof) of the processes that are at work within a celestial body that is deformed and excited by tides.

Furthermore, the parameter Q/k_2 determines the secular change of the semi major axis and rotation rates, so a good constraint on Q/k_2 is critical for successful predictions of the dynamical evolution of planetary systems. The argument can also be reversed. If Q and k_2 are constrained, this may help to improve our understanding

of inner processes of the tidally excited body.

Historically, Q/k_2 was first investigated for the Earth-Moon system. With the advent of the space age, attempts were made to constrain Q/k_2 in the Solar System and this was used to gain knowledge on the inner structure of bodies different from the Earth and the Moon, even when in-situ measurements are not possible. Selected publications will be discussed in the following to gain insight about the possible magnitude of Q/k_2 and the timescales on which dynamical evolution due to tidal friction takes place.

Furthermore, it will be shown that for the stellar tidal dissipation factor $\frac{Q_*}{k_{2,*}}$, there are large uncertainties that cover several orders of magnitude. Indeed, these uncertainties provide one of the the main motivations for this work which puts constraints on $\frac{Q_*}{k_{2,*}}$ and explains why different approaches yield different $\frac{Q_*}{k_{2,*}}$-values.

It should be noted that in many works discussed in this section, Q/k_2 is regarded as approximately constant over time. This basic assumption and its limitations will be discussed in more details in the next Chapter, in Section 3.1.

2.8.1 Q/k_2 in the Solar System

Earth and Moon

Already *Thomson* (1863*a*) derived $k_{2,Earth} = 0.36$ from measuring the solid body tide of the Earth. From this and the Lunar Laser ranging (LLR) measurements, the tidal dissipation factor Q of the Earth can be deduced. LLR measurements determined the rate at which the Moon's semi major axis increases to be: $\dot{a} = 3.74$ cm/yr (*Murray and Dermott*, 1999; *Lambeck*, 1977). Inserting $\dot{a}$ into equation (2.6.17), the current

ratio of tidal dissipation factor over Love number is derived:

$$\frac{Q_{Earth,\,current}}{k_{2,Earth,\,current}} \approx 12.$$

For the tidal dissipation factor and Love number of the Moon, the following parameters were derived based on measurements from the Apollo seismic network (*Lambeck*, 1977):

$$Q_{Moon} \approx 300 \text{ for the central region},$$

$$Q_{Moon} \approx 1000 \text{ for the upper } 500 - 600 \text{ km},$$

$$k_{2,Moon} \approx 0.02. \tag{2.8.1}$$

Mars

Pollack (1977) estimates $\frac{Q_M}{k_{2,M}} \approx 100$ based on the measured secular decrease of the semi major axis of Phobos (*Born and Duxbury*, 1975; *Shor*, 1975) due to tidal friction because of tides raised by Phobos on Mars. This work was revised by *Lainey et al.* (2007) who derived:

$$Q_{Mars} = 79.9 \pm 0.7$$

$$k_{2,Mars} = 0.152,$$

based on the measured decay rate of Phobos' semi major axis (20 cm/yr) taken from observations between 1877 and 2005 and spacecraft observations from Mars Express and Mars Global Surveyor.

For the Mars moon **Phobos**, *Lambeck* (1979) derived:

$$Q_{Phobos} \approx \frac{1}{5} Q_{Mars}$$

$$k_{2,Phobos} = 10^{-4}, \tag{2.8.2}$$

assuming that Phobos was captured by Mars about four billion years ago and that the initially high eccentricity that such captured asteroids usually show was damped by tidal friction.

Jupiter, Saturn and Uranus

Starting in the 60s of the last century, several authors estimated $Q_{Jupiter}$ and Q_{Saturn} based on the fact that many of the satellites of these gas giants are in orbit resonances. Most notably, the mean motions of the Galilean moons Io, Europa and Ganymede (n_1, n_2 and n_3, respectively) obey the following relation: $n_1 - 3n_2 + 2n_3 = 0$. Furthermore, the saturnian satellites Enceladus and Dione as well as Mimas and Thethys each form a pair with mean motion resonances. Assuming that the satellites have evolved into this state due to tidal friction and are now stable, the time averaged Q was estimated by *Goldreich* (1965) to be:

$$Q_{Jupiter} \approx (1-2) \times 10^5$$

$$Q_{Saturn} \approx (6-7) \times 10^4.$$

k_2, on the other hand, was assumed as

$$k_2 = \frac{3}{2} \left(1 + \frac{19\mu}{2g\rho R_P}\right)^{-1} \approx 1, \qquad (2.8.3)$$

where g, ρ, μ, and R_P are the surface gravity, density, rigidity and radius of the gas giants, respectively (See Section 2.4.1).

In 1977, *Goldreich and Nicholson* (1977) contradicted *Goldreich* (1965) by stating that if turbulent viscosity in the atmosphere of Jupiter is the dominant mechanism by which energy is dissipated then $Q_{Jupiter} \approx 5 \times 10^{13}$. This would mean that no tidal evolution of the Galilean moons could have occurred and that the amount of energy

dissipated within Jupiter is negligible. Note the difference in Q by eight orders of magnitude. *Dermott* (1979*b*) on the other hand states that energy dissipation in the solid or quasi-solid core of gas giants is important ($Q_e \approx 60$ in the core). The total averaged Q for Jupiter and Saturn can then be in the orders of 10^5 and allow for the tidal evolution of the inner Jupiter and Saturn satellites; but only if it is assumed that the dense cores of Jupiter and and Uranus have volumes twice as large as that of the Earth. For Saturn, a dense core of eight times the Earth's volume is required. Today, it is still uncertain if Jupiter has a dense core and how large it is (*Saumon and Guillot*, 2004). A dense core, however, is postulated for the core-instability or core-accretion mechanism that explains the formation of gas giants (*Pollack et al.*, 1986; *Wuchterl*, 1993). Furthermore, a number of extrasolar gas giants have been discovered that confirm this scenario. The planet HD 149026, for example, probably has a 67 Earth mass core (*Sato et al.*, 2005).

Later investigations derived tidal dissipation factors in the orders of $10^4 - 10^5$ for Solar System gas giants and not in the orders of 10^{13}: In 1990, *Tittemore and Wisdom* (1990) constrained Q for Uranus by investigating the tidal evolution of Miranda, Umbriel and Ariel and derived $1.1 \times 10^4 \leq Q_{Uranus} \leq 3.9 \times 10^4$.

Only recently, *Lainey et al.* (2009) derived the following values for Jupiter and Io from astrometric observations:

$$\frac{k_{2,Io}}{Q_{Io}} = 0.015 \pm 0.003$$
$$\frac{k_{2,Jup}}{Q_{Jup}} = (1.102 \pm 0.023) \times 10^{-5}.$$

Leconte et al. (2011) derived k_2 based on numerical models and compared them with

observations. They give for Jupiter and Saturn planets:

$$k_{2,Jup} \approx 0.5 \tag{2.8.4}$$

$$k_{2,Sat} \approx 0.3. \tag{2.8.5}$$

A comparison of the different $\frac{Q_P}{k_{2,P}}$ values within the Solar System allows to draw the following conclusion: rocky planets and moons apparently have $\frac{Q_P}{k_{2,P}} \approx 10 - 100$ and gas giants have $\frac{Q_P}{k_{2,P}} \approx 10^4 - 10^5$. Therefore, rigid bodies are much more efficient in dissipating tidal energy than gaseous bodies, as expected intuitively. Furthermore, for very small rocky bodies like the Moon and Phobos the Love number is very small. There is almost no feedback effect due to the self-gravity of the tidal bulge. In contrast to that, the Earth, Jupiter and Saturn allow for moderate feedback effects. $k_{2,Jup} \approx 0.5$, for example, means that the tidal deformation is 1.5 times the amplitude of the tidal equilibrium tide ζ_{Jup}.

2.8.2 Q/k_2 in extrasolar planet systems

Q/k_2 for brown dwarfs

Heller et al. (2010) constrain Q_P for brown dwarfs by:

$$Q_P > 10^{4.5} \tag{2.8.6}$$

to allow the eclipsing brown dwarf binary 2MASSJ05352184-0546085 to become synchronized. The Love number for brown dwarfs is assumed as $k_2 = 0.286$. The Love number and tidal dissipation factor found by *Heller et al.* (2010) agree with the Love number and tidal dissipation factor found for gas giants. This would mean that

brown dwarfs dissipate tidal energy and are tidally deformed like gas giants and not like main sequence stars.

$\frac{Q_*}{k_{2,*}}$ for main sequence stars

Leconte et al. (2011) give the following simple equation to derive the Love number $k_{2,*}$:

$$k_{2,*} = \frac{3}{2} \left(I_* \frac{5}{2} \right)^2 \left(1 - \frac{n}{5} \right), \tag{2.8.7}$$

where I_* is the normalized moment of inertia and n is the polytropic index used for the modeling of the inner stellar density and pressure by the Lane-Emden equation (for example *Prialnik* (2000)). It is beyond the scope of this work to describe stellar models in detail. It shall be sufficient to state that for main sequence stars, $n \approx 3$ is used and the normalized moment inertia is assumed as $I_* = 0.074$ (See Section 2.11). From this, the stellar Love number is derived:

$$k_{2,*} = 0.018. \tag{2.8.8}$$

Hut (1981) gives $k_{2,*} \approx 0.01$ which agrees within order of magnitude.

Therefore, when comparing tidal interaction models in the literature one has to check if $\frac{Q_*}{k_{2,*}}$ or Q_* is discussed, because both values may differ by a factor of 50 just due to the Love number. Throughout this work, $k_{2,*} = 0.018$ is assumed. This small number indicates that almost no feedback occurs due to the self-gravity of the tidal bulge in contrast to planets like Earth or Jupiter. The tidal deformation is almost identical to the equilibrium tide indicating that main sequence stars behave in that respect like a rigid sphere covered by a zero-density fluid (Section 2.4.1).

In the following, several $\frac{Q_*}{k_{2,*}}$ values are discussed derived in the last two decades. In 1996, shortly after the discovery of the first extrasolar planets, *Rasio et al.* (1996)

calculated wether jovian planets like 51 Pegasi b could be stable under tidal friction. It was assumed that the star is a slowly rotating main-sequence star like our Sun ($P_{Sun} \approx 27$ days) and that the planet has a circular orbit with a short revolution period of a few days. In such a case, the stellar rotation rate is smaller than the revolution rate ($\Omega_* < n$) and consequently the application of (2.6.17) or (2.7.33) for $e = 0$ yields a decrease of the planet's semi major axis. (In the following, the star is regarded as the primary whose parameters are denoted by subscript $*$, whereas Pl denotes planetary parameters. The planet is the secondary in the tidal friction context.).

The authors estimated the orbital decay rate τ_a assuming that the tidal energy is entirely dissipated within the convective envelope by viscous dissipation:

$$\frac{1}{\tau_a} = \frac{|\dot{a}|}{a} = \frac{f}{\tau_c} \frac{M_{env}}{M_*} \frac{q}{1+q} \left(\frac{R_*}{a}\right)^8, \tag{2.8.9}$$

where M_* and R_* are the radius of the host star, a is the distance between the star and the extrasolar planet, q is the ratio of planetary mass to stellar mass, M_{env} is the mass of the convective outer layer in the main sequence star, τ_c is the eddy turnover time scale and f is a numerical value found by integrating viscous dissipation of tidal energy over the convective envelope. Comparing this equation with (2.7.33), it is obvious that the equations are very similar and can be related to each other to derive the corresponding tidal dissipation factor of the star $\frac{Q_*}{k_{2,*}}$.

$$\frac{f}{\tau_c} \frac{M_{env}}{M_*} = \frac{6k_{2,*}}{T_*} \frac{\Omega_* - n}{n}$$
$$= \frac{3k_{2,*}GM_*}{Q_* R_*^3 n}$$

with $n = \sqrt{G(M_* + M_{Pl})/a^3}$, where M_{Pl} is the mass of the exoplanet, and $T_* = R_*^3 Q_* 2(\Omega_* - n)/(GM_*)$. *Rasio et al. (1996) further derived $\tau_a \approx 4 \times 10^4$ Gyrs*

for a solar-like slowly rotating star ($M_* = M_{Sun}$, $R_* = R_{Sun}$, $M_{env}/M_{Sun} = 0.028$, $\Omega_* << n$) and an extrasolar planet with mass $M_{Pl} = 10^{-3}M_{Sun}$ and semi major axis $a = 11, R_{Sun} = 0.511$ AU. This corresponds to

$$\frac{Q_*}{k_{2,*}} \approx 4 \times 10^8 \tag{2.8.10}$$

or

$$Q_* = 8 \times 10^6. \tag{2.8.11}$$

This is more than one order of magnitude higher than the Q_{Pl}-values of the gas giants in the Solar system. This would indicate that if stars dissipate energy by turbulent viscosity in their convective envelope, they are even less efficient in dissipating tidal energy than gas giants who also contain a turbulent atmosphere. This is compatible with the discussion of $\frac{Q_{Pl}}{k_{2,Pl}}$ of gas giants in the 1970s, when it was found that turbulent viscosity is not an efficient energy dissipation mechanism. Instead, additional energy dissipation in dense cores had to be inferred to account for the observed $\frac{Q_{Pl}}{k_{2,Pl}}$ values. On the other hand, such a large $\frac{Q_*}{k_{2,*}}$ would mean that the planet is safe from orbital decay within the lifetime of the star; which is about 10 Gyrs for a main sequence star - much less than the decay time.

Recently, *Penev and Sasselov* (2011) derived $\frac{Q_*}{k_{2,*}}$ values of

$$\frac{Q_*}{k_{2,*}} = 10^8 - 3 \times 10^9, \tag{2.8.12}$$

based on numerical simulation of tidal energy dissipation in externally-perturbed convective volumes. Their work was stimulated by the fact *"(...)that a comprehensive theoretical understanding of turbulent dissipation in stellar convection zones is lacking."* These values agree nicely with the one given by *Rasio et al.* (1996) and also the

one derived by *Carone and Pätzold* (2007): $3 \times 10^7 \leq \frac{Q_*}{k_{2,*}} \leq 2 \times 10^9$ and *Pätzold and Rauer* (2002): $\frac{Q_*}{k_{2,*}} \geq 1.5 \times 10^8$.

These values are, however, much higher than those used by many other authors (*Jackson et al.* (2008) $\frac{Q_*}{k_{2,*}} = 10^{5.5}$, *Dobbs-Dixon et al.* (2004) $\frac{Q_*}{k_{2,*}} = 10^5 - 10^6$, and *Lin et al.* (1996), $\frac{Q_*}{k_{2,*}} = 10^5$). In summary, all given values cover the following range:

$$\frac{Q_*}{k_{2,*}} = 10^5 - 3 \times 10^9, \tag{2.8.13}$$

which would correspond to

$$Q_* = 2 \times 10^3 - 6 \times 10^7, \tag{2.8.14}$$

The lower values are derived from synchronization time scales of main sequence stellar binaries (*Meibom and Mathieu*, 2005).

This work aims to constrain $\frac{Q_*}{k_{2,*}}$ by applying tidal friction models to extrasolar planets and discussing their dynamical evolution. Indeed, it will be shown that *Penev and Sasselov* (2011)'s work will become particularly important when discussing the $\frac{Q_*}{k_{2,*}}$-constraints derived in this work. In any case, the variety of possible $\frac{Q_*}{k_{2,*}}$-values presented here shows how important it is to derive improved constraints on the stellar dissipation factor. Otherwise, it is almost impossible to predict the orbital evolution of a close-in extrasolar planet.

2.9 Stability of tidal equilibrium

If the orbit of a tide raising body is circular and $\Omega_P = \Omega_S = n$, then in principle no tidal friction can occur and the orbital elements will remain unchanged as long as no other mechanism removes angular momentum from the system. It will be proven that such a configuration can be achieved only under certain constraints.

Hut (1980) investigates the stability of such a state for a system of two celestial bodies which exchange significant tidal forces. The state of such a binary system is considered from the viewpoint of the barycentric orbit. Although *Hut* (1980) develops this formalism for stellar binary systems, the same method can be applied to a 'binary systems' composed of a star and a planetary companion. The binary system is determined in the most general case by the semi major axis a of the orbit and its eccentricity e, the angle i between the orbital angular momentum $\vec{L}_{orb}$ and the total angular momentum $\vec{L}_{tot}$ and the rotation rates $\vec{\Omega}_P$ and $\vec{\Omega}_S$ of the primary and the secondary (Figure 2.13) before it enters a double synchronous state.
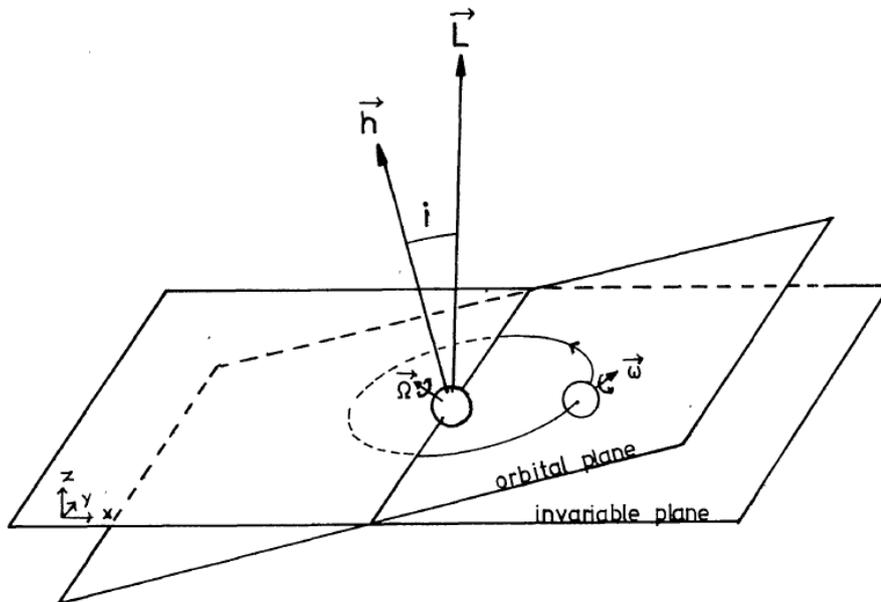
Figure 2.13: The barycentric orbit configuration of a binary system including its relevant parameters. $\vec{L}$ is the total angular momentum $\vec{L}_{tot}$ and $\vec{h}$ is the orbital angular momentum $\vec{L}_{orb}$ (*Hut*, 1980).

The total angular momentum $\vec{L}_{tot}$ is composed of the orbital angular momentum

and the rotation angular momenta:

$$\vec{L}_{tot} = \frac{M_P M_S}{M_P + M_S}\vec{n}a^2\sqrt{1 - e^2} + I_P M_P R_P^2 \vec{\Omega}_P + I_S M_S R_S^2 \vec{\Omega}_S, \qquad (2.9.1)$$

where I_P and I_S are the normalized moments of inertia of the primary and secondary with masses M_P and M_S and radii R_P and R_S, respectively, and $\vec{n}$ is the orbital revolution rate or orbital mean motion.

The total energy E_{tot} is composed of the orbital energy and the rotational energy of each body:

$$E_{tot} = -G\frac{M_P M_S}{2a} + \frac{1}{2}I_P M_P R_P^2 \left|\vec{\Omega}_P\right|^2 + I_S M_S R_S^2 \left|\vec{\Omega}_S\right|^2. \qquad (2.9.2)$$

A system is considered stable if its energy is minimal. In addition, the angular momentum needs to be conserved ($\frac{dL_{tot}}{dt} = 0$). A good way to solve this problem is the application of Lagrange multipliers, a mathematical method to find maxima and minima of a function subject to additional constraints.

For this example, the application of the Lagrange multipliers yields:

$$0 = \frac{\partial}{\partial x_i}E + \lambda_x\frac{\partial}{\partial x_i}L_{tot,x} + \lambda_y\frac{\partial}{\partial x_i}L_{tot,y} + \lambda_z\frac{\partial}{\partial x_i}L_{tot,z} \qquad (2.9.3)$$

where x_i are the nine free parameters that describe the system $a, e, i, \Omega_{P,x}, \Omega_{P,y}, \Omega_{P,z}, \Omega_{S,x}, \Omega_{S,y}$, and $\Omega_{S,z}$ and the Lagrange multiplicator $\vec{\lambda}$ is a constant vector.

Hut (1980) expresses the equations above in units of length $(I_P M_P R_P^2)^{1/2}M_P^{-1/2}$, units of time $G^{-1/2}M_P^{-5/4}(I_P M_P R_P^2)^{3/4}$ and units of mass M_P. In that case, M_P, $I_P M_P R_P^2$, and G can be set to one. In addition, a coordinate system was chosen where the z-axis is oriented along the vector $\vec{L}_{tot} = (0, 0, |L_{tot}|))$ and where $\vec{L}_{orb} = (|L_{orb}|\sin i, 0, |L_{orb}|\cos i)$ is in the (x, z)-plane.

The equations of total energy and total angular momentum reduce to:

$$E_{tot} = -\frac{q}{2a} + \frac{1}{2}\left(\Omega_{P,x}^2 + \Omega_{P,y}^2 + \Omega_{P,z}^2\right) + \frac{1}{2}\gamma\left(\Omega_{S,x}^2 + \Omega_{S,y}^2 + \Omega_{S,z}^2\right) \qquad (2.9.4)$$

and

$$L_{tot,x} = 0 = |L_{orb}|\sin i + \Omega_{P,x} + \gamma\Omega_{S,x} \qquad (2.9.5)$$

$$L_{tot,y} = 0 = \Omega_{P,y} + \gamma\Omega_{S,y}$$

$$L_{tot,z} = |L_{tot}| = |L_{orb}|\cos i + \Omega_{P,z} + \gamma\Omega_{S,z},$$

where q is the ratio of the masses $q = M_S/M_P$ and γ is the ratio of the moments of inertia $\gamma = I_S M_S R_S^2 / I_P M_P R_P^2$. Equations (2.9.5) now yield:

$$0 = \frac{q}{a} + \lambda_x |L_{orb}|\sin i + \lambda_z |L_{orb}|\cos i \qquad (2.9.6)$$

$$0 = \frac{e}{1-e^2}|L_{orb}|\left(\lambda_x \sin i + \lambda_z \cos i\right)$$

$$0 = \lambda_x \cos i - \lambda_z \sin i$$

$$0 = \Omega_{P,i} + \lambda_i \quad (i = x, y, z)$$

$$0 = \Omega_{S,i} + \lambda_i \quad (i = x, y, z).$$

The conditions above are met when:

$$\Omega_{P,z} = n \tag{2.9.7}$$

$$\Omega_{S,z} = n$$

$$e = 0$$

$$i = 0$$

$$\Omega_{P,x} = 0$$

$$\Omega_{P,y} = 0$$

$$\Omega_{S,x} = 0$$

$$\Omega_{S,y} = 0,$$

where $n = \sqrt{\frac{1+q}{a^3}}$ is the orbital revolution rate.

Therefore, the system is in equilibrium when the orbit is circular, all rotation vectors are parallel to each other and all rotation rates are equal ($\Omega_{P,z} = \Omega_{S,z} = n$). This is called a double synchronous state state.

The total angular momentum $L_{tot,doub}$ of a system in double synchronous state is

$$L_{tot,doub} = \frac{q}{(1+q)^{1/3}} n^{-1/3} + (1+\gamma)n. \tag{2.9.8}$$

Figure 2.14 shows the possible $L_{tot,doub}$-values with respect to n. A double synchronous equilibrium state is only possible if $L_{tot,doub}$ is greater than the critical angular momentum $L_{tot,crit}$. $L_{tot,crit}$ can be found with (2.9.8) by solving $\frac{dL_{tot,doub}}{dn} = 0$ for n. In modified units of time, mass and length this yields:

$$L_{tot,crit} = 4\left[\frac{1}{27}(1+\gamma)\frac{q^3}{1+q}\right]^{1/4} \tag{2.9.9}$$

or

$$L_{tot,crit} = 4\left[\frac{G^2}{27}\left(I_P M_P R_P^2 + I_S M_S R_S^2\right)\frac{M_P^3 M_S^3}{M_P + M_S}\right]^{1/4} \tag{2.9.10}$$

in SI-units.

For $L_{tot} = L_{tot,crit}$, the following holds for the individual components of the total angular momentum:

$$L_{orb,crit} = 3(1 + \gamma)n_{crit} \tag{2.9.11}$$

$$L_{rot,crit} = \Omega_P + \gamma\Omega_S = (1 + \gamma)n_{crit},$$

with n_{crit}:

$$n_{crit} = \frac{1}{3^{3/4}} \left(\frac{(1+\gamma)3\sqrt{1+q}}{q} \right)^{-3/4}. \tag{2.9.12}$$

In other words, a stable double synchronous state only exists if the orbital angular momentum is at least three times larger than the sum of the angular momenta contained in the rotation of the two individual bodies. Therefore, L_{orb} has to exceed the following critical value to allow for a stable double synchronous rotation state:

$$L_{orb} > L_{orb,crit} = 3\left(1 + \gamma\right)n_{crit} \tag{2.9.13}$$

in modified units and

$$L_{orb} > L_{orb,crit} = 3\left(I_P M_P R_P^2 + I_S M_S R_S^2\right)n_{crit} \tag{2.9.14}$$

in SI-units.

As can be seen in Figure 2.14, there exist two possible states where the rotation rates can be synchronized if $L_{tot} > L_{tot,crit}$. But only the state with the wider orbit i.e. the smaller n is stable, because here the total energy is minimal as well, whereas for the orbit with the larger n, the total energy is maximal. For $n = n_{crit}$ only one solution exists with $L_{tot} = L_{tot,crit}$, which is unstable because in that case $L_{orb} = L_{orb,crit}$, as well. And it was found previously that only orbits with $L_{orb} > L_{orb,crit}$ can establish a stable double synchronous state.
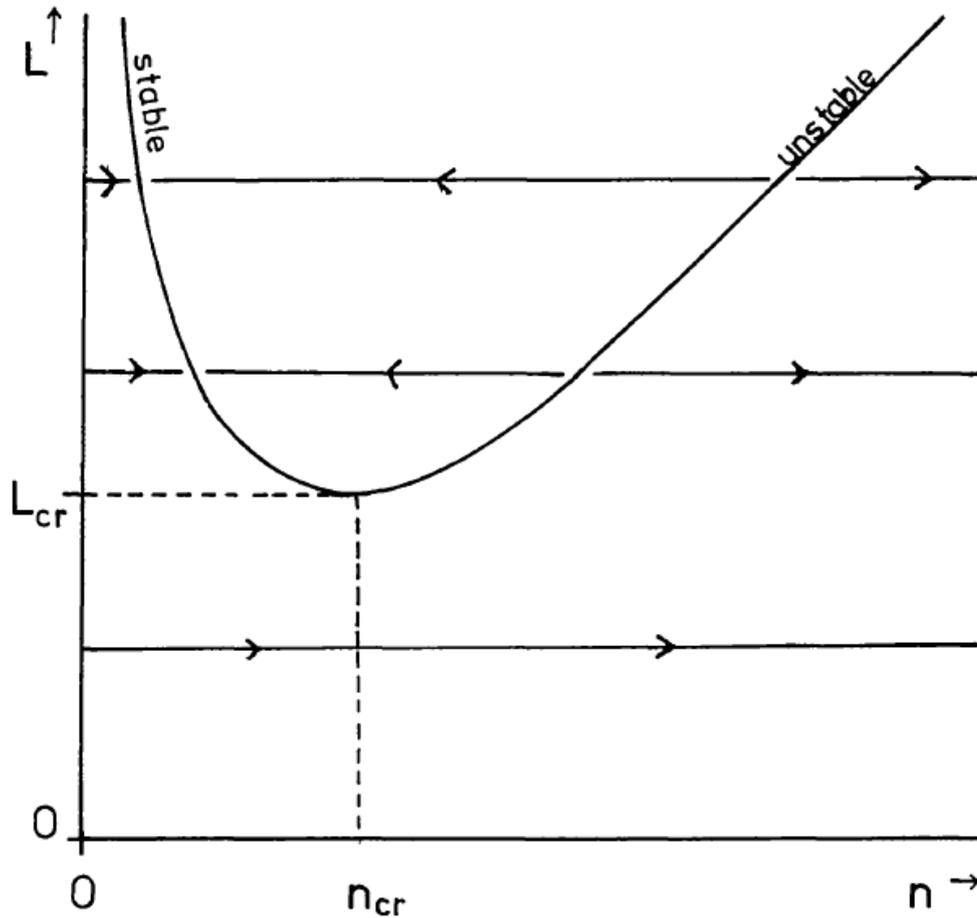
Figure 2.14: Total angular momentum of a binary system in double synchronous rotation $L_{tot,doub}$ versus orbital revolution rate n (*Hut*, 1980). For $n > n_{crit}$, two double synchronous states exist. Arrows show the direction of decreasing total energy. The stability of a given double synchronous state is determined by the total energy: Stability is only ensured if the total energy is minimal as well. For $n = n_{crit}$ only one solution with $L_{tot,doub} = L_{crit}$ exists. For $L_{tot,doub} < L_{crit}$, no double synchronous state can be achieved.

2.10 Evolution of the rotation of main sequence stars

To investigate tidal interactions between close-in extrasolar planets and their host stars, the evolution of the stellar rotation of main sequence stars needs to be included. Indeed, *Barnes* (2001) found that rotation rates of the host stars of extrasolar planets apparently are indistinguishable from a sample of near-by field stars. This observation will later help to constrain the strength of tidal friction acting on the planet's orbit as well as the star's rotation.

In general, the change in stellar angular momentum is:

$$\frac{\mathrm{d}J}{\mathrm{d}t}\frac{1}{J} = \frac{\mathrm{d}\Omega_*}{\mathrm{d}t}\frac{1}{\Omega_*} + \frac{\mathrm{d}C_*}{\mathrm{d}t}\frac{1}{C_*}, \tag{2.10.1}$$

where $J = C_*\Omega_*$ is the angular momentum. Ω_* is the stellar rotation rate and C_* is the moment of inertia of the star.

The second term on the right hand side of the equation, representing the change in the moment of inertia, is important for a pre main sequence (PMS) star that is still in process of formation and contraction. Figure 2.15 shows the evolution of the stellar radius and moment of inertia in the pre-main sequence phase.
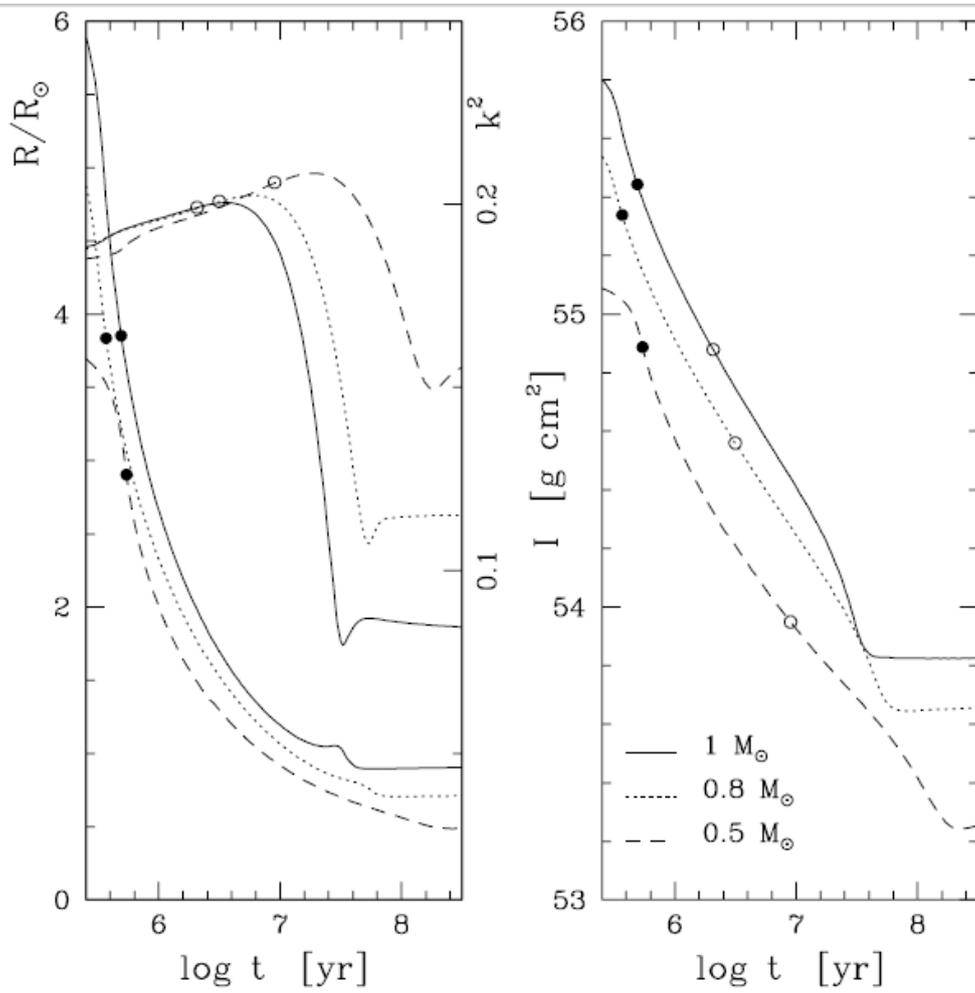
Figure 2.15: Evolution of the stellar radius, radius of gyration I (=moment of inertia C_* in the notation used in this work) for $0.5, 0.8$ and $1 M_{Sun}$ stars (*Bouvier et al.*, 1997).

The star enters the main sequence as a Zero age main sequence (ZAMS) star (*Bouvier et al.*, 1997) at an age of about $60 - 100$ million years. After that, the internal structure is settled and $\mathrm{d}C_*/\mathrm{d}t \simeq 0$ can be assumed. Only the first term on the right-hand side of the equation remains. In this work, main sequence stars are investigated therefore an age of 60 million years is selected as the starting point of the simulations.

Older main sequence stars, including the Sun, rotate much slower than younger stars that have just entered the main sequence. Therefore, although the stellar structure remains more or less the same over the course of billions of years and although stellar mass loss is negligible, something else must act on the star to reduce angular momentum.

In the 60s and 70s, remarkable progress was made to understand this phenomenon. *Weber and Davis* (1967) explain the underlying mechanism: Ionized material, the solar wind, is driven away from the Sun by thermal pressure. As the solar wind travels outward, it is forced into corotation with the Sun by a torque arising due to magnetic hydrodynamic (MHD) coupling of the solar wind with the roots of the magnetic field lines on the rotating solar surface. Effective corotation is established within the Alfven radius r_a. The torque acting on the solar wind generates magnetic stress which in turn results in an equal torque acting on the Sun and decelerates the solar rotation. This process is called 'magnetic braking'. *Weber and Davis* (1967) describe the angular momentum loss due to magnetic braking as:

$$\frac{\mathrm{d}J_{Sun}}{\mathrm{d}t} = \frac{2}{3}\Omega_{Sun}r_a^2\frac{\mathrm{d}M_{Sun}}{\mathrm{d}t} = -\frac{J_{Sun}}{\tau}, \qquad (2.10.2)$$

where J_{Sun} is the angular momentum of the Sun, Ω_{Sun} is the solar rotation rate

and τ is the characteristic time, which is about $\tau = 7 \times 10^9$ yrs for the Sun. The Alfvén radius r_a describes the distance at which the stellar wind is no longer able to magnetically couple to the stellar surface. This coupling is, however, a prerequisite for angular momentum transfer from the star to the stellar wind. The Alfven radius depends on the properties of the stellar wind and may lie between 15 to 50 solar radii for the Sun according to *Weber and Davis* (1967).

Skumanich (1972) uses a phenomenological approach and derives a scaling law for angular momentum loss of main sequence stars by comparing the rotation rates of several stars at different ages (Figure 2.16):

$$\Omega_* \propto t^{-0.5}, \tag{2.10.3}$$

where Ω_* is the stellar rotation rate and t is the star's age. Indeed, Figure 2.16 shows that not only the rotation rate represented by the rotation velocity $v_* = \Omega_* \cdot R_*$ follows the $t^{-0.5}$ scaling law, but also the lithium abundance and Ca^+ emission luminosity. Interestingly, Figure 2.16 also shows that the Lithium abundance of the Sun (age 4.5 Gyrs) is anomaly low.
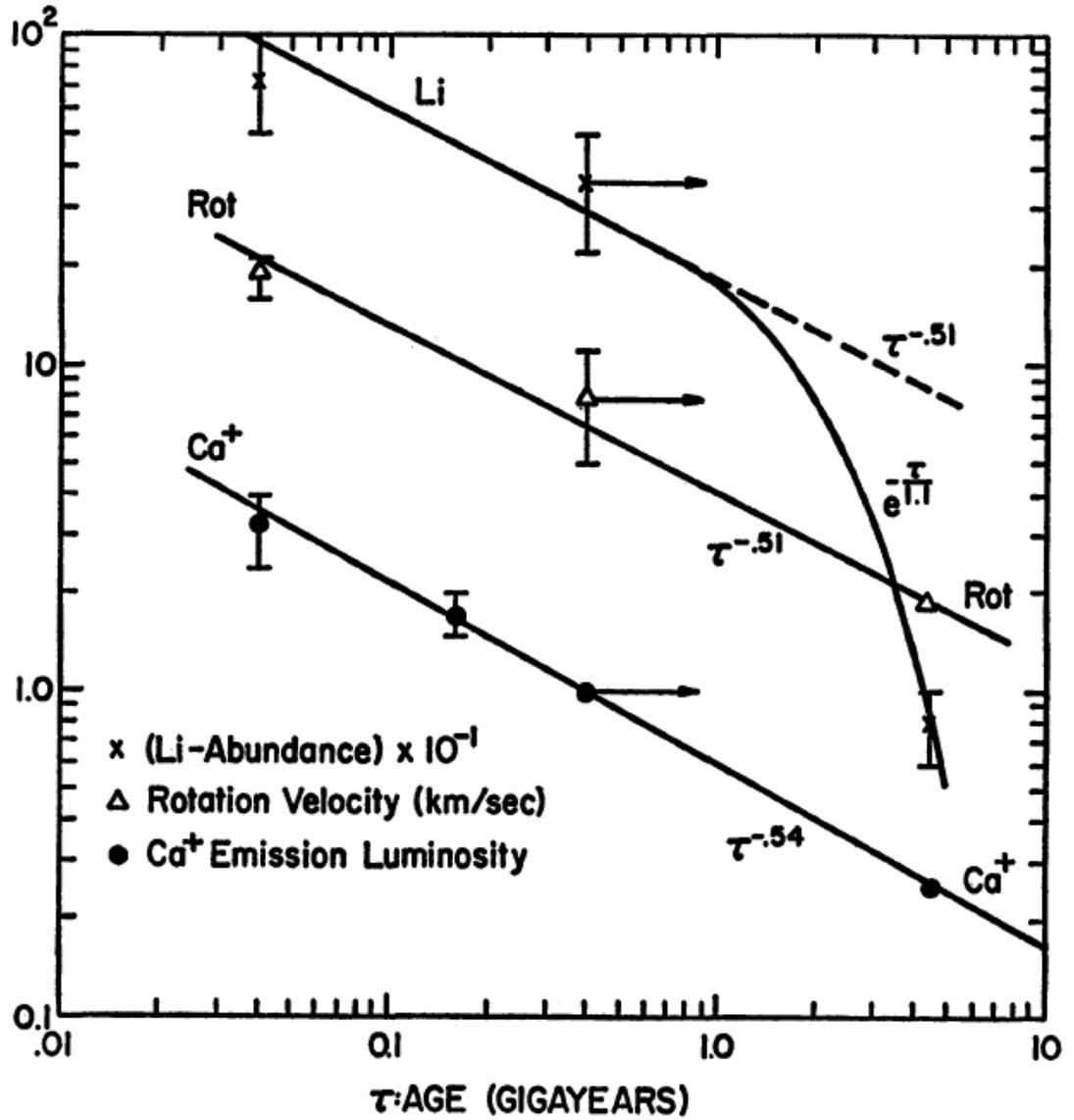
Figure 2.16: Ca^+ emission luminosity, rotation velocity and lithium abundance with age. Shown as an example are the properties of stars in the Pleidaes (0.04 Gyrs), Ursa Major (0.15 Gyrs), the Hyades Cluster (0.4 Gyrs) and the Sun (4.5 Gyrs). In 1972 the age estimate of the Hyades Cluster was controversial. Other age estimates would have resulted in a shift of the Pleiades data points along the x-axis as indicated by the arrows (*Skumanich*, 1972).

In this work, a description of stellar angular momentum evolution due to magnetic braking is used based on the work of *Bouvier et al.* (1997). This model is not only applicable to the Sun, like the model of *Weber and Davis* (1967), but for any sun-like star in the mass range $0.5 M_{Sun} - 1.1 M_{Sun}$. Furthermore, it is much better parameterized than the description of *Skumanich* (1972) which gives a rudimentary power law connecting stellar rotation and age.

The angular momentum loss by magnetic braking alone is modeled by:

$$\frac{\mathrm{d}J}{\mathrm{d}t} = - K\Omega_*^{1+4N/3} \left(\frac{R_*}{R_{Sun}}\right)^{2-N} \left(\frac{M_*}{M_{Sun}}\right)^{-N/3} \qquad \text{for} \quad \Omega_* < \omega_{sat} \qquad (2.10.4)$$

$$\frac{\mathrm{d}J}{\mathrm{d}t} = - K\Omega_*\omega_{sat}^2 \left(\frac{R_*}{R_{Sun}}\right)^{0.5} \left(\frac{M_*}{M_{Sun}}\right)^{-0.5} \qquad \text{for} \quad \Omega_* \geq \omega_{sat},$$

where $K = 2.7 \times 10^{40}$ Nms is a scaling factor, phenomenologically derived by *Bouvier et al.* (1997) from the rotation rates of star clusters of different age, R_* and M_* are the stellar radius and mass, R_{Sun} and M_{Sun} are the solar radius and mass, and ω_{sat} is a saturation rotation rate derived by *Bouvier et al.* (1997). ω_{sat} equals $3, 8,$ and $14\,\Omega_{Sun}$ for $0.5, 0.8,$ and $1.0\,M_{Sun}$ stars, respectively, where $\Omega_{Sun} = 2.9 \times 10^{-6}$ 1/s is the current solar rotation rate. This magnetic saturation accounts for the observation that the surface magnetic field of a star, which drives the angular momentum loss, increases with the angular velocity Ω_* but only up to $\Omega_* \approx 10\,\Omega_{Sun}$ (*Saar*, 1996). N is a magnetic parameter accounting for the geometry of the magnetic field. *Bouvier et al.* (1997) choose $N = 1.5$ to represent a field that is more radial than dipolar. This allows for a mixture of closed and open field lines, the latter allow the stellar angular momentum to be removed from the system by the ionized stellar wind (*Barnes*, 2003).

Interestingly enough, the *Bouvier et al.* (1997) model is an improvement of the relatively sketchy *Skumanich* (1972) relation. The $\frac{\mathrm{d}J}{\mathrm{d}t} \propto \Omega_*^3$-dependency is equivalent

to $\Omega_*(t) \propto \sqrt{t}$ as postulated by *Skumanich* (1972) (see *Barnes* (2003) for the proof).

It should be noted that for the model by *Weber and Davis* (1967) as well as for the model by *Bouvier et al.* (1997), the star is assumed to be a solid-body rotator. Indeed, this basic assumption is also used in this work for the modeling of the stellar rotation evolution due to tidal friction. That *Bouvier et al.* (1997) require a solid-body rotation can be interpreted physically in the following way: Although the angular momentum loss is mainly driven by the coupling of the outer convective envelope with the stellar winds, the rotation of the radiative core is slowed down as well. This requires strong coupling of the radiation core with the convection zone. *Barnes* (2003) suggests the magnetic field of the star as the origin of this coupling.

The efficiency of magnetic braking is, however, only firmly established for stars with masses $M_* < 1.1 M_{Sun}$, for G, K and M main-sequence stars. In the past years, many planets have been found around F main sequence stars with higher masses. Indeed, this work will model the stellar evolution of several F-stars under tidal friction.

Barnes (2003) gives a good overview of the uncertainties in magnetic braking: Whereas rotational spin down with increasing age is well established for G, K and M stars, at least some high mass stars beyond late F spectral type stars ($B - V < 0.5$) do not spin down at all with increasing age (Figure 2.17). *Schatzman* (1962) suggests that only stars with deep convective envelopes can loose angular momentum due to magnetic braking. Indeed, the observational data gathered by *Barnes* (2003) show that lower mass stars with very deep convection zones spin down faster than higher mass stars with shallower convection zones.

F stars ($B - V \approx 0.5 - 1$) seem to lie in a transition region. Their spin-down rate is reduced compared to lower mass stars, but at least some F-stars lose angular
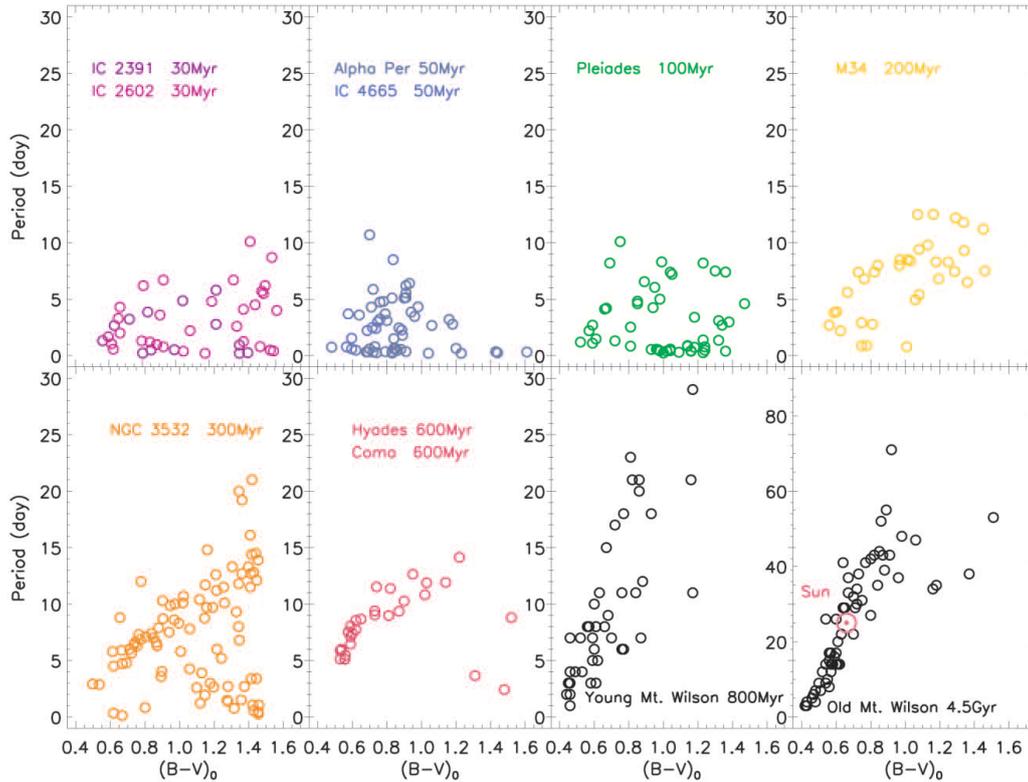
Figure 2.17: Color-period diagrams ($B - V$ versus rotation period, on a linear scale) for a series of open clusters and Mount Wilson stars with different ages. Note the change in scale for the old Mount Wilson stars. The higher $B - V$, the redder the star, the less hot the stellar surface and the lower the mass of the star. On the other hand, the smaller $B - V$, the bluer the star, the hotter the stellar surface, the higher the mass of the star (*Barnes*, 2003).

momentum over the course of billion of years. According to *Barnes* (2003), this 'failure' in magnetic braking can be explained by a different stellar magnetic field configuration. These stars do not have global but small-scale magnetic fields that are no longer able to couple the convection zone to the inner radiative core efficiently. In addition, the magnetic coupling of the convective zone to the outer region and therefore to the stellar wind is reduced as well. This outer coupling, however, is the reason for the angular momentum loss, and, therefore, reduced coupling leads to a

reduced rate of angular momentum depletion.

In subsequent Chapters (6, 7 and 8), this uncertainty in angular momentum loss and its effect on the long-term evolution of planetary systems due to tidal friction is investigated in more detail. Indeed, these investigations may even shed some light on the strength of angular momentum loss in F-stars.

2.11   Moment of Inertia

The evolution of stellar angular momentum due to magnetic braking was described in terms of $\frac{\mathrm{d}J}{\mathrm{d}t}$ in the previous section, where $J = C_* \Omega_*$ is the angular momentum. Therefore, to model the stellar rotation evolution, C_* is needed.

In general the moment of inertia C is:

$$C = \sum_{i=1}^{N} m_i r_i^2 \qquad (2.11.1)$$

for a body that consists of N mass elements m_i at distance r_i from the rotation axis. In this work, the stellar rotation axis is assumed to be perpendicular to the orbital plane.

In planetary science, it is common usage to divide C by MR^2, where M is the total mass and R is the mean radius of the planetary body. The quantity $I = \frac{C}{MR^2}$ is the normalized moment of inertia. Note that many astronomers call the normalized moment of inertia 'radius of gyration'.

Table 2.1 lists some normalized moments of inertia $I = \frac{C}{MR^2}$ for some ideal bodies and Table 2.2 gives normalized moment of inertia for some Solar System objects *Weissman et al.* (1999)[3].

---

[3]Values not found there were taken from NASA's planetary fact sheet: http://nssdc.gsfc.nasa.gov/planetary/factsheet/.

	I
solid ring of radius R and mass M	1
hollow sphere of radius R and mass M	2/3
homogenous sphere of radius R and mass M	2/5
point mass concentrated in center of mass	0

Table 2.1: Normalized moment of inertia for some ideal bodies

	I
Moon	0.393
Mars	0.365
Earth	0.3315
Neptune	0.29
Jupiter	0.26
Uranus	0.23
Saturn	0.20

Table 2.2: Normalized moment of inertia for some solar system bodies

As can be seen, by comparing the normalized moments of inertia I in Table 2.2 with the value for a homogenous sphere 0.4 and a point mass 0, the normalized moment of inertia indicates how the mass elements are distributed with respect to the rotation axis. Mars and Earth have I smaller than 0.4, which indicates that these bodies have a core of dense material (iron and nickel) and are covered by lighter silicates. The gas giants, Jupiter, Saturn, Uranus, and Neptune have even smaller normalized moments of inertia. Their masses are even more concentrated in the core whereas their deep atmosphere is composed of light materials like helium and hydrogen.

The normalized moment of inertia of the Sun is derived by using the values $M(r)$ and r listed in Figure 2.18[4] provided by *Dziembowski et al.* (1994) and by applying equation (2.11.1). This yields $I_{Sun} = 0.074$, consistent with the value used by other

---

[4]Available online at: http://gong.nso.edu/science/models/goode.html

authors. *Rasio et al.* (1996), for example, use $I_* = 0.08$ for sun-like stars. In the following, $I_* = 0.074$ will be used for all stars investigated in this work (*Pätzold et al.*, 2004).

SOLAR SEISMIC MODEL FROM BBSO & TENERIFE1 DATA

$r/R_\odot$	u (cm^2 s^{-2})	ρ (g cm^{-3})	P (dyne cm^{-2})	$M(r)/M_\odot$
0.00......	(1.556–1.598)E15	(1.410–1.467)E2	(2.258–2.283)E17	0
0.05......	(1.567–1.584)E15	(1.235–1.252)E2	(1.953–1.962)E17	(1.203–1.217)E−2
0.10......	(1.534–1.541)E15	(8.659–8.708)E1	(1.333–1.337)E17	(7.440–7.471)E−2
0.15......	(1.420–1.423)E15	(5.581–5.603)E1	(7.941–7.962)E16	(1.898–1.902)E−1
0.20......	(1.238–1.240)E15	(3.495–3.504)E1	(4.331–4.339)E16	(3.339–3.344)E−1
0.25......	(1.058–1.060)E15	(2.092–2.095)E1	(2.217–2.218)E16	(4.803–4.809)E−1
0.30......	(9.089–9.098)E14	(1.208–1.209)E1	(1.099–1.099)E16	(6.103–6.110)E−1
0.35......	(7.884–7.891)E14	(6.873–6.884)	(5.421–5.429)E15	(7.156–7.162)E−1
0.40......	(6.877–6.883)E14	(3.937–3.945)	(2.709–2.714)E15	(7.932–7.939)E−1
0.45......	(6.061–6.065)E14	(2.284–2.290)	(1.385–1.388)E15	(8.511–8.517)E−1
0.50......	(5.358–5.361)E14	(1.356–1.360)	(7.267–7.287)E14	(8.910–8.916)E−1
0.55......	(4.761–4.764)E14	(8.201–8.226)E−1	(3.906–3.919)E14	(9.208–9.213)E−1
0.60......	(4.218–4.220)E14	(5.082–5.098)E−1	(2.144–2.151)E14	(9.412–9.417)E−1
0.65......	(3.715–3.717)E14	(3.210–3.220)E−1	(1.193–1.197)E14	(9.598–9.602)E−1
0.70......	(3.169–3.170)E14	(2.094–2.101)E−1	(6.637–6.658)E13	(9.741–9.745)E−1
0.75......	(2.480–2.481)E14	(1.425–1.430)E−1	(3.535–3.546)E13	(9.830–9.832)E−1
0.80......	(1.854–1.855)E14	(9.202–9.233)E−2	(1.707–1.712)E13	(9.903–9.905)E−1
0.85......	(1.299–1.299)E14	(5.388–5.406)E−2	(6.998–7.022)E12	(9.953–9.954)E−1
0.90......	(8.014–8.014)E13	(2.616–2.625)E−2	(2.097–2.104)E12	(9.972–9.973)E−1
0.95......	(3.556–3.557)E13	(7.731–7.757)E−3	(2.750–2.759)E11	(9.982–9.984)E−1

Figure 2.18: The solar seismic model taken from *Dziembowski et al.* (1994). r is the radius from the center of the Sun, u is the square of isothermal speed of sound at radius r, ρ is the density at radius r, P is the pressure and $M(r)$ is the integrated mass up to r.

2.12 The Roche limit

As was already suggested in Section 2.8, some extrasolar planets may migrate towards their host star due to tidal friction. On their way they may meet the 'Roche limit', which is the distance between a small and a large body where the tidal force exerted by the large body is greater than the cohesive forces of the small body. Ultimately,

it is torn apart.

As a first approximation, the Roche limit can be calculated by regarding a test mass δm at the surface of a small body of mass M_S and radius R_S facing directly the larger body of mass M_L and radius R_L at distance d, where d is measured between the two centers of masses. The following gravitational force is attracting the mass element δm:

$$F_G = \frac{G \delta m M_S}{R_S^2}.$$
(2.12.1)

The following tidal force is pulling δm toward the large body:

$$F_{tide} = G \frac{2 M_L \delta m R_S}{d^3}.$$
(2.12.2)

F_{tide} is derived from (2.3.7) for the special case $r = R_S$ and $\Psi = 0$.

In addition, δm experiences a centrifugal force due to the rotation of the small body. This force is directed away from the center of mass of the small body:

$$F_C = \delta m \Omega^2 R_S.$$
(2.12.3)

If the sum of $F_{tide} + F_C$ exceeds the gravitational force F_G, δm breaks away from the small body.

Consequently, the limit of stability is derived by calculating the distance at which the following equation holds:

$$F_{tide} + F_C = F_G.$$
(2.12.4)

In such a situation, where the small body is close to being tidally disrupted, its spin-rate Ω is tidally locked with the revolution rate n (This will be shown in a latter chapter 3.2). The revolution rate is connected with the sum of the masses $M_L + M_S$ and the distance d between the centers of masses via Kepler's third law:

$$G(M_L + M_S)/a_{Roche}^3 \approx G M_L / a_{Roche}^3 = n^2,$$
(2.12.5)

that can be inserted into equation (2.12.3). Assuming $\Omega = n$, inserting (2.12.1) into (2.12.4), solving for d and setting $d = a_{Roche}$ yields the Roche limit:

$$d = a_{Roche} = R_S \left(3\frac{M_L}{M_S}\right)^{1/3}. \tag{2.12.6}$$

Assuming that both bodies are homogenous spheres, the masses in the equation above can be substituted with $M_L = 4\pi\rho_L/R_L^3$ and $M_S = 4\pi\rho_S/R_S^3$, where ρ_L and ρ_S are the densities of the large and small body, respectively:

$$a_{Roche,spher.} = R_L \left(3\frac{\rho_L}{\rho_S}\right)^{1/3}. \tag{2.12.7}$$

In the Solar System, the mean densities of Jupiter and the Sun are similar enough that the following approximation may be useful if the true density of a gas giant planet is not known:

$$a_{Roche,spher.,EGP} = 3^{1/3} \left(\frac{\rho_*}{\rho_P}\right)^{1/3} R_*$$
$$\approx 1.44 R_*, \tag{2.12.8}$$

where R_* and ρ_* are the stellar radius and density. The density of Jupiter is 1300kg/m^3 which is 0.94 times the solar density (1408kg/m^3). The third root of the ratio of the solar over the jovian mean density is 1.02. The Roche limit $a_{Roche,spher.}$ is, of course, only a rough estimate without considering any elastic forces and deformation due to tides and rotation.

Chandrasekhar (1987) uses a more detailed approach by calculating the Roche limit of a tidally locked prolate spheroid in hydrostatic equilibrium:

$$a_{Roche,hydro.} \approx 2.44 R_* \left(\frac{\rho_*}{\rho_P}\right)^{1/3}. \tag{2.12.9}$$

Following the argumentation above, it may be assumed $\left(\frac{\rho_*}{\rho_P}\right)^{1/3} \approx 1$ for extrasolar gas giant planets (EGP), and the following approximation may be used:

$$a_{Roche,hydro.,EGP} \approx 2.44 R_*. \qquad (2.12.10)$$

The region between $a_{Roche,hydro.}$ and $a_{Roche,spher.}$ is called the **'Roche zone'**. In the Solar System, the planetary rings are found in the respective Roche zones of the main body (*Murray and Dermott*, 1999). These are remnants of satellites that were tidally disrupted.

Therefore, it may be safe to assume that an extrasolar planet entering this zone will be destroyed. It will be shown in this work that the semi major axes of several extrasolar planets may decrease so fast within the Roche zone that no qualitative difference is found if the planet is assumed to be destroyed at $a_{Roche,hydro}$ or a little later at $a_{Roche,spher.}$.

Chapter 3

Critical examination of assumptions and approximations

At this point, it is worthwhile to check several key assumptions that are the basis of the tidal friction model of *Murray and Dermott* (1999) presented in Section 2.6 that will predominantly be used in this work.

3.1 The constant Q_*-assumption

In Section 2.5, the quality factor Q was introduced and set into relation with the tidal lag angle ϵ to be $2\epsilon = Q^{-1}$ (Eq. 2.5.10). ϵ is the angle between (a) the line connecting the centers of mass of the star and its planet, and (b) the line connecting the center of mass of the star and the center of the tidal bulge on the star raised by the tidal force of the planet. The tidal bulge is displaced by ϵ because the star does not instantly change its form to accommodate the tidal potential and the subsequent change of the internal gravity potential. The deformation takes a tidal lag time τ (Section 2.7). As already shown (Eq. 2.7.2), the following relation connects ϵ and τ:

$$\epsilon = (\Omega_* - n) \cdot \tau.$$

In Section 2.8 and in the literature using the formalism described in Section 2.5 and Section 2.6, two basic assumptions are made about the stellar dissipation factor Q_*: The system is assumed to be independent of resonance states. This is the weak friction assumption. Furthermore, Q_* is usually assumed to be constant.

3.1.1 Can Q_* be regarded as constant even though the system may meet resonant states?

As was shown in Section 2.5, in general Q is defined as

$$Q^{-1} = \frac{\omega/\tau_d}{\omega_0^2 - \omega^2}.$$

If $\omega \rightarrow \omega_0$, then $Q^{-1} \rightarrow \infty$ or $Q \rightarrow 0$. It can be argued, however, that the time average $\langle Q_* \rangle$ over billion of years is considered throughout this work. Therefore, the variation of Q_* when the system passes through resonant states is contained within this time averaged value.

The weak friction assumption is justified by *Hut* (1981) who investigates the tidal evolution of binary stars: *"A detailed description of the evolution in time of the orbital elements caused by tidal effects cannot be given in general form. One of the major complications arises from the possibility that the stars can be forced to oscillate in a variety of eigen modes."*

Hut (1981) further argues: *"In order to get a general qualitative picture of tidal evolution, one can investigate a simple model in which only equilibrium tides are described, with very small deviations in position and amplitude with respect to equipotential surfaces. Dynamical tides, where the stars oscillate, are then neglected."*

The simple tidal evolution model is still frequently used in general applications seeking answers over long timescales. For these types of analysis, that are also used
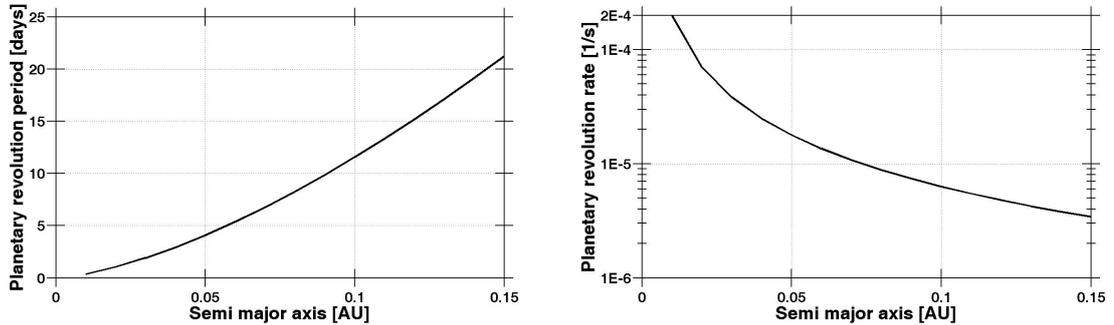
Figure 3.1: Left panel: Planetary revolution period versus semi major axis of a close-in extrasolar Jupiter analogue around a Sun-like star.
Right panel: Planetary revolution rate versus semi major axis of a close-in extrasolar Jupiter analogue around a Sun-like star.

in this work, simple models are parsimonious in providing sufficiently accurate predictions without the requirement to specify a high number of parameters.

Even if the model is found to be incorrect in some special cases, this failure in itself would also be a valuable result. In such a case, the tidal evolution of the system is strongly affected by dynamical tides (*Zahn*, 1977).

3.1.2 Can Q_* be regarded as constant although it is defined as frequency dependent?

As a repetition, the definition of Q_* for the weak friction assumption is given (Equation 2.5.7):

$$Q = \frac{|\omega_0^2 - \omega^2|}{\omega/\tau_d} \tag{3.1.1}$$

where $\omega = 2(\Omega_* - n)$ is the tidal frequency and τ_d is the damping time scale.

With the equation given above, the assumption that $Q_* = $ const can be justified for close-in extrasolar planets with semi major axes smaller than 0.05 AU by the following arguments:

- For $a < 0.05$ AU, the planetary revolution rate n changes by one to two orders of magnitude at most when the planet migrates toward the star (Figure 3.1).

- In many cases, the main sequence star in an extrasolar system rotates much slower (typically with a rotation period between 10-100 days, see Section 2.10, Figure 2.17) than the close-in planet revolves around the star (typically with a revolution period of a few days, Figure 3.1). Therefore $\Omega_* - n \approx -n$. In this case, $\dot{a} < 0$ (according to equation 2.6.17): The planet will migrate toward the star.

- When comparing different possible values for the stellar dissipation factor Q_* (Section 2.8), the possible values Q_* given by different energy dissipation models differ by several orders of magnitude. In the presence of such large uncertainties in the mechanism of energy dissipation within the star, a possible variation of Q_*, due to the underlying frequency dependency that is one to two orders of magnitudes, can safely be neglected.

3.1.3 What happens with Q_* when the system approaches double synchronicity?

For some exoplanetary systems discussed in this work, Ω_* is similar to n. Later, in Section 3.2, it will be shown that, in addition, the planetary rotation is probably synchronized with the planet's revolution, as well. Therefore, such systems may be in a double synchronous state.

When the planetary system approaches this state, it follows from equation 2.5.7 that in the weak friction assumption, $Q_*^{-1} \to 0$ or $Q_* \to \infty$. This strange result can be explained by considering the problem in the reference system centered on the star

and rotating with it. The tidal wave on the star forms because mass elements inside the star rearrange to accommodate the tidal potential of the planet and the subsequent change of the internal gravity potential of the star due to the tidal deformation. Because the tidal bulge follows the planet as it revolves around the star, from the viewpoint of the star, the tidal wave 'plows' through the star with the effective frequency $\omega = 2(\Omega_* - n)$. This process generates friction, and energy is dissipated within the star. More precisely, this can be envisioned at first order as a drag process within a plasma environment. The force acting on a propagating wave is typically either proportional to the velocity of the tidal wave v in the rotating frame or proportional to the square of said velocity v^2.

When $\omega = 0$ and the orbit is circular, the tidal wave is stationary, no energy is dissipated within the star (ΔE over one cycle in the quotient of the definition of Q (eq. 2.5.6) is zero), and no tidal friction takes place. Indeed, when looking at equations (2.6.17) and (2.6.18), the terms are zero if $\Omega_* = n$. If the requirements described in Section 2.9 are met, the system should remain in this equilibrium state unless external forces disrupt the equilibrium state.

In this work, some possible double synchronous systems are investigated for which $\Omega_* - n$ is already very small. In this context, the constant Q_* assumption may be used again but for a different frequency regime than the non-synchronous cases for which the tidal frequency is $|\omega| = 2|\Omega_* - n| \approx |2n| \approx 10^{-4} - 10^{-3}\mathrm{s}^{-1}$. In the double synchronous state $|\omega| = 2|\Omega_* - n| \approx 0$.

Other systems will be investigated evolving from a state with $\Omega_* > n$ to $\Omega_* \ll n$, crossing the $\Omega_* = n$ region. For these, the $Q_* = const$ assumption is at least questionable. It will be shown, however, that the constant Q_* may still be used in

this cases with some caveats.

It may be useful in the future to compare tidal friction models using a constant stellar dissipation function Q_* with tidal friction models using a constant tidal lag time τ_*.

3.1.4 Switching from the constant Q- to the constant τ-formalism.

The derivation of the model described by *Hut* (1981) (Section 2.7) is identical to the one described by *Murray and Dermott* (1999) (Section 2.6) if $e = 0$. The model by *Hut* (1981) is, however, more general as it also describes tidal friction for bodies on orbits with large eccentricities.

Apart from this, there is another major point where the formalisms deviate. As the system evolves over time, the model of *Hut* (1981) keeps the tidal lag time τ_* constant, whereas the model described by *Murray and Dermott* (1999) regards the tidal lag angle as ϵ or Q_* constant. Both quantities are connected via $2\epsilon = Q^{-1} = 2|\Omega_* - n|\tau_*$. As long as the tidal frequency remains more or less constant during the whole evolution, both models are equivalent.

Although the constant Q assumption is used in this work, one may easily switch to constant τ-model by using well-known examples as 'calibration points'.

Switch from Q_* to τ_*

The tidal dissipation factor $\frac{Q_*}{k_{2,*}}$ is constrained for the OGLE-TR-56-system to be $\frac{Q_*}{k_{2,*}} \geq 2 \times 10^7$ (*Carone and Pätzold*, 2007) and with $k_{2,*} = 0.018$ this corresponds to $Q_* \geq 4 \times 10^5$. The following parameters describe the OGLE-TR-56-system: $M_* = 1.17 \, M_{Sun}$, $M_{Pl} = 1.3 \, M_{Jup}$, $a = 0.0225$ AU, and the stellar rotation period is $P_* = 19$ days.

Consequently,

$$\Omega_* - n = \frac{2\pi}{P_*} - \sqrt{\frac{G(M_* + M_{Pl})}{a^3}} \qquad (3.1.2)$$
$$= \left(3.8 \times 10^{-6} - 6.38 \times 10^{-5}\right) s^{-1}$$
$$= -6 \times 10^{-5} s^{-1}.$$

From this, τ_* can be calculated by:

$$\tau_* = \frac{1}{2|\Omega_* - n|Q_*} \approx \frac{8333}{Q_*} s. \qquad (3.1.3)$$

Consequently, the lower limit of $Q_* = 4 \times 10^5$ corresponds to a tidal lag time $\tau_* \approx 2 \times 10^{-2}$ s. In the following, the equation above will be used to switch from Q_* to τ_*[1].

Switch from Q_P to τ_P for jovian planets

The following 'calibration point' can be used for the switch from the constant τ_{Pl} to a constant Q_{Pl} formalism for jovian planets: The Jupiter-Io-example. *Lainey et al.* (2009) derive $\frac{Q_P}{k_{2,P}} = 10^5$ for Jupiter and, with $k_{2,Pl} = 0.5$, the tidal dissipation factor is $Q_{Pl} = 5 \times 10^4$. The rotation period of Jupiter is 9.925 hours, and the revolution period of Io is 42.5 hours.

Consequently,

$$\Omega_{Pl} - n = \left(1.8 \times 10^{-4} - 4 \times 10^{-5}\right) s^{-1} = 1.4 \times 10^{-4} s^{-1}. \qquad (3.1.4)$$

The tidal lag time τ_{Pl} is:

$$\tau_{Pl} = \frac{1}{Q_{Pl}2|\Omega_{Pl} - n|} \approx \frac{3600}{Q_{Pl}} s. \qquad (3.1.5)$$

---

[1]As a sidenote, the OGLE-TR-56 example illustrates that $\Omega_* - n \approx -n$ is indeed justified.

τ_{Pl} and τ_* differ only by a constant factor of about 2 because $|\Omega_* - n|$ and $|\Omega_{Pl} - n|$ only differ by that factor. It follows that Jupiter, which experiences tides raised by Io, as well as a main sequence star, which experiences tides raised by a close-in planet, represent tidally oscillation systems with driving frequencies comparable in order. Therefore, the Q-value derived in both cases and the underlying energy dissipation mechanisms can be compared.

3.2   Is the planetary rotation tidally locked?

Throughout this work it is assumed that the planetary rotation is synchronized with its revolution rate and that the planets therefore rotate relatively slow with rotation periods of a few days. In other words, close-in extrasolar planets with semi major axes a smaller than 0.1 AU are considered to be in the so-called tidally locked state.

This assumption can be tested by evaluating τ_{synchr}, the time it takes for the planetary rotation to become synchronized with its revolution. τ_{synchr} is calculated as (*Murray and Dermott*, 1999) for circular orbits ($e = 0$):

$$\tau_{synchr} = \frac{|n - \Omega_{Pl}|}{\frac{3}{2} \frac{M_*}{M_{Pl}} \left(\frac{R_{Pl}}{a}\right)^3 \frac{GM_*}{a^3}} \cdot I_{Pl} \frac{Q_{Pl}}{k_{2,P}}, \qquad (3.2.1)$$

where n is the planetary revolution rate, Ω_{Pl} is the primordial rotation rate of the planet, I_{Pl} is the normalized moment of inertia of the planet, Q_{Pl} is the planetary dissipation constant and $k_{2,P}$ is the Love number of second order. Most of the stellar and planetary parameters are determined by the combination of the transit and radial velocity observations. Some planetary characteristics are unknown or poorly constrained but can be estimated within reasonable ranges, as will be shown in the following.

The normalized moment of inertia I_{Pl} is the mass distribution in the interior of a body with respect to the rotation axis. If the body is differentiated (a safe assumption for bodies larger than 1000 km in diameter), the mass is concentrated in the core and $I_{Pl} < 0.4$. The following I_{Pl} values are used in this work: $I_{Pl} = 0.35$ for terrestrial planets, $I_{Pl} = 0.25$ for gas giants and $I_{Pl} = 0.15$ for Brown Dwarfs (*Leconte et al.* (2011), see also Section 2.11).

The ratio of the planetary dissipation constant and the planetary Love number $\frac{Q_{Pl}}{k_{2,Pl}}$ is set to the corresponding values known from our Solar System. Terrestrial planets have values in the order of $10 - 1000$ and gas giants values in the order of $10^4 - 10^5$ (*Yoder*, 1995; *Mayor and Queloz*, 1995; *Goldreich and Soter*, 1966; *Lainey et al.*, 2009). Because τ_{synchr} is proportional to $\frac{Q_{Pl}}{k_{2,Pl}}$, the upper limits of these $\frac{Q_{Pl}}{k_{2,Pl}}$-values are used to calculate the upper limit of the spin-orbit synchronization times. The values are: $\frac{Q_{Pl}}{k_{2,Pl}}_{terrestrial} = 1000$ and $\frac{Q_{Pl}}{k_{2,Pl}}_{gas\ giants} = 10^5$ and $\frac{Q_{Pl}}{k_{2,Pl}}_{brown\ dwarfs} = 10^6$. In fact, the value used for brown dwarfs is one order of magnitude higher than the lower limit for $\frac{Q_{Pl}}{k_{2,Pl}}_{brown\ dwarfs}$ derived by *Heller et al.* (2010) (See Section 2.8). The derived upper limit for the synchronization time scale should give a safety margin under the assumption that the energy dissipation mechanism within the brown dwarfs discussed in this work are comparable with gas giants.

The primordial planetary rotation rate Ω_{Pl} before synchronization is not known, but to account for this uncertainty τ_{synchr} is calculated for a fast rotating (rotation period of 10 hours) and a slowly rotating (rotation period of 10 days) planet.

With these assumptions, τ_{synchr} is calculated for the CoRoT planets. τ_{snychr}-values for fast and slow primordial planetary rotation are listed in Table 3.1 and plotted in Figure 3.2. As can be seen, the time required for a planet to end in a

tidally locked state is less than the systems age except for two cases: (a) CoRoT-9b, the CoRoT-planet with the greatest semi major axis $a = 0.407$ AU and therefore the CoRoT-planet that experiences the weakest stellar tidal forces, and (b) CoRoT-20b, the youngest CoRoT-planet of an age of about 0.1 billion years that may not yet be tidally locked.

Still this example shows that, unless the system is very young, planets with semi major axes smaller than 0.1 AU can safely be assumed to be tidally locked. This assumption is further supported by at least two observational evidences:

System	$\tau_{synchr,slow\,rotator}$ [10^6 years]	$\tau_{synchr,fast\,rotator}$ [10^6 years]	I_{Pl}	$\frac{Q_{Pl}}{k_{2,Pl}}$
CoRoT-1	4×10^{-4}	0.0013	0.2	10^5
CoRoT-2	0.02	0.0078	0.2	10^5
CoRoT-3	3	49	0.15	10^6
CoRoT-4	0.012	3	0.2	10^5
CoRoT-5	0.003	0.043	0.2	10^5
CoRoT-6	0.06	11.8	0.2	10^5
CoRoT-7	3×10^{-5}	3.5×10^{-5}	0.35	1000
CoRoT-8	0.05	1.7	0.2	10^5
CoRoT-9	2.3×10^3	6.3×10^4	0.2	10^5
CoRoT-10	1	95	0.2	10^5
CoRoT-11	0.007	0.058	0.2	10^5
CoRoT-12	0.0022	0.018	0.2	10^5
CoRoT-13	0.032	0.47	0.2	10^5
CoRoT-14	0.008	0.024	0.2	10^5
CoRoT-15	2.9	26	0.15	10^6
CoRoT-16	0.01	0.27	0.2	10^5
CoRoT-17	0.029	0.34	0.2	10^5
CoRoT-18	0.0037	0.016	0.2	10^5
CoRoT-19	0.006	0.082	0.2	10^5
CoRoT-20	0.17	53	0.2	10^5
CoRoT-21	0.0075	0.058	0.2	10^5

Table 3.1: Synchronization time scale τ_{synchr} for the CoRoT-planets. A slow rotator is a planet with an initial rotation period $P_{Pl} = 10$ days, a fast rotator is a planet with an initial rotation period of $P_{Pl} = 10$ hours.
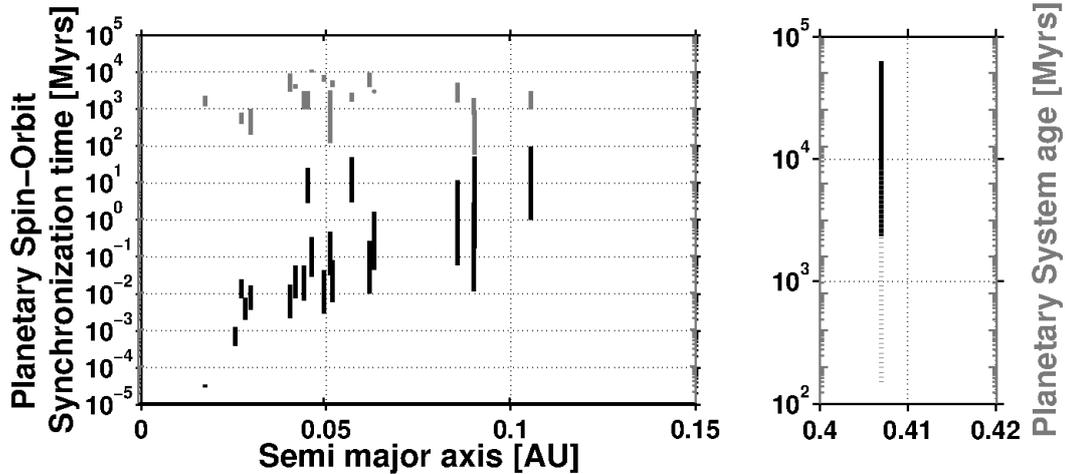
Figure 3.2: Synchronization time scales τ_{synchr} and the age of the CoRoT planets versus their semi major axes. The black solid lines represent τ_{synchr} calculated for a slow (10 days) and a fast (10 hours) primordial planetary rotation. The grey lines represent the system ages within the limit of uncertainties. The age of CoRoT-9b, a planet orbiting its star beyond 0.4 AU, is represented by a dotted grey line. In this case, the system age and the possible synchronization time scale overlap each other.

The planetary emissions of υ Andromeda b (*Harrington et al.*, 2006) and of HD 189733 (*Knutson et al.*, 2007) in the infrared show day/night variations consistent with tidally locked planets. Figure (3.3) shows the substellar hot spot on the planet. The day side is constantly heated by the star, the heating being strongest at the substellar point. In contrast, the night side, which always points away from the star, attains less heat via wind transfer from the day side. If the tidal locking assumption would not be valid, the planet would show a more uniform heat emission due to stellar irradiation over the whole surface.
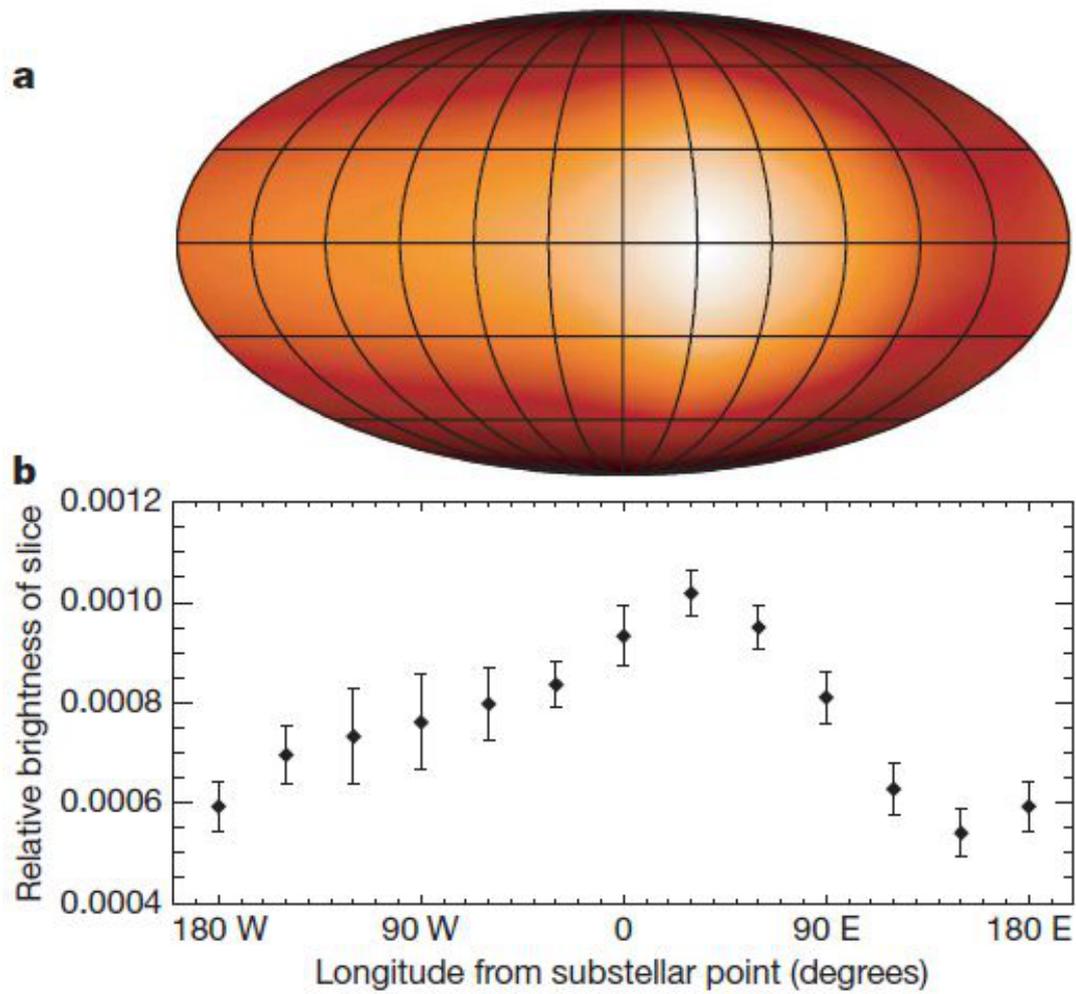
Figure 3.3: Relative brightness in the infrared estimated for 12 longitudinal strips on the surface of the planet HD 189733. Data are shown as a colour map (a) and in graphical form (b) (*Knutson et al.*, 2007).

3.3 Energy and angular momentum in close-in extrasolar planetary systems

It is useful to calculate the energies and angular momenta within a typical extrasolar system because these quantities ultimately determine the tidal evolution of the system.

For this purpose, the following hypothetical test case is evaluated: An extrasolar Jupiter analogue of mass $M_{Pl} = 1\,M_{Jup}$ and radius $R_{Pl} = 1\,R_{Jup}$ around a solar-like star of mass and radius $M_* = 1\,M_{Sun}, R_* = 1\,R_{Sun}$ orbiting the star in a circular orbit at semi major axis $a = 0.02$ AU is assumed.

The orbital energy is:

$$E_{orbit} = G\frac{M_{Pl}M_*}{2a} \tag{3.3.1}$$
$$= 4.2 \times 10^{37}\,\mathrm{J}.$$

The stellar rotational energy is:

$$E_{rot,*} = \frac{1}{2}I_*M_*R_*^2\Omega_*^2 \tag{3.3.2}$$
$$= 2.83 \times 10^{35}\,\mathrm{J},$$

where Ω_* is set to the rotation rate of the sun: $\Omega_* = \Omega_{Sun} = 2.9\times10^{-6}\mathrm{s}^{-1}$ (*Bouvier et al.*, 1997) and the normalized moment of inertia is $I_* = 0.074$ (see Section 2.11).

The planet's rotational energy is:

$$E_{rot,Pl} = \frac{1}{2}I_{Pl}M_{Pl}R_{Pl}^2\Omega_{Pl}^2 \tag{3.3.3}$$
$$= 4.45 \times 10^{33}\,\mathrm{J},$$

where the planet's rotation rate is set to its revolution rate because spin-orbit synchronization is expected: $\Omega_{Pl} = n = \sqrt{G(M_* + M_{Pl})/a^3} = 7 \times 10^{-5}s^{-1}$. The normalized

moment of inertia I_{Pl} of a gas giant is assumed: $I_{Pl} = 0.2$.

Therefore, the rotational energy stored within a close-in extrasolar planet is two orders of magnitude smaller than the stellar rotational energy and four orders of magnitude smaller than the orbital energy, respectively. This comparison also shows that in general more dynamical energy is stored in the planetary orbit than in the stellar rotation.

The comparison between angular momenta with the parameters as defined above yields:

$$L_{orb} = \frac{M_{Pl} \cdot M_*}{M_{Pl} + M_*} a^2 n \tag{3.3.4}$$
$$= 1.2 \times 10^{42} \text{Nms}$$

$$L_{rot,*} = I_* M_* R_*^2 \Omega_* \tag{3.3.5}$$
$$= 2 \times 10^{41} \text{Nms}$$

$$L_{rot,Pl} = I_{Pl} M_{Pl} R_{Pl}^2 \Omega_{Pl} \tag{3.3.6}$$
$$= 1.3 \times 10^{38} \text{Nms}.$$

The amount of angular momentum in the planetary rotation is two orders of magnitude smaller than the amount of angular momentum in the stellar rotation and four orders of magnitude smaller than the orbital angular momentum. This comparison also shows that the amount of angular momentum stored in the planetary orbit exceeds the amount of stellar angular momentum by one order of magnitude. Therefore, transfer of angular momentum from the planet's orbit to the star needs to

be treated with care. It cannot be readily neglected because it affects the evolution of stellar rotation. Furthermore, it is justified to neglect the planet's rotation about its spin-axis when calculating the long-term dynamical evolution of the planetary system due to tidal interactions between the planet and the star.

3.3.1 Possible pitfalls in the calculation of the Roche zone

The approximations (eq. 2.12.10) and (eq. 2.12.8) used in Section 2.12 to calculate the Roche zone are used if the planet's density is unknown. The equations, however, are valid only if $\left(\frac{\rho_*}{\rho_{Pl}}\right)^{1/3} \approx 1$ which is true for Solar System gas giants and the Sun. The calculation of the Roche limits with the true density derived from transiting exoplanets, however, may shed light onto the limitations of these approximations.

The Roche limits $a_{Roche,spher.}$ and $a_{Roche,hydro.}$ are computed for some CoRoT planets for which the stellar and planet's density are known and listed in Table 3.2. Their parameters are listed in Section 1.4. As can be seen, for some systems the assumption $\sqrt[3]{\rho_{Pl}} \approx \sqrt[3]{\rho_*}$ holds, but for many other systems it doesn't. Figure 3.4 shows the density of all transiting exoplanets in units of Jupiter density. For example, several exoplanets have been found with average densities much smaller than the density of Jupiter [2]. Brown dwarfs (CoRoT-3b and CoRoT-15, for example), on the other hand, don't satisfy the $\sqrt[3]{\rho_{Pl}} \approx \sqrt[3]{\rho_*}$-assumption because they are much denser than Jupiter planets. These objects lie in the transition region between the mass regimes of gas giants and the smallest stars (see Section 1.1). An object in the 'brown Dwarf desert' is approximately the size of Jupiter although it may contain up to eighty Jupiter masses.

---

[2]The mechanism responsible for the inflation of some short-period extrasolar gas giants is still disputed.
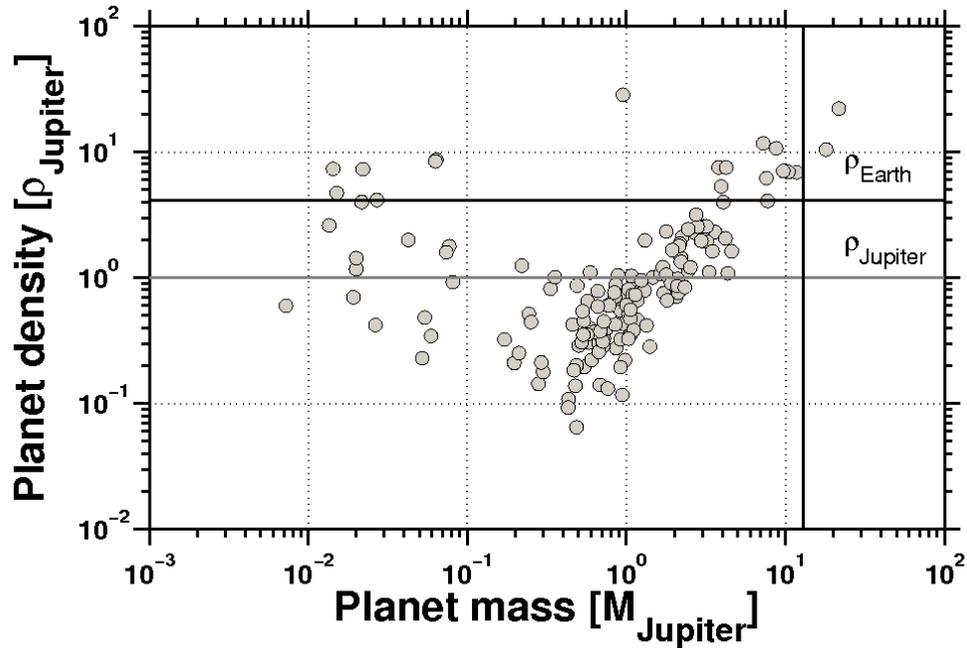
Figure 3.4: Density of transiting exoplanets versus their mass.

If the planet is inflated, the extent of the Roche zone is underestimated. If the companion is a brown dwarf or a terrestrial planet like CoRoT-7b, the extent of the Roche zone is overestimated. This needs to be considered when using (eq. 2.12.10) and (eq. 2.12.8).

As a side remark, it is interesting to note that the 'true' Roche zone of Brown Dwarfs lies **within** the star; see the derived Roche limits of CoRoT-3b and CoRoT-15b (Table 3.2). This would mean that brown dwarfs can approach their stars and be engulfed by them without being tidally disrupted during their approach.

System	$a_{Roche,spher.}$ $[R_*]$	$a_{Roche,hydro}$ $[R_*]$	ρ_* $[\rho_{Sun}]$	ρ_{Pl} $[\rho_{Jup}]$	$(\rho_*/\rho_{Pl})^{1/3}$
CoRoT-1	1.86	3.19	0.70	0.32	1.27
CoRoT-2	1.54	2.63	1.32	1.08	1.05
CoRoT-3	0.37	0.63	0.36	21.65	0.25
CoRoT-4	1.70	2.91	0.73	0.44	1.16
CoRoT-5	2.15	3.67	0.59	0.18	1.46
CoRoT-6	1.15	1.96	0.98	1.92	0.78
CoRoT-7	0.90	1.54	1.65	6.73	0.61
CoRoT-8	1.68	2.86	1.93	1.22	1.14
CoRoT-9	1.68	2.88	1.19	0.75	1.15
CoRoT-10	1.20	2.05	1.81	3.10	0.82
CoRoT-11	1.22	2.08	0.49	0.82	0.83
CoRoT-12	1.94	3.31	0.77	0.32	1.32
CoRoT-13	1.18	2.01	1.06	1.94	0.80
CoRoT-14	0.82	1.41	1.13	6.04	0.56
CoRoT-15	0.30	0.51	0.42	46.40	0.21

Table 3.2: Comparison of Roche limit approximations

Chapter 4

Close-in extrasolar planets as playground for tidal friction models

This work focuses on tidal friction due to tides raised by the planet on the star (stellar tidal friction) and on the consequences for the exoplanet's semi major axis and the stellar rotation. As derived from Sections (2.6) and (2.7), massive exoplanets with very short semi major axes are the most interesting in this context. It will be shown that the planetary systems discovered by CoRoT provide an ideal playground for investigating tidal evolution and to derive constraints on $\frac{Q_*}{k_{2,*}}$.

4.1 The tidal stability maps for planets around main sequence stars

In most cases, an extrasolar planet with semi major axis less than 0.1 AU revolves faster about the star than the star rotates ($\Omega_* < n$). Therefore, tidal friction as a result of the delay of the tidal bulge on the star leads to a decrease in the planet's semi major axis and consequently to the spin-up of the star. The planet may even reach the Roche zone and may be destroyed there (Section 2.12). It is worthwhile investigating which $\frac{Q_*}{k_{2,*}}$ is required for a planet to reach the Roche limit within the

planetary system's lifetime and how many planets may be destroyed due to tidal friction.

The time τ_{Roche} it takes for a planet on a circular orbit to reach the Roche zone due to tidal friction can be calculated by (*Pätzold and Rauer*, 2002):

$$\tau_{Roche} = \frac{\frac{1}{13}\left[a_{Present}^{13/2} - a_{Roche}^{13/2}\right]}{\frac{3k_{2,*}M_{Pl}}{2Q_*M_*}R_*^5\sqrt{GM_*}}, \tag{4.1.1}$$

where $a_{Present}$ is the current semi major axis of the planet, a_{Roche} is the Roche limit, M_{Pl} is the planet's mass, M_* and R_* are the stellar mass and radius, respectively, G is the gravitational constant, Q_* is the stellar tidal dissipation factor and $k_{2,*}$ is the stellar Love number.

As was explained in Section 2.12, several estimates exist for the Roche limit. Here, $a_{Roche,hydro} = 2.46R_*\left(\frac{\rho_*}{\rho_{Pl}}\right)^{1/3}$, which defines the outer boundary of the 'Roche zone', is used for the calculation of τ_{Roche}.

Of all the parameters needed to calculate τ_{Roche}, the ratio of the stellar tidal dissipation factor over Love number $\frac{Q_*}{k_{2,*}}$ is the least constrained. Indeed, estimates of the stellar dissipation factor cover several orders of magnitude. In the following, a $\frac{Q_*}{k_{2,*}}$ between 10^5 and 10^9 is assumed to cover the whole range of estimates of the amount of tidal energy dissipated within a main sequence star (See Section 2.8.2).

τ_{Roche} is calculated here under the constant Q_* assumption. As outlined in Section 3.1.2, the validity of this assumption requires the following: The star rotates much slower than the planet revolves around it ($\Omega_* \ll n$) to satisfy the approximation ($\Omega_* - n$) $\approx -n$, where $2(\Omega_* - n)$ is the tidal frequency. Furthermore, the revolution rate n should remain approximately constant throughout the calculation.

As was outlined in Section 3.1.2, n varies by one and a half order of magnitude between 0.02 and 0.15 AU which is acceptable given the large uncertainties of Q_*. The time scale τ_{Roche} will now be investigated systematically for different 'model' planets placed in close proximity to the star.

At the center of these model planetary systems, a main sequence star of spectral type K, G, and F is placed. For each spectral type, there exists a CoRoT exoplanet host star (Table 1.2). One of these was selected as a representative of spectral type K and F (Table 4.1). For spectral type G, the Sun was selected as a representative to show that the investigation of tidal interactions in extrasolar planetary systems helps to place our own Solar System in a greater context and to potentially learn something about solar properties. If $\frac{Q_*}{k_{2,*}}$ is constrained for a solar-like star, this result is also applicable to energy dissipation processes within our Sun.

Spectral type	name	T_{eff} [K]	mass $[M_{Sun}]$	radius $[R_{Sun}]$	reference
K1V	CoRoT-8	5080	0.88	0.77	*Bordé et al.* (2010)
G2V	Sun	5780	1	1	*Unsoeld and Baschek* (2001)
F7V	CoRoT-15	6350	1.32	1.46	*Bouchy et al.* (2011)

Table 4.1: The parameters of the central stars used for the calculation of the tidal stability maps. Real stars were selected as representatives of K-, G- and F-spectral type stars, respectively.

The following exoplanets are investigated exemplarily for each star: A high-mass Brown Dwarf (HBD) like CoRoT-15b, a low-mass Brown Dwarf like CoRoT-3b (LBD), a hot Jupiter (HJ) like CoRoT-1b, an extrasolar hot Neptune analogue planet (HN), an extrasolar Super Earth like CoRoT-7b (SE), an extrasolar Earth analogue planet (EE) and an extrasolar Mercury analogue planet (EM). See Table 4.2 for their parameters.

Exoplanet type	name	mass $[M_{Jup}]$	radius $[R_{Jup}]$	reference
High mass brown dwarf	CoRoT-15b	63	1.12	*Bouchy et al.* (2011)
low mass brown dwarf	CoRoT-3b	21.66	1.01	*Deleuil et al.* (2008)
hot Jupiter	CoRoT-1b	1.03	1.49	*Barge et al.* (2008)
hot Neptune	Neptune	0.054	0.36	*Unsoeld and Baschek* (2001)
Super Earth	CoRoT-7b	0.023	0.15	*Hatzes et al.* (2011), *Bruntt et al.* (2010)
Exo-Earth	Earth	0.0032	0.092	*Unsoeld and Baschek* (2001)
Exo-Mercury	Mercury	1.74×10^{-4}	0.035	*Unsoeld and Baschek* (2001)

Table 4.2: The parameters of the exoplanets placed around each star (Table 4.1) for the calculation of the tidal stability map. A real planet was selected as a representative for each exoplanet category.

Now τ_{Roche} is calculated for planets with semi major axis greater than $a_{Roche,hydro}$ but within 0.15 AU and for $\frac{Q_*}{k_{2,*}} = 10^5 - 10^9$. τ_{Roche} is compared with the total lifetime of the star, the time for which the star remains on the main sequence. It is reasonable to investigate if a planet will survive during that time.

For main sequence stars, the stellar lifetime can be calculated approximately by (*Prialnik*, 2000):

$$T_0 = 10^{10} \left(\frac{M_*}{M_{Sun}} \right)^{-2.8} \text{ years.} \tag{4.1.2}$$

With these assumptions, 'tidal stability maps' can be calculated (Figures 4.1, 4.2, and 4.3). They show unstable semi major axes for combinations of specific planets and stars in dependence of $\frac{Q_*}{k_{2,*}}$. Instability herein means that the planet may reach the Roche zone within the remaining lifetime. Furthermore, $a_{threshold}$ is given for each $\frac{Q_*}{k_{2,*}} = 10^5 - 10^9$ that is the semi major axis where τ_{Roche} equals the total lifetime of

the central star.

Planets within $a_{threshold}$ are the most interesting 'test cases' for different stellar tidal dissipation models as these systems should be affected by tidal friction on astronomical time scales. As can be seen (Figures 4.1, 4.2, and 4.3), the more massive the planet and also the more massive the host star, the further outwards extends the region of orbital instability. In addition, when comparing the parameters of the CoRoT planetary systems (Tables 1.3 and 1.2) with the tidal stability maps, it will become apparent that several CoRoT planets lie in unstable regions.
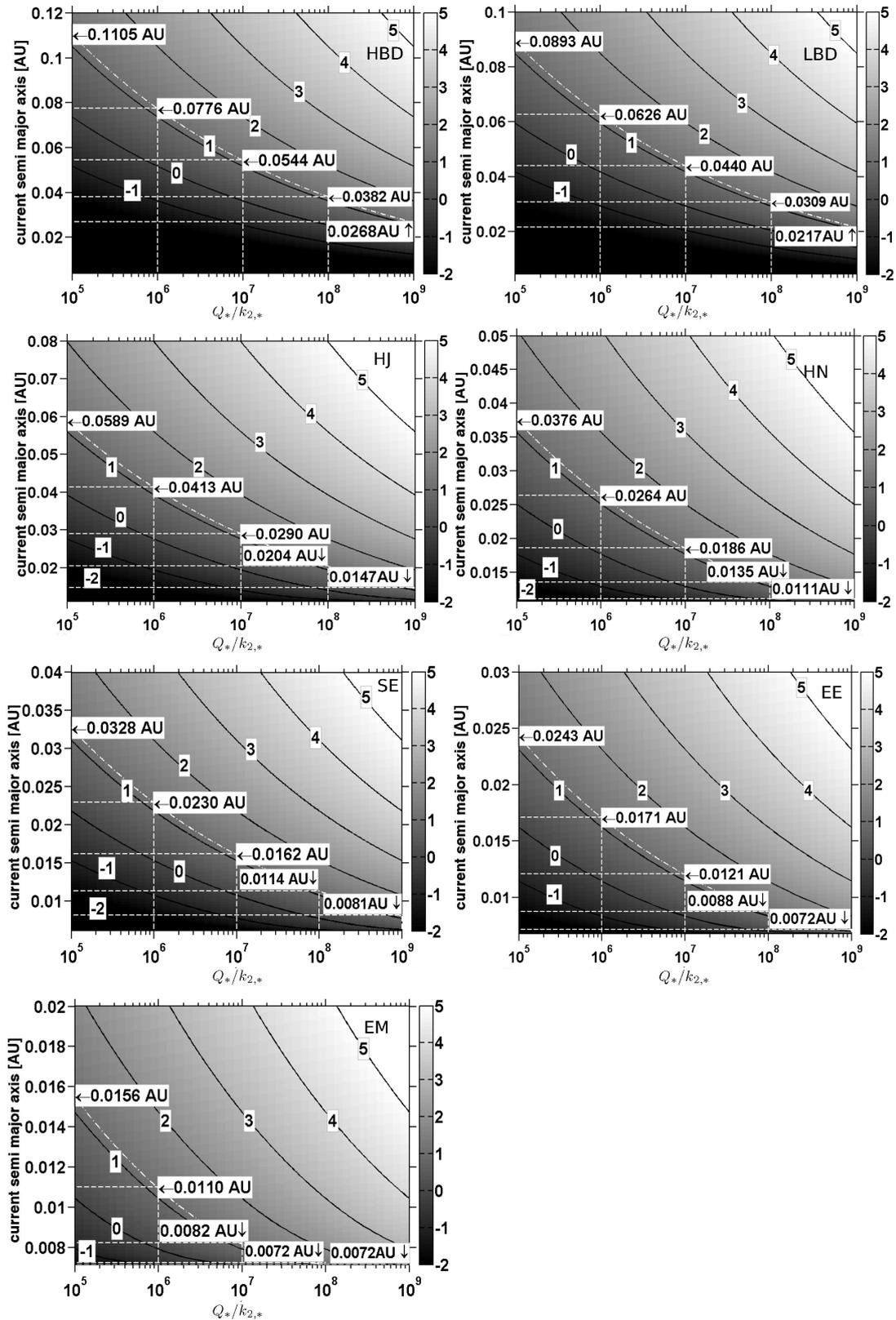
Figure 4.1: Tidal stability maps for different exoplanets around a K-star. From top to bottom, from left to right: A high mass brown dwarf, a low mass brown dwarf, a hot Jupiter, a Neptune, a Super-Earth, an Earth and a Mercury planet. The grey color gives the time scale τ_{Roche} in $\log(10^9$ years). The total lifetime of the star is indicated as a white dashed line. The black lines are the isochrones of τ_{Roche}. The horizontal and vertical dashed white lines indicate the stability limit $a_{threshold}$ for every $\frac{Q_*}{k_{2,*}}$.
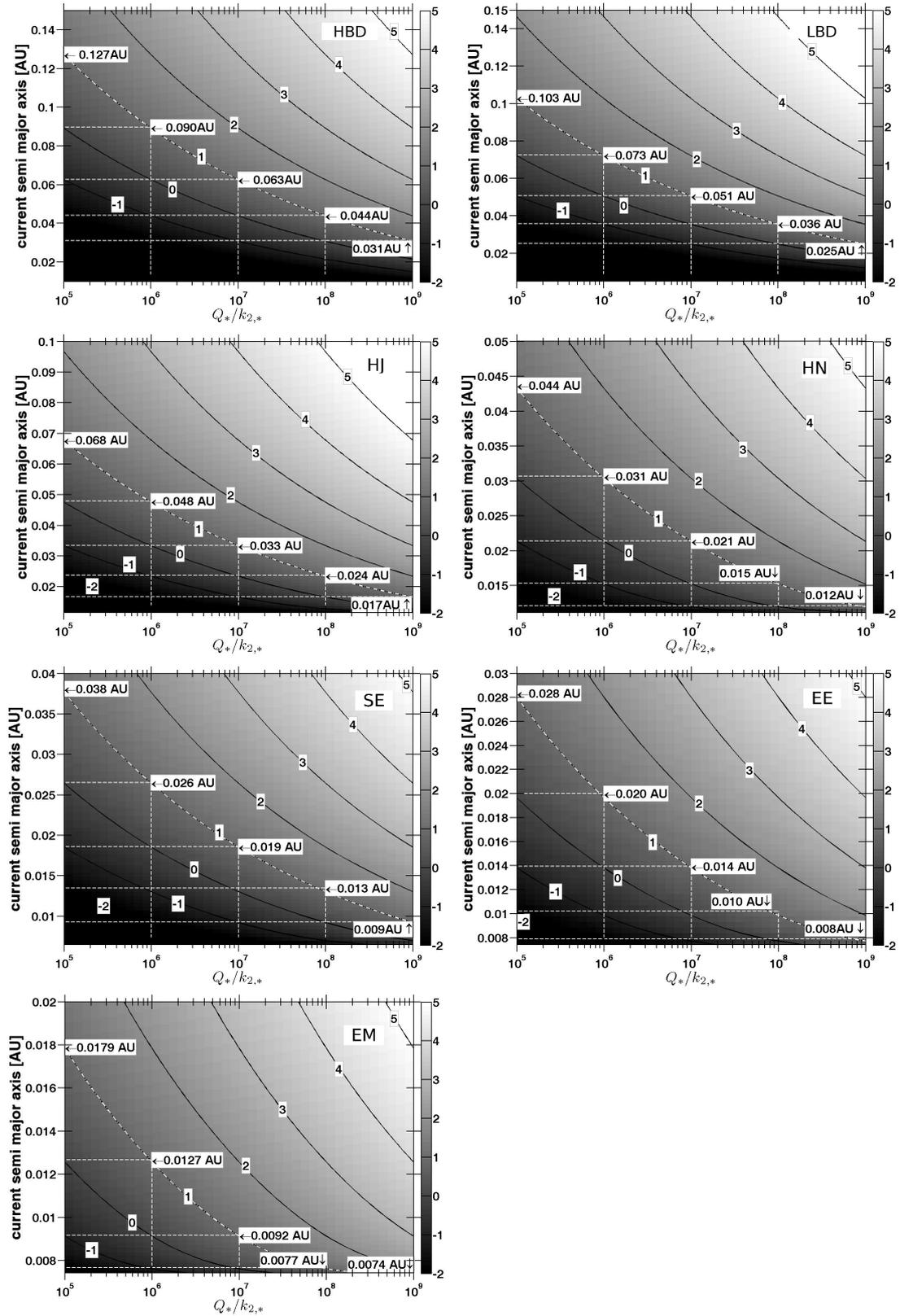
Figure 4.2: Tidal stability maps for different exoplanets around a G-star. See also Figure 4.1.
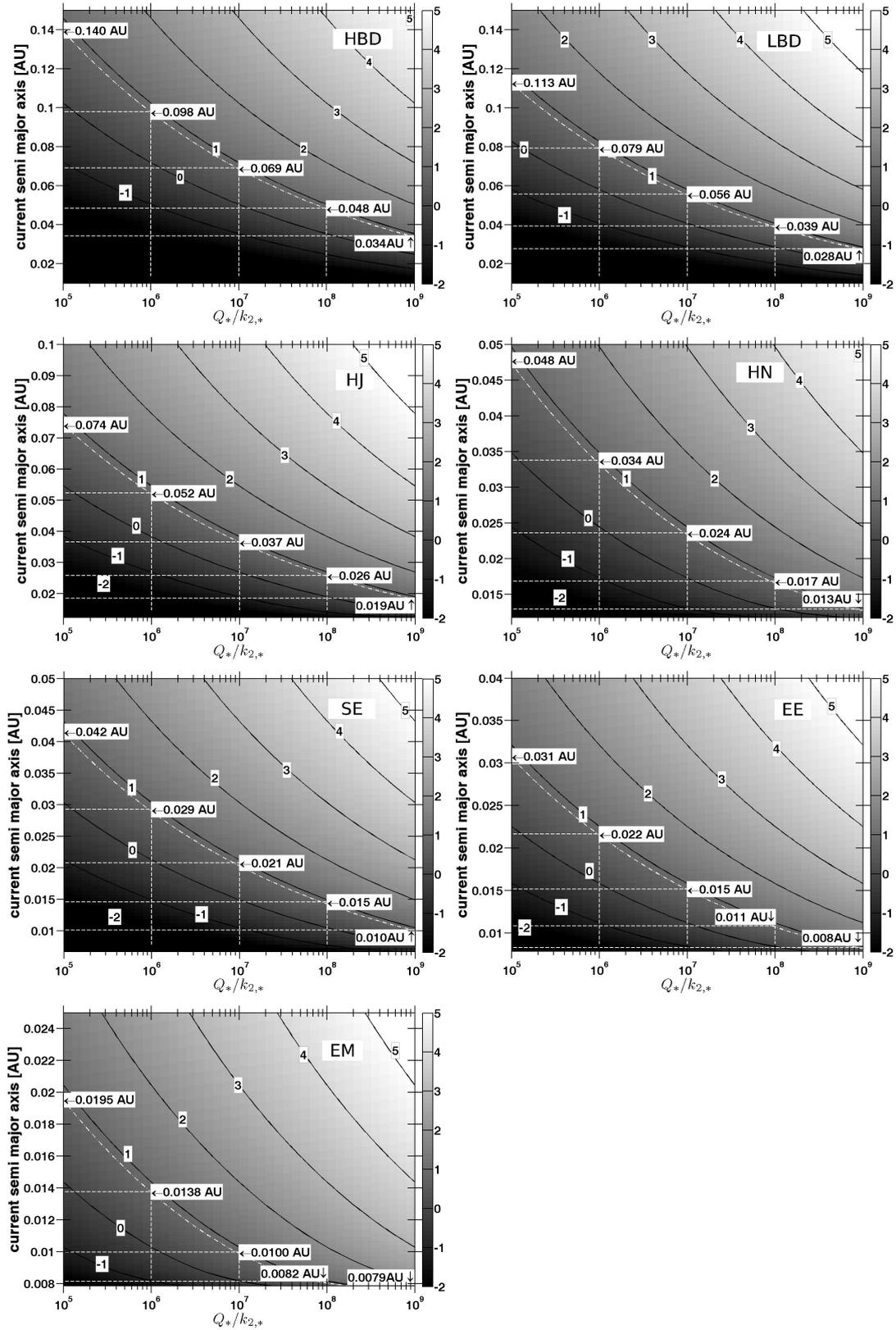
Figure 4.3: Tidal stability maps for different exoplanets around an F-star. See also Figure 4.1.

4.1.1 CoRoT systems most strongly affected by tidal friction

It became apparent in the previous section that the majority of the orbits of the majority of the CoRoT planets would be unstable under tidal friction for $\frac{Q_*}{k_{2,*}} = 10^5$. There are four clear cases that are stable for all assumed values of $\frac{Q_*}{k_{2,*}} = 10^5 - 10^9$ because their semi major axes are greater than the respective $a_{threshold}$: CoRoT-4b,-6b,-8b, and -9b. CoRoT-16b lies barely below $a_{threshold}$ for $\frac{Q_*}{k_{2,*}} = 10^5$. CoRoT-20b and CoRoT-10b appear at first glance to be stable. Their orbits, however, are in contrast to most other CoRoT planets very eccentric. Subsequent chapters will show that these planets are sufficiently long in the unstable regions to be affected by tidal friction.

Apart from the tidal stability maps, there are two other parameters that can be used to identify systems strongly affected by tidal friction: the Doodson constant Do and the tidal property factor PF.

The Doodson constant

The Doodson constant (see *Doodson* (1921) and *Pätzold et al.* (2004)) is defined as:

$$Do = \frac{3}{4} \frac{GM_{Pl}}{a^3} R_*^2. \tag{4.1.3}$$

This is the amplitude of the tidal potential (equation 2.3.8) and is a direct measure of the strength of the tidal force acting on the star [1]. Figure 4.4 shows the Doodson constant for tides raised by the CoRoT-planets on their stars. In comparison some Doodson constants are given for the Solar System.

Compared to tidal forces in the Solar System (Earth-Moon, Sun-any planet), the tidal forces between the CoRoT stars and planets are orders of magnitudes larger.

---

[1]The factor 3/4 arises to ensure that the amplitude of the angle dependent part of the tidal potential, that is the Legendre polynomial of second order $P_2(\cos\theta)$, is scaled to unity.
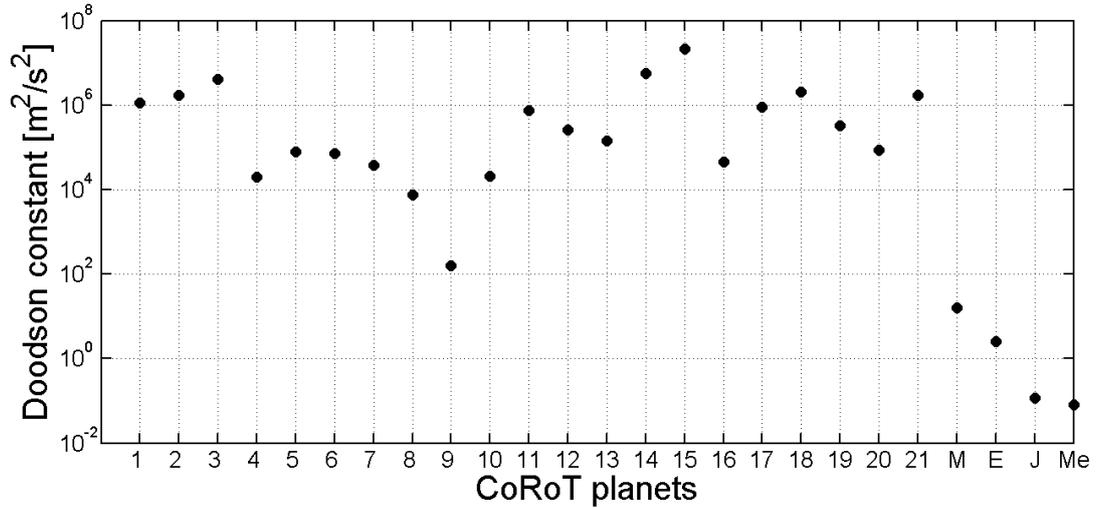
Figure 4.4: Doodson constants for tides raised on the star by CoRoT-1 to CoRoT-21b and several Solar System bodies. M marks the Doodson constant for tides raised by the Earth on the Moon, E denotes the Doodson constant for lunar tides raised on Earth, J denotes tides raised by Jupiter on the Sun and Me denotes the Doodson constant for tides raised by Mercury on the Sun.

CoRoT-planets are much closer to their stars than the planets in the Solar System. Mercury, the innermost planet in the Solar System, orbits at $a = 0.387$ AU. In addition, many CoRoT-planets are massive objects like gas giants and Brown Dwarfs. In the Solar System, the gas giants orbit far away from the Sun. Jupiter, the innermost gas giant, orbits at $a = 5.2$ AU. Within the CoRoT planetary systems, the following planets stand out due to their large Doodson numbers: CoRoT-1b,-2b,-3b,-14b,-15b,-18b, and -21b. In contrast to that, CoRoT-4b,-8b,-10b, and especially CoRoT-9b are the CoRoT planets with the smallest Doodson constant. CoRoT-9b is the transiting planet with the largest semi major axes found to date, therefore, the small Doodson number comes as no surprise. CoRoT-4b was already identified by the stability maps as a planetary system where planetary tides raised on the star have little consequences. The Doodson constant of CoRoT-10b, on the other hand, may be misleading due to

CoRoT-10b's large orbital eccentricity and because the Doodson constant is only valid for circular orbits.

The tidal property factor

The tidal property factor PF determines the secular orbital change (equation 2.6.19) and is described in *Pätzold and Rauer* (2002):

$$PF = \frac{M_{Pl}}{\sqrt{M_*}} R_*^5. \tag{4.1.4}$$
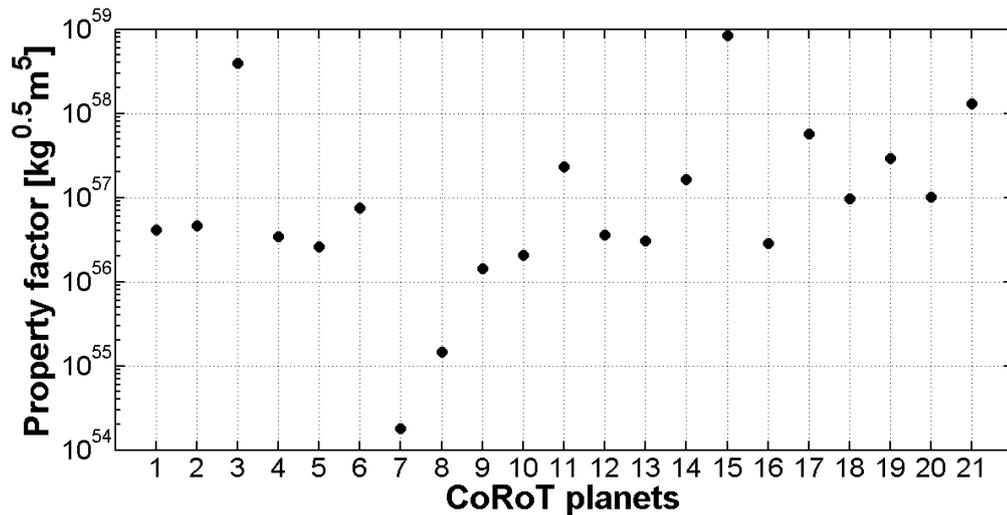
Figure 4.5: The tidal property factor for tides raised by the planets CoRoT-1b to CoRoT-21b on their stars.

Figure 4.5 shows the property factor for tides raised by the CoRoT planets and their stars. Four planets stand out: The brown dwarfs CoRoT-3b and CoRoT-15b have by far the largest property factor and reflect the fact that the mass ratio between the star and these companions is unusually high compared to other extrasolar planet systems. Consequently, it comes as no surprise that the least massive CoRoT planet, the Super Earth CoRoT-7b, has the lowest property factor. CoRoT-8b on the other

hand has such a small property factor because it orbits the smallest CoRoT exoplanet host star. CoRoT-8 is a K star with a radius of only $0.77\,R_{Sun}$.

In short, planetary companions, that stand out due to their large tidal property factor or Doodson constant or that lie in the unstable region of the tidal stability map, are particularly worthwhile candidates for tidal interaction investigations. This would be here: The brown dwarfs CoRoT-3b and CoRoT-15b, the jovian exoplanets CoRoT-1b,-2b,-3b, -5b,-11b,-13b,-14b,-18b,-19b, and -21b with semi major axis between 0.0254 AU and 0.057 AU. The tidal evolution of the Super Earth CoRoT-7b at $a = 0.0172$ AU is worthwhile investigating, as well. The tidal stability maps show that the planet lies in an unstable region around its star making it a worthwhile candidate for tidal interaction investigations even though it has the smallest property factor and a comparatively small Doodson constant. This example shows that, strictly speaking, a comparison of Doodson constants and property factors is better reserved for planets of the same class. Otherwise one may incorrectly judge a Super Earth to be an unsuited object for tidal interaction investigations when it is directly compared with much more massive Brown Dwarfs.

CoRoT-4b,-6b,-8b,and -9b have large semi major axes $a = 0.063 - 0.407$ AU, which lie in the stable regions of the tidal stability and have small tidal property factors and Doodson constants. For these systems, tidal friction is expected to play a minor role in their dynamical evolution.

When comparing the stellar rotation periods with the revolution periods (Table 1.4), many CoRoT systems are identified for which the stellar rotation is slower than the planetary revolution which may lead to the planet's migration towards the star, as expected. For other systems, however, this assumption does not hold: In

the CoRoT-6, CoRoT-11 and CoRoT-9 system, the stellar rotation is faster than the planet's revolution, consequently, the planet may migrate away from the star. Furthermore, the stellar rotation and planetary revolution appears to be very similar in the CoRoT-3, CoRoT-4, CoRoT-15 system, and maybe the CoRoT-20 system, which marks them as potential double synchronous states. Finally, four systems are identified with substantial orbital eccentricity $e = 0.3 - 0.562$: CoRoT-9, CoRoT-10, CoRoT-16, CoRoT-20. These are worthwhile investigating for this fact alone.

In summary, the CoRoT planets not only present a number of systems potentially unstable under tidal friction. In addition, many more scenarios with very different parameter constellations are encountered, worthwhile investigating in terms of tidal interactions. Consequently, the CoRoT-planetary systems can be divided into five categories which will be investigated separately in the course of this work:

- Planets on circular orbits around slowly rotating low-mass stars: CoRoT-1b, CoRoT-2b, CoRoT-7b, CoRoT-8b, CoRoT-12b, CoRoT-13b, CoRoT-17b, and CoRoT-18b.

- Planets on circular orbits around slowly rotating F-stars and one subgiant: CoRoT-5, CoRoT-14b, CoRoT-19b, and CoRoT-21b (around a subgiant)

- Planets on eccentric orbits: CoRoT-9b, CoRoT-10b, CoRoT-16b, and CoRoT-20b.

- Planets around fast-rotating stars: CoRoT-6b and CoRoT-11b

- Possible double synchronous systems: CoRoT-3, CoRoT-4, CoRoT-15, and CoRoT-20.

Chapter 5

Constraining $\frac{Q_*}{k_{2,*}}$ by requiring orbital stability of close-in planets around slowly rotating stars

In this chapter, the tidal semi major axes evolution of planets around slowly rotating stars is investigated. The constant-Q_*-assumption is justified at least for systems with planets on circular orbits because $\Omega_* - n < 0$ during the whole evolution time and because $\Omega_* - n$ does not vary by more than one and a half orders of magnitude at most during the whole evolution time. This is verified in Chapter 6 that investigates the stellar rotation evolution and in the Appendix (Figures C.1, C.2, C.3, and C.4). The planets discussed here may migrate towards their star and even enter the Roche zone within the lifetime of the star. It will be investigated for which $\frac{Q_*}{k_{2,*}}$ the system may be regarded as stable.

5.1 Tidal evolution of the semi major axis of CoRoT-Planets on circular orbits

Because the star rotates more slowly than the planet revolves around it ($\Omega_* < n$), the evolution of a planet's semi major axis on a circular orbit is modeled by:

$$\dot{a} = -\frac{3k_{2,*}M_{Pl}}{Q_*M_*}\left(\frac{R_*}{a}\right)^5 na \tag{5.1.1}$$

according to Section 2.6, Eq. (2.6.17). In Chapter E, the integration method used in this work is described and in Chapter F a model sensitivity analysis is performed for several selected CoRoT-systems.

The start time of the semi major axis evolution was set to 60 million years because at this age the inner structure of the CoRoT stars has settled (see Section 2.10, Figure 2.15). Even in cases where the minimum age cannot be constrained further by observations (CoRoT-1), this gives the lower limit for the age. The end time of the evolution was set to 1.5×10^{10} years to accommodate even the system with the largest lifetime and to keep the evolution of all systems comparable. The results of the semi major axis evolution are discussed in terms of the remaining lifetime, the total lifetime of each system minus the estimated age.

The semi major axis evolution is calculated for $\frac{Q_*}{k_{2,*}} = 10^5 - 10^9$ to account for the uncertainty of the stellar tidal dissipation factor. Furthermore, $\frac{Q_{Pl}}{k_{2,Pl}} = 10^5$ is assumed for the tidal evolution of Jupiter-like planets on circular orbits in agreement with calculations in Section 3.2. These planets can be regarded as tidally locked ($\Omega_{Pl} = n$) and tidal friction due to tides raised on the planet by the star is neglected[1].

---

[1] For the Super-Earth CoRoT-7, $Q_{Pl} = 10 - 100$ is probably more realistic, in agreement with Q_{Pl} found for terrestrial bodies in our own Solar System. For the investigations in this work, this only means that the planet's rotation is more easily synchronized with the planet's revolution. Therefore,

In the following, planets around low mass and higher mass stars are discussed separately. The need for this additional sub-division will become clear when discussing the stellar rotation evolution due to tidal friction in Chapter 6.

5.1.1 Tidal evolution of the semi major axis of CoRoT-Planets on circular orbits around low mass stars

CoRoT systems with a close-in planet on a circular orbit and a low mass star ($M_* < 1.1M_{Sun}$) are: CoRoT-1, CoRoT-2, CoRoT-7, CoRoT-8, CoRoT-12, CoRoT-13, CoRoT-17, and CoRoT-18. The eccentricities of the orbits of CoRoT-12b and CoRoT-18b are sufficiently small ($e = 0.07 \pm 0.06$ and $e \leq 0.08$, respectively) that they can be assumed to be zero, as well.

Figure 5.1 shows the evolution of the planets' semi major axis for the next 1.5×10^{10} years into the future with the equation (5.1.1) given above. The vertical lines mark how much time is left until the star evolves away from the main sequence, i.e., until its hydrogen fuel is depleted enough so that the star changes its inner structure dramatically in very short time, astronomically speaking (see for example *Unsoeld and Baschek* (2001)). The estimated total lifetime is listed in Table 5.1[2]. For CoRoT-17, the estimated total lifetime is actually smaller than the age of the system. This is not surprising because the relation by *Prialnik* (2000) (Eq 4.1.2) is a very simplified estimate that can be 'off' by one to two billion years. When taking into account, however, the error bars for the age of main sequence stars (Table 5.1), it becomes apparent that such a deviation is acceptable.

As can be seen from Figure 5.1, CoRoT-8 is the only planet within this subsample

---

it is a safe assumption that CoRoT-7b is tidally locked, as well.

[2]The age of CoRoT-1 is unknown. Therefore, the system is assumed to be at the beginning of its evolution.
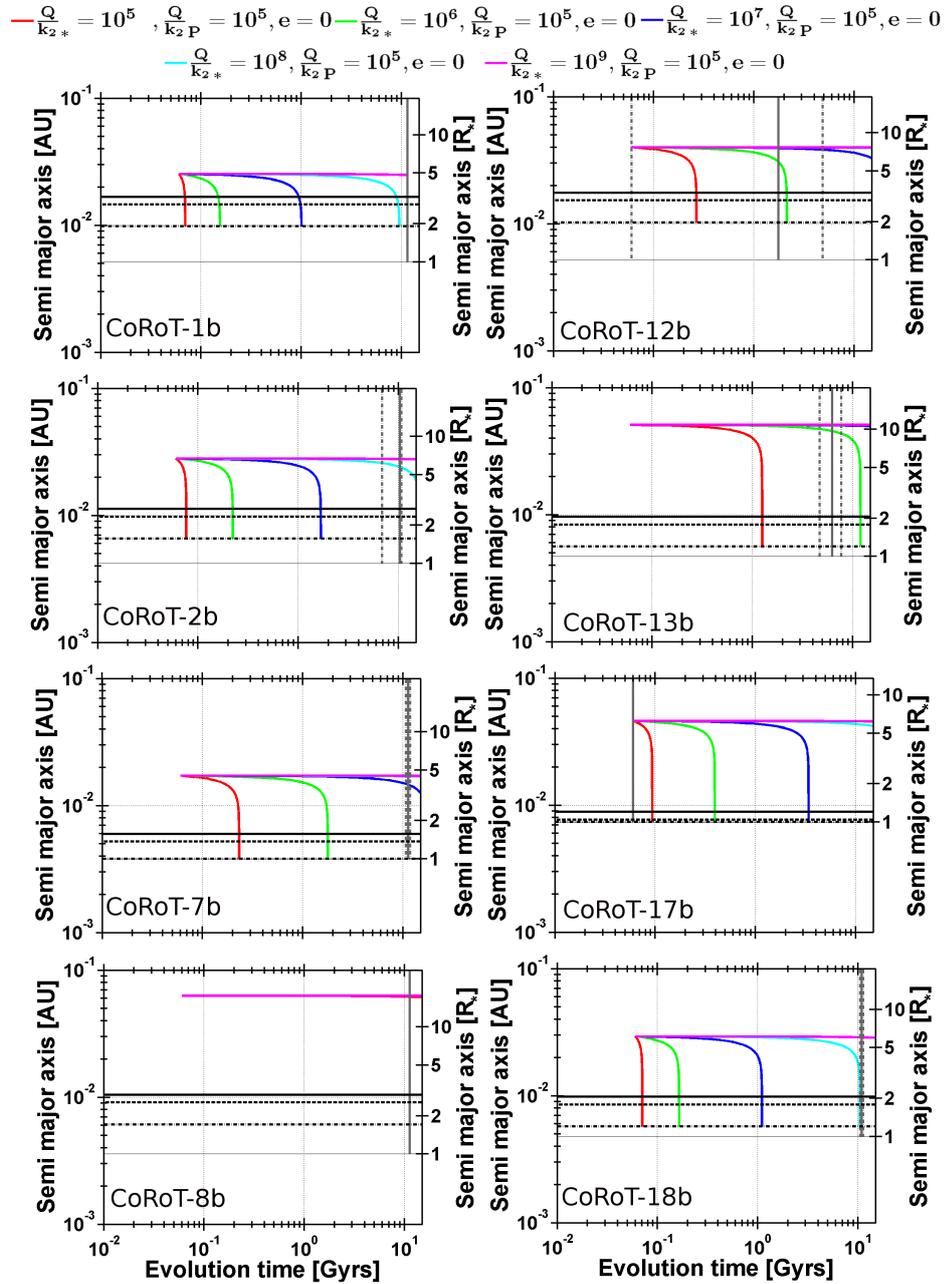
Figure 5.1: The tidal evolution of the semi major axis of the planets CoRoT-1b, -2b, -7b, -8b, -12b, -13b, -17b and -18b for the next 1.5×10^{10} years and for $\frac{Q_*}{k_{2,*}} = 10^5 - 10^9$. The horizontal lines mark Roche limits (from top to bottom: $a_{Roche,hydro}, a_{Roche,inter}, a_{Roche,rigid}$) which span the Roche zone (Section 2.12). At the distance $a = 1R_*$, another horizontal line marks the stellar surface. The vertical grey lines show the remaining lifetime of the system. The solid vertical line is the total lifetime of the star computed by 4.1.2 minus the age of the system. The dotted vertical lines are the minimum and maximum remaining lifetime of the system (lifetime − age ± Δage). For CoRoT-1, no age is known. A black vertical line marks the total lifetime. CoRoT-17 has reached the end of its lifetime, this is indicated by a black vertical line at the start point of the evolution.

which does not change its semi major axis significantly for any investigated $\frac{Q_*}{k_{2,*}} = 10^5 - 10^9$ during the next 15 billion years. This was already inferred in the previous Chapter 4.1.1 by the tidal stability map, the Doodson constant and the property factor. Apparently, these three measures are useful in distinguishing between tidally evolved and tidally stable systems.

CoRoT-1b, -2b, -7b, -13b, and -18b, on the other hand, may become unstable within the remaining lifetime of the system. CoRoT-12b and CoRoT-17b, whose stars may already be at the end of their lifetime, can still be considered as unstable if $\frac{Q_*}{k_{2,*}} = 10^5$, in which case these planets may enter the Roche zone on timescales of ten to hundred million years. This is a fate they share with CoRoT-1b, -2b, -7b and -18b.

This is very short when compared to the remaining lifetime of several billion years. It would be unlikely to observe such planets just as they plunge toward their host star, but detections of close-in hot Jupiters are by no means rare events. Intuitively, $\frac{Q_*}{k_{2,*}}$ would be expected to be much higher than 10^5 to allow long-term survival for such very short-period extrasolar planets. The same conclusion may be tentatively drawn for Super-Earths like CoRoT-7b. The Kepler-10 system, for example, has very similar properties to CoRoT-7 with one noteworthy exception (*Batalha et al.*, 2011): Kepler-10 (age: 12 billion years) is about ten billion years older than CoRoT-7 (age: 1-2 billion years). Kepler-10b looks like an older version of CoRoT-7b, which also hints to a long-term stability of such systems.

The $\frac{Q_*}{k_{2,*}}$-limit of stability necessary for a given planet to survive under tidal friction can be derived more accurately by setting the remaining lifetime $\tau_{rem.lifetime} = \tau_{Roche}$,

inserting it into equation 4.1.1 and by solving for $\frac{Q_*}{k_{2,*}}$:

$$\frac{Q_*}{k_{2,*}}_{stable} \geq \frac{\tau_{rem.lifetime} \frac{3M_{Pl}}{2M_*} R_*^5 \sqrt{GM_*}}{\frac{1}{13}\left[a_{Present}^{13/2} - a_{Roche}^{13/2}\right]}, \tag{5.1.2}$$

where $\tau_{rem.lifetime}$ is the estimated total lifetime minus the age of the system (Table 5.1), for the Roche limit a_{Roche}, the outermost limit of the Roche zone was selected $a_{Roche,hydro} = 2.46 R_* \left(\frac{\rho_*}{\rho_{Pl}}\right)^{1/3}$, and $a_{Present}$ is the current semi major axis of the planet.

The derived limits of stability are given in Table 5.1. It should be noted that for CoRoT-12b, a confidence interval of the estimated stability is computed due to the large uncertainty in the age of the system. The given values represent the stability limit for the minimum, average and maximum remaining lifetime. The minimum estimated remaining lifetime of CoRoT-12 is zero because the system may already be at the end of its lifetime. $\frac{Q_*}{k_{2,*}} = 10^7 - 10^8$ emerges as a common limit of stability from Table 5.1.

a) No error bars for the age of the system are given in the detection paper (*Bordé et al.*, 2010)

b) The given age is larger than the estimated total lifetime. Therefore, the system is assumed to be at the end of its lifetime.

System	$\frac{Q_*}{k_{2,*}}_{stable}$	total lifetime [Gyrs]	age [Gyrs]
CoRoT-1	1.3×10^8	11.5	-
CoRoT-2	$6^{+1}_{-2} \times 10^7$	11	$0.5^{+3.5}_{-0.3}$
CoRoT-7	$6.9^{+0.3}_{-0.7} \times 10^6$	13	$1.7^{+0.6}_{-0.5}$
CoRoT-8	stable for $10^5 - 10^{10}$	14	3^a
CoRoT-12	$-/8 \times 10^5/2 \times 10^6$	8	$6.3^{+3.1}_{-3.1}$
CoRoT-13	$5.2^{+1.3}_{-2.5} \times 10^5$	8	$1.6^{+1.5}_{-1.5}$
CoRoT-17	already at the end of lifetime	8^b	10.7^{+1}_{-1}
CoRoT-18	$1 \pm 0.02 \times 10^8$	11.5	$0.6^{+0.4}_{-0.4}$

Table 5.1: Required $\frac{Q_*}{k_{2,*}}_{stable}$ for the planet's orbit to stay outside the Roche limit within the minimum, average, and maximum remaining lifetime of the star.

5.1.2 Tidal evolution of the semi major axis of planets on circular orbits around F stars and subgiants

The orbit stability of the CoRoT-planets on circular orbits around F-stars is investigated: These are CoRoT-5b, CoRoT-14b, CoRoT-19b, and CoRoT-21b orbiting a subgiant.
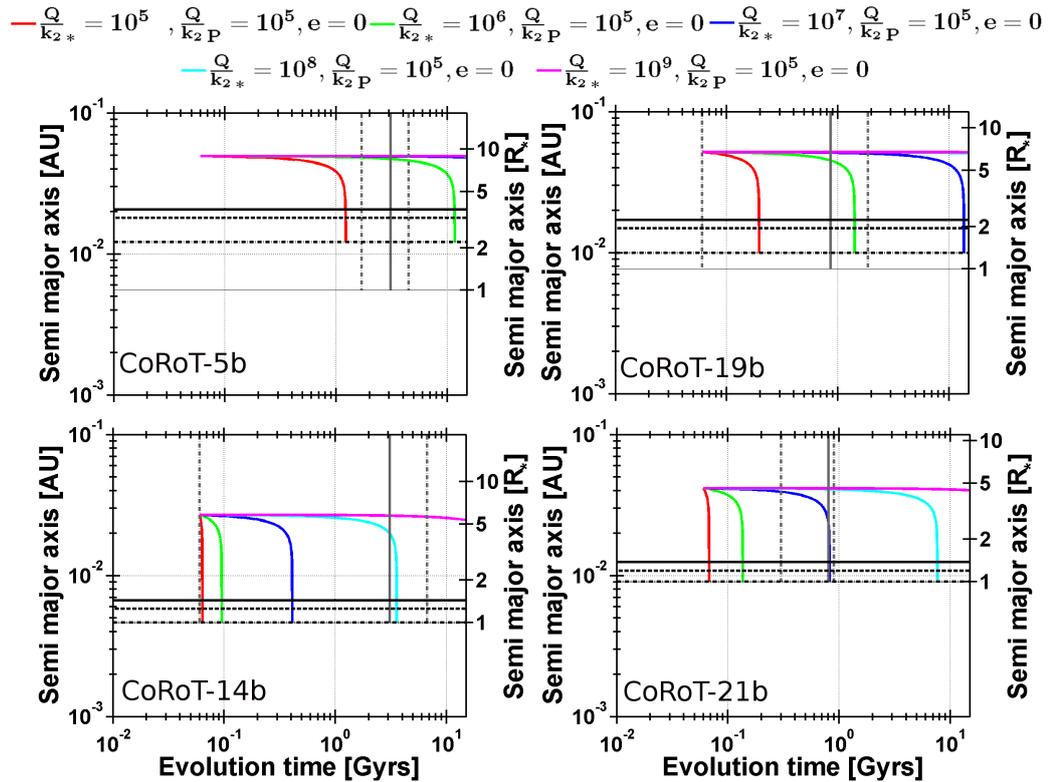
Figure 5.2: The tidal evolution of the semi major axis of the planets CoRoT-5b, 14b, 19b, and -21b for the next 1.5×10^{10} years and for $\frac{Q_*}{k_{2,*}} = 10^5 - 10^9$. The horizontal lines span the Roche zone. The horizontal line at $a = 1R_*$ marks the stellar surface. The vertical lines show the remaining lifetime of the system. See Figure 5.1 for a more detailed description.

Figure 5.2 shows the evolution of the planets' semi major axes. All planets investigated in this subsection may reach the Roche zone within their remaining lifetime.

System	$\frac{Q_*}{k_{2,*}}_{stable}$	total lifetime [Gyrs]	age [Gyrs]
CoRoT-5	$2.7^{+1.2}_{-1.2} \times 10^5$	10	$6.9^{+1.4}_{-1.4}$
CoRoT-14	$-/9 \times 10^7/1.9 \times 10^8$	7.1	$4^{+4}_{-3.6}$
CoRoT-19	$-/6.3 \times 10^5/1.4 \times 10^6$	5.9	5^{+1}_{-1}
CoRoT-21	$1^{+0.2}_{-0.6} \times 10^7$	4.9	$4.1^{+0.5}_{-0.1}$

Table 5.2: Required $\frac{Q_*}{k_{2,*}\,stable}$ (eq. 5.1.2) for the planet's orbit to stay outside the Roche limit within the remaining lifetime of the star.

The age of CoRoT-14 and -19 are not very well constrained and it cannot be excluded that the systems are already at the end of their lifetimes. Strictly speaking, $\frac{Q_*}{k_{2,*}}$ cannot be constrained by requiring the planets CoRoT-14b and -19b to survive for the next few billion years. Still, the CoRoT-14 system would already be destroyed within the next few hundred million years if $\frac{Q_*}{k_{2,*}} \leq 10^7$. The same is true for CoRoT-21b. If $\frac{Q_*}{k_{2,*}}$ is indeed as small as 10^5, it should be unlikely to observe such systems on the 'brink of destruction'.

Equivalent to the approach in the previous section, $\frac{Q_*}{k_{2,*}\,stable}$ is calculated as a lower limit that would allow the planet to survive the remaining lifetime under tidal friction (Table 5.2).

Again, $\frac{Q_*}{k_{2,*}} = 10^7 - 10^8$ emerges as a common limit of stability; even though the systems in this subset have much shorter lifetimes than the systems with low mass stars, discussed previously (Table 5.1)

5.2 Tidal evolution of the semi major axis and eccentricity of planets on eccentric orbits

The following CoRoT-systems with non-negligible orbit eccentricity are identified: CoRoT-9, CoRoT-10, CoRoT-16 and CoRoT-20. CoRoT-9b's semi major axis, however, is so great that no substantial orbital evolution is expected. Furthermore, CoRoT-9 rotates much faster than the planet revolves around it. Consequently, even if tidal friction would be a factor in the system's evolution, it would drive the planet away from the star. That tidal friction plays no role in the orbital evolution of CoRoT-9b is confirmed by the computation (Appendix, Figure B.2). In the following, the semi major axis and eccentricity evolution of CoRoT-10b, CoRoT-16b and CoRoT-20b are investigated in more detail.

The relevant set of equations are:

$$\frac{\mathrm{d}a}{\mathrm{d}t} = -3\frac{k_{2,*}}{Q_*}\frac{M_{Pl}}{M_*}\left(\frac{R_*}{a}\right)^5 na(1-e^2)^{-15/2}\frac{\left[f_1(e)n - (1-e^2)^{3/2}f_2(e)\Omega_*\right]}{|n - \Omega_*|}$$
$$-3\frac{k_{2,Pl}}{Q_{Pl}}\frac{M_*}{M_{Pl}}\left(\frac{R_{Pl}}{a}\right)^5 na(1-e^2)^{-15/2}\frac{\left[f_1(e)n - (1-e^2)^{3/2}f_2(e)\Omega_{Pl}\right]}{|n - \Omega_{Pl}|}$$

$$(5.2.1)$$

$$\frac{\mathrm{d}e}{\mathrm{d}t} = -\frac{27}{2}\frac{k_{2,*}}{Q_*}\frac{M_{Pl}}{M_*}\left(\frac{R_*}{a}\right)^5 ne(1-e^2)^{-13/2}\frac{\left[f_3(e)n - \frac{11}{18}(1-e^2)^{3/2}f_4(e)\Omega_*\right]}{|n - \Omega_*|}$$
$$-\frac{27}{2}\frac{k_{2,Pl}}{Q_{Pl}}\frac{M_*}{M_{Pl}}\left(\frac{R_{Pl}}{a}\right)^5 ne(1-e^2)^{-13/2}\frac{\left[f_3(e)n - \frac{11}{18}(1-e^2)^{3/2}f_4(e)\Omega_{Pl}\right]}{|n - \Omega_{Pl}|}$$

$$(5.2.2)$$

$$\frac{\mathrm{d}\Omega_*}{\mathrm{d}t} = \frac{3}{2I_*}\frac{k_{2,*}}{Q_*}\frac{M_{Pl}}{M_* + M_{Pl}}\frac{M_{Pl}}{M_*}\left(\frac{R_*}{a}\right)^3 n^2\left(1-e^2\right)^{-6}\frac{\left[f_2(e)n - (1-e^2)^{3/2}f_5(e)\Omega_*\right]}{|n - \Omega_*|}$$
$$+\frac{\mathrm{d}\Omega_*}{\mathrm{d}t}_{m.braking}$$

$$(5.2.3)$$

$$\frac{\mathrm{d}\Omega_{Pl}}{\mathrm{d}t} = \frac{3}{2I_{Pl}}\frac{k_{2,Pl}}{Q_{Pl}}\frac{M_*}{M_* + M_{Pl}}\frac{M_*}{M_{Pl}}\left(\frac{R_{Pl}}{a}\right)^3 n^2\left(1-e^2\right)^{-6}\frac{\left[f_2(e)n - (1-e^2)^{3/2}f_5(e)\Omega_{Pl}\right]}{|n - \Omega_{Pl}|},$$

$$(5.2.4)$$

where

$$f_1(e) = 1 + \frac{31}{2}e^2 + \frac{225}{8}e^4 + \frac{185}{16}e^6 + \frac{25}{64}e^8 \qquad (5.2.5)$$

$$f_2(e) = 1 + \frac{15}{2}e^2 + \frac{45}{8}e^4 + \frac{5}{16}e^6$$

$$f_3(e) = 1 + \frac{15}{4}e^2 + \frac{15}{8}e^4 + \frac{5}{64}e^6$$

$$f_4(e) = 1 + \frac{3}{2}e^2 + \frac{1}{8}e^4$$

$$f_5(e) = 1 + 3e^2 + \frac{3}{8}e^4,$$

$$\frac{\mathrm{d}\Omega_*}{\mathrm{d}t}_{m.braking} = -\frac{K}{I_*M_*R_*^2}\Omega_*^3\left(\frac{R_*}{R_{Sun}}\right)^{1/2}\left(\frac{M_*}{M_{Sun}}\right)^{-1/2} \text{ if } \Omega_* < \omega_{sat} \qquad (5.2.6)$$

$$= -\frac{K}{I_*M_*R_*^2}\Omega_*^2\omega_{sat}\left(\frac{R_*}{R_{Sun}}\right)^{1/2}\left(\frac{M_*}{M_{Sun}}\right)^{-1/2} \text{ if } \Omega_* > \omega_{sat}. \qquad (5.2.7)$$

As can be seen, apart from tidal friction due to tides raised on the star (stellar tidal friction), the effect of tidal friction due to tides raised on the planet (planetary tidal friction) are taken into account as well. The latter were neglected for planets on circular orbits due to tidal locking of the planet's spin. The influence of stellar and planetary tidal friction on the orbit are added; just as it was done by *Matsumura et al.* (2010) based on the *Hut* (1981) equations described in Section 2.7[3]. *Matsumura et al.* (2010) calculates tidal friction, however, in the constant τ_* and τ_{Pl} formalism but discusses his results using Q_* and Q_{Pl} values which the authors derives by the well known relation:

$$\tau = \frac{1}{2|\Omega - n|Q}.$$

In this work, the relation above is already applied to (Eq. 5.2.1, 5.2.2, 5.2.3, and 5.2.4) to keep the discussion consistent throughout this work. The constant Q assumption is used with care, keeping in mind that it requires $2|\Omega_* - n| \approx$ const and $2|\Omega_{Pl} - n| \approx$ const[4] The calculations shown here should therefore be handled with care and may need to be revised in the future. For now, the constant Q assumption is used as a first order approach to gain insights about the possible tidal evolution for planets on eccentric orbits.

When comparing the stellar rotation period P_* and the orbital period P_{orb} for the CoRoT-10, the CoRoT-16, and the CoRoT-20 system (Table 1.4), several conclusions can already be drawn. For the CoRoT-10 and 16 system, the stellar rotation is slower than the orbital revolution ($\Omega_* < n$), the planet should migrate towards the star. For the CoRoT-20 system, the situation is uncertain, because here $P_* = 11.5 \pm 2.6$ days

---

[3]Contrary to *Matsumura et al.* (2010), stellar obliquity ϵ_* is neglected ($\cos \epsilon_* \approx 1$).

[4]It was shown that for planets on circular orbits (Chapter 3.2) $|\Omega_{Pl} - n| \approx 0$. For planets on eccentric orbits, however, $|\Omega_{Pl} - n| = n \left(6e^2 + \frac{3}{8}e^4 + \frac{223}{8}e^6\right)$ (See Appendix D).

and $P_{orb} = 9.244 \pm 0.001$. Therefore, either $\Omega_* < n$, $\Omega_* = n$, or $\Omega_* > n$ within limits of uncertainty. In this section, the average stellar rotation period $P_* = 11.5$ days is used as a starting point of the evolution. Another possible starting point $P_* = 8.9$ days is investigated in Section 8.4.1 when discussing possible double synchronous systems.

To distinguish the influence of planetary tidal friction from that of stellar tidal friction, the tidal evolution of the planetary semi major axes are not only investigated for different $\frac{Q_*}{k_{2,*}}$-values but also for different planetary tidal dissipation factors. The exoplanets discussed here are jovian planets, therefore $\frac{Q_{Pl}}{k_{2,Pl}} \approx 10^5$ (from Section 2.8) is a good first choice for the investigation of tidal evolution. To be on the safe side, a $\frac{Q_{Pl}}{k_{2,Pl}}$-range covering three orders of magnitude is investigated, $\frac{Q_{Pl}}{k_{2,Pl}} = 10^4, 10^5, 10^6$. This $\frac{Q_{Pl}}{k_{2,Pl}}$-range is also adopted by *Dobbs-Dixon et al.* (2004) and *Jackson et al.* (2008).

Exemplarily, the semi major axis evolution of eccentric planets for $\frac{Q_{Pl}}{k_{2,Pl}} = 10^4$ (Figure 5.3) is discussed:

Semi major axis evolution of CoRoT-10b, $\frac{Q_{Pl}}{k_{2,Pl}} = 10^4$

If $\frac{Q_*}{k_{2,*}} \geq 10^6$, the semi major axes of CoRoT-10b will decrease for the next two billion years until the orbit settles at 0.076 AU and remains there. If $\frac{Q_*}{k_{2,*}} = 10^5$, the planet settles on a slightly smaller semi major axis after an initial decrease and will even start to migrate moderately towards the star after several billion years.

Semi major axis evolution of CoRoT-16b, $\frac{Q_{Pl}}{k_{2,Pl}} = 10^4$

The orbital evolution of CoRoT-16b also goes through two stages of tidal orbital migration. At first, there is an initial decrease on timescales of tens of million years. The orbit remains stable for the next billion years. After several billion years, a decrease in the semi major axis follows that depends on $\frac{Q_*}{k_{2,*}}$. For the smallest $\frac{Q_*}{k_{2,*}} =$
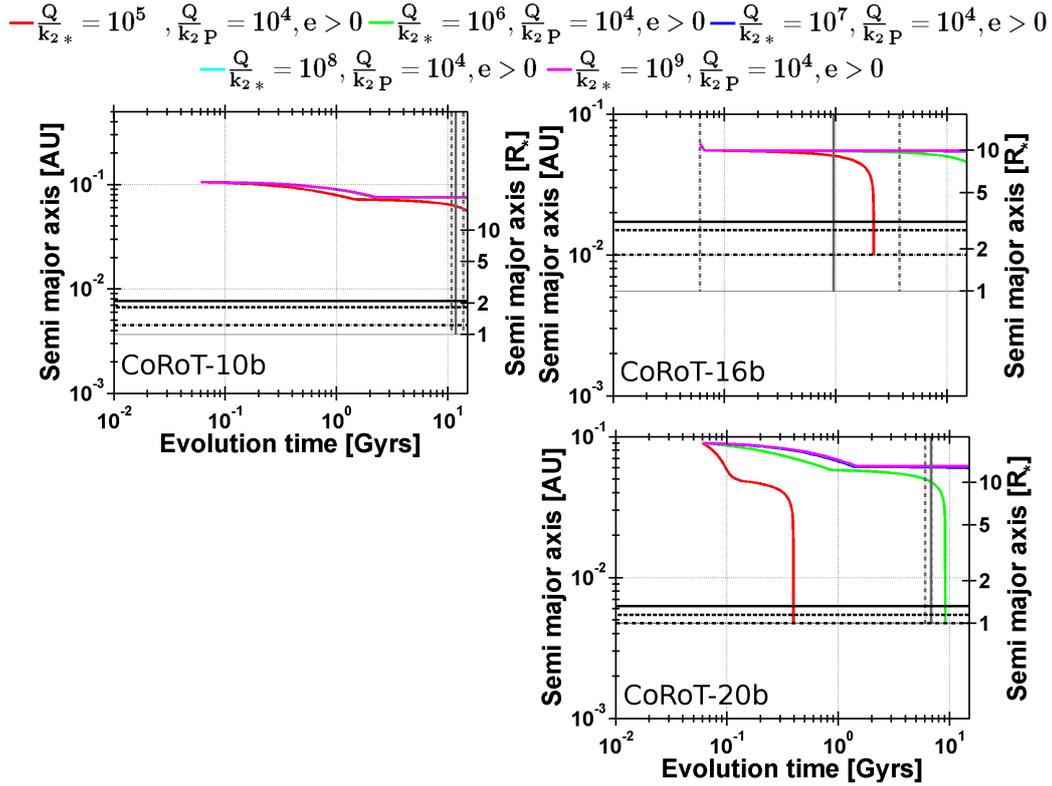
Figure 5.3: The tidal evolution of the semi major axis of the planets CoRoT-10b, -16b, and CoRoT-20b for the next 1.5×10^{10} years, for $\frac{Q_*}{k_{2,*}} = 10^5, 10^6, 10^7, 10^8, 10^9$ and $\frac{Q_{Pl}}{k_{2,Pl}} = 10^4$. The horizontal lines span the Roche zone. The horizontal line at $a = 1 R_*$ marks the stellar surface. The vertical lines show the remaining lifetime of the system. See Figure 5.1 for a more detailed description.

10^5, the planet will reach the Roche limit after two billion years. For $\frac{Q_*}{k_{2,*}} = 10^6$, the planet may start to migrate towards the star after 10 billion years. The system is, however, foreseen to survive only the next 4 billion years at most. Therefore, the orbit of CoRoT-16b will remain stable within the remaining lifetime for $\frac{Q_*}{k_{2,*}} \geq 10^6$. Only for $\frac{Q_*}{k_{2,*}} = 10^5$, the planet may be destroyed and only at the end of the system's remaining lifetime.

Semi major axis evolution of CoRoT-20b, $\frac{Q_{Pl}}{k_{2,Pl}} = 10^4$

The semi major axis evolution of CoRoT-20b is more complicated. If $\frac{Q_*}{k_{2,*}} \geq 10^7$, the orbit evolution is very similar to that of CoRoT-10b: After a decrease in semi major axis within the next two billion years, the semi major axis settles at 0.063 AU. For smaller $\frac{Q_*}{k_{2,*}} \leq 10^6$, two stages of orbit evolution are again discernible. There is a fast initial decrease within 100 million years if $\frac{Q_*}{k_{2,*}} = 10^5$, within 900 million years if $\frac{Q_*}{k_{2,*}} = 10^6$. For $\frac{Q_*}{k_{2,*}} = 10^5$, the planet remains only for about one hundred million years at $a \approx 0.05$ AU, showing a moderate migration towards the star during this time. Then, the planet's migration towards the star accelerates rapidly and CoRoT-20b reaches the Roche limit within 400 million years evolution time. For $\frac{Q_*}{k_{2,*}} = 10^6$, the planet remains at $a \approx 0.06$ AU for several billion years until the planet migrates toward the star and reaches the Roche limit after nine billion years evolution time.

Orbital eccentricity evolution of CoRoT-10b, $\frac{Q_{Pl}}{k_{2,Pl}} = 10^4$

When taking into account the tidal eccentricity evolution (Figure 5.4), it becomes clearer why there are two stages of tidal orbital evolution. The orbital eccentricity of CoRoT-10b will decrease within the next 2.5 billion years until the orbit is circular, for any $\frac{Q_*}{k_{2,*}}$. This is exactly the time for which a semi major axis decrease is observed.
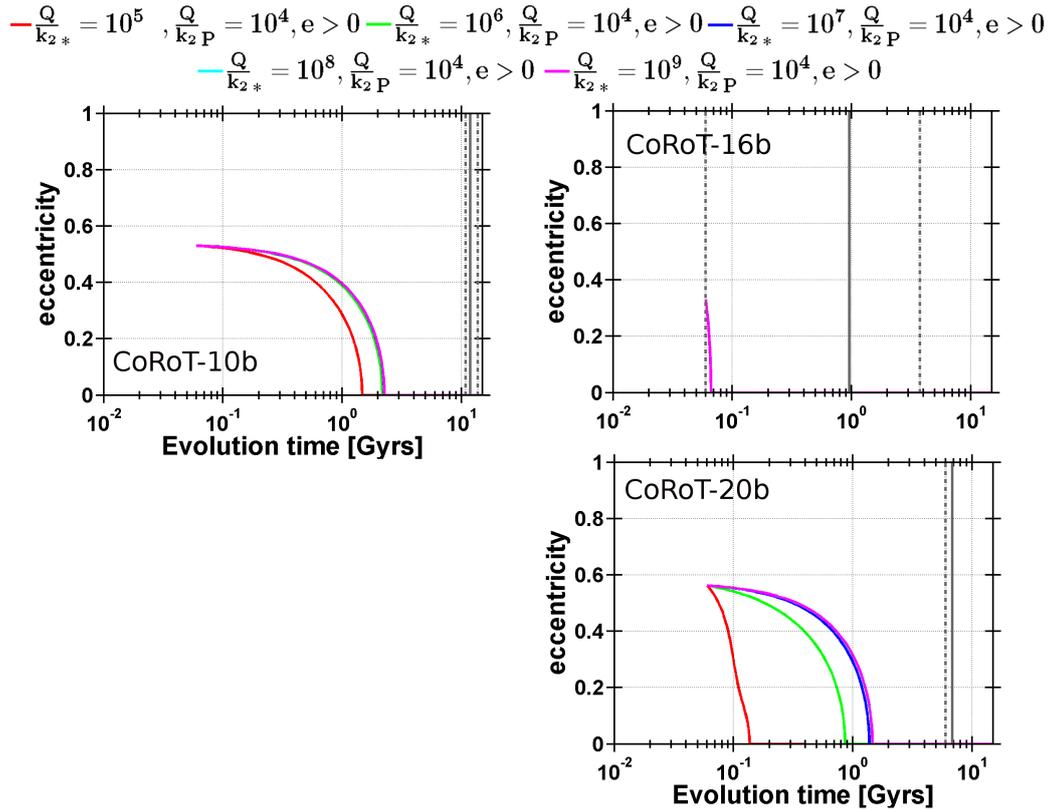
Figure 5.4: The tidal evolution of the orbit eccentricity of CoRoT-10b, -16b, and CoRoT-20b for the next 1.5×10^{10} years, for $\frac{Q_*}{k_{2,*}} = 10^5 - 10^9$ (solid lines) and $\frac{Q_{Pl}}{k_{2,Pl}} = 10^4$. The vertical lines show the remaining lifetime of the system.

Apparently, the orbital evolution during this time is driven mainly by planetary tidal friction. When $e = 0$, the terms in equation (5.2.1) depending on $\frac{Q_{Pl}}{k_{2,Pl}}$ vanish, as was already discussed previously. Only for $\frac{Q_*}{k_{2,*}} \leq 10^6$, a small contribution of stellar tidal friction to the initial semi major axis and eccentricity evolution is visible (Figures 5.5 and 5.6).

For the long-term stability of the CoRoT-10 system it can be concluded that the system is stable and unaffected by stellar tidal friction, if $\frac{Q_*}{k_{2,*}} \geq 10^6$. Because the orbit settles at 0.076 AU after orbit circularization, the planet is too far away from the star to experience tidal migration within the remaining lifetime.
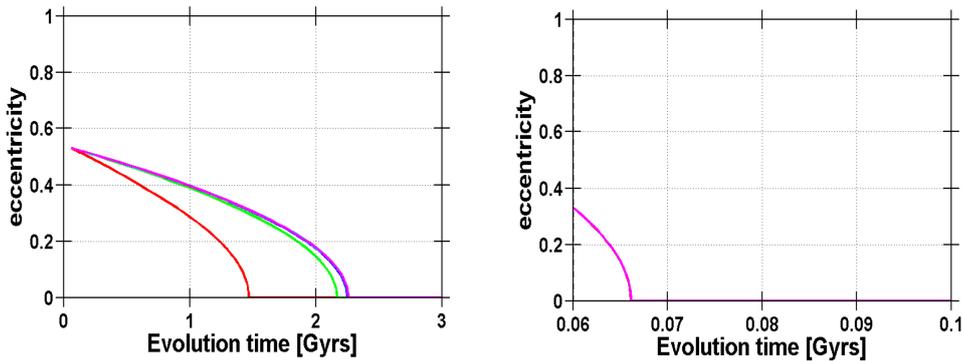
Figure 5.5: Close-up of the orbit eccentricity evolution of CoRoT-10b and -16b due to tides for $\frac{Q_*}{k_{2,*}} = 10^5 - 10^9$ and $\frac{Q_{Pl}}{k_{2,Pl}} = 10^4$.

For $\frac{Q_*}{k_{2,*}} = 10^5$, on the other hand, the combination of stellar and planetary tidal friction leads to a stronger decrease in semi major axis during this initial evolution phase. The planet settles at a lower orbit than compared with evolution tracks with $\frac{Q_*}{k_{2,*}} \geq 10^6$, $a = 0.071$ AU. This small difference is sufficient to lead to a destabilization of the orbit on timescales of billion years due to stellar tidal friction.
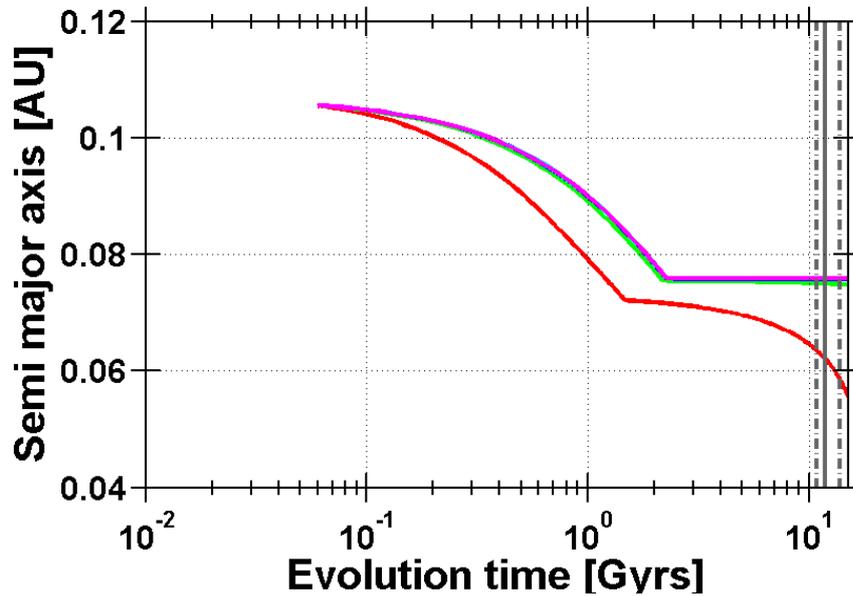
Figure 5.6: The tidal evolution of the semi major axis of the planets CoRoT-10b for the next 1.5×10^{10} years in more detail, for $\frac{Q_*}{k_{2,*}} = 10^5 - 10^9$ and $\frac{Q_{Pl}}{k_{2,Pl}} = 10^4$. The vertical lines show the remaining lifetime of the system.

Orbital eccentricity evolution of CoRoT-16b, $\frac{Q_{Pl}}{k_{2,Pl}} = 10^4$

The orbital eccentricity of CoRoT-16b will already be zero after ten million years, this is so fast that no influence on the eccentricity evolution is seen due to stellar tidal friction. The evolution is the same for each $\frac{Q_*}{k_{2,*}}$ (Figure 5.5). This very fast circularization corresponds to a fast decrease in the semi major axis of CoRoT-16b (Figure 5.3). After that, only stellar tidal friction may affect the system and only if $\frac{Q_*}{k_{2,*}} = 10^5$. In that case, however, the planet reaches the Roche limit within the next three billion years.

Orbital eccentricity evolution of CoRoT-20b, $\frac{Q_{Pl}}{k_{2,Pl}} = 10^4$

While for any $\frac{Q_*}{k_{2,*}}$, the influence of stellar and planetary tidal friction on the orbital parameters of the planets CoRoT-10b and CoRoT-16b could be divided into an early phase driven mainly by planetary tidal friction and a possible later phase driven only by stellar tidal friction, for CoRoT-20b, only orbital evolution tracks with $\frac{Q_*}{k_{2,*}} \geq 10^7$ show this behavior. In that case, the orbit of CoRoT-20b is circularized within the next two billion years and the semi major axis finally settles at 0.063 AU, too far away to be affected by stellar tidal friction.

For smaller $\frac{Q_*}{k_{2,*}} \leq 10^6$, stellar tides have a non-negligible influence on the eccentricity evolution of CoRoT-20b in the initial phase and lead to further damping such that the orbit becomes circular much earlier within 150 million years ($\frac{Q_*}{k_{2,*}} \geq 10^5$) and 900 million years $\frac{Q_*}{k_{2,*}} \geq 10^6$, respectively. In addition, the semi major axis is reduced so much for $\frac{Q_*}{k_{2,*}} = 10^5$ due to the combined action of planetary and stellar tidal friction, that the orbit decays within the remaining lifetime.

5.2.1 How does the semi major axis and eccentricity evolution change with larger $\frac{Q_{Pl}}{k_{2,Pl}}$

Figures 5.7, 5.8, and 5.9, 5.10 show the semi major axis and eccentricity evolution for $\frac{Q_{Pl}}{k_{2,Pl}} = 10^5$ and $\frac{Q_{Pl}}{k_{2,Pl}} = 10^6$, respectively. Any change in the evolution tracks compared to the $\frac{Q_{Pl}}{k_{2,Pl}} = 10^4$-scenario can be ascribed to the reduction in planetary tidal friction strength.
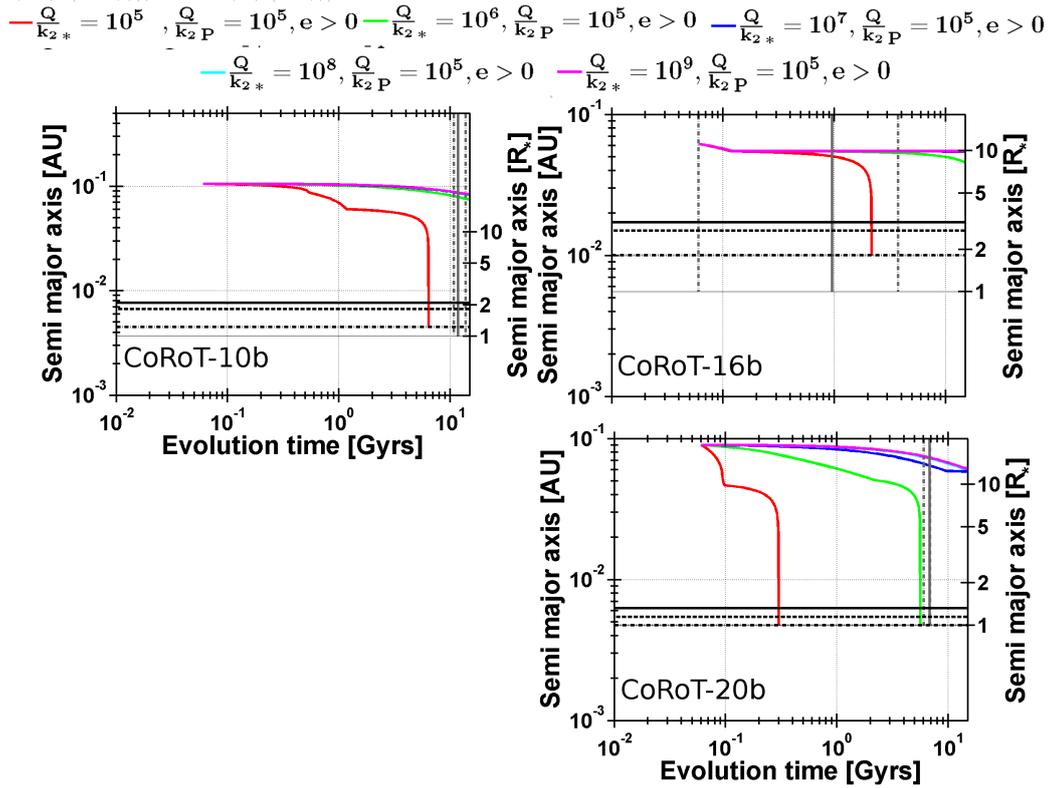
Figure 5.7: The tidal evolution of the semi major axis of CoRoT-10b, -16b, and CoRoT-20b for the next 1.5×10^{10} years, for $\frac{Q_*}{k_{2,*}} = 10^5 - 10^9$ and $\frac{Q_{Pl}}{k_{2,Pl}} = 10^5$. The horizontal lines span the Roche zone. The horizontal line at $a = 1R_*$ marks the stellar surface. The vertical lines show the remaining lifetime of the system. See Figure 5.1 for a more detailed description.
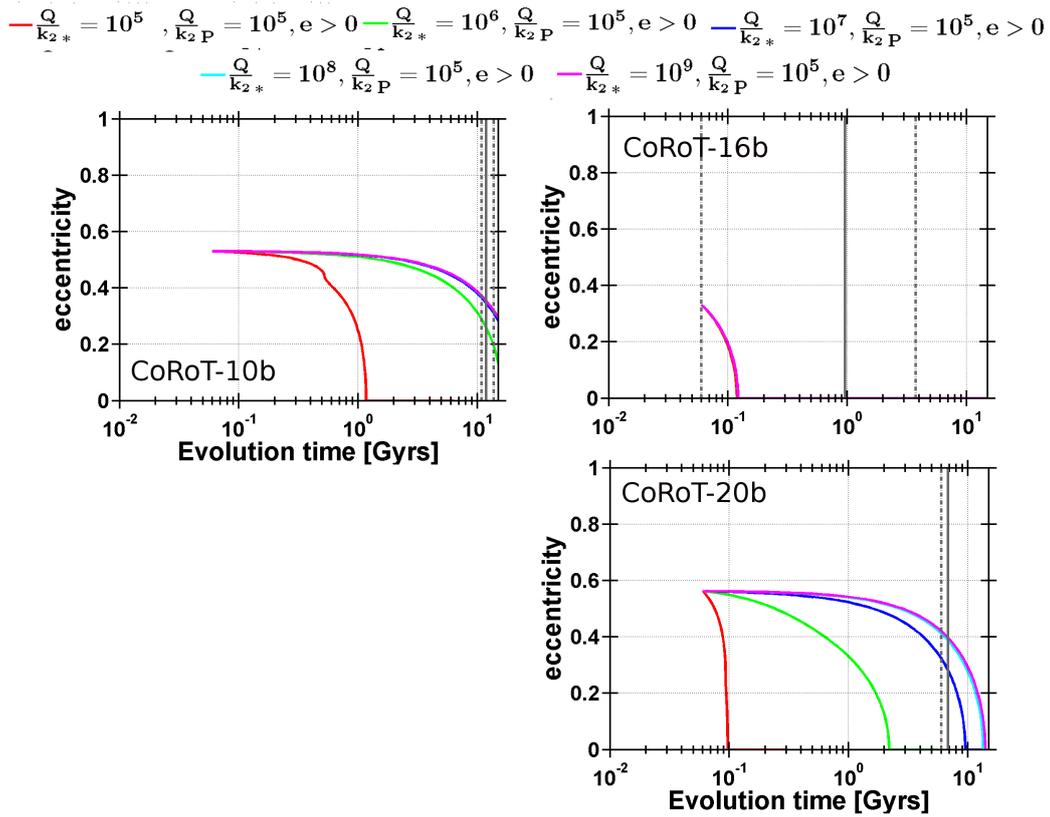
Figure 5.8: The tidal evolution of the orbit eccentricity of CoRoT-10b, -16b, and CoRoT-20b for the next 1.5×10^{10} years, for $\frac{Q_*}{k_{2,*}} = 10^5 - 10^9$ (solid lines) and $\frac{Q_{Pl}}{k_{2,Pl}} = 10^5$. The vertical lines show the remaining lifetime of the system.
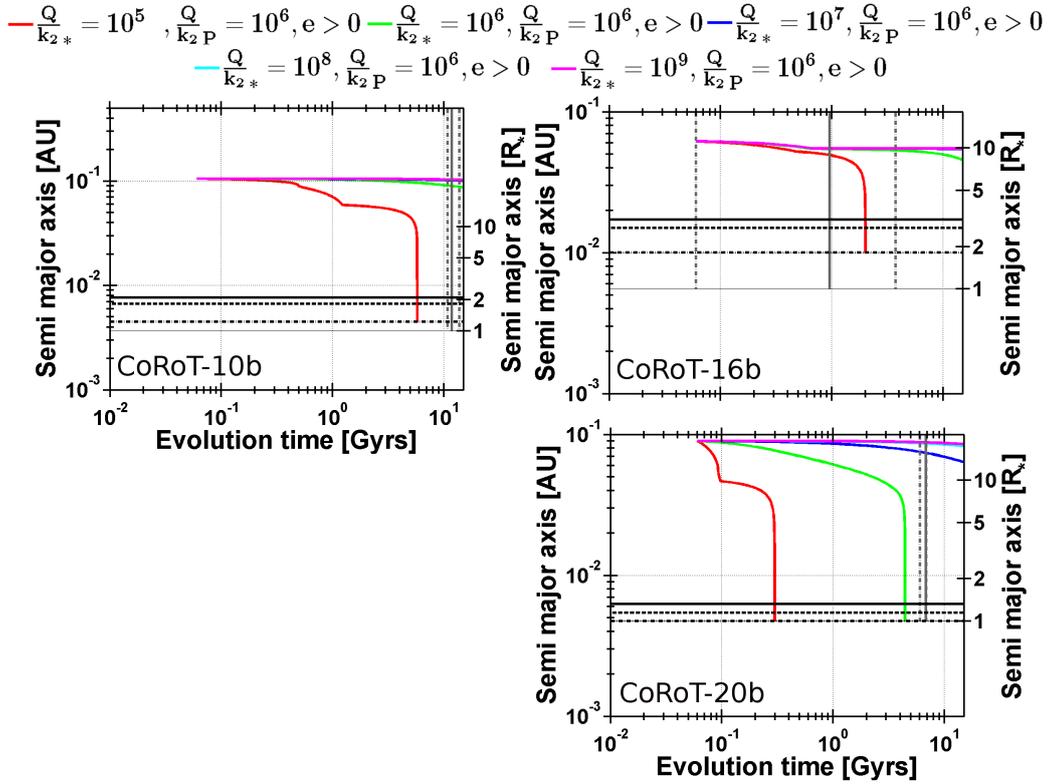
Figure 5.9: The tidal evolution of the semi major axis of CoRoT-10b, -16b, and CoRoT-20b for the next 1.5×10^{10} years, for $\frac{Q_*}{k_{2,*}} = 10^5 - 10^9$ and $\frac{Q_{Pl}}{k_{2,Pl}} = 10^6$. The horizontal lines span the Roche zone. The horizontal line at $a = 1R_*$ marks the stellar surface. The vertical lines show the remaining lifetime of the system. See Figure 5.1 for a more detailed description.
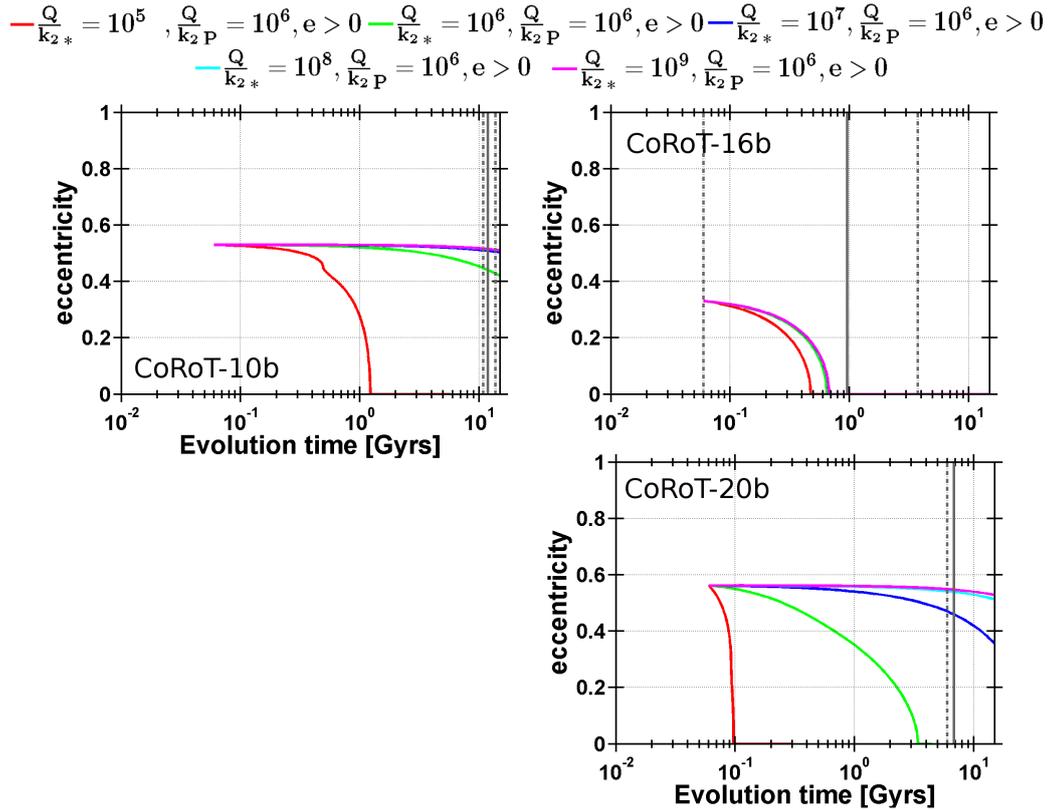
Figure 5.10: The tidal evolution of the orbit eccentricity of CoRoT-10b, -16b, and CoRoT-20b for the next 1.5×10^{10} years, for $\frac{Q_*}{k_{2,*}} = 10^5 - 10^9$ (solid lines) and $\frac{Q_{Pl}}{k_{2,Pl}} = 10^6$. The vertical lines show the remaining lifetime of the system.

Orbital evolution of CoRoT-16b, $\frac{Q_{Pl}}{k_{2,Pl}} = 10^5 - 10^6$

The evolution of CoRoT-16b will be discussed first, as an example for planets with moderate to low orbit eccentricity $e \leq 0.3$. The discussion starts with this case because comparing the different $\frac{Q_{Pl}}{k_{2,Pl}}$ is more straightforward for this case than for the other two CoRoT planets with larger eccentricities, as will be shown later.

For CoRoT-16b, it will take longer for the eccentricity to become zero with increasing $\frac{Q_{Pl}}{k_{2,Pl}}$. In any case, the eccentricity will be damped to zero within a few hundred million years which is very fast when compared to the total stellar lifetime of several billion years. Most importantly, the semi major axis evolution after the eccentricity is damped to zero is independent of $\frac{Q_{Pl}}{k_{2,Pl}}$: The semi major axis after circularization, let's call it a_{equiv}, is the same.

The equivalent semi major axis a_{equiv}

Therefore, a_{equiv} can be used for CoRoT-16b, a planet on an orbit with $e = 0.3$, to derive the orbital long-term stability limit $\frac{Q_*}{k_{2,*}}_{stable}$ from calculations developed for circular orbits.

a_{equiv} can be derived keeping in mind that planetary tidal friction requires conservation of total angular momentum L_{tot}, where the total angular momentum in this case is the sum of the orbital angular momentum and the angular momentum of the planet's rotation. Because the latter is negligible as discussed in Section 3.3, the total angular momentum is approximately equal the orbital angular momentum.

Before circularization, this is (using Kepler's third law $n = \sqrt{G(M_* + M_{Pl})/a^3}$):

$$
\begin{aligned}
L_{orb,e>0} &= \frac{M_{Pl}M_*}{M_{Pl} + M_*} na^2 \sqrt{1 - e^2} \\
&= \frac{M_{Pl}M_*}{M_{Pl} + M_*} \sqrt{G(M_* + M_{Pl})} \sqrt{a} \sqrt{1 - e^2},
\end{aligned}
$$

Planet	semi major axis [AU]	eccentricity	a_{equiv} [AU]
CoRoT-9b	0.407	0.11	0.402
CoRoT-10b	0.1055	0.53	0.076
CoRoT-16b	0.0618	0.3	0.056
CoRoT-20b	0.092	0.562	0.063

Table 5.3: Equivalent semi major axis a_{equiv} (equation 5.2.8) of the CoRoT-planets on eccentric orbits.

and after circularization this is:

$$L_{orb,e=0} = \frac{M_{Pl}M_*}{M_{Pl} + M_*}\sqrt{G(M_* + M_{Pl})}\sqrt{a_{equiv}}.$$

Because $L_{orb,e>0} \approx L_{orb,e=0}$, combining the equations above and solving for a_{equiv} yields:

$$a_{equiv} = a\left(1 - e^2\right). \tag{5.2.8}$$

The equivalent semi major axes of CoRoT-9b, CoRoT-10b, CoRoT-16b, and CoRoT-20b for a circular orbit are listed in Table (5.3).

When comparing a_{equiv} of CoRoT-20b instead of the 'normal' semi major axis of the eccentric orbit with the tidal stability maps (Section 4.1), it is no longer surprising that CoRoT-20b may become unstable for $\frac{Q_*}{k_{2,*}} = 10^5 - 10^6$. It should also be noted that the a_{equiv}-values of CoRoT-10b and CoRoT-20b given in Table 5.3 are the semi major axes values on which the planets settle after an initial eccentricity damping phase for $\frac{Q_{Pl}}{k_{2,Pl}} = 10^4$ and $\frac{Q_*}{k_{2,*}} \geq 10^7$.

It has to be stressed, however, that the calculations used to derive a_{equiv} are only valid as long as planetary tidal friction acts on much shorter timescales than stellar tidal friction. Only then it can be assumed that the orbital angular momentum is conserved during eccentricity damping by planetary tidal friction.

The eccentricities of the orbits of CoRoT-10b and CoRoT-20b are, however, relatively large ($e > 0.5$). For these planets, it will be shown that planetary and stellar tidal friction may act on the same timescale if $\frac{Q_*}{k_{2,*}} \leq 10^6$ and, therefore, it can no longer be assumed that the orbital angular momentum is always conserved during eccentricity damping. The long-term stability of the orbits depends on $\frac{Q_*}{k_{2,*}}$ **and** $\frac{Q_{Pl}}{k_{2,Pl}}$.

5.2.2 Positive feedback effect for planets on orbits with $e > 0.5$

Orbital evolution of CoRoT-10b, $\frac{Q_{Pl}}{k_{2,Pl}} = 10^5 - 10^6$

For CoRoT-10, an increased $\frac{Q_{Pl}}{k_{2,Pl}} = 10^5 - 10^6$ results in an inefficient orbit circularization if $\frac{Q_*}{k_{2,*}} \geq 10^7$. The eccentricity will never be zero within the remaining lifetime. Furthermore, the eccentricity evolution tracks are the same for each $\frac{Q_*}{k_{2,*}}$, suggesting that the eccentricity damping is driven by planetary tidal friction alone.

For $\frac{Q_*}{k_{2,*}} \leq 10^6$, stellar tidal friction is no longer negligible for the eccentricity damping, leading to a faster decrease in eccentricity. This becomes even more apparent when considering the semi major axis evolution. As the semi major axis decreases, stellar and planetary tidal friction increase in strength. This leads to an accelerating decrease in semi major axis.

For $\frac{Q_*}{k_{2,*}} = 10^5$, the positive feedback effect is the strongest: When the eccentricity becomes zero, the semi major axis of the circularized orbit is so small and stellar tidal friction is so efficient that the planet becomes unstable within the next seven billion years well within the system's remaining lifetime. Apparently, the assumptions used to calculate a_{equiv} no longer hold. Namely, that the orbital angular momentum is conserved during circularization because planetary tidal friction acts on much shorter timescales than stellar tidal friction. When discussing the stellar rotation evolution

in the next chapter, it will become obvious that the missing amount of orbital angular momentum during the orbit circularization is transferred to the star by stellar tidal friction. It is surprising that a planet with the same orbital angular momentum as CoRoT-10b would be regarded as stable if the orbit were circular. Due to the large eccentricity of the orbit of CoRoT-10b, the planet will instead reach the Roche limit if $\frac{Q_*}{k_{2,*}} = 10^5$ and $\frac{Q_{Pl}}{k_{2,Pl}} \geq 10^5$.

Orbital evolution of CoRoT-20b, $\frac{Q_{Pl}}{k_{2,Pl}} = 10^5 - 10^6$

The early evolution of the semi major axis of CoRoT-20 gives even stronger evidence for the positive feedback effect of the combined influence of stellar and planetary tidal friction, when comparing the semi major axis evolution in the $\frac{Q_{Pl}}{k_{2,Pl}} = 10^4$-scenario with those of the $\frac{Q_{Pl}}{k_{2,Pl}} = 10^5$- and $\frac{Q_{Pl}}{k_{2,Pl}} = 10^6$-scenarios. In the $\frac{Q_{Pl}}{k_{2,Pl}} = 10^4$-scenario, the semi major axis reaches the Roche limit only for $\frac{Q_*}{k_{2,*}} = 10^5$ within the remaining lifetime but then very fast within the next 400 million years. When $\frac{Q_{Pl}}{k_{2,Pl}}$ increases, the $\frac{Q_*}{k_{2,*}} = 10^6$ evolution track reaches the Roche limit within the remaining lifetime as well. Within five to six billion years, if $\frac{Q_{Pl}}{k_{2,Pl}} = 10^5 - 10^6$.

5.2.3 Orbital stability for planets on eccentric orbits

In summary, for low $\frac{Q_*}{k_{2,*}} \leq 10^6$, planetary tidal friction can not be neglected when investigating the orbital long term stability of planets with large orbital eccentricities $e > 0.5$ like CoRoT-20b and CoRoT-10b. In this case, planetary and stellar tidal friction act on similar timescales to decrease the semi major axis. Therefore, the orbit stability depends on $\frac{Q_*}{k_{2,*}}$ as well as on $\frac{Q_{Pl}}{k_{2,Pl}}$. To derive the stability limit, the orbital evolution is modeled with different $\frac{Q_*}{k_{2,*}}$, where $\frac{Q_*}{k_{2,*}}$ is incremented logarithmically in steps of $10^{0.2}$, beginning with $\frac{Q_*}{k_{2,*}} = 10^6$, until the evolution track is found on which

a) using eq.(5.1.2) with a_{equiv}
b) orbit simulation with stepwise $\frac{Q_*}{k_{2,*}}$-increase

System	$\frac{Q_*}{k_{2,*}}{}_{stable}$	$\frac{Q_{Pl}}{k_{2,Pl}}$	total lifetime [Gyrs]	age [Gyrs]
CoRoT-9	stable for $10^5 - 10^{10}$	$10^4 - 10^6$	10	$0.15 - 8$
CoRoT-10	stable for $10^5 - 10^{10}$	10^4	14	2 ± 1
CoRoT-10[b]	$10^{5.2}$	10^5	14	2 ± 1
CoRoT-10[b]	$10^{5.4}$	10^6	14	2 ± 1
CoRoT-16[a]	$-/8 \times 10^4/1.6 \times 10^5$	$10^4 - 10^6$	7.7	6.7 ± 2.8
CoRoT-20[b]	10^6	10^4	6.9	$0.1^{+0.8}_{-0.04}$
CoRoT-20[b]	$10^{6.2}$	10^5	6.9	$0.1^{+0.8}_{-0.04}$
CoRoT-20[b]	$10^{6.2}$	10^6	6.9	$0.1^{+0.8}_{-0.04}$

Table 5.4: Required $\frac{Q_*}{k_{2,*}}{}_{stable}$ for the planet's orbit to stay outside the Roche limit within the minimum, average and maximum remaining lifetime of the star.

the planet enters the Roche zone at the end of the remaining lifetime. For CoRoT-16b, a_{equiv} can be inserted into eq.(5.1.2) to yield the stability limit.

$\frac{Q_*}{k_{2,*}}{}_{stable}$ for all eccentric planets, CoRoT9b, -10b, CoRoT-16b, CoRoT-20b, are listed in Table 5.4[5]. CoRoT-16 may very well be at the end of its lifetime. Therefore, $\frac{Q_*}{k_{2,*}}$ cannot be constrained for the upper limit of the remaining lifetime.

As can be seen, the orbits of CoRoT-16b and CoRoT-10b are stable for $\frac{Q_*}{k_{2,*}} \gg 10^5$. The orbit of CoRoT-20b for $\frac{Q_*}{k_{2,*}} \gg 10^6$, which agrees nicely with the stability limit $10^7 - 10^8$ derived in previous sections. If $\frac{Q_*}{k_{2,*}} \geq 10^7$, the planets may settle after orbit circularization at the equivalent semi major axes listed in (Table 5.3) and will remain stable there.

[5]CoRoT-9 is only included for completeness.

5.3 Limits of stability on potentially unstable systems

The common limit of stability is $\frac{Q_*}{k_{2,*}} \geq 10^7$ for all cases discussed in this chapter. If $\frac{Q_*}{k_{2,*}}$ is indeed so large, this would explain why close-in extrasolar planets are frequently discovered. Otherwise, some of these planets would exist only for several hundred million years or even less if $\frac{Q_*}{k_{2,*}} = 10^6$. This is very small in astronomical time scales and it would be very improbable to observe such a planet before it reaches the Roche zone and is tidally disrupted.

So far, the tidal evolution of the stellar rotation was not discussed in detail. It was only assumed that the tidal frequency $2|\Omega_* - n|$, which contains the stellar rotation, is more or less constant during the computation and that at all times $\Omega_* \ll n$. It will be shown that the evolution of stellar rotation itself bears surprises that may help to constrain the stellar tidal dissipation factor based on other arguments.

Chapter 6

Constraining $\frac{Q_*}{k_{2,*}}$ by stellar rotation evolution of slowly rotating stars

In the previous chapter, the tidal evolution of the orbit of CoRoT planets around slowly rotating stars due to stellar tidal friction - and planetary tidal friction, in the case of eccentric orbits - was investigated. It was shown that, for the lower values of $\frac{Q_*}{k_{2,*}} \leq 10^6$, the semi major axis of many planets may decay considerably over astronomical timescales. In consequence, the orbital angular momentum of these planets decreases. Due to conservation of total angular momentum, the angular momentum has to be transferred somewhere else. As was outlined in Sections 2.6 and 2.7, it is transferred to the extrasolar planet host star. To gain further insight into this process, the stellar rotation evolution is investigated in this chapter. It has to be noted that the stellar rotation period might have large error bars, in particular, when the rotation is slow. In this work, the average rotation period is used as a starting point of evolution to obtain qualitative results on the expected stellar rotation evolution in the presence of tidal friction. It will be shown that the derived conclusions with respect to $\frac{Q_*}{k_{2,*}}$ do not depend strongly on the stellar rotation starting point. A more detailed model sensitivity analysis with respect to the limits of uncertainties of the

initial parameters is given in Appendix, Chapter F.

Like in the previous chapter, the following categories of CoRoT systems are investigated: low mass main sequence host stars of planets on circular orbit, host stars of F-spectral type and one subgiant of planets on circular orbit and host stars of planets on eccentric orbits.

6.1 Tidal rotation evolution of the host stars of CoRoT-Planets on circular orbits

The star rotates more slowly than the planet revolves around it ($\Omega_* < n$) and the tidal evolution of the stellar rotation is modeled according to Section 2.6 with equation (2.6.18). Because main sequence stars lose angular momentum due to magnetic braking, the model used here also has to account for this effect. The model of *Bouvier et al.* (1997) is adopted as described in Section 2.10. Therefore, the following set of equations describe the stellar rotation evolution:

$$\dot{\Omega}_* = \frac{3k_{2,*}}{2I_*Q_*} \frac{M_{Pl}^2}{M_*(M_* + M_{Pl})} \left(\frac{R_*}{a}\right)^3 n^2 \qquad (6.1.1)$$
$$+ \frac{\mathrm{d}\Omega_*}{\mathrm{d}t}_{m.braking},$$

where

$$\frac{\mathrm{d}\Omega_*}{\mathrm{d}t}_{m.braking} = -\frac{K}{I_*M_*R_*^2}\Omega_*^3 \left(\frac{R_*}{R_{Sun}}\right)^{1/2} \left(\frac{M_*}{M_{Sun}}\right)^{-1/2} \text{ if } \Omega_* < \omega_{sat} \qquad (6.1.2)$$
$$= -\frac{K}{I_*M_*R_*^2}\Omega_*^2\omega_{sat} \left(\frac{R_*}{R_{Sun}}\right)^{1/2} \left(\frac{M_*}{M_{Sun}}\right)^{-1/2} \text{ if } \Omega_* > \omega_{sat} \qquad (6.1.3)$$
$$. \qquad (6.1.4)$$

As stellar normalized moment of inertia $I_* = 0.074$ (see Section 2.11) is adopted. The scaling factor K determines the effectiveness of magnetic braking.

6.1.1 Tidal rotation evolution of low mass host stars of CoRoT-Planets on circular orbits

CoRoT systems with a close-in planet on a circular orbit and a low mass star ($M_* < 1.1 M_{Sun}$) are: CoRoT-1, CoRoT-2, CoRoT-7, CoRoT-8, CoRoT-12, CoRoT-13, CoRoT-17, and CoRoT-18. For these stars, the effectiveness of magnetic braking is well established and the scaling factor $K = 2.7 \times 10^{40}$ Nms is adopted from *Bouvier et al.* (1997).

Figure 6.1 shows the evolution of the stellar rotation due to stellar tidal friction for the next 15 billion years. In addition, the remaining lifetime with all uncertainties due to the age of the system is marked. For comparison, the evolution of the orbital period is included as well.

As can be seen by comparing Figure 6.1 with Figure 5.1, when the planet approaches the star and enters the Roche zone (i.e. if $\frac{Q_*}{k_{2,*}} \leq 10^6$), tidal friction is in general efficient enough to compensate for angular momentum loss due to magnetic braking and to spin up the star. In the end, the star rotates with a rotation period in the order of magnitude of several days. Therefore, the stellar rotation evolution of main sequence stars with very close-in massive substellar companions may differ from the regular rotation evolution of main sequence stars.

The only unstable planet unable to spin up the star in this sample is the Super-Earth CoRoT-7b. Only for very small $\frac{Q_*}{k_{2,*}} \leq 10^6$, a small effect on the stellar rotation is visible just before the planet is tidally disrupted. This is not surprising because the angular momentum stored in the orbit of a planet, which is then transferred onto
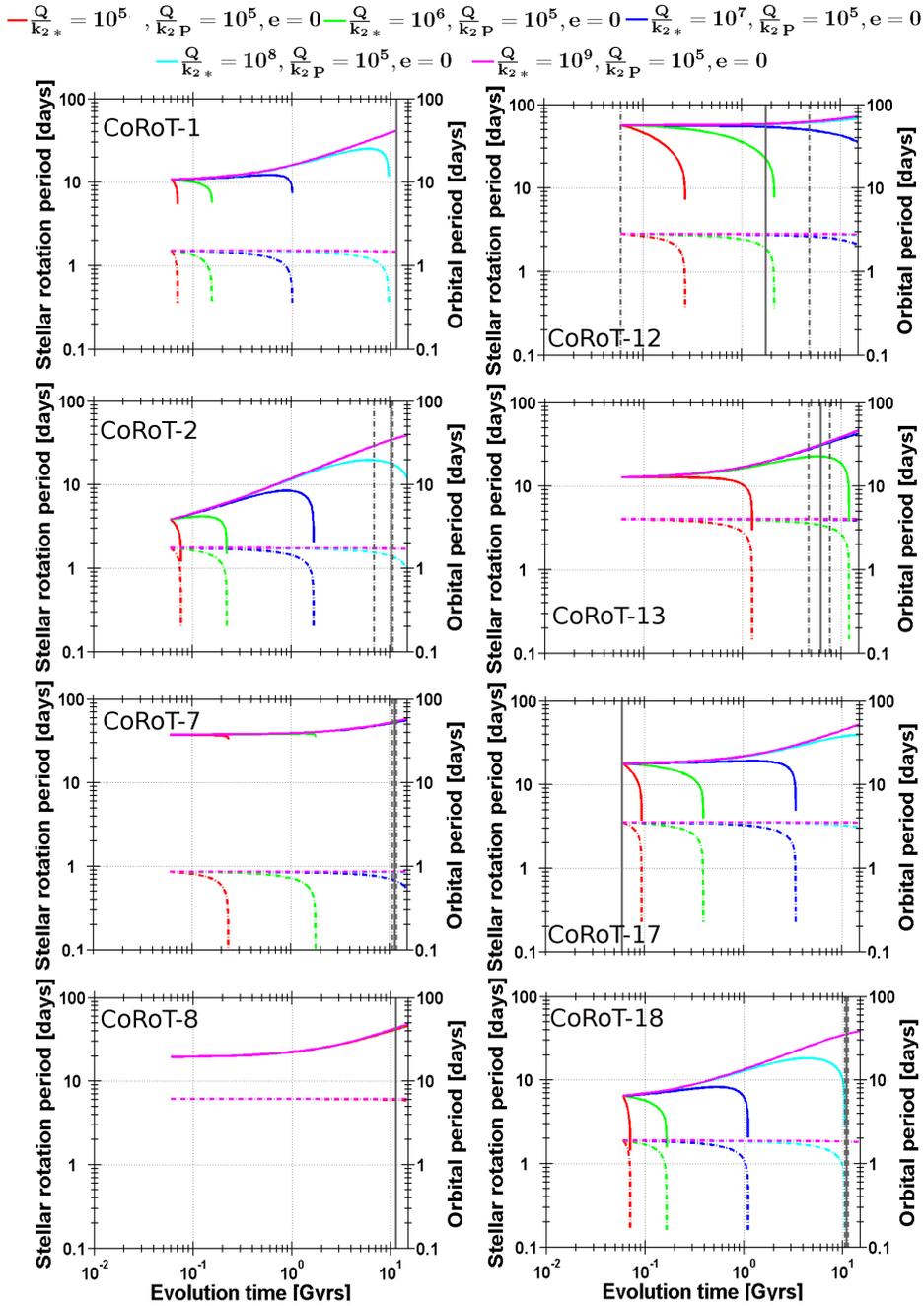
Figure 6.1: The tidal evolution of the stellar rotation of CoRoT-1, -2, -7, -8, -12, -13, -17 and -18 for the next 1.5×10^{10} years and for $\frac{Q_*}{k_{2,*}} = 10^5 - 10^9$ (solid lines). The dashed-dotted lines show the evolution of the orbital period of the corresponding close-in planet for comparison. The vertical lines show again (like in Figure 5.1) the remaining lifetime of the system.

the star due to tidal friction, is proportional to the mass of the planet (Section 3.3). The mass of the Super-Earth CoRoT-7b (≈ 8 Earth masses) is about 10^{-2} times the mass of a Jupiter analogue. Therefore, CoRoT-7b's orbital angular momentum is 10^{-2} times the orbital angular momentum of a Jupiter-mass planet. This amount is negligible compared to the angular momentum of a main sequence star. In summary, only close-in companions with minimum masses approximately that of Jupiter can spin up the star due to tidal friction.

Not only planets with fast orbital evolution that reach the Roche zone within the remaining lifetime of the star affect the stellar rotation. Even planets that only migrate moderately towards the star at the end of the stellar lifetime spin-up their star due to conservation of total angular momentum.

The tidal evolution of CoRoT-12 system is now discussed as an example (Figure 6.1): If $\frac{Q_*}{k_{2,*}} \leq 10^6$ below the threshold of orbital stability (Table 5.1), the star is spun up in the future as the planet migrates towards the Roche limit (Figure 5.1). When the planet enters the Roche zone, the final rotation period $P_* \approx 8$ days of CoRoT-12 is virtually identical for $\frac{Q_*}{k_{2,*}} = 10^5$ and $\frac{Q_*}{k_{2,*}} = 10^6$; no matter how long it takes for the planet to reach the Roche limit – either a few hundred million years or a few billion years.

If $\frac{Q_*}{k_{2,*}} = 10^7$, the planet is not destroyed within the remaining lifetime, but only starts to migrate towards the Roche limit just before the end of the lifetime. Even this moderate migration is accompanied by an angular momentum transfer to the star which spins up the star considerably, in the end. Apparently, the stellar rotation is even more susceptible to stellar tidal friction than the extrasolar planet's orbit. This can be explained by comparing the stellar and orbital angular momentum. In

Section 3.3 it was found that the bulk of the total angular momentum is stored in the planet's orbit (Section 3.3). In addition, a main sequence star loses a considerable amount of its angular momentum over time. Therefore, it comes as no surprise that old stars are very susceptible to spin-up due to stellar tidal friction.

It should be noted that even for small values of $\frac{Q_*}{k_{2,*}} = 10^5$, although the star is spun up rapidly as the planet approaches the Roche limit, the stellar rotation and planetary revolution are never synchronized. Indeed, it will be shown in Chapter 8 that only few CoRoT systems fulfill the requirements to achieve rotation-revolution synchronization. Therefore, the assumption that $\Omega_* - n$ does not vary by more than two orders of magnitude remains valid in this Section (see Figure C.1).

6.1.2 Tidal rotation evolution of F-spectral type host stars of CoRoT-Planets on circular orbits

CoRoT systems with a close-in planet on a circular orbit and an F spectral type star rotating slower than the planet's revolution are CoRoT-5, CoRoT-14, and CoRoT-19. CoRoT-21b orbits a subgiant. For all intents and purposes, CoRoT-21 is treated like an F star in this work to gain first insights about the stability and evolution of this special system for the next few billion years. The stellar rotation evolution due to stellar tidal friction is modeled by the same set of equations used above - with one difference: The magnetic braking term.

The effectiveness of magnetic braking in F-stars is not so clear as for low mass stars discussed in the previous section (See Section 2.10). There are many indications that these stars experience either inefficient or no magnetic braking at all.

To account for this uncertainty in magnetic braking efficiency, the magnetic braking term used above adopted from *Bouvier et al.* (1997) is used again but with different

scaling factors K:

- $K = 2.7 \times 10^{40}$ Nms for 'full magnetic braking', adopting the same scaling factor as for low mass main sequence stars,

- $K = 2.7 \times 10^{39}$ Nms for 'reduced magnetic braking',

- $K = 0$ for a model without magnetic braking.

This allows to constrain the possible stellar rotation evolution. Consequently, three instead of one panel with stellar rotation evolution tracks are shown (Figures 6.2, 6.3, and 6.4).

When comparing stellar rotation evolution with the equivalent semi major axis evolution of their planets (Figure 5.2), the following becomes apparent: If the planet approaches the Roche limit, the star is spun up significantly in the end. The presence of magnetic braking may only delay the on-set of stellar tidal spin-up in the near future. When the planet enters the Roche zone, however, even full magnetic braking (Figure 6.2) is finally overcome by stellar tidal friction. The star is rapidly rotating; regardless whether the spin-up was initially counteracted by magnetic braking or not. This is again due to the fact that the amount of angular momentum stored in the orbit is much larger than the angular momentum stored in the stellar rotation. In addition, it is found that at the end of the stellar lifetime even a moderate migration of the planet towards the star is enough to result in stellar spin-up.
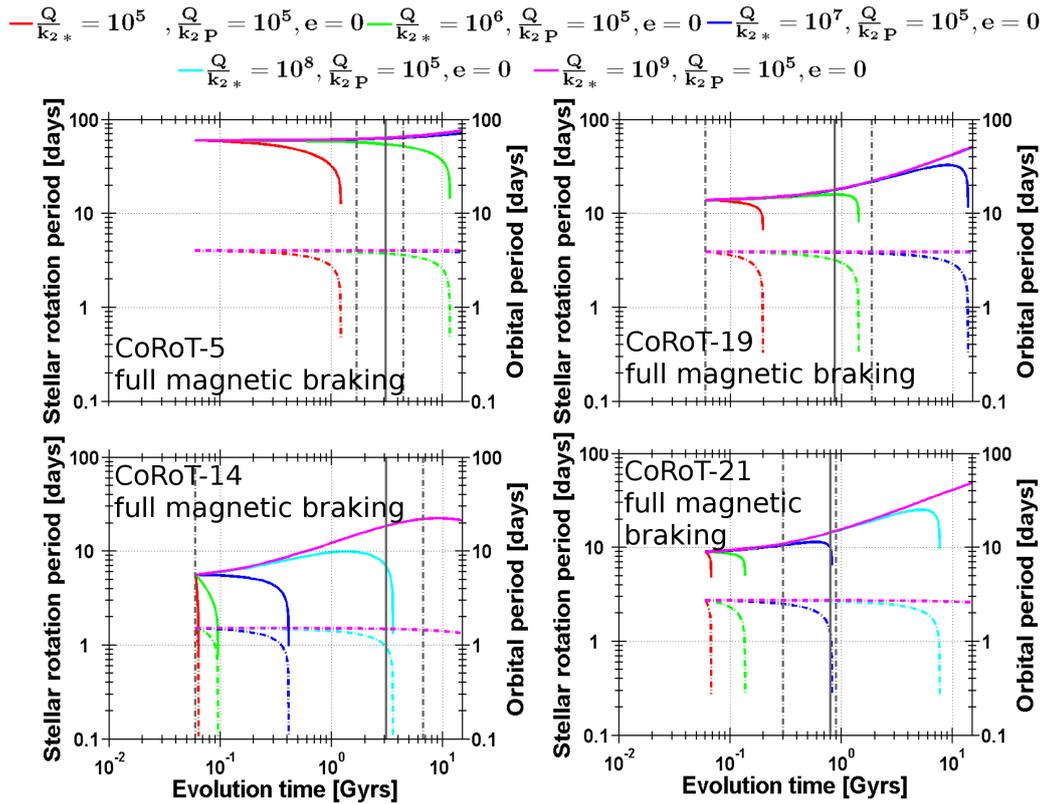
Figure 6.2: The tidal evolution of the stellar rotation of CoRoT-5, -14, 19, and -21 for the next 1.5×10^{10} years and for $\frac{Q_*}{k_{2,*}} = 10^5 - 10^9$ (solid lines) in the presence of full magnetic braking. The dashed-dotted lines show the evolution of the orbital period of the corresponding close-in planet for comparison. The vertical lines show the remaining lifetime of the system.
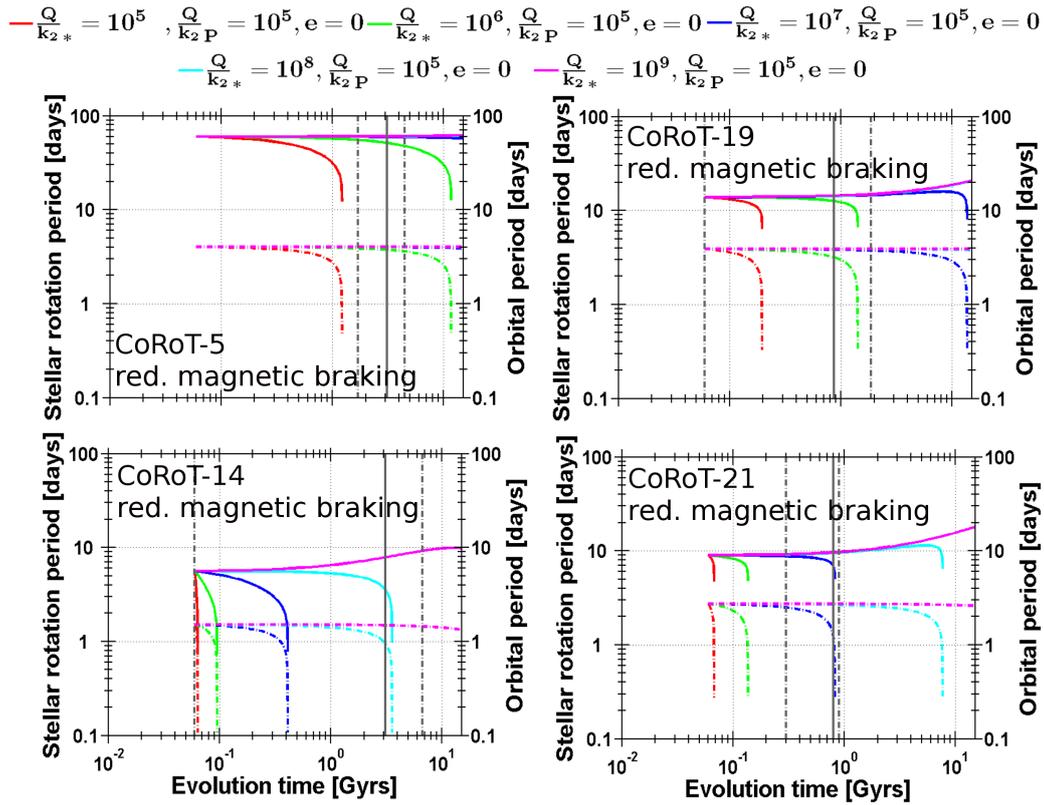
Figure 6.3: The tidal evolution of the stellar rotation of CoRoT-5, 14, 19, and -21 for the next 1.5×10^{10} years and for $\frac{Q_*}{k_{2,*}} = 10^5 - 10^9$ (solid lines) in the presence of reduced magnetic braking.
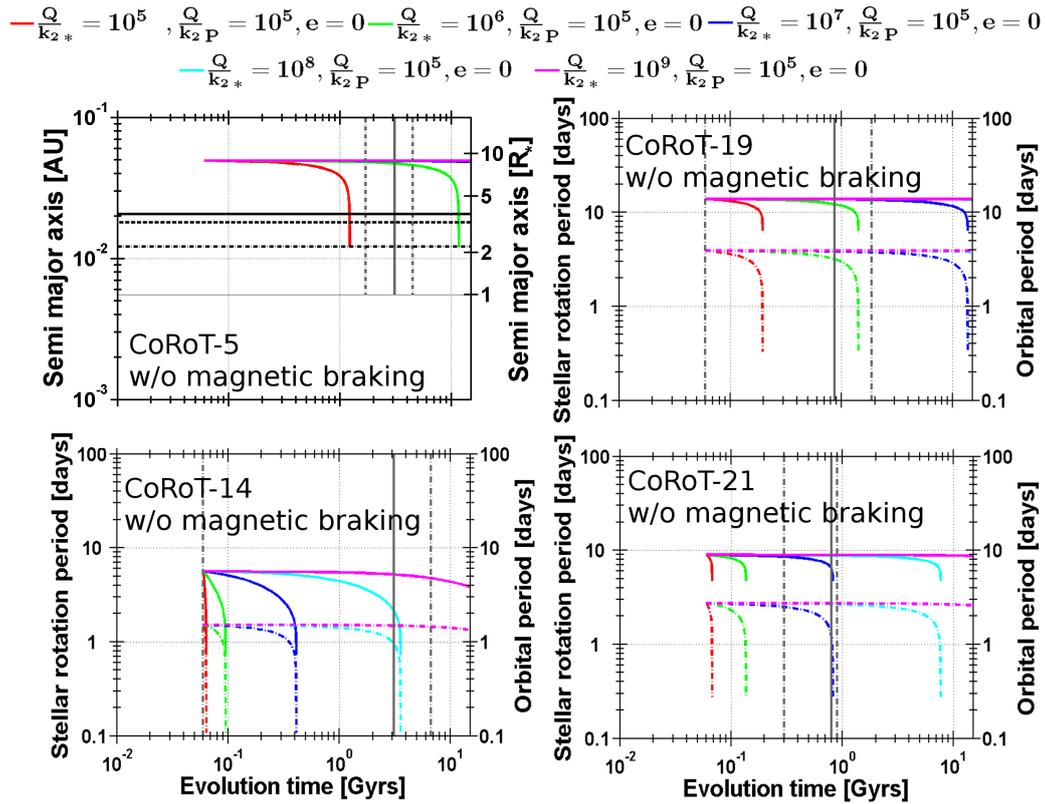
Figure 6.4: The tidal evolution of the stellar rotation of CoRoT-5, 14, 19, and -21 for the next 1.5×10^{10} years and for $\frac{Q_*}{k_{2,*}} = 10^5 - 10^9$ (solid lines) without magnetic braking.

Take as an example CoRoT-19: If $\frac{Q_*}{k_{2,*}} \geq 10^8$, the stellar rotation evolution is not affected at all by tidal friction and determined by magnetic braking only (Figures 6.2, 6.3, and 6.4).

Either the stellar rotation will decelerate unhindered for either full and reduced magnetic braking, or without magnetic braking (Figure 6.4) will remain the same as today.

If $\frac{Q_*}{k_{2,*}} = 10^7$, the stellar rotation will decelerate for the next few billion years or will remain the same. In the presence of full magnetic braking, tidal friction reduces the deceleration of the star's rotation after four billion years, and after ten billion years it will become more efficient than magnetic braking and the star will be spun up again. Without magnetic braking, the tidal spin-up will become apparent after four billion years, as the star will start to rotate faster. Actually, the difference between the evolution with reduced and no magnetic braking is minor for $\frac{Q_*}{k_{2,*}} = 10^7$. In both cases, the star rotates at the end of the system's lifetime with a rotation period in the order of six to eight days.

If $\frac{Q_*}{k_{2,*}} = 10^6$ and in the presence of either full or reduced magnetic braking, the stellar rotation will slightly decelerate in the next few hundred million years. The deceleration stops after about 600 million years, and the star will be spun-up rapidly as the planet approaches the Roche zone after one and a half billion years. If no magnetic braking is acting, then the stellar rotation will remain unchanged for the first 400 million years, before it will be spun up earlier than in the presence of magnetic braking.

In any case, for $\frac{Q_*}{k_{2,*}}$ below the limit of stability $10^7 - 10^8$ given in Table 5.2, not only is the planet destroyed, the star is spun-up even in the presence of full magnetic

braking. Furthermore, no matter how long it takes for the planet to reach the Roche limit - either a few hundred million years or a few billion years - and regardless if the star experiences magnetic braking or not: the star is rapidly rotating at about the same rotation rate, in the end. Apparently, the amount of angular momentum lost by magnetic braking is more than compensated for by angular momentum transferred by tidal friction from the planet's orbit to the stellar rotation.

Whereas all the stars in the previous subsection settled at a rotation period of a few days, once the planet has been destroyed in the Roche zone, there are two stars in this section for which this conclusion does not hold: CoRoT-5 ends up with a comparatively slow rotation period of 12 days when the planet reaches the Roche zone. This is due to the fact that this star starts its rotation evolution with an unusually long rotation period of 60 days although CoRoT-5 is an F-star. F-stars typically rotate faster than that (see Section 2.10). The rotation period of CoRoT-5, however, is not very well constrained with a measured value of $60^{+\infty}_{-30}$ (Table 1.4). Even taking into account that the stellar rotation period could be as low as 30 days, this star stands out in this section due to its slow rotation. Chapter F shows that even such large uncertainties in P_* do not affect the qualitative results derived in this Section and the previous Chapter for very slow stellar rotators. CoRoT-14, on the other hand, represents the other extreme. Here, the stellar rotation is relatively low $P_* = 14 \pm 2.4$ days to begin with and the star ends up with a rotation period below 1 day when the planet reaches the Roche zone. Although this rotation is relatively fast, in Chapter H, it is shown that stars with rotation periods much larger than 0.1 days don't run the risk of being disrupted due to centrifugal forces. In summary, when a star is tidally spun-up its final rotation period can range between more than

10 days to less than 1 day. It is still rotating much faster than expected for a star of its age.

6.2 Tidal rotation evolution of host stars of CoRoT-Planets on eccentric orbits

The following CoRoT-systems with non-negligible orbit eccentricity are identified: CoRoT-9, CoRoT-10, CoRoT-16 and CoRoT-20. In the previous chapter it was already shown that CoRoT-9b is too far away to cause a significant tidal evolution of the orbit. The same is true for the stellar rotation (Figure B.2) In the following, the stellar rotation evolution of CoRoT-10, CoRoT-16 and CoRoT-20 is investigated.

As already outlined in Section 5.2, the tidal evolution for systems with planets on eccentric orbits need to take into account stellar as well as planetary tidal friction terms. Consequently, the stellar rotation evolution is modeled by the following set of equations repeated here:

$$
\begin{aligned}
\frac{\mathrm{d}\Omega_*}{\mathrm{d}t} =& \frac{3}{2I_*} \frac{k_{2,*}}{Q_*} \frac{M_{Pl}}{M_* + M_{Pl}} \frac{M_{Pl}}{M_*} \left(\frac{R_*}{a}\right)^3 n^2 \left(1 - e^2\right)^{-6} \frac{\left[f_2(e)n - (1 - e^2)^{3/2} f_5(e)\Omega_*\right]}{|n - \Omega_*|} \\
&+ \frac{\mathrm{d}\Omega_*}{\mathrm{d}t}_{m.braking} \\
\frac{\mathrm{d}\Omega_{Pl}}{\mathrm{d}t} =& \frac{3}{2I_{Pl}} \frac{k_{2,Pl}}{Q_{Pl}} \frac{M_*}{M_{Pl}} \frac{M_*}{M_* + M_{Pl}} \left(\frac{R_{Pl}}{a}\right)^3 n^2 \left(1 - e^2\right)^{-6} \frac{\left[f_2(e)n - (1 - e^2)^{3/2} f_5(e)\Omega_{Pl}\right]}{|n - \Omega_{Pl}|},
\end{aligned}
$$

where

$$f_1(e) = 1 + \frac{31}{2}e^2 + \frac{225}{8}e^4 + \frac{185}{16}e^6 + \frac{25}{64}e^8$$

$$f_2(e) = 1 + \frac{15}{2}e^2 + \frac{45}{8}e^4 + \frac{5}{16}e^6$$

$$f_3(e) = 1 + \frac{15}{4}e^2 + \frac{15}{8}e^4 + \frac{5}{64}e^6$$

$$f_4(e) = 1 + \frac{3}{2}e^2 + \frac{1}{8}e^4$$

$$f_5(e) = 1 + 3e^2 + \frac{3}{8}e^4,$$

$$\left.\frac{\mathrm{d}\Omega_*}{\mathrm{d}t}\right|_{m.braking} = -\frac{K}{I_* M_* R_*^2}\Omega_*^3 \left(\frac{R_*}{R_{Sun}}\right)^{1/2} \left(\frac{M_*}{M_{Sun}}\right)^{-1/2} \text{ if } \Omega_* < \omega_{sat} \qquad (6.2.1)$$

$$= -\frac{K}{I_* M_* R_*^2}\Omega_*^2 \omega_{sat} \left(\frac{R_*}{R_{Sun}}\right)^{1/2} \left(\frac{M_*}{M_{Sun}}\right)^{-1/2} \text{ if } \Omega_* > \omega_{sat}, \qquad (6.2.2)$$

Like in the previous chapter, the tidal evolution is discussed first for $\frac{Q_{Pl}}{k_{2,Pl}} = 10^4$ and $\frac{Q_*}{k_{2,*}} = 10^5 - 10^9$ (Figure 6.5).
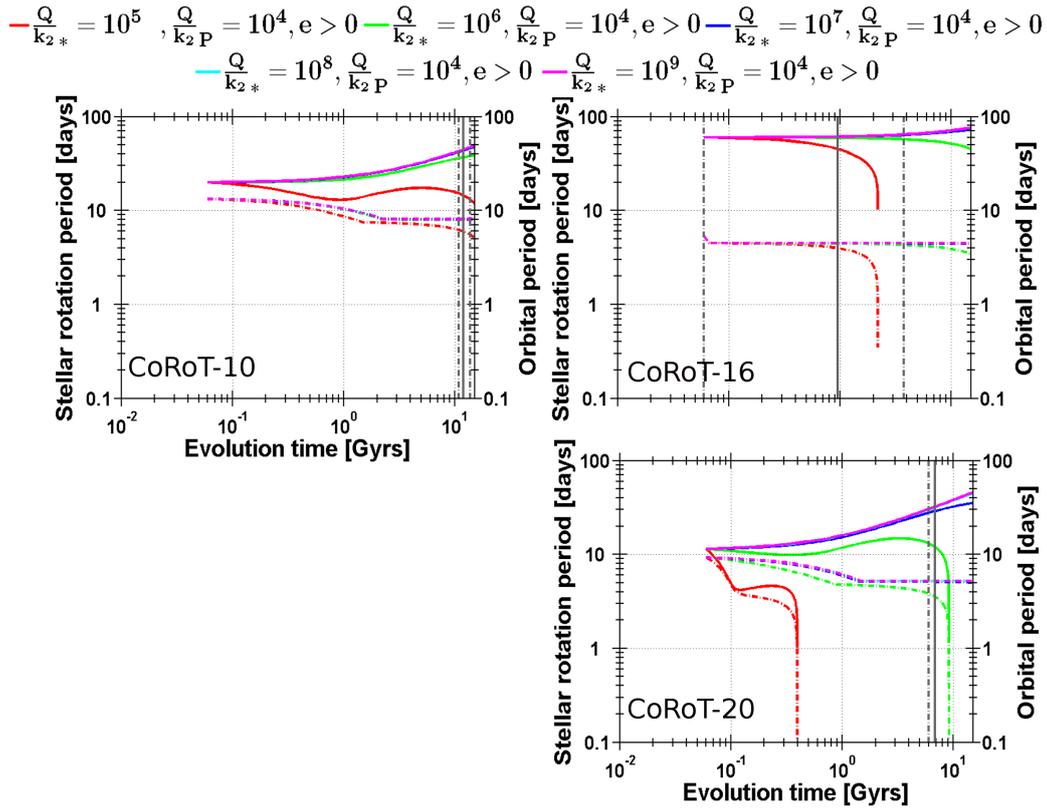
Figure 6.5: The tidal evolution of the stellar rotation of CoRoT-9,-10, -16, and CoRoT-20 for the next 1.5×10^{10} years, for $\frac{Q_*}{k_{2,*}} = 10^5 - 10^9$ (solid lines) and $\frac{Q_{Pl}}{k_{2,Pl}} = 10^4$. The dashed-dotted lines show the evolution of the orbital period of the corresponding close-in planet for comparison. The vertical lines show the remaining lifetime of the system.

Stellar rotation evolution of CoRoT-16, $\frac{Q_{Pl}}{k_{2,Pl}} = 10^4$

CoRoT-16 experiences tidal spin-up for $\frac{Q_*}{k_{2,*}} \leq 10^6$ as the planet CoRoT-16b moves toward the star (Figure 5.3) due to stellar tidal friction, just as it was found for several stars discussed in the previous section. During the first tens of million of years (Figure 5.4) – when the eccentricity is damped to zero due to planetary tidal friction – no influence is seen on the stellar rotation. But then again this is expected because planetary tidal friction only transfers angular momentum within the orbit and from the planet's rotation.

Stellar rotation evolution of CoRoT-10, $\frac{Q_{Pl}}{k_{2,Pl}} = 10^4$

If $\frac{Q_*}{k_{2,*}} = 10^6$, the rotation of CoRoT-10 is affected - albeit not strongly - by tidal spin-up although the corresponding orbital migration due to stellar and planetary tidal friction is small. If $\frac{Q_*}{k_{2,*}} = 10^5$, the spin-up is much stronger due to the positive feedback effect explained in Section 5.2 that leads to moderate planetary migration.

Stellar rotation evolution of CoRoT-20, $\frac{Q_{Pl}}{k_{2,Pl}} = 10^4$

The rotation of CoRoT-20 is already affected for $\frac{Q_*}{k_{2,*}} = 10^6$ by the positive feedback between stellar and planetary tidal friction, which is to be expected considering the orbital evolution of CoRoT-20b (Figures 5.3 and 5.4) for small $\frac{Q_*}{k_{2,*}} \leq 10^6$. In the initial tidal evolution phase, stellar and planetary tidal friction decrease the planet's semi major axis and eccentricity more efficiently than each would acting on its own. Consequently, a comparatively large amount of angular momentum is transferred from the orbit to the star, which is observed as rapid spin-up already at an early evolution stage. This is in contrast to the stellar rotation evolution of stars with close-in planets on circular orbits where the spin-up is the strongest at the end of the

tidal evolution. When e has become zero, stellar tidal friction alone is less efficient in spinning-up the star, but catches up as the planet approaches the star.

For $\frac{Q_*}{k_{2,*}} = 10^7$, the star experiences weak tidal spin-up at the end of the full evolution time, which is not strong enough to compensate magnetic braking. This evolution is driven by moderate planetary migration (Figure 5.3) due to stellar tidal friction. For larger $\frac{Q_*}{k_{2,*}}$, the stellar rotation evolution is unaffected.

6.2.1 How does the stellar rotation evolution change with larger $\frac{Q_{Pl}}{k_{2,Pl}}$

Now, the tidal evolution scenario for $\frac{Q_{Pl}}{k_{2,Pl}} = 10^4$ is compared with tidal evolution tracks for $\frac{Q_{Pl}}{k_{2,Pl}} = 10^5$ and $\frac{Q_*}{k_{2,*}} = 10^5 - 10^9$ (Figure 6.6), and finally $\frac{Q_{Pl}}{k_{2,Pl}} = 10^6$ and $\frac{Q_*}{k_{2,*}} = 10^5 - 10^9$ (Figure 6.7)

Stellar rotation evolution of CoRoT-16, $\frac{Q_{Pl}}{k_{2,Pl}} = 10^5 - 10^6$

The stellar rotation evolution of CoRoT-16 does not change when $\frac{Q_{Pl}}{k_{2,Pl}}$ is increased. Therefore, planetary tidal friction has no influence on the star. The stellar rotation may only be affected by stellar tidal friction and for the smallest $\frac{Q_*}{k_{2,*}} \leq 10^6$.

6.2.2 Positive feedback effect for planets on orbits with $e > 0.5$

Stellar rotation evolution of CoRoT-10, $\frac{Q_{Pl}}{k_{2,Pl}} = 10^5 - 10^6$

Comparing the stellar rotation evolution of CoRoT-10 for different $\frac{Q_{Pl}}{k_{2,Pl}}$-scenarios shows that for $\frac{Q_*}{k_{2,*}} = 10^6$ the stellar spin-up due to the combination of stellar and planetary tidal friction becomes stronger with increasing $\frac{Q_{Pl}}{k_{2,Pl}}$. Still, the stellar rotation period of CoRoT-10 never falls below fifteen days and, at the end of the system's lifetime, the stellar rotation period is always larger than 25 days. It would be very
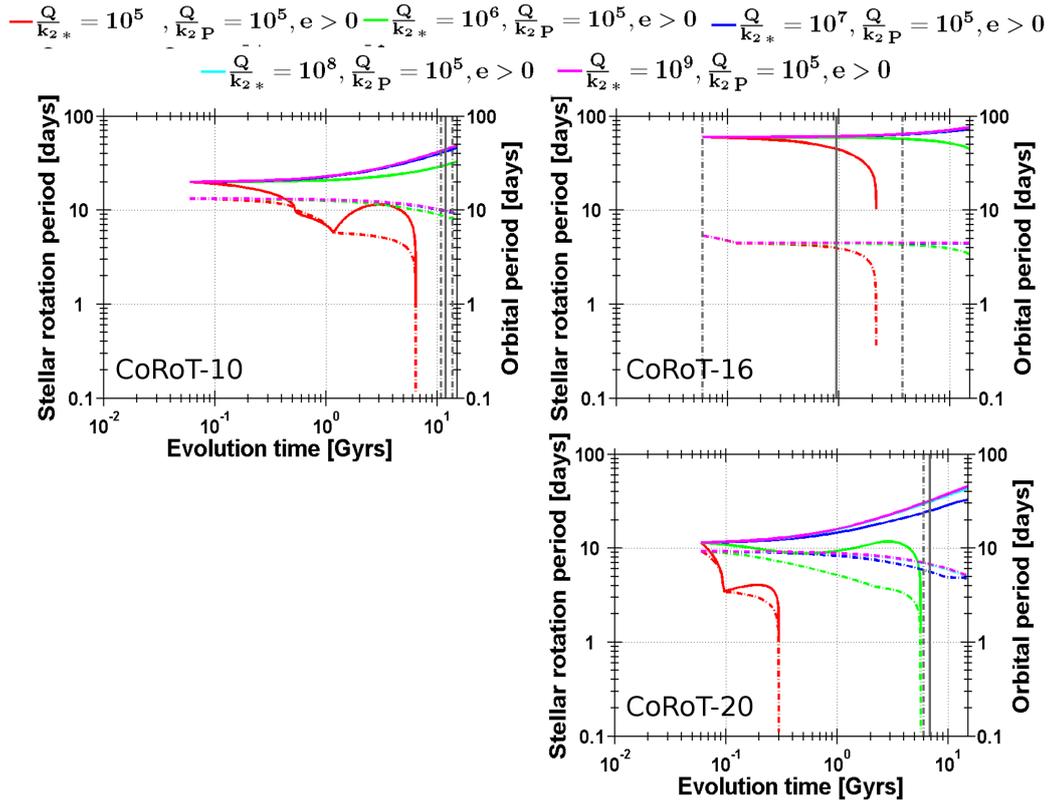
Figure 6.6: The tidal evolution of the stellar rotation of CoRoT-9,-10, -16, and CoRoT-20 for the next 1.5×10^{10} years, for $\frac{Q_*}{k_{2,*}} = 10^5 - 10^9$ (solid lines) and $\frac{Q_{PL}}{k_{2,Pl}} = 10^5$. The dashed-dotted lines show the evolution of the orbital period of the corresponding close-in planet for comparison. The vertical lines show the remaining lifetime of the system.
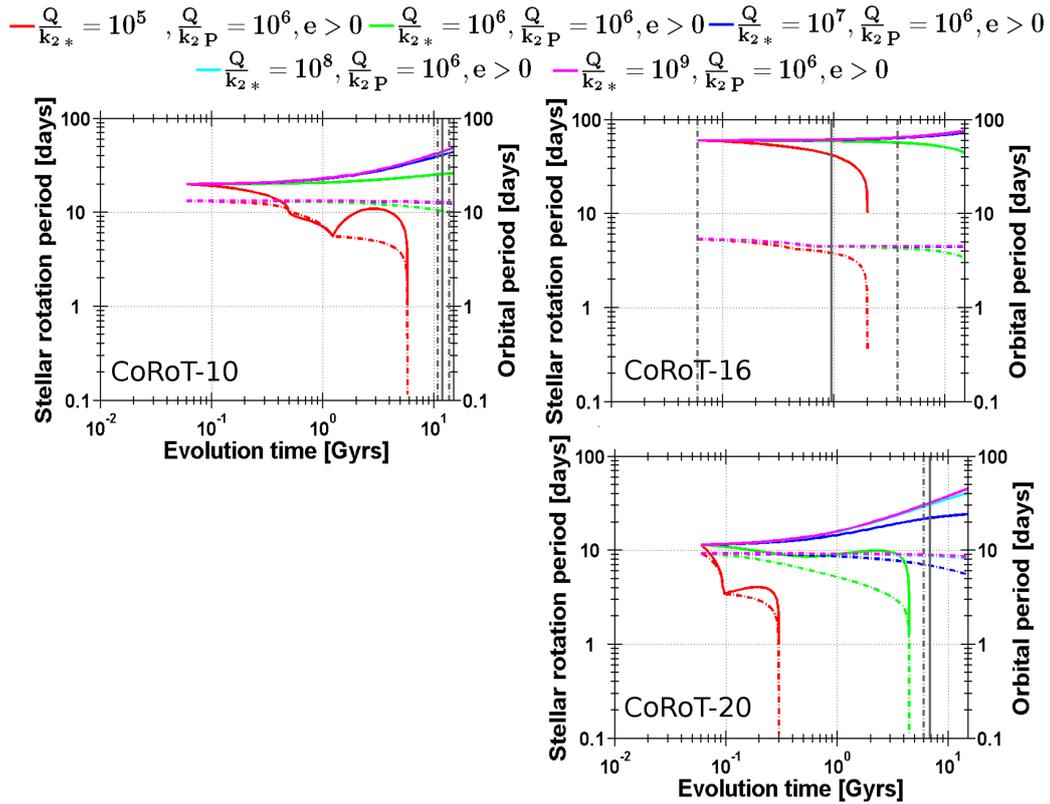
Figure 6.7: The tidal evolution of the stellar rotation of CoRoT-9,-10, -16, and CoRoT-20 for the next 1.5×10^{10} years, for $\frac{Q_*}{k_{2,*}} = 10^5 - 10^9$ (solid lines) and $\frac{Q_{PL}}{k_{2,Pl}} = 10^6$. The dashed-dotted lines show the evolution of the orbital period of the corresponding close-in planet for comparison. The vertical lines show the remaining lifetime of the system.

hard to identify such abnormally fast rotating state, especially due the difficulties when measuring the rotation of a slowly rotating star where error bars can span tens of days (See Table 1.4).

For $\frac{Q_*}{k_{2,*}} = 10^5$, the combination of stellar and planetary tidal friction acting on similar timescales affects the stellar rotation more strongly than if stellar tidal friction would act individually. The combined tidal spin-up is even stronger than magnetic braking, leading to a net spin-up of the star at an early evolution stage as long as planetary tidal friction is strong. Apparently, the strength of planetary tidal friction diminishes over time as the eccentricity approaches zero (Figures 5.8 and 5.10). As the planet approaches the star, stellar tidal friction eventually becomes stronger than magnetic braking and is spinning up the star again. If the planet reaches the Roche limit, which only happens if $\frac{Q_P}{k_{2,P}} \geq 10^5$, the star would rotate with a rotation period of one day, in the end.

Stellar rotation evolution of CoRoT-20, $\frac{Q_{Pl}}{k_{2,Pl}} = 10^5 - 10^6$

The same feedback effect is also seen in the stellar rotation evolution of CoRoT-20, if $\frac{Q_*}{k_{2,*}} \leq 10^6$. Indeed, when comparing the rotational evolution of the different $\frac{Q_P}{k_{2,P}}$ scenarios, the tidal spin-up due to the combination of stellar and planetary tidal friction becomes stronger with increasing $\frac{Q_{Pl}}{k_{2,Pl}}$. But this only holds for the next forty million years, if $\frac{Q_*}{k_{2,*}} = 10^5$, and for the next one billion years, if $\frac{Q_*}{k_{2,*}} = 10^6$. After that, magnetic braking takes over as the eccentricity is damped to zero (Figures 5.8 and 5.10). Afterwards, the star may be spun-up again due to stellar tidal friction alone when the planet enters the Roche zone (Figures 5.7 and 5.9). If CoRoT-20b enters the Roche zone, the stellar rotation finally ends up with a rotation period of about one day; regardless of the initial evolution phases and how long it took to

reach the Roche zone. Looking at Figures 6.5, 6.6, and 6.7, it appears that the stellar rotation comes very close to the planetary revolution.

A detailed inspection of $\Omega_* - n$ shows that while for $\frac{Q_{Pl}}{k_{2,Pl}} = 10^4$ the stellar rotation always exceeds the planetary revolution (Figure C.5), Ω_* will be synchronized with n very briefly for $\frac{Q_{Pl}}{k_{2,Pl}} = 10^4 - 10^5$ (Figures C.6 and C.7). Here, $P_* = 11.5$ days was selected as a start point for the model. It will be shown in Section 8.4.1 and Chapter F that the CoRoT-20 system may synchronize the stellar rotation with the planet's revolution starting with a different initial stellar rotation period within limits of uncertainties $P_* = 11.5 \pm 2.6$ days. The system, however, will fail to maintain a stable double synchronous orbit because magnetic braking removes the required angular momentum from the system.

6.3 Using stellar rotation as a 'smoking gun' for the influence of tidal friction

In this chapter, it was shown for several examples that the stellar rotation is affected very strongly by tidal friction, even when the orbit remains stable over the remaining stellar lifetime. Tidal spin-up may be even efficient enough to compensate magnetic braking. Old stars, in particular, are noticeably affected. Geochronology may yield false results for the age of a system that once harbored or may still harbor a close-in massive extrasolar planet.

To gain an insight about what can be learned in terms of $\frac{Q_*}{k_{2,*}}$ from an abnormally rotating star, $\frac{Q_*}{k_{2,*}\ spin-up\ limit}$ is computed for the previously discussed main sequence stars for which tidal friction may overcome magnetic braking.

For the host stars of planets on circular orbits, mainly the ones described in

a) No error bars for the age of the system are given in the detection paper (*Bordé et al.* (2010))

b) The given age is larger than the estimated total lifetime. Therefore, the system is assumed to be at the end of its lifetime.

System	$\frac{Q_*}{k_{2,*}}_{spin-up\,limit}$	age [Gyrs]
CoRoT-1	$\leq 5 \times 10^6$	-
CoRoT-2	$\leq 5 \times 10^5$	$0.5^{+3.5}_{-0.3}$
CoRoT-7	$\leq 4 \times 10^4$	$1.7^{+0.6}_{-0.5}$
CoRoT-8	$\leq 10^3$	3^a
CoRoT-12	$\leq 4 \times 10^7$	$6.3^{+3.1}_{-3.1}$
CoRoT-13	$\leq 10^5$	$1.6^{+1.5}_{-1.5}$
CoRoT-17	$\leq 2 \times 10^7$	10.7^{+1}_{-1}
CoRoT-18	$\leq 2 \times 10^6$	$0.6^{+0.4}_{-0.4}$

Table 6.1: Required $\frac{Q_*}{k_{2,*}}$ for tidal friction to compensate magnetic braking at the planet's current position.

Section 6.1, the following can be found when comparing the tidal friction and magnetic braking term and solving for $\frac{Q_*}{k_{2,*}}$:

$$\frac{\mathrm{d}\Omega_{tidal\,friction}}{\mathrm{d}t} < \frac{\mathrm{d}\Omega_{magnetic\,braking}}{\mathrm{d}t}$$

$$\frac{Q_*}{k_{2,*}} < \frac{3}{2}\frac{M_{Pl}^2}{M_*+M_{Pl}}\left(\frac{R_*}{a}\right)^3 n^2 \frac{R_*^2}{K\Omega_*^3}\left(\frac{R_*}{R_{Sun}}\right)^{-1/2}\left(\frac{M_*}{M_{Sun}}\right)^{1/2} \quad (6.3.1)$$

Consequently, Table 6.1 lists the $\frac{Q_*}{k_{2,*}}$ for which the stellar rotation would be dominated by stellar tidal friction in the near future.

CoRoT-7 and CoRoT-8 are currently not spun up stronger than magnetic braking can decelerate the star because tidal friction is too inefficient to affect the stellar rotation for the whole investigated $\frac{Q_*}{k_{2,*}}$-range $10^5 - 10^9$. This is different for the other stars in the sample: The youngest stars in this sample, CoRoT-2, CoRoT-13, and CoRoT-18, require $\frac{Q_*}{k_{2,*}}$ smaller than $10^5 - 2 \times 10^6$. Consequently, only the smallest investigated $\frac{Q_*}{k_{2,*}}$-values are sufficient to spin-up the star at this young age.

The oldest stars, CoRoT-12 and CoRoT-17, which are the best indicators for tidal spin-up, require 4×10^7 and 2×10^7, respectively. Indeed, CoRoT-12 rotates today ($P_* = 57^{+\infty}_{-28}$ days) rather slowly showing no indication of considerable spin-up but rather a rotation period that is expected if the past evolution was dominated by magnetic braking. Such an evolution requires $\frac{Q_*}{k_{2,*}} = 4 \times 10^7$ which agrees nicely with the limit derived for orbit stability in the previous chapter. CoRoT-17, on the other hand, appears to be rotating rather fast for a star at the end of its lifetime ($P_* = 18 \pm 2$ days), but the rotation period is still larger than 10 days (Figure 6.8). This may indicate moderate tidal spin-up and planetary migration due to tidal friction with $\frac{Q_*}{k_{2,*}} \approx 10^7$. CoRoT-1, for which no age constraint is given, requires $\frac{Q_*}{k_{2,*}}$ less than 5×10^6.
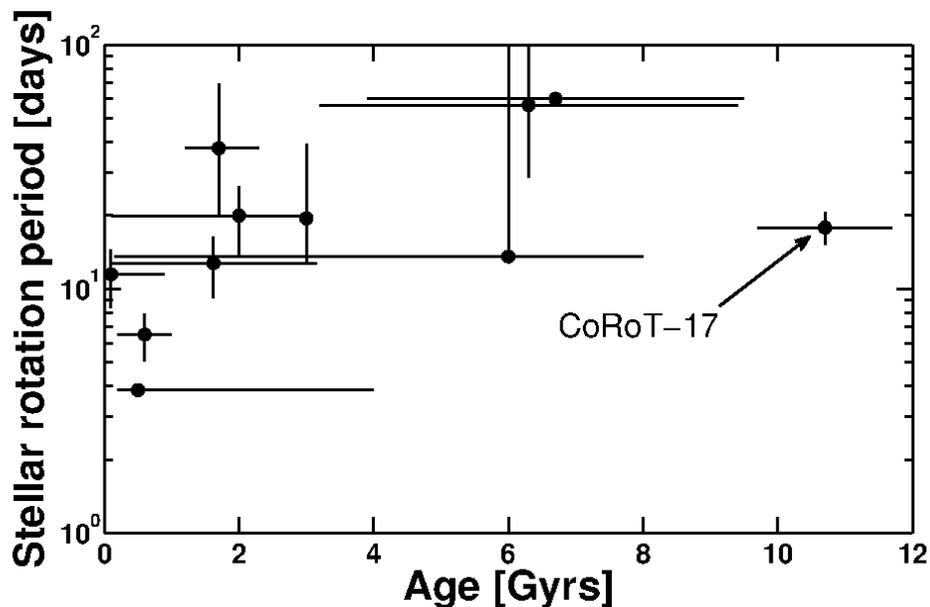
Figure 6.8: The stellar rotation periods of the CoRoT-stars of spectral type K and G versus age including the limits of uncertainties. The stellar rotation of CoRoT-17 stands out because it is faster than expected for such an old star.

For stars with uncertain magnetic braking efficiency, equation (6.3.1) cannot be

used. However, CoRoT-5 is rotating slowly ($P_* = 60^{+\infty}_{-30}$) and is several billion years old (Figure 6.9). As was shown in Section 6.1.2, such a star would be spun up considerably over billion years if $\frac{Q_*}{k_{2,*}} \leq 10^6$. One may therefore tentatively assume that in this system in the past $\frac{Q_*}{k_{2,*}} \gg 10^5$, because otherwise the star would currently rotate much faster. When looking at Figure 6.9 one may tentatively assume that at least the rotations of CoRoT exoplanet host stars of spectral type F seem to show a deceleration trend with increasing age, hinting to a reduced magnetic braking scenario.
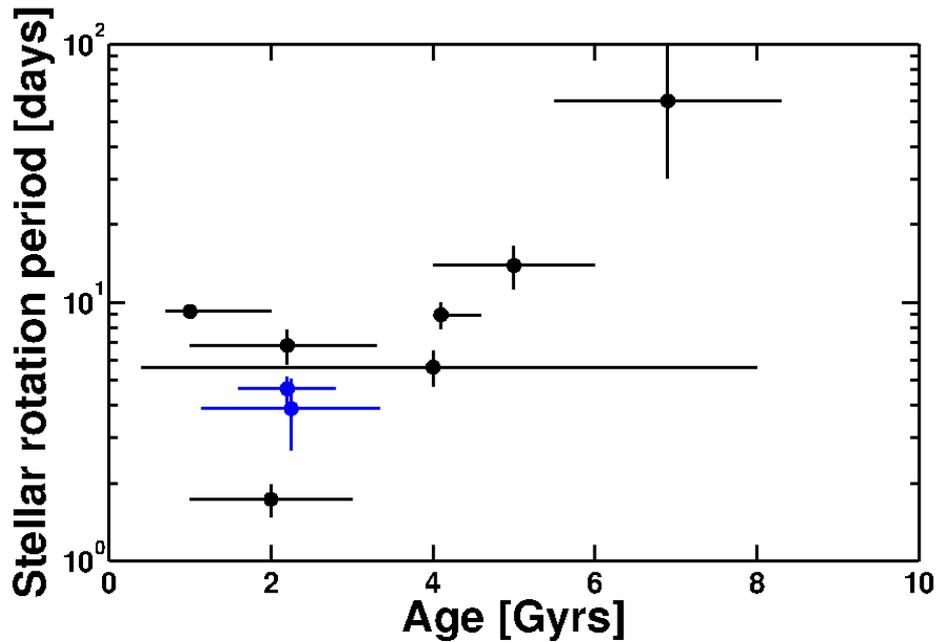
Figure 6.9: The stellar rotation periods of the spectral type F CoRoT-stars versus age including the limits of uncertainties. The blue crosses are the rotation periods and the age of CoRoT-3 and CoRoT-15.

For host stars of planets on eccentric orbits, CoRoT-10, CoRoT-16 and CoRoT-20, $\frac{Q_*}{k_{2,*}}_{spin-up\ limit}$ can be derived, required for tidal friction to spin up the star stronger than magnetic braking can decelerate it. The tidal stellar rotation evolution of

Table 6.2: Required $\frac{Q_*}{k_{2,*}}$ for tidal friction to compensate magnetic braking for planets on eccentric orbits at the current position.

System	$\frac{Q_*}{k_{2,*}\ spin-up\ limit}$	$\frac{Q_{Pl}}{k_{2,Pl}}$	age [Gyrs]
CoRoT-9[a]	not affected by tidal friction	$10^4 - 10^6$	$0.15 - 8$
CoRoT-10	$10^{5.6}$	$10^4 - 10^6$	2 ± 1
CoRoT-16	2.3×10^6	$10^4 - 10^6$	6.7 ± 2.8
CoRoT-20	$10^{6.2}$	$10^4 - 10^6$	$0.1^{+0.8}_{-0.04}$

a) included for completeness.

CoRoT-16 is solely driven by stellar tidal friction after the orbit has become circular. Therefore, the limiting $\frac{Q_*}{k_{2,*}}$ can be found by using the equivalent semi major axis $a_{equiv} = 0.063$ AU (see previous chapter) and inserting it into equation (6.3.1) derived for circular orbits.

For CoRoT-10 and CoRoT-20, the stellar rotation evolution depends on stellar and planetary tidal friction, therefore it depends on the combination of $\frac{Q_{Pl}}{k_{2,Pl}}$ and $\frac{Q_*}{k_{2,*}}$ if a stellar rotation evolution is dominated by magnetic braking or tidal friction. The limiting $\frac{Q_*}{k_{2,*}}$ can be found, however, by the same method by which the orbit stability limit was found in the previous chapter: by modeling the stellar evolution for $\frac{Q_{Pl}}{k_{2,Pl}} = 10^4, 10^5$, and 10^5 and by increasing the stellar tidal dissipation factor – beginning with $\frac{Q_*}{k_{2,*}} = 10^5$ for CoRoT-10 and $\frac{Q_*}{k_{2,*}} = 10^6$ for CoRoT-20 in each scenario – until the value is found for which tidal friction spin-up equals magnetic braking. The results for eccentric orbits are collected in Table 6.2.

Again, stellar spin-up at the current position due to tidal friction is only possible for very low $\frac{Q_*}{k_{2,*}} = 10^5 - 10^6$. CoRoT-16's low stellar rotation ($P_* > 60$ days) at an age of several billion years does not allow for tidal spin-up due to tidal friction. Consequently, for this system $\frac{Q_*}{k_{2,*}} \gg 10^5$ can be tentatively assumed.

6.4 Evaluating evidence for tidal spin up

In summary, it was shown that for slowly rotating host stars of very close-in massive extrasolar planets considerable spin-up of the stellar rotation is expected when the planet's orbit is unstable due to tidal friction. During the migration of the planet towards the Roche zone, considerable angular momentum is transferred onto the star whose own angular momentum due to its rotation is in general much smaller than orbital angular momentum. Furthermore, the amount of angular momentum lost by magnetic braking is more than compensated by tidal friction. In addition, it was found that old stars in particular are prone to being spun-up even by moderate tidal friction.

At last, a limit of $\frac{Q_*}{k_{2,*}}$ was derived for which the stellar rotation evolution is dominated by tidal friction between the star and the planet at the current position. Several old or middle-aged stars, CoRoT-5, CoRoT-12, and CoRoT-16, have been found which rotate very slowly. This is only feasible if in the past $\frac{Q_*}{k_{2,*}} > 10^5 - 10^6$. CoRoT-17, a very old star at the end of its lifetime on the main sequence, may show moderate tidal spin-up, which would require $\frac{Q_*}{k_{2,*}} \approx 10^7$.

Therefore, it seems implausible that CoRoT planet host stars have very low values of $\frac{Q_*}{k_{2,*}} = 10^5 - 10^6$ requiring an efficient tidal energy dissipation mechanism. Not only would the orbit of many planets be very unstable (Chapter 5), but the stars would be tidally spun-up so efficiently that not even magnetic braking would be able to compensate. Apart from CoRoT-17, no signs of tidal spin-up stronger than magnetic braking is seen in the CoRoT host stars.

The tidal spin-up of host stars to close-in massive planetary companions may,

in addition, affect one method to determine the age of a main sequence star. Gyrochronology assumes that main sequence stars rotate slower with increasing age and that, therefore, the stellar rotation can be used to estimate it's age. The results derived in this section, however, show that this assumption may not be valid for stars with close-in massive extrasolar planets. It may not even be valid for stars that don't currently have a close-in companion because the stars may have had a planet in the past that is now lost due to tidal disruption. The only sign of the existence of the tidally disrupted planet would be the spin-up of the star which may be mistaken for an indication of young stellar age. The danger of determining a false age by gyrochronology is the greatest for old stars. These may be spun up even by moderate tidal friction i.e. $\frac{Q_*}{k_{2,*}} \approx 10^8$.

6.5 A word regarding the evolution of the tidal frequencies

The constant Q_* and Q_{Pl} model requires the tidal frequencies $2|\Omega_* - n|$ and $2|\Omega_{Pl} - n|$ at least not to vary strongly. This is a valid assumption for CoRoT planetary systems with circular orbits (Figures C.1, C.2, C.3, C.4) and planets with small to moderate orbital eccentricties like CoRoT-16b ($e \leq 0.3$). The constant Q assumption warrants further investigation for planets with large orbital eccentricities ($e > 0.5$) because $|\Omega_* - n|$(Figures C.5, C.6, and C.6) and $|\Omega_{Pl} - n|$ (Chapter D) may vary strongly during the evolution. It is worthwhile investigating, if the tidal evolution of the CoRoT-10 and CoRoT-20 system changes for tidal friction models by switching to the constant τ_* and τ_{Pl} formalism, for example, as described in Section 3.1.4. This shall be reserved for future investigations.

Chapter 7

Tidal evolution of close-in exoplanets around fast rotating stars

In the systems CoRoT-6 and CoRoT-11, the stars rotate faster than the planets revolve around them. In contrast to the systems previously discussed this means: $\Omega_* > n$ (Table 1.4). Consequently, the planets currently migrate outwards and the stellar rotation is slowed down by tidal friction. Furthermore, it will be found that a state $\Omega_* = n$ may be reached. Therefore, the orbital and stellar rotation evolution can not be modeled independent from each other but are closely linked.

Although, the assumption $\Omega_* - n \approx$ const, in principle, no longer holds all the time, it will be shown that the synchronicity $\Omega_* = n$ is, in most cases, not achieved by tidal friction. Furthermore, it will be shown that at least for the CoRoT-11 system, apart from a brief initial evolution phase, $|\Omega_* - n| \approx$ const is still a valid assumption on timescales of billion years.

The relevant set of equations for modeling the system's tidal evolution are:

$$\dot{a} = \text{sign}(\Omega_* - n) \frac{3k_{2,*}M_{Pl}}{Q_*M_*} \left(\frac{R_*}{a}\right)^5 na$$

$$\dot{\Omega}_* = -\text{sign}(\Omega_* - n) \frac{3k_{2,*}}{2I_*Q_*} \frac{M_{Pl}^2}{M_*(M_* + M_{Pl})} \left(\frac{R_*}{a}\right)^3 n^2$$

$$+ \left.\frac{d\Omega_*}{dt}\right|_{m.braking},$$

where

$$\left.\frac{d\Omega_*}{dt}\right|_{m.braking} = -\frac{K}{I_*M_*R_*^2}\Omega_*^3 \left(\frac{R_*}{R_{Sun}}\right)^{1/2} \left(\frac{M_*}{M_{Sun}}\right)^{-1/2} \text{ if } \Omega_* < \omega_{sat} \qquad (7.0.1)$$

$$= -\frac{K}{I_*M_*R_*^2}\Omega_*^2\omega_{sat} \left(\frac{R_*}{R_{Sun}}\right)^{1/2} \left(\frac{M_*}{M_{Sun}}\right)^{-1/2} . \text{if } \Omega_* > \omega_{sat} \qquad (7.0.2)$$

$$(7.0.3)$$

Another point of uncertainty is the stellar rotation evolution. CoRoT-6 and CoRoT-11 are F-stars. Therefore, the evolution of the CoRoT-6 and -11 system is calculated with full magnetic braking ($K = 2.7 \times 10^{40}$ Nms), reduced magnetic braking ($K = 2.7 \times 10^{39}$ Nms) and without magnetic braking ($K = 0$). This yields three different evolution tracks for the stellar rotation, and for the semi major axes of the planets. Contrary to the evolution of the planets previously discussed, the orbit evolution in this chapter depends on when and if the state $\Omega_* = n$ is reached. Luckily, the stellar rotation period of fast rotating stars has small error bars: $P_* = 7 \pm 1$ days for CoRoT-6 and 1.4 ± 0.3 days for CoRoT-11. Therefore, it is justified to use the mean value as starting point of the stellar rotation evolution. See also Chapter F for a model sensitivity analysis that shows that the general evolution will not change drastically with different start points.

Figure 7.1 shows the evolution of the semi major axes of the planets CoRoT-11b and CoRoT-6b with full, reduced and no magnetic braking in constant Q_*-formalism.

Figure 7.2 shows the corresponding evolution of the stellar rotation of CoRoT-11 and CoRoT-6.
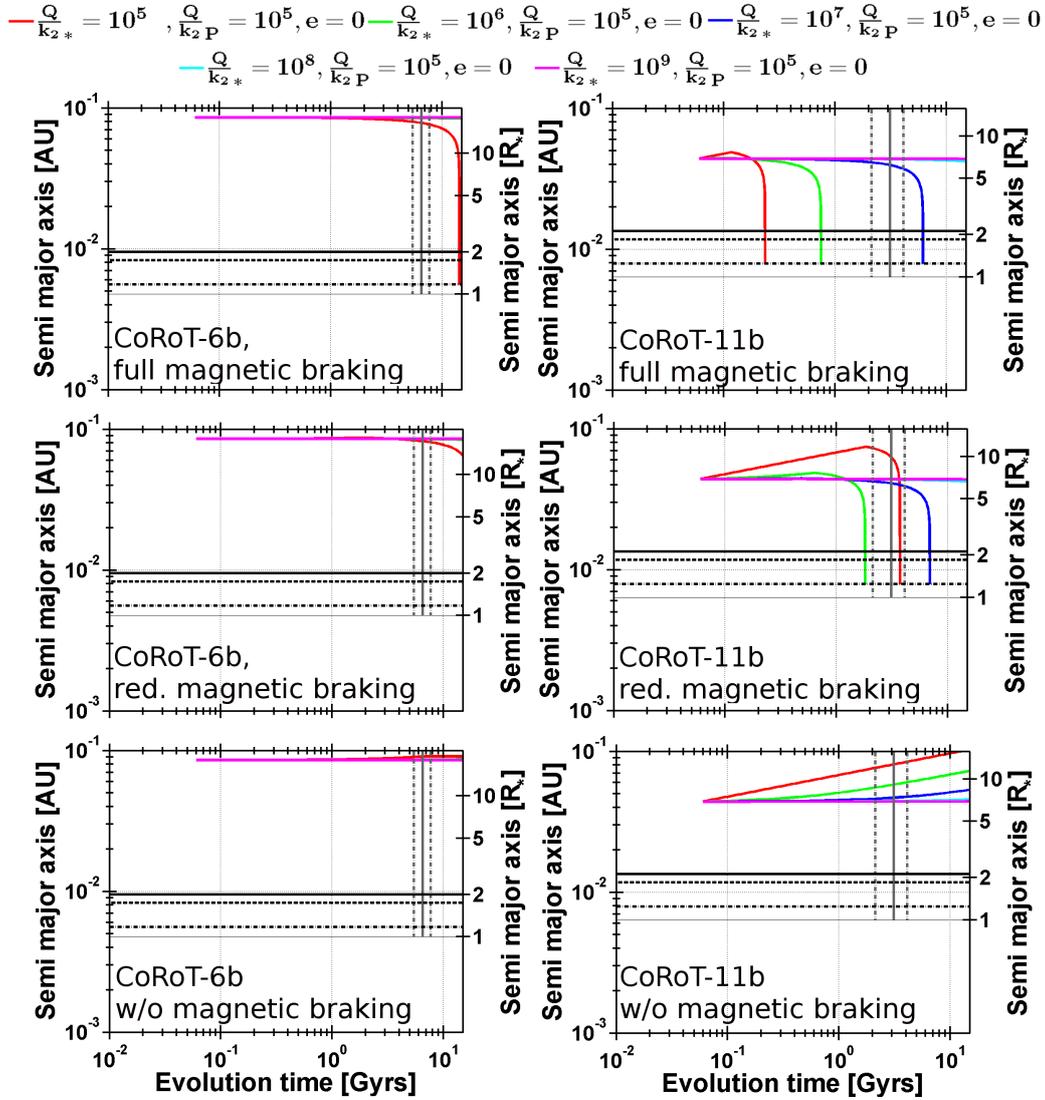
Figure 7.1: The tidal evolution of the semi major axis of the planets CoRoT-6b, and -11b for the next 1.5×10^{10} years and for $\frac{Q_*}{k_{2,*}} = 10^5 - 10^9$. The horizontal lines span the Roche zone. The horizontal line at $a = 1R_*$ marks the stellar surface. The vertical lines show the remaining lifetime of the system. See Figure 5.1 for a more detailed description).
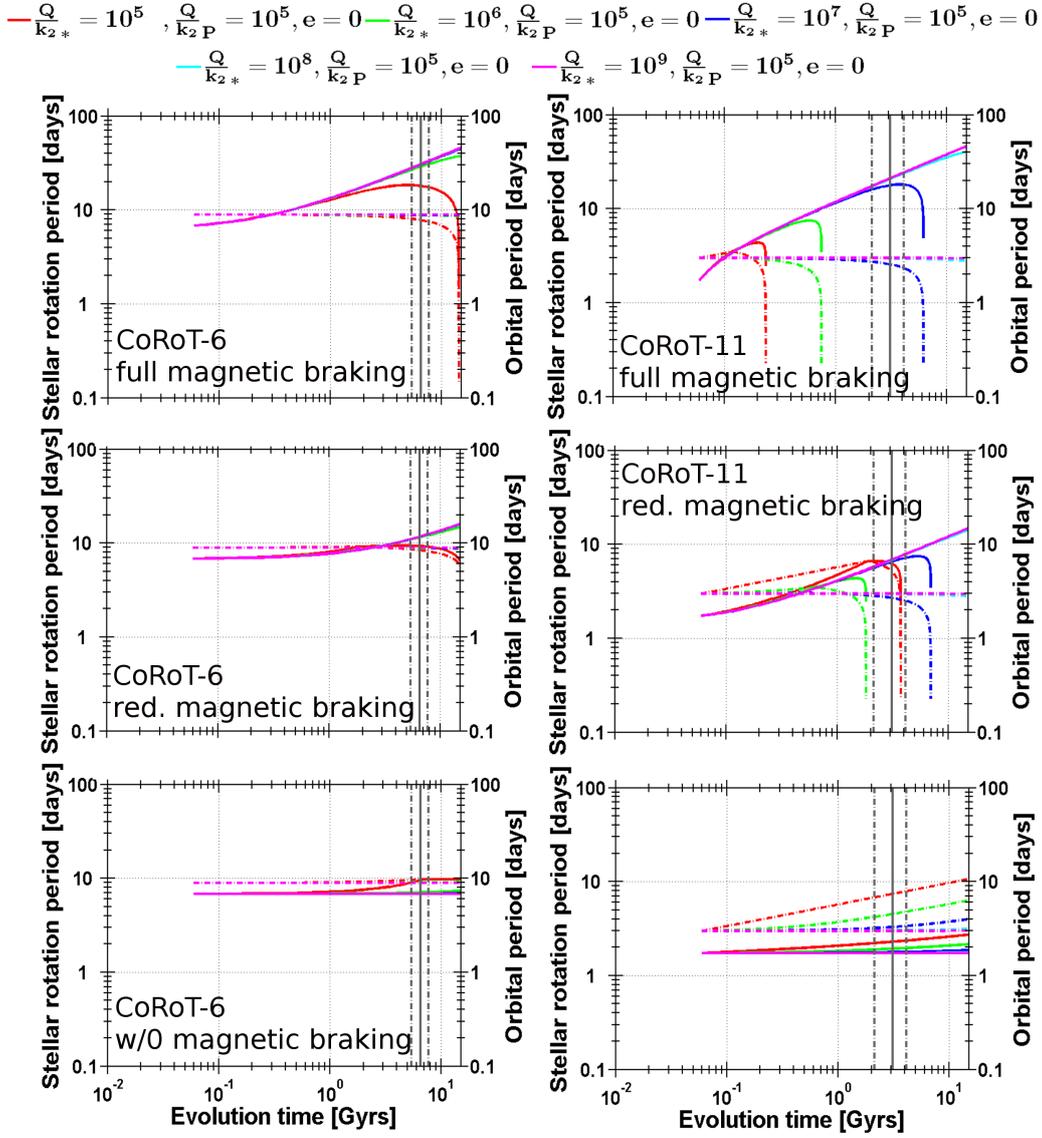
Figure 7.2: The tidal evolution of the stellar rotation of CoRoT-6, and -11 for the next 1.5×10^{10} years and for $\frac{Q_*}{k_{2,*}} = 10^5 - 10^9$ (solid lines) with full, reduced and without magnetic braking. The dashed-dotted lines show the evolution of the orbital period of the corresponding close-in planet for comparison. The vertical lines show the remaining lifetime of the system.

7.1 The tidal evolution of the CoRoT-6 system

The orbit of CoRoT-6b and the stellar rotation of its host star do not change significantly under tidal friction for $\frac{Q_*}{k_{2,*}} = 10^6 - 10^9$. On closer inspection (Figure 7.3), it becomes apparent that the orbit of CoRoT-6b may change after ten billion years if $\frac{Q_*}{k_{2,*}} = 10^5$. In contrast to the cases discussed in previous sections, the orbit change depends on the evolution of the relation $\Omega_* - n$ in the near future which is closely linked to the stellar rotation evolution (Figure 7.2).
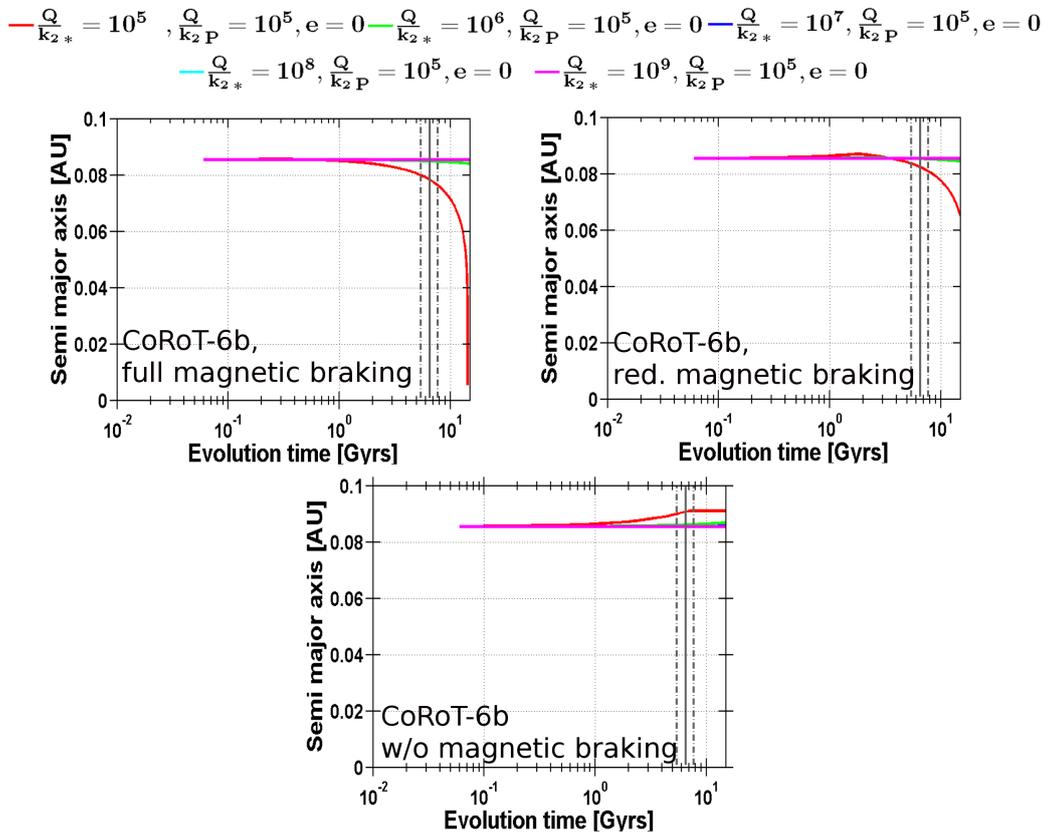
Figure 7.3: The tidal evolution of the semi major axis of the planets CoRoT-6b for the next 1.5×10^{10} years and for $\frac{Q_*}{k_{2,*}} = 10^5 - 10^9$. The y-axis is this time set to linear scale and spans from 0.04 to 0.1 AU.

Full magnetic braking

For full magnetic braking, the stellar rotation is decelerated within the next three hundred million years, crosses the $\Omega_* - n = 0$ state and is decelerated further. The CoRoT-6 system then becomes a planetary system with a close-in planet around a slowly rotating star with $\Omega_* \ll n$, like the planetary systems discussed previously. CoRoT-6b will then start to migrate towards the star, but will fail to reach the Roche limit within the remaining lifetime.

Reduced magnetic braking

For reduced magnetic braking, the planet may migrate slightly away from the star before the stellar rotation rate is decelerated into a state where again $\Omega_* < n$. After that, the planet starts to migrate towards the star after ten billion years. Consequently, the orbit will never near the Roche limit even after fifteen billion years.

No magnetic braking

Without magnetic braking, Ω_* remains larger than n until tidal friction kicks in and starts to synchronize the stellar rotation period and the planetary revolution period by increasing both (See also Figure C.8). The planet will migrate only slightly outwards. This will be discussed in more detail in Chapter 8.

Summary

Apparently, the early stellar rotation evolution may only be affected by magnetic braking. Tidal friction may affect the stellar rotation only on longer timescales of billion of years. Because the tidal friction evolution starts very late into the system's evolution time, $|\Omega_* - n| \approx const$ for the majority of the evolution and, therefore, the

constant Q_* assumption is a valid approach (See also Figure C.8).

In any case, even for $\frac{Q_*}{k_{2,*}} = 10^5$ and for all magnetic braking scenarios, tidal friction leaves the orbit virtually unchanged and stable during the remaining lifetime. This confirms the conclusions drawn in Section 4.1, where the semi major axis of CoRoT-6b $a = 0.0855$ AU places the planet in the stable region around an F-star for all investigated $\frac{Q_*}{k_{2,*}}$. Only the stellar rotation may be affected significantly within this time, leading either to a moderate tidal spin-up in the presence of magnetic braking or to a slight spin-down of the stellar rotation if no magnetic braking is acting on the star.

7.2 The tidal evolution of the CoRoT-11 system

The CoRoT-11 system, on the other hand, is one system that is expected to evolve strongly due to tidal friction within the remaining lifetime, as can already inferred by looking at the tidal stability maps (Section 4.1), the Doodson constant and the property factor (Section 4.1.1). Here, the close connection between the semi major axis and the stellar rotation evolution is even more apparent.

Full magnetic braking

In the presence of full magnetic braking acting on the star, the planet hardly has time to migrate outwards (Figure 7.1). Even for the smallest $\frac{Q_*}{k_{2,*}}$ the stellar rotation is braked so efficiently that it reaches the state $\Omega_* = n$ within 100 million years (Figure 7.2). Only for $\frac{Q_*}{k_{2,*}} = 10^5$ will the planet move noticeably outwards in this brief time. After that, magnetic braking slows down the stellar rotation further. Apparently, the early stellar rotation evolution is dominated again by magnetic braking and not by tidal friction. Therefore, the planet will start to migrate towards the star

again in the long run. apart from the first two hundred million years evolution time, the tidal evolution of the CoRoT-11 system is similar to the evolution of the CoRoT-systems with close-in planets around slowly rotating stars discussed in Section 5.1.2 (See also Figure C.8).

Reduced magnetic braking

For reduced magnetic braking acting on the star, the stellar rotation will be faster than the planet's revolution only for the the first 600 million years if $\frac{Q_*}{k_{2,*}} \geq 10^6$ and for the next one billion years if $\frac{Q_*}{k_{2,*}} \geq 10^5$.

During the first evolution stage, while $\Omega_* - n > 0$ and $\frac{Q_*}{k_{2,*}} \leq 10^6$, the planet will migrate quite a distance outwards. Indeed, when the state $\Omega_* = n$ is reached, the distance between the planet and its star is very different for $\frac{Q_*}{k_{2,*}} = 10^5 - 10^7$, and $\frac{Q_*}{k_{2,*}} \geq 10^8$.

For $\frac{Q_*}{k_{2,*}} \geq 10^8$, the planet is approximately at the same position as today. If $\frac{Q_*}{k_{2,*}} = 10^7$, the semi major axis does not change initially but will decrease long after the stellar rotation has slowed down beyond the $\Omega_* = n$ state. Then, the planet will migrate towards the star and will even reach the Roche zone within the next seven billion years. This is, however, longer than the remaining stellar lifetime.

For $\frac{Q_*}{k_{2,*}} = 10^6$, the planet will have migrated noticeably outwards until $\Omega_* = n$. After the star is decelerated further by magnetic braking, CoRoT-11b will then start to migrate towards the star again and will reach the Roche zone within the next two billion years evolution time; well within the remaining lifetime of the system. For $\frac{Q_*}{k_{2,*}} = 10^5$ the planet will have migrated even farther outwards until $\Omega_* = n$. When the stellar rotation is decelerated further, the planet will again 'turn around' and migrate towards the star. It will reach the Roche limit after more than three billion

years, much later than compared to the $\frac{Q_*}{k_{2,*}} = 10^6$-evolution track. Figure 7.4 shows this in more detail.
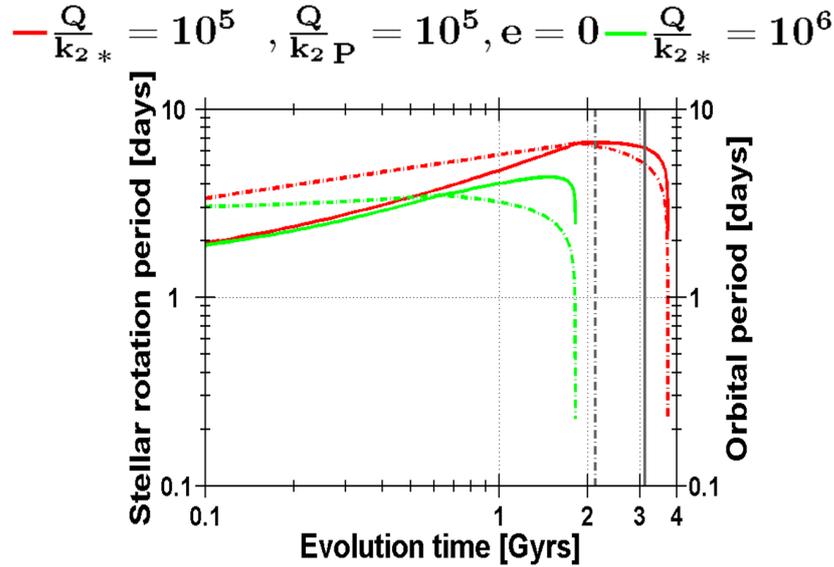
Figure 7.4: The tidal evolution of the stellar rotation of CoRoT-11 with reduced magnetic braking for the next three billion years and for $\frac{Q_*}{k_{2,*}} = 10^5$ and 10^6.

In this detailed view, it is apparent that tidal friction is already efficient enough during the next hundred million years of evolution time, if $\frac{Q_*}{k_{2,*}} = 10^5$, and that it will cause a noticeable additional spin-down of the stellar rotation. At the same time, the planet's semi major axis and the planet's revolution period increase considerably due to tidal friction. The $\Omega_* - n = 0$ state will be met at 1 billion years, later than for $\frac{Q_*}{k_{2,*}} \geq 10^6$. For $\frac{Q_*}{k_{2,*}} \geq 10^6$, the stellar rotation evolution is driven mainly by magnetic braking at this early state and the system will reach $\Omega_* - n = 0$ after 600 million years. If $\frac{Q_*}{k_{2,*}} = 10^5$, not only does CoRoT-11b show the strongest outwards migration compared to larger $\frac{Q_*}{k_{2,*}}$-values, it also has more time to migrate outwards. Therefore, the planet's semi major axis at the 'turning point' $\Omega_* - n = 0$ is so large that tidal friction is less efficient compared to the $\frac{Q_*}{k_{2,*}} = 10^6$-scenario where the distance at

the turning point lies much nearer towards the star. The strength of tidal friction depends more strongly on the semi major axis a (with the power to five) than on $\frac{Q_*}{k_{2,*}}$ (linear dependency). This is the only situation found so far where the $\frac{Q_*}{k_{2,*}} = 10^6$-semi major axis evolution track overtakes the $\frac{Q_*}{k_{2,*}} = 10^5$-semi major axis evolution track during the planet's migration towards the star. In any case, the stellar rotation rate will never match the orbital revolution rate again, even when the planet enters the Roche zone.

If $\frac{Q_*}{k_{2,*}} \geq 10^6$ the stellar rotation decreases even due to reduced magnetic braking very fast such that $\Omega_* \ll n$ before tidal friction can have a noticeable effect on the system. The constant Q_* assumption is again valid on timescales of billion of years on which tidal friction acts. For $\frac{Q_*}{k_{2,*}} = 10^5$, this assumption may be shaky for the first billion years because tidal spin-up can not be neglected at this early stage. After that, $\Omega_* \ll n$ is established and therefore, even in this case, the constant Q_* assumption can be assumed as valid at the later evolution phase at least (Figure C.8).

No magnetic braking

If no magnetic braking is acting on the star, the turning point $\Omega_* - n = 0$ is never reached and $|\Omega_* - n| \approx$ const (See also Figure C.8). The planet will migrate noticeably outwards for the whole evolution time if $\frac{Q_*}{k_{2,*}} \leq 10^7$. At the same time, the stellar rotation is slowed down by a negligible amount due to tidal friction. Even after 15 billion years of evolution and for $\frac{Q_*}{k_{2,*}} = 10^5$, the stellar rotation period changes from about 1.5 days to 3 days. For higher values of $\frac{Q_*}{k_{2,*}}$, tidal friction is too weak to noticeably affect the system within the next 15 billion years.

7.3   Orbital stability

While the orbit of CoRoT-6b is stable within the remaining lifetime, CoRoT-11b may reach the Roche zone, depending on $\frac{Q_*}{k_{2,*}}$ and the strength of magnetic braking which decelerates the stellar rotation.

Without magnetic braking, the planet will never come in the vicinity of the star for any $\frac{Q_*}{k_{2,*}}$. On the contrary, the planet may migrate outwards for small $\frac{Q_*}{k_{2,*}} \leq 10^7$. The stellar rotation can be regarded as unaltered for any $\frac{Q_*}{k_{2,*}}$.

If magnetic braking is decelerating the star, the system will evolve within the remaining lifetime into a configuration where a close-in extrasolar planet revolves around a slowly rotating star $(\Omega_* \ll n)$, like the systems discussed in previous chapters. In consequence, the planet may reach the Roche zone depending on $\frac{Q_*}{k_{2,*}}$. For reduced magnetic braking, it is safe to use the current semi major axis to investigate orbital stability using equation (5.1.2). For full magnetic braking, equation (5.1.2) can not be used because the evolution of the semi major axis depends on how far the planet has migrated during the $\Omega_* > n$-state. To derive the stability limit, the orbital evolution is simulated beginning with $\frac{Q_*}{k_{2,*}} = 10^6$ and increasing $\frac{Q_*}{k_{2,*}}$ in steps of $10^{0.2}$, until the evolution track is found for which the planet enters the Roche zone exactly at the end of the remaining lifetime. The results are listed in Table 7.1.

7.4   Results of the stellar rotation evolution

The fact that stellar rotation is decelerated by even reduced magnetic braking into a slowly rotating state $(\Omega_* \ll n)$ shows that fast rotating host stars of close-in extrasolar planets must either be very young or cannot experience magnetic braking. According to *Barnes* (2003), only F stars may meet the last criterion. Furthermore, *Bouvier et al.*

System	$\frac{Q_*}{k_{2,*}}_{stable}$	K	total lifetime	age
		[Nms]	[Gyrs]	[Gyrs]
CoRoT-6	stable for $10^5 - 10^{10}$	all K	8.7	$2.5 - 4$
CoRoT-11	$10^{6.4}/10^{6.6}/10^{6.8}$	2.7×10^{40}	5.1	2 ± 1
CoRoT-11	stable if $\leq 10^{5.4}$ or $\geq 10^{6.4}/$ $\leq 10^5$ or $\geq 10^{6.6}/$ $\geq 10^{6.8}$	2.7×10^{39}	5.1	2 ± 1
CoRoT-11	stable for $10^5 - 10^{10}$	0	5.1	2 ± 1

Table 7.1: Required $\frac{Q_*}{k_{2,*}}_{stable}$ for the planet's orbit to stay outside the Roche limit within the remaining lifetime of the star.

(1997) show that there are many stars that enter the main sequence as fast rotators. In principle, there should be no shortage of fast rotating F-stars as exoplanet host-stars with $P_* \ll 3$ days. Instead, even in the CoRoT planet subsample that contains seven F-spectral type main sequence host stars, there are only two systems found for which the F-star is clearly rotating faster than the planet revolves around it. And there is only one star, CoRoT-11, with $P_* \ll 3$ days.

It may therefore be speculated, based on a very small subsample, that fast rotators are under-represented in exoplanet host stars of spectral type F. Either these stars lose angular momentum due to magnetic braking or there is another effect at play braking such stars during the formation of the planetary system. *Bouvier et al.* (1997), for example, suggest that a primordial planetary dust-disc may be locked with the star and breaks the stellar rotation down during planet formation. If this is correct, F-stars without a primordial dust-disc and without a planet may be fast rotators whereas F-stars with planets should tend to be slower rotators.

The latter explanation, however, is contradicted by the existence of the CoRoT-11 planetary system with a very fast rotating star ($P_* = 1.4$ days) and a massive planetary companion. The first explanation, that angular momentum loss by magnetic

braking is at play, is corroborated by the rotation rates and ages of the F-stars found in the CoRoT-planetary system sample (Figure 6.9). CoRoT-11, the fastest rotation F-star, is relatively young with an age of 2 ± 1 billion years. CoRoT-5, the oldest F-star in this sample with an age of $5-8$ billion years, is also the slowest rotating F-star ($P_* > 30$ days). The other F-stars, with ages between one to five billion years show rotation periods between CoRoT-11's and CoRoT-5's. This is exactly the expected age-rotation period-relation if such stars lose angular momentum due to magnetic braking. At the same time, the rotation periods of F-stars are at all times - with the exception of CoRoT-5 - noticeably smaller than that of other main sequence stars. This would indicate reduced magnetic braking as pointed out by *Barnes* (2007). As was shown in this chapter, reduced magnetic braking is sufficient to break the system out of the $\Omega_* > n$ state.

As a side effect, the investigation of tidal effects within close-in extrasolar systems may shed light upon the efficiency of magnetic braking in higher mass main sequence stars.

Furthermore, it was shown that the CoRoT-11 system does not settle at the $\Omega_* - n = 0$-state and that the CoRoT-6 system may only settle at $\Omega_* - n = 0$ in the absence of magnetic braking and at the end of the remaining lifetime. In the next chapter, several CoRoT-systems will be investigated that may indeed settle on a double synchronous state within the remaining stellar lifetime.

Chapter 8

Double synchronous states

The CoRoT-systems CoRoT-3, CoRoT-4 and CoRoT-15 may be in double synchronous rotation ($|\Omega_* - n| \approx 0$). CoRoT-6 may evolve into a double synchronous state in the absence of magnetic braking (see Chapter 7), CoRoT-10 and 20 may briefly establish a double synchronous state (see Section 6.2). Indeed, in all these cases (except for CoRoT-10) the planetary revolution rate n is very similar to the stellar rotation rate Ω_* (See Section 1.4, Table 1.4). Therefore, the possibility of tidal equilibrium states warrants in-depth investigation.

8.1 The stability of the double synchronous CoRoT systems

In the previous chapters it was shown that the evolution of the stellar rotation is driven by two mechanisms that in most cases counteract each other: Tidal friction decreases the planet's orbit and consequently spins up the stellar rotation, in particular for very small $\frac{Q_*}{k_{2,*}} \approx 10^5 - 10^6$. Magnetic braking, on the other hand, reduces the stellar rotation.

While tidal friction is found to be very efficient in spinning up the star, in most

219

cases, it is not efficient enough to actually catch up with the planetary revolution rate n that will usually be larger than the stellar rotation rate Ω_*.

What is the difference between the CoRoT-systems in apparent double synchronous rotation and other systems? With the exception of CoRoT-4, the main difference lies in the mass of the companions: CoRoT-3b and CoRoT-15b are the most massive CoRoT planetary companions (Table 1.3). CoRoT-6b, the planet that may evolve into a double synchronous rotation at the end of the system's lifetime, is with a mass of about $3\,M_{Jup}$ also relatively massive. The orbits of massive planets and brown dwarfs should contain more angular momentum than the orbits of the less close-in Super-Earths, for example.

Indeed, *Hut* (1980) showed that energy and angular momentum considerations are necessary to evaluate the stability of double synchronous states. See section 2.9 for the mathematical derivation.

'Binary systems' can end up in a double synchronous rotation state only if their total angular momentum, L_{tot}, exceeds a critical value $L_{tot,crit}$ (2.9.10):

$$L_{tot,crit} = 4 \left[\frac{G^2}{27} \left(I_* M_* R_*^2 + I_{Pl} M_{Pl} R_P^2 \right) \frac{M_*^3 M_{Pl}^3}{M_* + M_{Pl}} \right]^{1/4}. \qquad (8.1.1)$$

Furthermore, this state can only be stable if the orbital angular momentum, L_{orb}, exceeds a critical value $L_{orb,crit}$ (2.9.14):

$$L_{orb,crit} = 3 \left(I_* M_* R_*^2 + I_{Pl} M_{Pl} R_*^2 \right) n. \qquad (8.1.2)$$

Figure (8.1) shows the total angular momentum of each CoRoT system in comparison with the total critical angular momentum $L_{tot,crit}$ and the orbital angular momentum of each CoRoT planet in comparison with the critical value $L_{orb,crit}$.
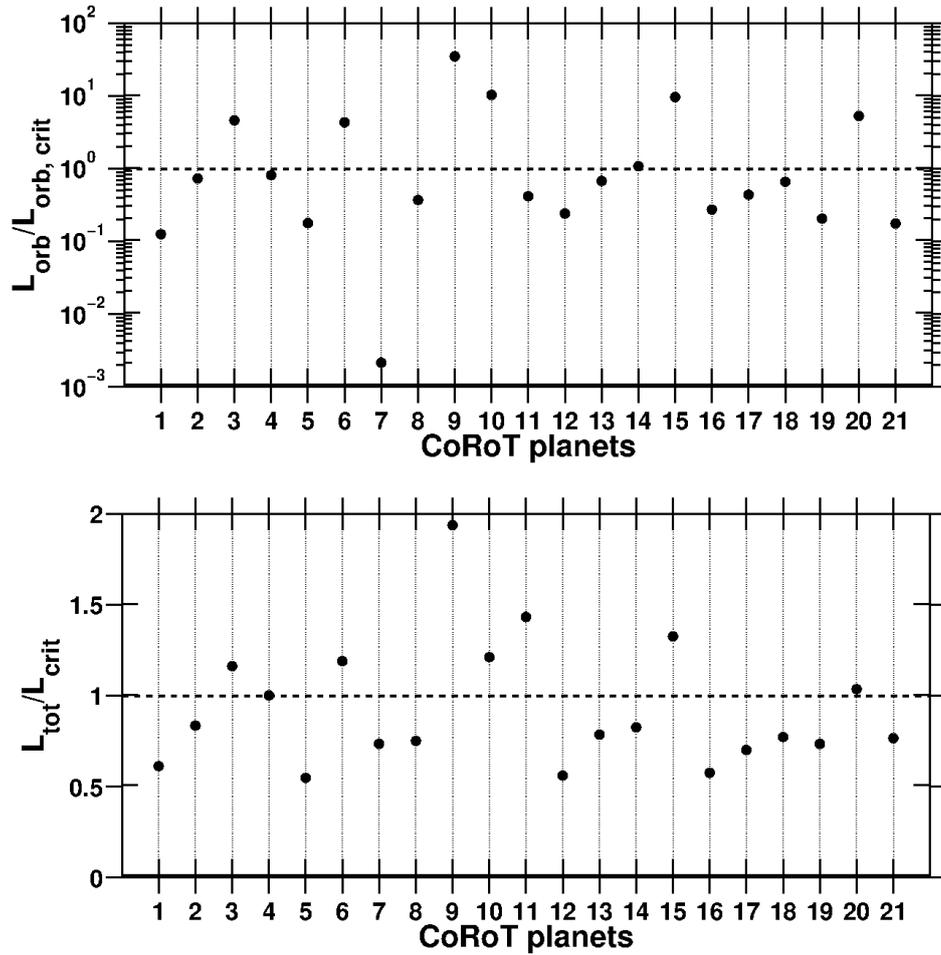
Figure 8.1: Comparison of the total angular momentum, L_{tot}, of the CoRoT planets with the critical angular momentum, $L_{tot,crit}$, and comparison of the orbital angular momentum of the CoRoT systems, L_{orb}, with the critical orbital angular momentum L_{orb}. Top: The ratio L_{tot} over $L_{tot,crit}$ for each CoRoT system. Bottom: The ratio of L_{orb} and $L_{orb,crit}$ for each CoRoT system.

The following eight CoRoT-systems have a total angular momentum which allows the existence of a double synchronous state: CoRoT-3, CoRoT-4, CoRoT-6, CoRoT-9, CoRoT-10, CoRoT-11, CoRoT-15 and CoRoT-20. Such a state, however, is only stable if the orbital angular momenta of the planets exceed the critical value $L_{orb,crit}$.

Indeed, CoRoT-4 and CoRoT-11 fail this test. The evolution of CoRoT-11 was investigated in the previous chapter, and the detailed simulation of the tidal evolution of this system shows that the $\Omega_* = n$ is only a transient state. In the end, the planet will migrate towards the host star and may be unstable under tidal friction.

The 'false' double synchronous case of CoRoT-4

Why are the orbital period of CoRoT-4b and the rotation period of CoRoT-4 almost identical, when the CoRoT-4 system fails the angular momentum requirement for achieving a stable double synchronous state? Furthermore, it was found in Section 4.1.1 that the Doodson constant of CoRoT-4b is one of the smallest among the CoRoT planets. In addition, its orbit is in a region of tidal stability for $\frac{Q_*}{k_{2,*}} = 10^5 - 10^9$ when considering the tidal stability map. Therefore, the orbit and stellar rotation are not expected to be affected strongly within the complete stellar lifetime. Indeed, the computation of the tidal evolution of the CoRoT-4 system confirms this result (Figure B.1). Even if a stable double synchronous state would be possible for the CoRoT-4 system, it is hard to understand how the system should evolve into such state under tidal friction within its lifetime.

Another explanation is needed for the apparent synchronicity of stellar rotation and planetary revolution within the CoRoT-4 system: It may just be coincidence to find a planet around such a star with just about the 'correct' revolution period. The stellar rotation of CoRoT-4 of nine days is a typical value for F-stars (See for

instance *Bouvier et al.* (1997) or *Barnes* (2007)). The stellar rotation is not a very precisely determined property and therefore might be 'off' within limits of uncertainty ($P_* = 9.2^{+1.7}_{-1.3}$ days and $P_{orb} = 9.20205 \pm 0.00037$ days).

'True' potentially double synchronous systems

The following six CoRoT-systems may end up in a **stable** double synchronous state due to angular momentum considerations: CoRoT-3, CoRoT-6, CoRoT-9, CoRoT-10, CoRoT-15, and CoRoT-20.

CoRoT-6b, however, is relatively far away from its star and was shown to end up in a double synchronous state very late only in the absence of magnetic braking and if $\frac{Q_*}{k_{2,*}} = 10^5$ (Chapter 7, Figure 7.2). Interestingly, CoRoT-6b's semi major axis ($a = 0.0855$ AU) is similar to that of CoRoT-4b ($a = 0.09$ AU), which also orbits an F-star. But CoRoT-6b ($M_{Pl} = 2.96\,M_{Jup}$) is four times as massive than CoRoT-4 ($M_{Pl} = 0.72\,M_{Jup}$) and, consequently, stellar tidal friction acting in the CoRoT-6 system is four times as efficient than stellar tidal friction acting in the CoRoT-4 system.

CoRoT-9b ($a = 0.407$ AU) is even farther away from its star and tidal forces are too weak to force the systems into double synchronous states. Indeed, the stellar rotation and orbital period are not similar and will not converge within the remaining lifetime of the systems.

In the end, only four CoRoT-systems remain that may be 'true' examples of double synchronous tidal equilibrium states within the lifetime of the star: CoRoT-3, CoRoT-5, CoRoT-10 and CoRoT-20. These will be discussed in more detail in the following sections.

The examples of the systems CoRoT-6, and CoRoT-9 illustrate that the energy

and angular momentum considerations of *Hut* (1980) 'only' allow to draw the conclusion that such systems may end up **in principle** in stable double synchronous states. If **in reality** a double synchronous state is achieved in reasonable time, i.e., within the lifetime of the system, is another matter entirely that depends on the strength of stellar tidal friction (and planetary tidal friction for eccentric orbits), and also on the strength of magnetic braking, in the case of the CoRoT-6 system,.

8.2 Constraints on $\frac{Q_*}{k_{2,*}}$ to achieve a double synchronous state in the presence of magnetic braking

To force a star into corotation and to maintain this double synchronous orbit, stellar tidal friction has to act efficiently. This depends on $\frac{Q_*}{k_{2,*}}$. It will be shown that planetary tidal friction may help to establish a double synchronous state but, in the long run, planetary tidal friction will not maintain the double synchronous orbit as the orbital eccentricity is forced rapidly towards zero.

In the following, the evolution of such a system around the double synchronous rotation state $(\Omega_* - n \approx 0)$ is investigated in the presence of at least reduced magnetic braking.

Several justified assumptions to simplify the calculations are:

- The tidal equilibrium state is stable; that is, the stability criteria discussed in the previous section are fulfilled.

- The system is assumed to be double synchronous if $\Omega_* = n$ is achieved, because the planetary rotation is already synchronized with the planets revolution (Section 3.2).

- Once the system is in double synchronous rotation it remains there.

- The orbit is circular; indeed it will be shown that the potential double synchronous systems either have circular orbits or evolve quickly into circular orbits.

- In consequence, the tidal frequency $\omega = 2|\Omega_* - n| \approx 0$ during the whole calculation.

- Therefore, the constant Q_* assumption that requires the tidal frequency or tidal lag angle to be approximately constant (see Section 2.5), can be used to investigate the further evolution.

It should be noted, however, that the constant Q_* required for $\omega \approx 0$ in this chapter can, and in fact should, differ from the constant Q_* required for $\omega = 2|\Omega_* - n| \approx 2n$ in previous sections for planetary systems with slowly rotating stars where $\Omega_* \ll n$. This should be kept in mind during the discussion of the results.

The systems evolution can be modeled using equations derived in Section 2.6 and 2.10 by:

$$\frac{\mathrm{d}a}{\mathrm{d}t} = \mathrm{sign}\left(\Omega_* - n\right) \frac{3k_{2,*}}{Q_*} \frac{M_{Pl}}{M_*} \left(\frac{R_*}{a}\right)^5 na \tag{8.2.1}$$

$$\frac{\mathrm{d}\Omega_*}{\mathrm{d}t} = -\,\mathrm{sign}\left(\Omega_* - n\right) \frac{3k_{2,*}}{2 * I_* Q_*} \frac{M_{Pl}^2}{M_*(M_* + M_{Pl})} \left(\frac{R_*}{a}\right)^3 n^2 \tag{8.2.2}$$
$$-\,\frac{K}{I_* M_* R*^2} \Omega_*^3 \left(\frac{R_*}{R_{Sun}}\right)^{1/2} \left(\frac{M_*}{M_{Sun}}\right)^{-1/2}.$$

In the following, the constant terms are expressed as follows to simplify the equations:

$$A = \frac{3k_{2,*}}{Q_*} \frac{M_{Pl}}{M_*} R_*^5 \tag{8.2.3}$$

$$B = \frac{3k_{2,*}}{2 * I_* Q_*} \frac{M_{Pl}^2}{M_*(M_* + M_{Pl})} R_*^3 \tag{8.2.4}$$

$$C = \frac{K}{I_* M_* R*^2} \left(\frac{R_*}{R_{Sun}}\right)^{1/2} \left(\frac{M_*}{M_{Sun}}\right)^{-1/2} \tag{8.2.5}$$

$$B' = \frac{B}{G(M_{Pl} + M_*)}$$

Then the equations governing the evolution of the system shortly before entering the doubly synchronous state can be written as:

$$\frac{\mathrm{d}a}{\mathrm{d}t} = \mathrm{sign}\,(\Omega_* - n)\, A \frac{n}{a^4} \tag{8.2.6}$$

$$\frac{\mathrm{d}\Omega_*}{\mathrm{d}t} = -\mathrm{sign}\,(\Omega_* - n)\, B \frac{n^2}{a^3} - C\Omega_*^3 \tag{8.2.7}$$

$$= -\mathrm{sign}\,(\Omega_* - n)\, B' n^4 - C\Omega_*^3, \tag{8.2.8}$$

where in addition Kepler's third law $a^3 = G(M_* + M_{Pl})/n^2$ is used to express the equation describing $\dot{\Omega}_*$ in terms of n and Ω_* instead of a, n and Ω_*.

Furthermore, it is advisable to describe the situation with respect to the fictive double synchronous orbit for any given Ω_* (Figure 8.2). This is the orbit for which the mean motion is exactly $n = \Omega_*$. If the planet is revolving faster around the star than the star rotates about its axis of symmetry, $n > \Omega_*$, and the planet's orbit would lie **inside** the synchronous orbit. After all, $a^3 = G(M_* + M_{Pl})/n^2$ according to Kepler's law. Such a configuration is sometimes called a **sub**synchronous orbit in the literature (*Lanza* (2010) and *Levrard et al.* (2009), for example). If $n < \Omega_*$, the planet's orbit lies **outside** the double synchronous orbit.
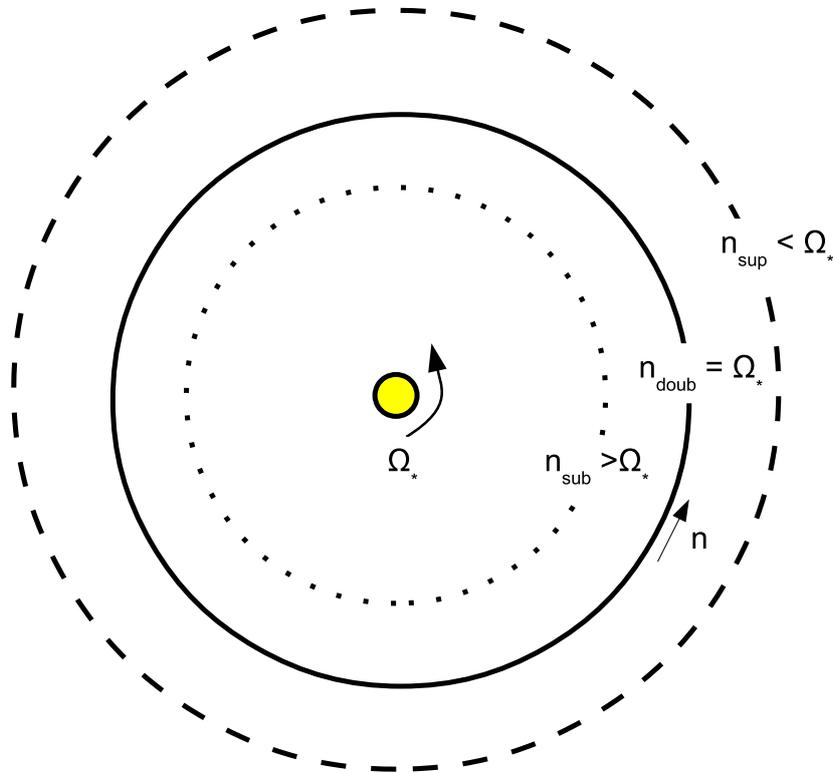
Figure 8.2: The orbit of a planet around a star with respect to the double synchronous orbit ($n = \Omega_*$, solid line). If $n < \Omega_*$, the orbit lies outside the double synchronous orbit (dashed line). If $n > \Omega_*$, the orbit lies inside the double synchronous orbit (dotted line)

In the following, the evolution into and around the double synchronous state is investigated in several steps:

Step 0: One time step before double synchronicity As a start point of investigation, a situation was chosen where the star rotates slower $(\Omega_{*,0})$ than a close-in planet with semi major axis a_0 and mean motion n_0 revolves around it. Consequently, $\Omega_{*,0} < n_0$ shortly before entering double synchronous rotation. The orbit lies inside the double synchronous orbit for which $n_{doub,0} = \Omega_{*,0}$.

This initial situation is selected because it is more difficult to achieve the double synchronous state from inside the double synchronous orbit: tidal friction spins up the star and forces the star and planet into corotation. Magnetic braking, on the other hand, decelerates the star away from the double synchronous rotation state[1]. Therefore sign $(\Omega_* - n) = -1$. In this case, the following set of equations describe the evolution of the system under stellar tidal friction:

$$\frac{\mathrm{d}a}{\mathrm{d}t} = -A\frac{n_0}{a_0^4} \tag{8.2.9}$$

$$\frac{\mathrm{d}\Omega_*}{\mathrm{d}t} = B'n_0^4 - C\Omega_{*,0}^3. \tag{8.2.10}$$

Step 1: Double synchronous orbit achieved After a time step δt, the semi major axis a_1 and stellar rotation rate $\Omega_{*,1}$ are:

$$a_1 = a_0 + \frac{\mathrm{d}a}{\mathrm{d}t}\delta t$$

$$\Omega_{*,1} = \Omega_{*,0} + \frac{\mathrm{d}\Omega_*}{\mathrm{d}t}\delta t.$$

or

$$a_1 = a_0 - A\frac{n_0}{a_0^4}\delta t$$

$$\Omega_{*,1} = \Omega_{*,0} + (B'n_0^4 - C\Omega_{*,0}^3)\delta t.$$

This new orbit should be double synchronous: $\Omega_{*,1} = n_1 = n_{doub,1}$, with $n_1 = \sqrt{G(M_{Pl} + M_*)/a_1^3}$. This is shown in Figure 8.3. The new planetary orbit is

---

[1]If $\Omega_{*,0} > n_0$ is chosen as initial situation, both, magnetic braking and tidal friction, would decelerate the stellar rotation. From this starting point, the double synchronous state is easier to achieve.

inside the old orbit, but the new double synchronous orbit should be inside the old double synchronous orbit as well.
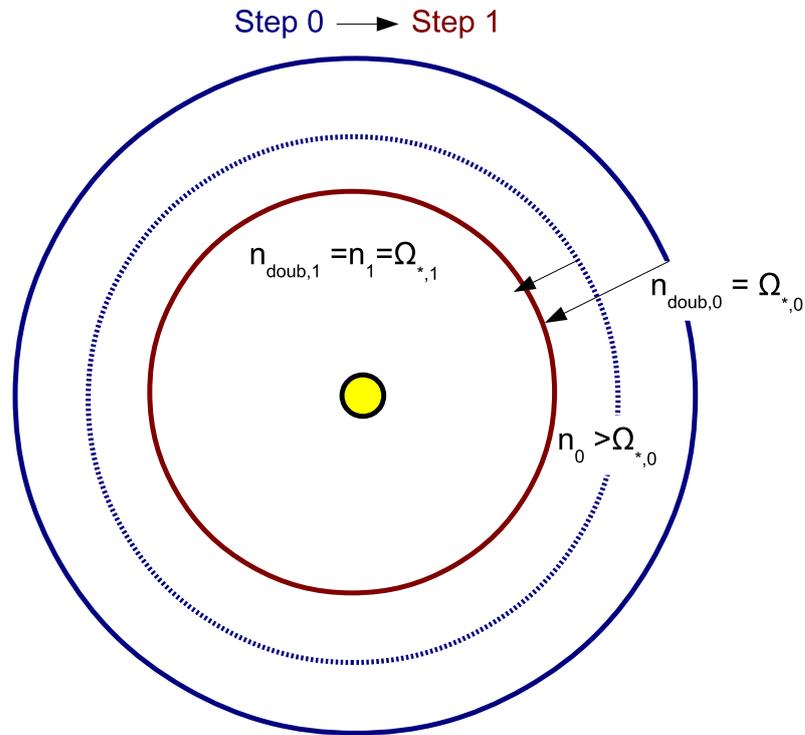
Figure 8.3: Evolution of the subsynchronous orbit $n_0 > \Omega_{*,0}$ represented by the dotted blue circle with respect to the double synchronous orbit represented by the solid blue circle into a double synchronous orbit $n_1 = \Omega_{*,1}$ represented by the red solid circle.

Therefore, magnetic braking has to be less efficient than tidal friction to ensure that the stellar rotation rate increases.

The first condition therefore is:

$$\dot{\Omega}_{*,0} > 0. \tag{8.2.11}$$

If this condition is not fulfilled, the planet's orbit and the double synchronous

orbit will evolve away from each other (Figure 8.4).

The condition above can also be expressed as:

$$B'n_0^4 - C\Omega_{*,0}^3 > 0. \tag{8.2.12}$$

It is at this point safe to assume that n_0 and $\Omega_{*,0}$ are already very similar just before entering the double synchronous state: $n_0 \approx \Omega_{*,0}$. Therefore the relation above reduces to

$$B'n_0 > C. \tag{8.2.13}$$

Or fully expressed and solved for $\frac{Q_*}{k_{2,*}}$:

$$\frac{3k_{2,*}}{2I_*Q_*}\frac{M_{Pl}^2}{GM_*(M_{Pl}+M_*)^2}R_*^3 n_0 > \frac{K}{I_*M_*R_*^2}\left(\frac{R_*}{R_{Sun}}\right)^{1/2}\left(\frac{M_*}{M_{Sun}}\right)^{-1/2} \tag{8.2.14}$$

$$\frac{3}{2}\frac{k_{2,*}}{Q_*}\frac{M_{Pl}^2}{G(M_{Pl}+M_*)^2}R_*^5 n_0 > K\left(\frac{R_*}{R_{Sun}}\right)^{1/2}\left(\frac{M_*}{M_{Sun}}\right)^{-1/2} \tag{8.2.15}$$

$$\frac{Q_*}{k_{2,*}} < n_0\frac{3}{2}\frac{M_{Pl}^2}{G(M_{Pl}+M_*)^2}R_*^5\frac{1}{K}\left(\frac{R_*}{R_{Sun}}\right)^{-1/2}\left(\frac{M_*}{M_{Sun}}\right)^{1/2} \tag{8.2.16}$$

This is the upper limit of $\frac{Q_*}{k_{2,*}}$ required to force a planetary system in double synchronous rotation despite magnetic braking. It depends on the planetary revolution rate n or on $a^{-3/2}$ (using Kepler's third law). The larger the semi major axis and the lower n is, the lower is the required $\frac{Q_*}{k_{2,*}}$ for establishing double synchronous rotation.

Up to now, it was only made sure that the double synchronous orbit decreases as well as the planet's orbit. Close inspection of Figure 8.3 makes another
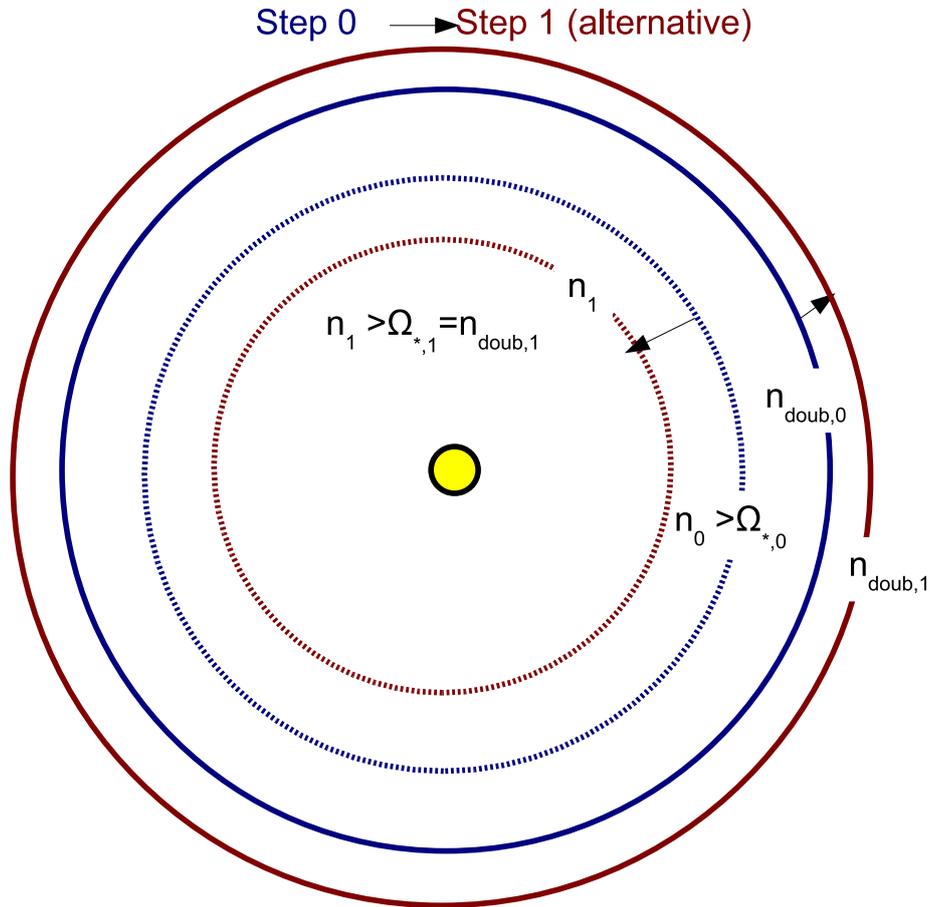
Figure 8.4: Evolution of a subsynchronous orbit $n_0 > \Omega_{*,0}$ represented by the dotted blue circle with respect to the double synchronous orbit represented by the solid blue circle if magnetic braking is more efficient than tidal friction. In the next time step, the planet's orbit would shrink (dotted red circle) but the stellar rotation would decrease and lead to a double synchronous orbit with even larger radius, where $n_1 = \Omega_{*,1}$, represented by the red solid circle.

condition apparent: The double synchronous orbit must decrease faster than the planet's orbit for the two to meet.

$$\dot{n}_{doub,0} = \dot{\Omega}_{*,0} > \dot{n}_0. \tag{8.2.17}$$

If $C = 0$, that is, if no magnetic braking is counteracting tidal friction, equation (8.2.17) is equivalent to equation (8.1.2). This is proven in detail in Chapter G[2]. Without magnetic braking, therefore the system has no problem to achieve a double synchronous state, as long as the orbital angular momentum exceeds the critical value $L_{orb,crit}$.

If $C > 0$, the orbital angular momentum has not only to exceed $L_{orb,crit}$ but the sum of $L_{orb,crit} + \Delta L_{magnetic\ braking}$, where $\Delta L_{magnetic\ braking}$ is the total angular momentum that magnetic braking removes from the system during the stellar lifetime. Incidently, in a subsequent section there will be investigated a CoRoT system that fulfills the requirement $L_{orb} > L_{orb,crit}$ but fails the stronger requirement $L_{orb} > L_{orb,crit} + \Delta L_{magnetic\ braking}$.

In summary, two requirements were identified that must be fulfilled to achieve a double synchronous state even in the presence of magnetic braking. $\frac{Q_*}{k_{2,*}}$ must be lower than the upper limit defined by 8.2.16. In addition to the requirements given in the previous section for the orbital and total angular momentum (equations (8.1.1) and (8.1.2)), the orbital angular momentum has to exceed: $L_{orb,crit} + \Delta L_{magnetic\ braking}$ to achieve a double synchronous state.

Whether the system ends up in a double synchronous state in reasonable time - on time scales of several billion years - is another matter entirely and will be investigated in a subsequent section.

---

[2]It should be noted that this proof is original work and not adopted from other authors.

8.3 Long-term stability of double synchronous orbits in the presence of magnetic braking

Can tidal interactions maintain this state in the future despite magnetic braking, once the double rotation state is established? To answer this question, the evolution of the system is investigated starting with the system in double synchronous rotation (Figure 8.5):

Step 2 The system's parameters at this point are:

$$a_1 = (G(M_{Pl} + M_*)/n_1^2)^{1/3}$$

$$\Omega_{*,1} = n_1.$$

Therefore, from equations 8.2.6 and 8.2.8 the following set of equations govern the further evolution:

$$\frac{\mathrm{d}a}{\mathrm{d}t}\bigg|_1 = 0$$
$$\frac{\mathrm{d}\Omega_*}{\mathrm{d}t}\bigg|_1 = -Cn_1^3.$$

In the presence of magnetic braking, Ω_* always decreases once the system is in a double synchronous state. This is the same as stating that the double synchronous orbit is forced outside of the the planet's orbit by magnetic braking.

Step 3 = Step 0 The system is in the following configuration

$$a_2 = a_1$$

$$\Omega_{*,2} > \Omega_{*,1} = n_1.$$

The system is again in a subsynchronous rotation state as described in the previous section as 'step 0' and depicted in Figure 8.3.

Step 2 $\longrightarrow$ Step 3

$$n_1 = n_2 > \Omega_{*,2}$$

$$n_{doub,2} = \Omega_{*,2}$$
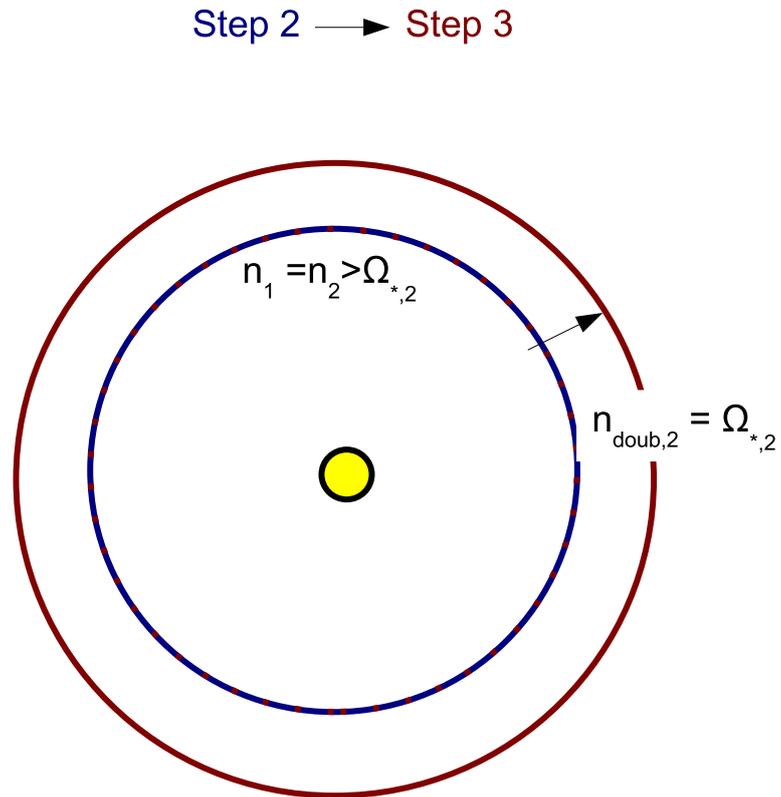
Figure 8.5: Evolution of double synchronous orbit $n_1 = \Omega_{*,1}$ represented by the solid blue circle in the presence of magnetic braking. The stellar rotation becomes slower and as a consequence the radius of the new double synchronous orbit is larger than the radius of the previous one (solid red circle), while the planet's orbit (dotted red circle) remains at its position. This is the same situation than depicted in Figure 8.3.

Therefore, the same requirements than given in the previous section have to be met to achieve double synchronous rotation, but from an orbit closer to the star than compared to the orbit at 'step 0'. If the stellar rotation and the planet's spin can not be synchronized again, the stellar rotation remains slower than the planet's revolution and $\Omega_* \leq n$. The system would become another case of a planet around a slowly rotating star with an evolution as described in Sections 5 and 6.

The first criterion for establishing double synchronicity is that tidal friction is more efficient than magnetic braking (equation (8.2.16)):

$$\frac{Q_*}{k_{2,*}} < n_1 \frac{3}{2} \frac{M_{Pl}^2}{G(M_{Pl} + M_*)^2} R_*^5 \frac{1}{K} \left(\frac{R_*}{R_{Sun}}\right)^{-1/2} \left(\frac{M_*}{M_{Sun}}\right)^{1/2}$$
$$\frac{Q_*}{k_{2,*}} < n_1 \operatorname{const}.$$

In the previous section it was already established that $\frac{Q_*}{k_{2,*}} < n_0 \operatorname{const}$ had to be fulfilled to establish a double synchronous state in the first place. This double synchronous orbit is inside the previous double synchronous orbit therefore $n_1 > n_0$ and the following relation holds as well:

$$\frac{Q_*}{k_{2,*}} < n_0 \operatorname{const} < n_1 \operatorname{const}. \tag{8.3.1}$$

Therefore, once a double synchronous orbit is established, stellar tidal friction will always be stronger than magnetic braking, if $\frac{Q_*}{k_{2,*}}$ does not change drastically but remains more or less constant. This is not surprising because, as stated time and again, stellar tidal friction depends strongly on the orbit's semi major axis. In consequence, a double synchronous orbit with smaller radius than the previous one is achieved in the next timestep. In the next timestep, the star loses angular momentum again by magnetic braking and the new double synchronous orbit for this rotation state will be outside the planet's orbit. Subsequently, the system is forced by tidal

friction on a double synchronous orbit with an even smaller radius and so forth and so forth (Figure 8.6).

This creates the strange situation of a system in or near double synchronous rotation which is not stable. The orbit still decays as the stellar rotation is 'dragged along' and always kept close to the orbital mean motion. Therefore, a planetary system cannot be regarded as tidally stable if $\Omega_* \approx n$, unless stellar angular momentum loss by magnetic braking is investigated.

Another point of concern is that the system loses orbital angular momentum as well as the double synchronous orbit decays, therefore $L_{orb} > L_{orb,crit} + \Delta L_{magnetic\ braking}$ may at one point not be fulfilled anymore as the double synchronous orbit moves closer and closer to the star. Should that happen, synchronicity can not be reestablished again and the double synchronous orbit will lag behind the planet's orbit: the planetary system will become unstable.

In any case, in the presence of magnetic braking a double synchronous orbit may be unstable.

8.3.1 The possible decay of the double synchronous orbit due to magnetic braking

A step-wise calculation of the decay of the double synchronous orbit as described above would be very cumbersome and computationally challenging. In the following, it will be investigated how this can be achieved more efficiently.

The key to a better description is again the angular momentum:

Step 1 The system is in double synchronous rotation. The total angular momentum of a double synchronous system can be expressed in terms of orbital revolution rate $n_{doub,1}$. Because $\Omega_{*,1} = n_1$ and Kepler's third law is used to replace a_1 with
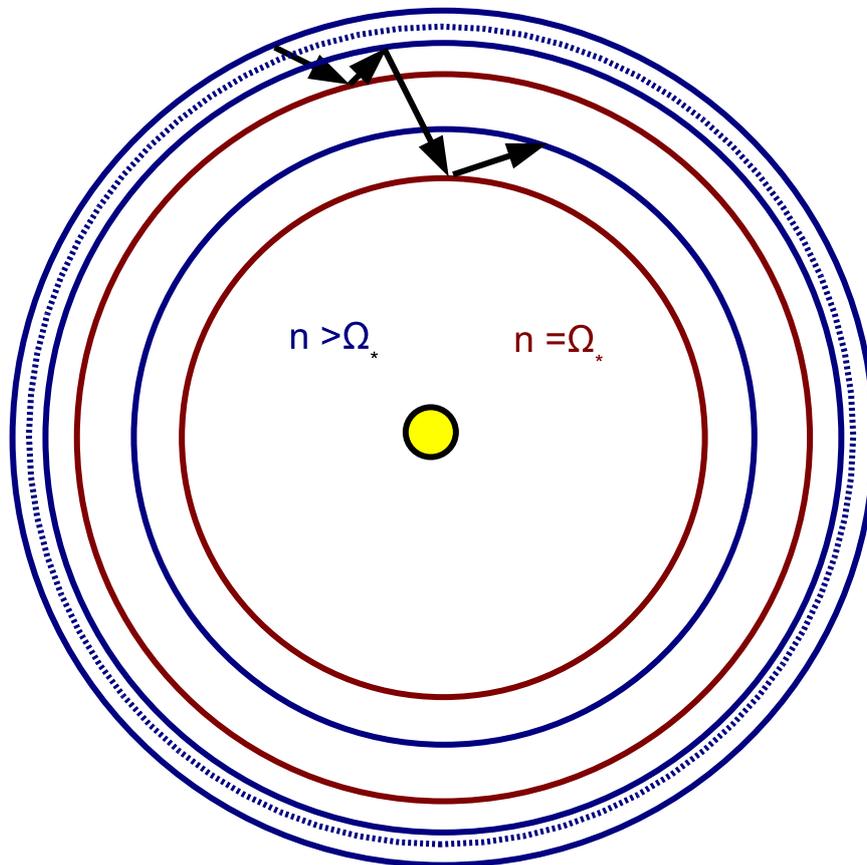
Figure 8.6: The decay of a double synchronous orbit (red circles) in the presence of magnetic braking starting with a subsynchronous planetary orbit (the blue dotted circle is the planet's orbit, the blue solid line is the 'fictive' double synchronous orbit that lies outside the planet's orbit). In the first step, the planetary and double synchronous orbit converge to a new double synchronous orbit with smaller radius(red). In the next step, the stellar rotation decreases and for this state the 'fictive' double synchronous orbit (blue) would lie outside the 'old' double synchronous state where the planet is still orbiting the star. In the next step, the planet's and double synchronous orbit converge into a new double synchronous orbit with even smaller radius etc. In consequence, the planetary orbit continually shrinks. The double synchronous orbit alternatively shrinks and expands, as indicated by the black arrows.

$n_1 = n_{doub,1}$:

$$L_1 = L_{tot} = I_* M_* R_*^2 n_{doub,1} + \frac{M_{Pl} M_*}{M_{Pl} + M_*} \mu^{2/3} n_{doub,1}^{-1/3}, \qquad (8.3.2)$$

where $\mu = G(M_{Pl} + M_*)$.

Step 2 The star loses angular momentum δL_1 due to magnetic braking according to equation (2.10.4):

$$L_2 = L_1 - \delta L_1 = I_* M_* R_*^2 \Omega_{*,2} + \frac{M_{Pl} M_*}{M_{Pl} + M_*} \mu^{2/3} n_2^{-1/3}, \qquad (8.3.3)$$

where $\Omega_{*,2} < n_2$ and $n_2 = n_1 = n_{doub,1}$ as explained in the previous section.

Step 3 Now tidal friction acts to synchronize the stellar rotation and orbital revolution rate again, but only if tidal friction is more efficient than magnetic braking ($\dot{\Omega}_{mag.braking} < \dot{\Omega}_{tidalfriction}$). This is a condition that may safely be regarded as fulfilled as was proven in previous sections (equation 8.2.11). This is equivalent to saying that from the point of view of magnetic braking, tidal friction acts 'instantly' to reestablish a new double synchronous state. Therefore, there will only be a transfer of angular momentum from the orbit to the star during the synchronization:

$$L_3 \approx L_2 = I_* M_* R_*^2 n_{doub,2} + \frac{M_{Pl} M_*}{M_{Pl} + M_*} \mu^{2/3} n_{doub,2}^{-1/3}. \qquad (8.3.4)$$

The system will settle again on a new double synchronous orbit that lies beneath the previous one ($n_{doub,2} < n_{doub,1}$).

Because the total amount of angular momentum loss does not change from **step 2** to **step 3**, the amount of angular momentum lost by magnetic braking can be

calculated using equation (2.10.4). The equation only depends on constants and $n_{doub,1}$. Therefore, the new double synchronous rotation rate $n_{double,2}$ can be calculated by going from **step 0** directly to **step 2**.

Therefore, the decay of the double synchronous orbit in the presence of magnetic braking can be modeled using equation 2.10.4 and setting it equal to $\frac{dL_{tot}}{dt}$:

$$\frac{dJ}{dt} = I_* M_* R_*^2 \dot{n}_{doub} + \frac{M_{Pl} M_*}{M_{Pl} + M_*} \mu^{2/3} \frac{1}{3} n_{doub}^{-4/3} \dot{n}_{doub}. \tag{8.3.5}$$

Solving for $\dot{n}_{doub}$ gives:

$$\frac{dn_{doub}}{dt} = \frac{d\Omega_*}{dt} = \frac{\frac{dJ}{dt}}{C_* + B n_{doub}^{-4/3}}, \tag{8.3.6}$$

where $C_* = I_* M_* R_*^2$ is the stellar moment of inertia and $B = \frac{1}{3} \frac{M_{Pl} M_*}{M_{Pl} + M_*} \mu^{2/3}$.

As a reminder, the angular momentum loss due to magnetic braking, $\frac{dJ}{dt}$, is once again shown at full length:

$$\frac{dJ}{dt}_{\Omega_*} = -K\Omega_*^3 \left(\frac{R_*}{R_{Sun}}\right)^{0.5} \left(\frac{M_*}{M_{Sun}}\right)^{-0.5} \qquad \text{for} \quad \Omega_* < \omega_{sat} \tag{8.3.7}$$

$$\frac{dJ}{dt}_{\Omega_*} = -K\Omega_* \omega_{sat}^2 \left(\frac{R_*}{R_{Sun}}\right)^{0.5} \left(\frac{M_*}{M_{Sun}}\right)^{-0.5} \qquad \text{for} \quad \Omega_* \geq \omega_{sat},$$

where K is the phenomenologically derived scaling constant ($K = 2.7 \times 10^{40}$ Nms for low-mass main sequence stars).

Using equation (8.3.6), the evolution of the systems CoRoT-3 and CoRoT-15 can be calculated (Figures 8.7 and 8.8), as long as the orbital and total angular momentum fulfill equations (8.1.2) and (8.1.1).

8.4 Tidal evolution of the CoRoT-3 and CoRoT-15 system

The tidal evolution of CoRoT-3 and CoRoT-15 systems are modeled using Equations (5.1.1) and (6.1.1), as long as $\Omega_* < n$. To account for the uncertainty in magnetic braking in the F-stars CoRoT-3 and CoRoT-15, the semi major axis and stellar rotation evolution is simulated with full, reduced and without magnetic braking (See also Section 5.1.2) by using different scaling factors K:

- $K = 2.7 \times 10^{40}$ Nms for 'full magnetic braking', adopting the same scaling factor as for low mass main sequence stars,

- $K = 2.7 \times 10^{39}$ Nms for 'reduced magnetic braking',

- $K = 0$ for a model without magnetic braking.

As soon as a state $\Omega_* = n$ is reached, the further evolution is modeled using Equation 8.3.6 as a 'short cut' saving computation time.

Figures 8.7 and 8.8 show the evolution of the planet's orbit and the stellar rotation for the next 15 billion years. Figures 8.9 and 8.10 show a close-up of the first billion years of evolution. This allows to better identify the conditions for which the CoRoT-3 and CoRoT-15 system may enter the double synchronous state.(See also Figures C.9 for the $\Omega_* - n$ evolution). The evolution was modeled with the average stellar rotation period as given in Table 1.4. It should be considered that a variation of the stellar rotation period at the start of the computations may change the semi major axis and stellar rotation evolution because the $\Omega_* = n$ state may be met earlier or later than computed here. This does not affect, however, the qualitative results derived in terms of magnetic braking and $\frac{Q_*}{k_{2,*}}$ (See also Chapter F).
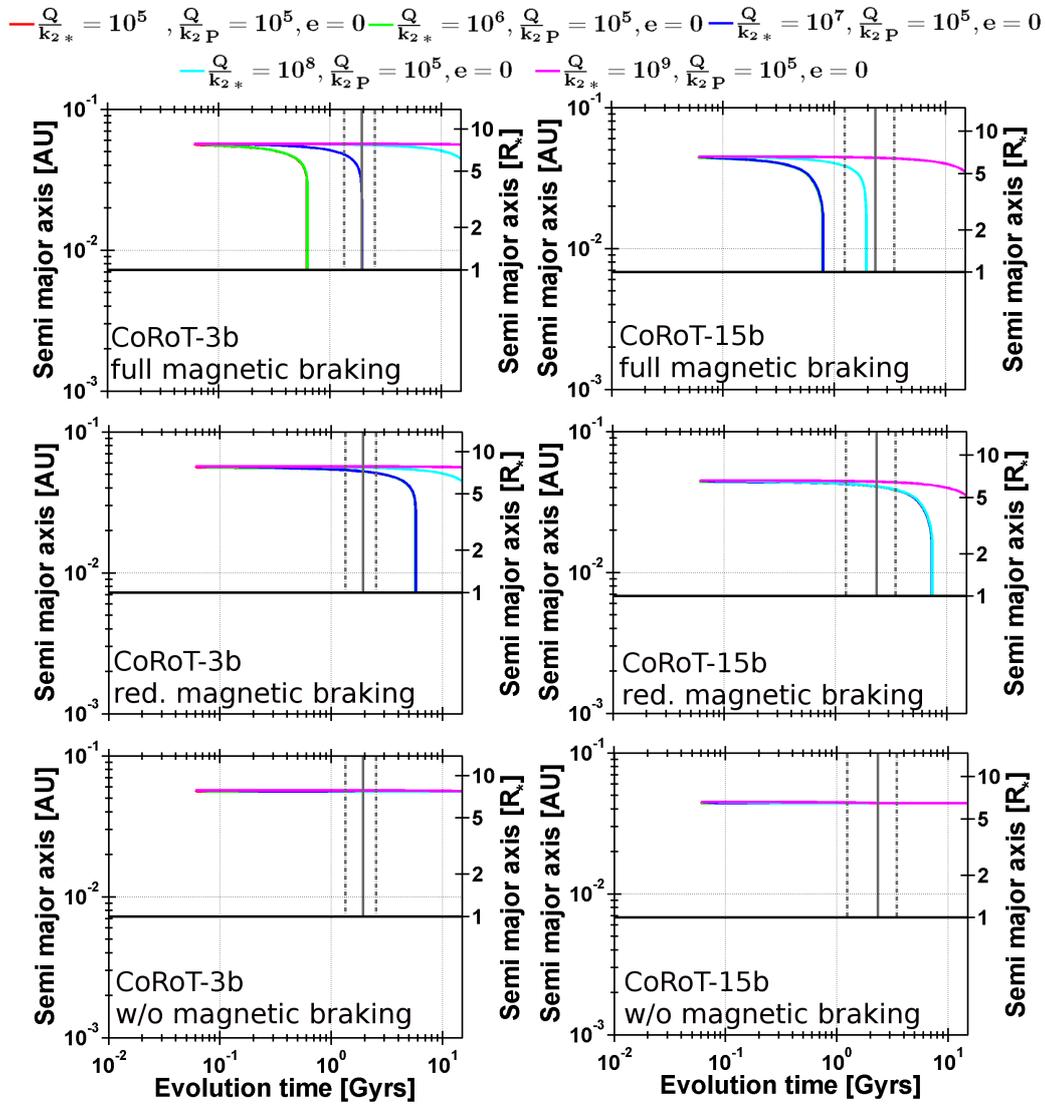
Figure 8.7: The tidal evolution of the semi major axis of the brown dwarfs CoRoT-3b, and -15b for the next 1.5×10^{10} years and for $\frac{Q_*}{k_{2,*}} = 10^5 - 10^9$. The horizontal lines span the Roche zone. The horizontal line at $a = 1R_*$ marks the stellar surface. The vertical lines show the remaining lifetime of the system.
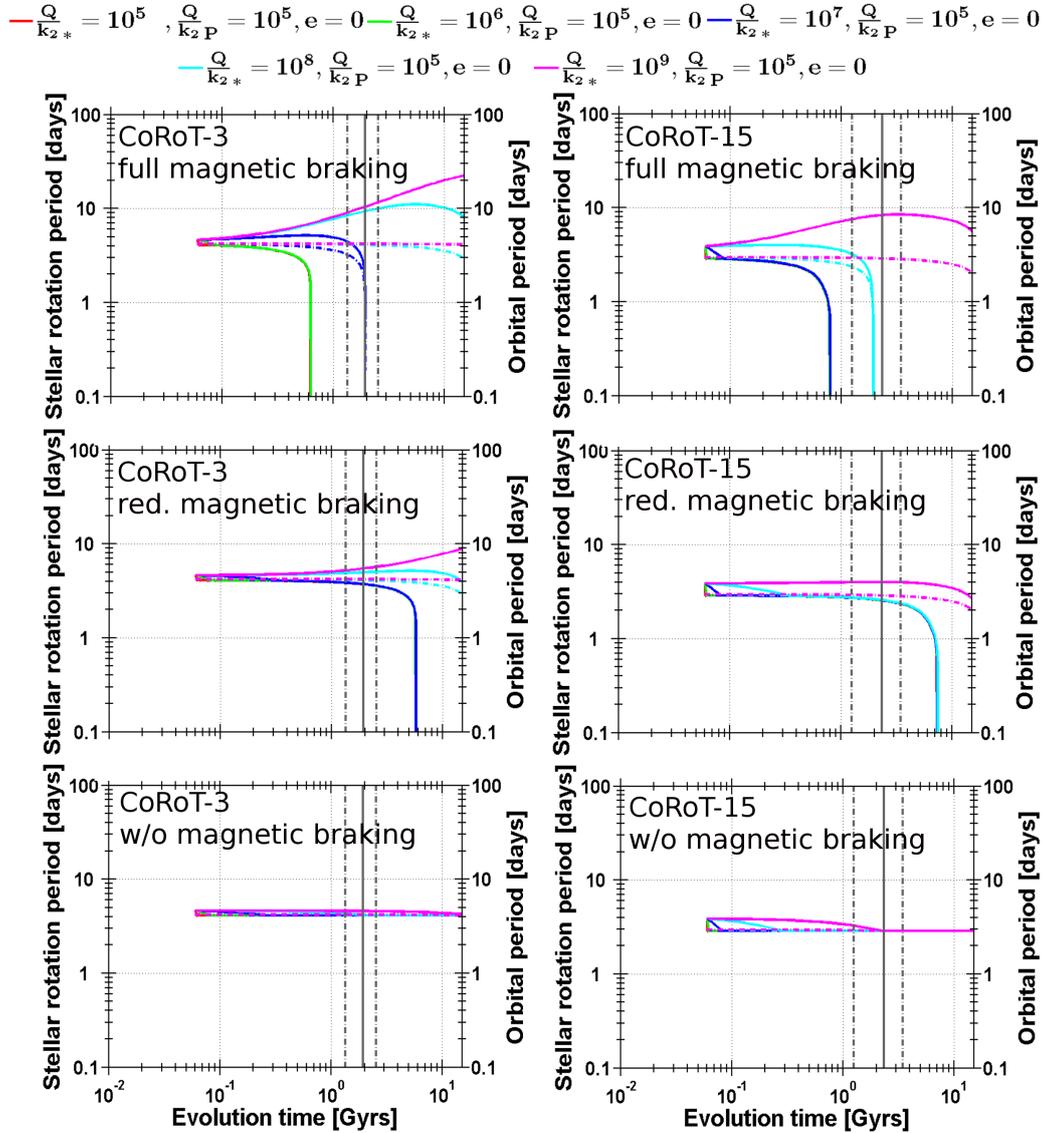
Figure 8.8: The tidal evolution of the stellar rotation of CoRoT-3, and -15 for the next 1.5×10^{10} years and for $\frac{Q_*}{k_{2,*}} = 10^5 - 10^9$ (solid lines) with full, reduced and without magnetic braking. The dashed-dotted lines show the evolution of the orbital period of the corresponding close-in planet for comparison. The vertical lines show the remaining lifetime of the system.
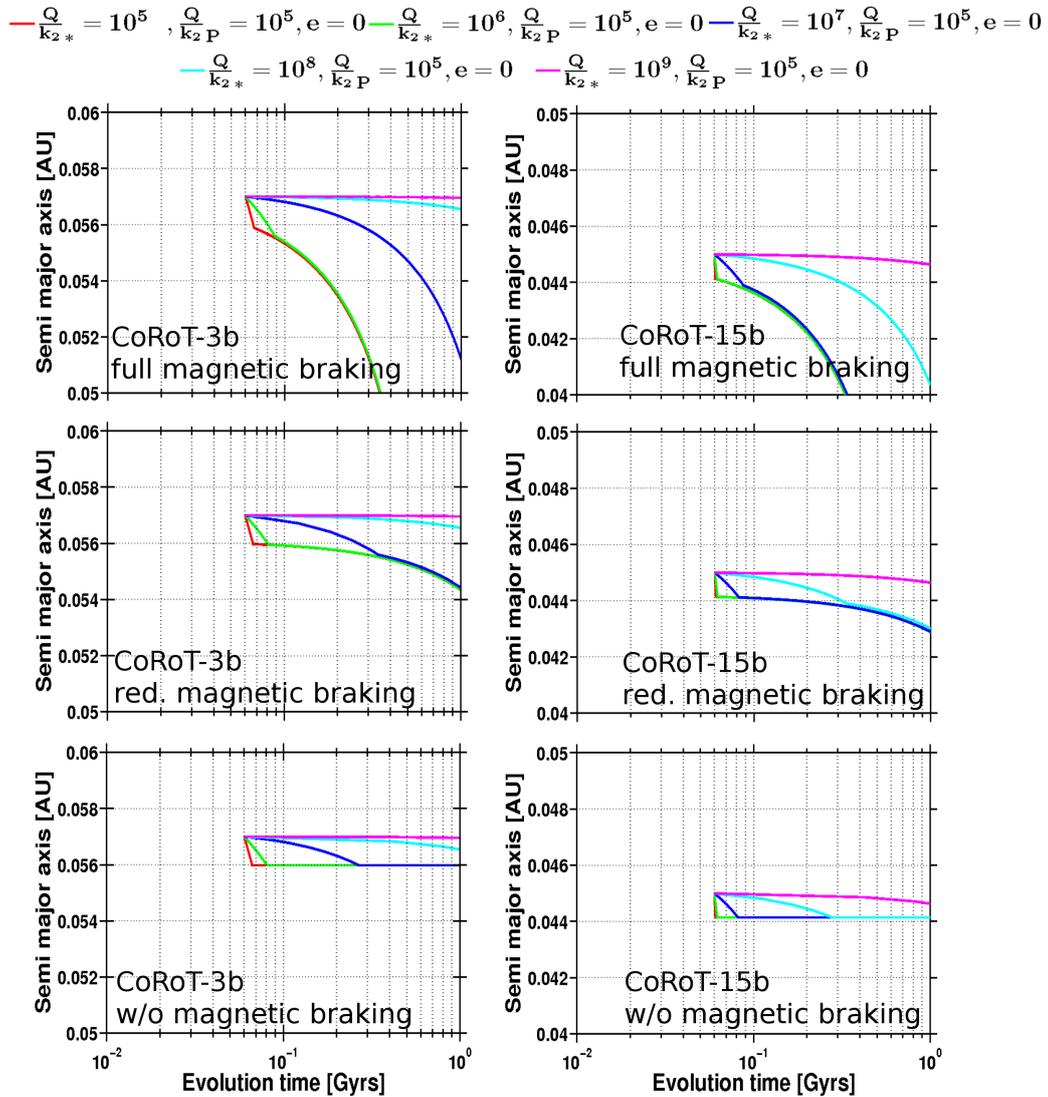
Figure 8.9: Close-up of the tidal evolution of the semi major axis of the Brown Dwarfs CoRoT-3b, and -15b for the next one billion years and for $\frac{Q_*}{k_{2,*}} = 10^5 - 10^9$.
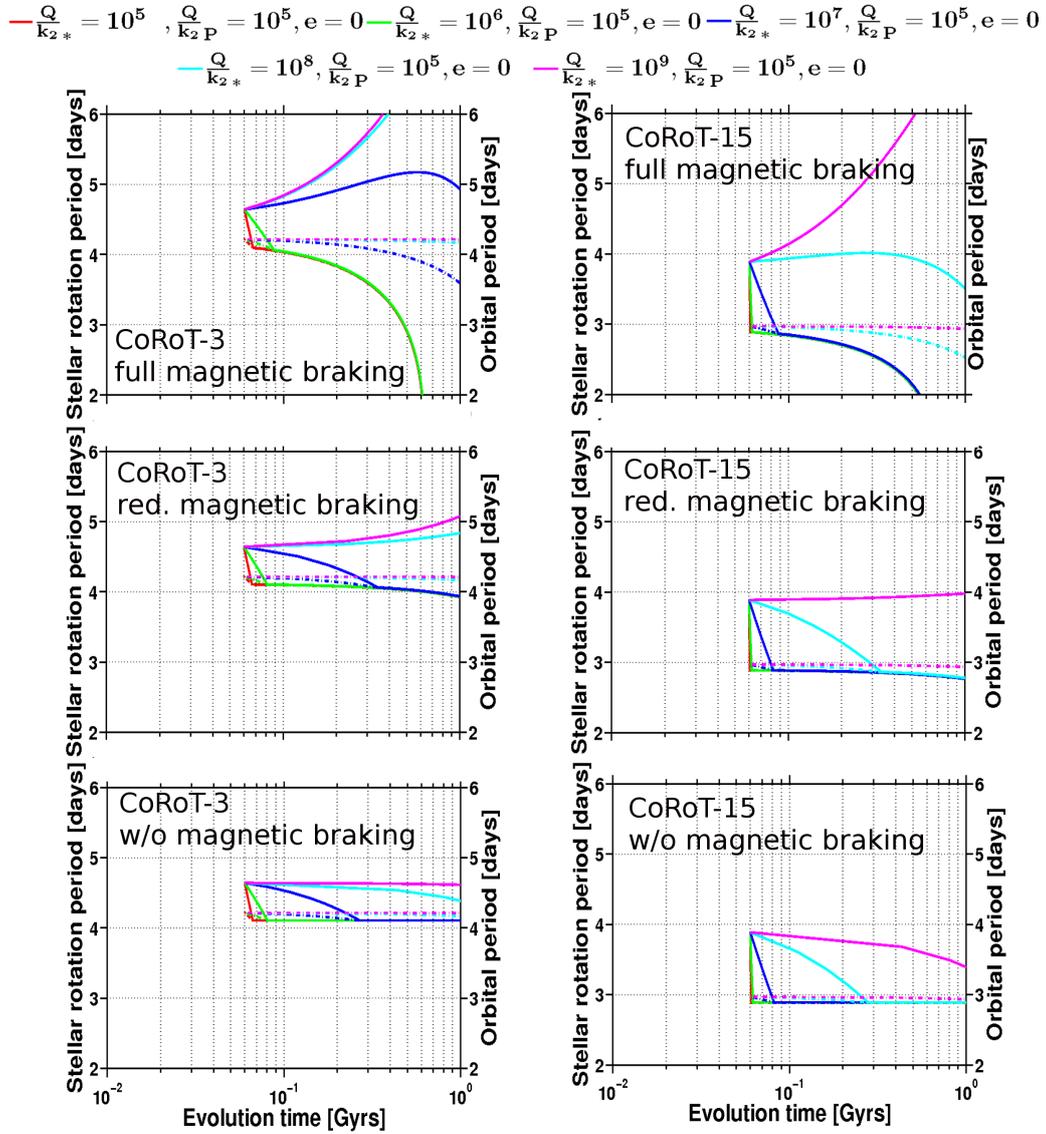
Figure 8.10: Close-up of the tidal evolution of the stellar rotation of CoRoT-3, and -15 for the next one billion years and for $\frac{Q_*}{k_{2,*}} = 10^5 - 10^9$ (solid lines) with full, reduced and without magnetic braking. The dashed-dotted lines show the evolution of the orbital period of the corresponding close-in planet for comparison.

The CoRoT-3 system, full magnetic braking

With full magnetic braking, the CoRoT-3-system will not reach the double synchronous state if $\frac{Q_*}{k_{2,*}} \geq 10^8$, although the system is near the double synchronous $\Omega_* = n$ state and although the system in principle fulfills the energy and angular momentum criteria for a stable double synchronous state. But magnetic braking is stronger than tidal friction and slows the stellar rotation efficiently away from the near-double synchronous state. For $\frac{Q_*}{k_{2,*}} = 10^8$, tidal friction appears to catch up in strength with magnetic braking after several billion years and begins to dominate the stellar rotation and semi major axis evolution. But even then it will not come near the double synchronous state at the end of the evolution time, that is, after 15 billion years. If $\frac{Q_*}{k_{2,*}} = 10^7$, tidal friction will 'win' after two billion years and force the system in double synchronous rotation. After that, the system will continue to lose angular momentum due to magnetic braking. As a consequence, the double synchronous orbit will decay and will even reach the Roche limit very quickly one hundred million years later. In principle, the orbit is already on its way towards the Roche limit when stellar rotation catches up with the planet's revolution rate.

If $\frac{Q_*}{k_{2,*}} \leq 10^6$, the double synchronous state will be reached within the next few ten million years. After that, the double synchronous orbit will decay. As shown in the section above, once inside the double synchronous state, the decay will not depend on $\frac{Q_*}{k_{2,*}}$ but only on the strength of magnetic braking and the revolution rate of the double synchronous orbit n_{doub}. Because the double synchronous revolution rate that is reached for $\frac{Q_*}{k_{2,*}} = 10^5$ and $\frac{Q_*}{k_{2,*}} = 10^6$ is almost the same, the further evolution is virtually the same for both $\frac{Q_*}{k_{2,*}}$-values.

The CoRoT-3 system, reduced magnetic braking

With reduced magnetic braking, the system will reach the double synchronous state already after a few hundred million years for $\frac{Q_*}{k_{2,*}} \leq 10^7$. The evolution of this double synchronous state is same for very $\frac{Q_*}{k_{2,*}} \leq 10^7$. Consequently, the decay of the double synchronous orbit will be identical. The decay will take, however, longer than for full magnetic braking. The orbit will reach the Roche zone after ca. six billion years. For $\frac{Q_*}{k_{2,*}} \geq 10^8$, even for reduced magnetic braking, tidal friction is still not strong enough to force the system into corotation.

The CoRoT-3 system, no magnetic braking

In the absence of magnetic braking, the orbit will not decrease any further once the double synchronous state is reached (Figure 8.11). That will happen within the next ten million years if $\frac{Q_*}{k_{2,*}} = 10^5$, the next twenty million years if $\frac{Q_*}{k_{2,*}} = 10^6$, within the next two hundred million years if $\frac{Q_*}{k_{2,*}} = 10^7$ and ca. after two billion years if $\frac{Q_*}{k_{2,*}} = 10^8$. Even for $\frac{Q_*}{k_{2,*}} = 10^9$ the system may gradually evolve towards the double synchronous state over billions of years, but not quite reach it after 15 billion years.

The CoRoT-15 system, full magnetic braking

The CoRoT-15 system will evolve into a double synchronous state within the next few ten million years if $\frac{Q_*}{k_{2,*}} \leq 10^7$ in the presence of full magnetic braking. Even for $\frac{Q_*}{k_{2,*}} = 10^8$ the system will be in double synchronous rotation after two billion years. For $\frac{Q_*}{k_{2,*}} = 10^9$, tidal friction will have compensated magnetic braking after three billion years and spin-up the star. The system will not reach the double synchronous state, however, within the evolution time of 15 billion years.
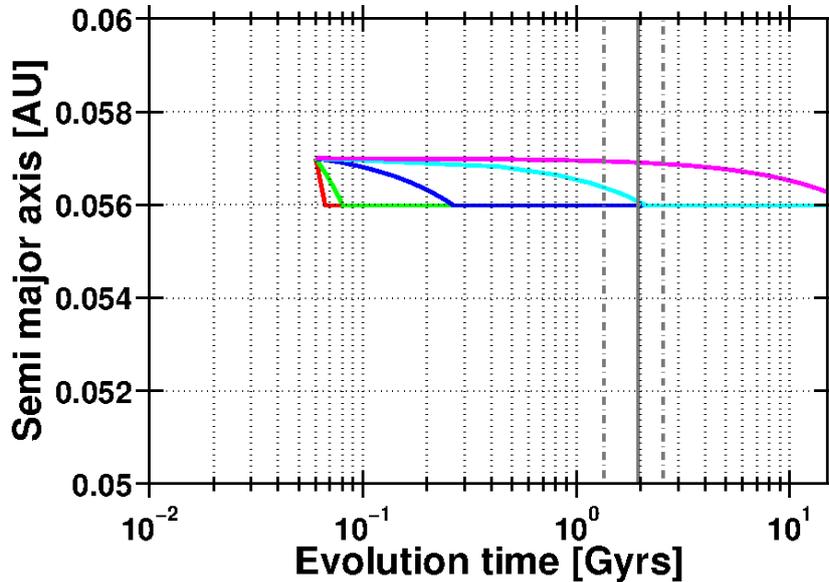
Figure 8.11: Close-up of the tidal evolution of the semi major axis of the Brown Dwarfs CoRoT-3b for the next 15 billion years and $\frac{Q_*}{k_{2,*}} = 10^5 - 10^9$. Vertical lines denote the minimum, average and maximum remaining lifetime.

The CoRoT-15 system, reduced magnetic braking

In the presence of reduced magnetic braking the system will still evolve very fast (within the next few ten million years) towards the double synchronous state if $\frac{Q_*}{k_{2,*}} \leq 10^7$. For $\frac{Q_*}{k_{2,*}} = 10^8$, the system will be caught within the next few hundred million years in a double synchronous state already. The subsequent decay of the double synchronous orbit, on the other hand, will take much longer than with full magnetic braking. The orbit may reach the Roche zone after ca. eight billion years, which is probably longer than the remaining lifetime. Indeed, within the remaining lifetime, the double synchronous orbit will only migrate moderately. If $\frac{Q_*}{k_{2,*}} = 10^9$, the system will hardly evolve. A slow evolution towards a double synchronous state can be seen after eight billion years. The system, however, will not have reached the double

synchronous state at the end of the simulation time.

The CoRoT-15 system, no magnetic braking

Without magnetic braking, the system will still evolve within a few ten million years towards the double synchronous state for $\frac{Q_*}{k_{2,*}} \leq 10^7$. Apparently, tidal friction is so efficient for these $\frac{Q_*}{k_{2,*}}$-values that magnetic braking hardly changes anything. If $\frac{Q_*}{k_{2,*}} = 10^8$, the system may be a little earlier in a double synchronous state than with reduced magnetic braking. The difference is, however, negligible. If $\frac{Q_*}{k_{2,*}} = 10^9$, the system may reach the double synchronous state as well and even within the remaining lifetime of the star. Once the system is in double synchronous rotation, it will stay there and will not evolve further. As was shown in Section 2.9, the double synchronous state is stable if the angular and energy criteria are fulfilled.

Summary of the results of the CoRoT-3 and CoRoT-15 evolution

The lessons learned from these scenarios are:

a Only relatively massive substellar companions i.e. Brown Dwarfs on close orbit are capable to spin-up the star sufficiently within the remaining lifetime of the star to achieve a double synchronous state from state $\Omega_* < n$.

b To achieve a double synchronous state within the remaining lifetime $\frac{Q_*}{k_{2,*}} \leq 10^7$ for the CoRoT-3 system, and $\frac{Q_*}{k_{2,*}} \leq 10^8$ for the CoRoT-15 system is required.

c If the system has been forced by tidal friction into a double synchronous state, the double synchronous orbit will decay in the presence of magnetic braking, in any case, and may even reach the Roche limit within the remaining lifetime for full magnetic braking.

d The orbital decay may take several billion years for reduced magnetic braking, which is, however, too long to lead to significant decay within the remaining stellar lifetime. Therefore, the double synchronous orbits of CoRoT-3b and CoRoT-15b can be regarded as stable in the reduced magnetic braking scenario.

e Without magnetic braking, a double synchronous system will be stable and the planet will be 'safe' from migrating towards the star. Furthermore, a rather massive companion ($M_{Pl} \approx 60 M_{Jup}$) like CoRoT-15b will evolve within the remaining stellar lifetime into a double synchronous state for every $\frac{Q_*}{k_{2,*}} = 10^5 - 10^9$.

f In any case, a double synchronous orbit is more stable than the 'normal' non-synchronous orbit if $\frac{Q_*}{k_{2,*}} \leq 10^6$. Even in the presence of full magnetic braking, the decay rate of the double synchronous orbit is much smaller than the decay rate of the non-synchronous planetary orbit if $\frac{Q_*}{k_{2,*}} \leq 10^6$.

8.4.1 Why will CoRoT-20 not be able to maintain a stable double synchronous state?

In section 2.9, the CoRoT-20 system was identified as one of three systems that may end up in a stable double synchronous state configuration. Its tidal evolution was already investigated in Sections 5.2 and 6.2 as an example of a potentially unstable system where the planet may reach the Roche zone within the lifetime of the start. Figures C.6 and C.7 suggest that for $\frac{Q_*}{k_{2,*}} = 10^5$ and $\frac{Q_{Pl}}{k_{2,Pl}} \geq 10^5$, the CoRoT-20 system may come very close to $\Omega_* = n$ at an evolution time of 90 million years for a very brief time. Still, it can safely be concluded that the system never settles at a double synchronous orbit.

Decay of total angular momentum by magnetic braking

This can be explained by looking in more detail into the angular momentum evolution. The system's total angular momentum currently exceeds the critical value, but only barely (Figure 8.1).

The critical total angular momentum, $L_{tot,crit}$, for the CoRoT-20 system is:

$$L_{tot,crit} = 4 \left[\frac{G^2}{27} \left(I_* M_* R_*^2 + I_{Pl} M_P R_{Pl}^2 \right) \frac{M_*^3 M_{Pl}^3}{M_* + M_{Pl}} \right]^{1/4}$$
$$= 9.74 \times 10^{42} \text{kg} \frac{\text{m}^2}{\text{s}}. \tag{8.4.1}$$

Currently, the total angular momentum, L_{tot} of the CoRoT-30 system is the sum of the orbital angular momentum and the angular momenta of the rotation of CoRoT-20 and CoRoT-20b:

$$L_{tot} = L_{orb} + L_{rot,Pl} + L_{rot,*}$$
$$= \frac{M_{Pl} M_*}{M_{Pl} M_*} n^2 a \sqrt{1 - e^2} + M_{Pl} \cdot R_{Pl}^2 \cdot I_{Pl} \Omega_{Pl} + M_* + R_*^2 * I_* \Omega_*$$
$$= \left[9.5 \times 10^{42} + 1.5 \times 10^{38} + 5.05 \times 10^{41} \right] \text{kg} \frac{\text{m}^2}{\text{s}}$$
$$= 1 \times 10^{43} \text{kg} \frac{\text{m}^2}{\text{s}} \tag{8.4.2}$$

It was confirmed again that, even for rather massive exoplanets, the angular momentum of the planet's rotation is negligible. More importantly is the following result: The total angular momentum of the CoRoT-20 system is only slightly larger than the critical total angular momentum to begin with.

In the next few billion years, the system loses angular momentum by magnetic

braking. The angular momentum loss rate is currently (Section 2.10):

$$\frac{\mathrm{d}J}{\mathrm{d}t} = -K\Omega_*^3 \left(\frac{R_*}{R_{Sun}}\right)^{1/2} \left(\frac{M_*}{M_{Sun}}\right)^{-1/2}$$
$$= -7.23 \times 10^{24} kg \frac{m^2}{s^2}. \tag{8.4.3}$$

This value can be used to roughly estimate the angular momentum loss in the next one billion years by assuming that $\frac{\mathrm{d}J}{\mathrm{d}t}$ is more or less constant over this time period $\Delta t = 1$ Gyrs:

$$\Delta J = \frac{\mathrm{d}J}{\mathrm{d}t} \times \Delta t$$
$$= -2.3 \times 10^{41} \mathrm{kg} \frac{m^2}{s}. \tag{8.4.4}$$

As can be seen, when subtracting ΔJ from L_{tot}, the system has already lost so much angular momentum after one billion years that $L_{tot} \approx L_{tot,crit}$. Because the star continues to lose angular momentum, the system is expected to have a total angular momentum L_{tot} smaller than $L_{tot,crit}$ after more than one billion years. As *Hut* (1980) has shown, a double synchronous state is not possible in such a case. This is, however, only a quick 'back of the envelope' calculation. Figure 8.12 shows the evolution of the total angular momentum for magnetic braking and tidal friction with $\frac{Q_P}{k_{2,P}} = 10^5$ and $\frac{Q_*}{k_{2,*}} = 10^6$ as modeled in Sections 5.2 and **??**. As can be seen, the total angular momentum decreases due to magnetic braking and falls below $L_{tot,crit}$ even earlier than estimated above. After 600 hundred million years already, the total angular momentum does not exceed $L_{tot,crit}$ anymore, which is the prerequisite for a double synchronous state.
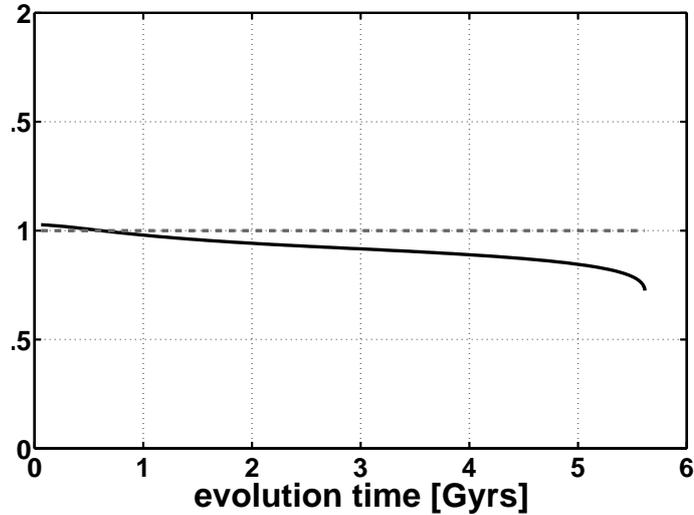
Figure 8.12: The evolution of the ratio of total angular momentum L_{tot} over critical total angular momentum $L_{tot,crit}$ for the CoRoT-20 system under tidal friction and magnetic braking with $\frac{Q_{Pl}}{k_{2,Pl}} = 10^5$ and $\frac{Q_*}{k_{2,*}} = 10^6$. The horizontal dashed line marks $L_{crit,tot}$.

Alternative evolution of the CoRoT-20 system with $P_* = 8.9$ days

In Sections 5.2 and 6.2, however, $P_* = 11.5$ days was selected as initial condition for the tidal evolution ($\Omega_* < n$). It was already stated there that the limits of uncertainties of the stellar rotation $P_* = 11.5 \pm 2.6$ days allow also for an evolution with $\Omega_* = n$, and $\Omega_* > n$.

In the following, tidal evolution tracks of the CoRoT-20 system using $P_* = 8.9$ days as initial condition are discussed, with $\frac{Q_*}{k_{2,*}} = 10^5 - 10^9$ and $\frac{Q_{Pl}}{k_{2,Pl}} = 10^4 - 10^6$ (Figures 8.13, 8.14, and 8.15). The evolution tracks were calculated using Equations (5.2.1), (5.2.2), (5.2.3), and (5.2.4) (See Section 5.2).
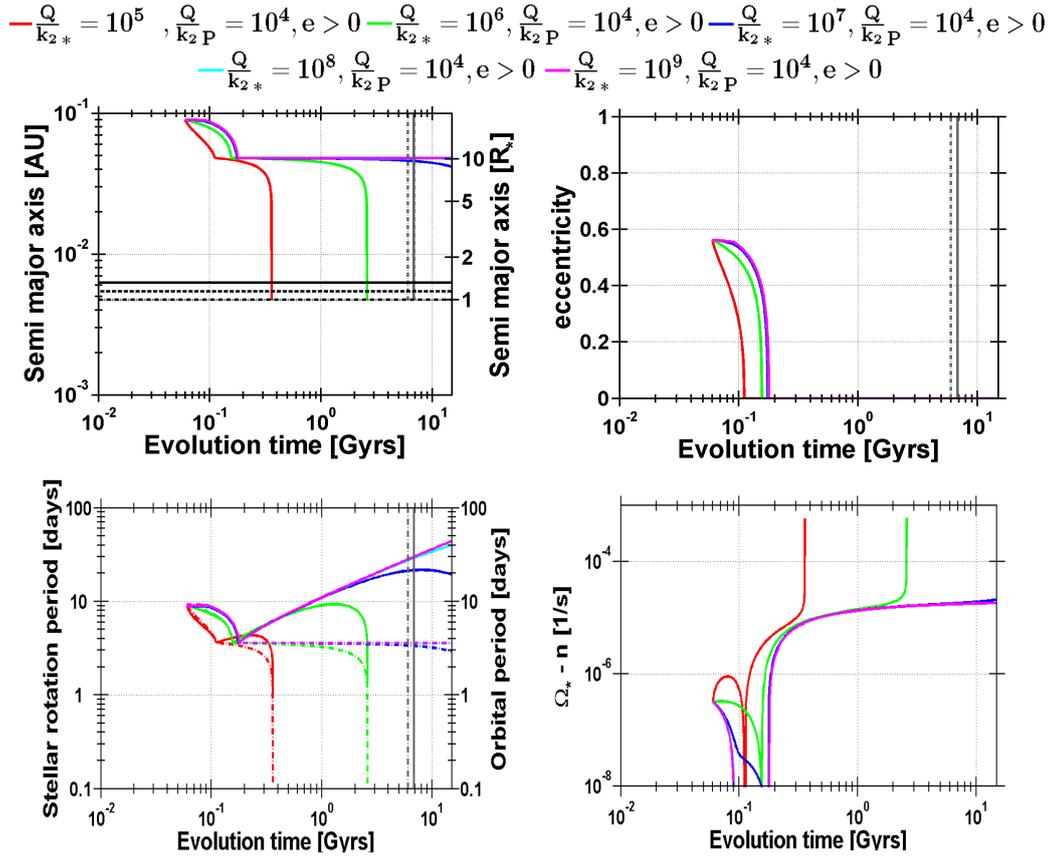
Figure 8.13: Tidal evolution of the CoRoT-20 system with $P_* = 8.9$ days as initial condition of the stellar rotation. The panels show the evolution of the semi major axis, the eccentricity, the stellar rotation (solid lines) and planetary orbital revolution period (dashed lines), and of $|\Omega_* - n|$ for $\frac{Q_*}{k_{2,*}} = 10^5 - 10^9$ and $\frac{Q_{Pl}}{k_{2,Pl}} = 10^4$. The vertical lines show the remaining stellar lifetime with limits of uncertainty.
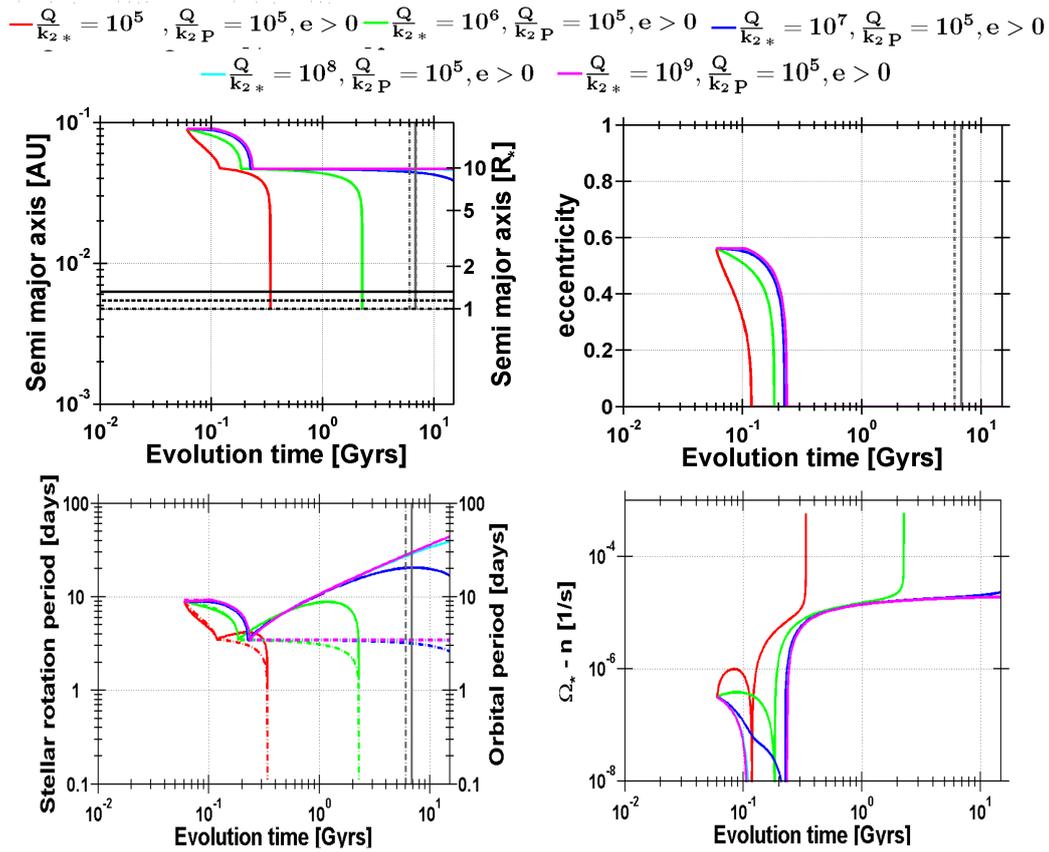
Figure 8.14: Tidal evolution of the CoRoT-20 system with $P_* = 8.9$ days as initial condition of the stellar rotation. The panels show the evolution of the semi major axis, the eccentricity, the stellar rotation (solid lines) and planetary orbital revolution period (dashed lines), and of $|\Omega_* - n|$ for $\frac{Q_*}{k_{2,*}} = 10^5 - 10^9$ and $\frac{Q_{Pl}}{k_{2,Pl}} = 10^5$. The vertical lines show the remaining stellar lifetime with limits of uncertainty.
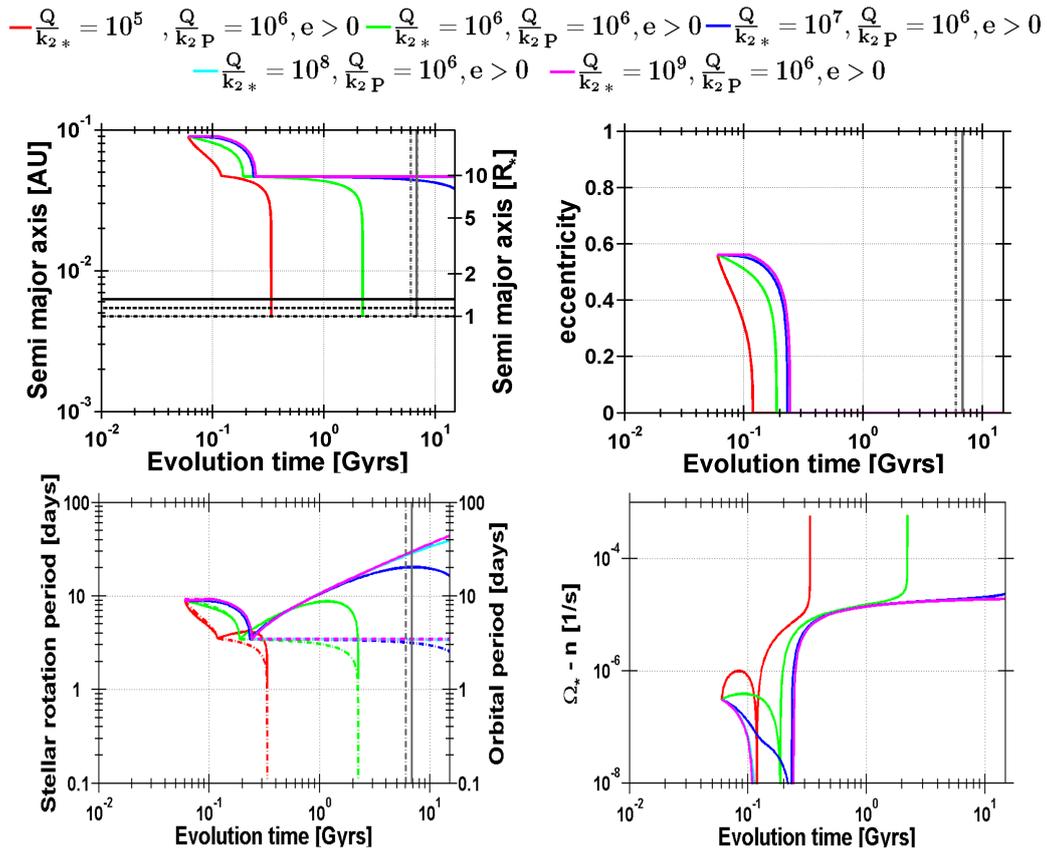
Figure 8.15: Tidal evolution of the CoRoT-20 system with $P_* = 8.9$ days as initial condition of the stellar rotation. The panels show the evolution of the semi major axis, the eccentricity, the stellar rotation (solid lines) and planetary orbital revolution period (dashed lines), and of $|\Omega_* - n|$ for $\frac{Q_*}{k_{2,*}} = 10^5 - 10^9$ and $\frac{Q_{Pl}}{k_{2,Pl}} = 10^6$. The vertical lines show the remaining stellar lifetime with limits of uncertainty.

Apparently, the tidal evolution of the CoRoT-20 system changes only slightly for different $\frac{Q_{Pl}}{k_{2,Pl}} = 10^4 - 10^6$ if $P_* = 8.9$ days is chosen as initial condition. Therefore, this tidal evolution scenario will be discussed in detail for $\frac{Q_*}{k_{2,*}} = 10^5 - 10^9$ and the average $\frac{Q_{Pl}}{k_{2,Pl}} = 10^5$, only.

The system will evolve for every $\frac{Q_*}{k_{2,*}} = 10^5 - 10^9$ and $\frac{Q_{Pl}}{k_{2,Pl}}$ into a double synchronous state within one hundred million years. This is in contrast to the evolution of CoRoT-20 described in Sections 5.2 and 6.2. There, the system reached the double synchronous state only for $\frac{Q_*}{k_{2,*}} = 10^5$ and $\frac{Q_{Pl}}{k_{2,Pl}} \geq 10^5$.

This confirms one statement from Section 8.2: It is much easier to achieve a double synchronous state $\Omega_* = n$ from an initial condition $\Omega_* > n$ (a supsynchronous orbit) than from an initial condition $\Omega_* < n$ (a subsynchronous orbit). As can be seen on detailed inspection (Figure 8.16), tidal evolution is not even necessary to achieve this state. If $\frac{Q_*}{k_{2,*}} \geq 10^7$, magnetic braking on its own moves the 'fictive' double synchronous state outwards towards the planetary orbit. Neither the semi major axis nor the eccentricity changes during this brief initial phase.

Once a state $\Omega_* = n$ is reached, apparently stellar and planetary tidal friction, even for $\frac{Q_*}{k_{2,*}} = 10^9$ and $\frac{Q_{Pl}}{k_{2,Pl}} = 10^4 - 10^6$, are sufficient to force the system into a 'true' double synchronous state. The most telling sign for the double synchronous orbit evolution is the efficient eccentricity dampening. As was described in Section 2.9, a stable double synchronous orbit is not only characterized by $\Omega_* = n$. Furthermore, the total and orbital angular momentum need to exceed $L_{tot,crit}$ and $L_{orb,crit}$, which is currently true for the CoRoT-20 system (Section 8.1). In addition, a true double synchronous orbit can not be eccentric. Indeed, the evolution tracks here show that, once the $\Omega_* = n$ is reached, the eccentricity is damped very fast within the next one
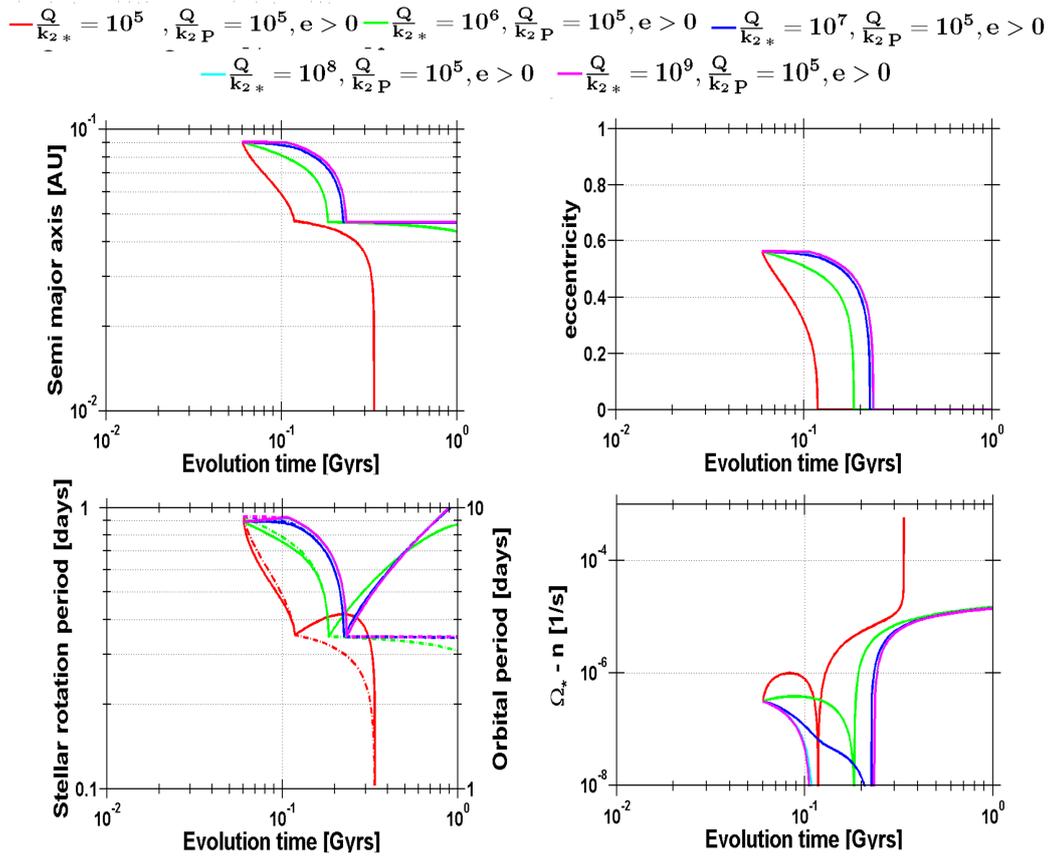
Figure 8.16: Tidal evolution of the CoRoT-20 system with $P_* = 8.9$ days as initial condition of the stellar rotation focusing on the first one billion years evolution time. The panels show the evolution of the semi major axis, the eccentricity, the stellar rotation (solid lines) and planetary orbital revolution period (dashed lines), and of $|\Omega_* - n|$ for $\frac{Q_*}{k_{2,*}} = 10^5 - 10^9$ and $\frac{Q_{Pl}}{k_{2,Pl}} = 10^5$.

hundred million years to zero for any $\frac{Q_*}{k_{2,*}} = 10^5 - 10^9$ and $\frac{Q_{Pl}}{k_{2,Pl}}$. In contrast to that, the non-synchronous evolution of the CoRoT-20 system shows that the eccentricity may never reach zero within the remaining lifetime if $\frac{Q_*}{k_{2,*}} \geq 10^8$ and $\frac{Q_{Pl}}{k_{2,Pl}}$ (Sections 5.2 and 6.2). The fast eccentricity dampening in a true double synchronous configuration shows that although $\Omega_* = n$ is in principle a possible state for the CoRoT-20 system within the limits of uncertainty, the large eccentricity of the orbit of CoRoT-20b shows that the system cannot truly be in a double synchronous state.

Furthermore, once the eccentricity is damped to zero, magnetic braking immediately decelerates the stellar rotation and stellar tidal friction on its own and is not able to compensate by spinning-up the star at the current position. Apparently, even with this favorable initial condition $P_*(initial) = 8.9$ days, the positive feedback effect between stellar and planetary tidal friction is needed to maintain a double synchronous state despite magnetic braking. This result supports the reasoning explained in Section 8.2, which leads to the condition that an upper $\frac{Q_*}{k_{2,*}}_{spinup}$ limit is required to guarantee that tidal friction can maintain a stable double synchronous orbit in the presence of magnetic braking.

Stellar tidal friction may, in principle, be able to spin up CoRoT-20 at a later point in evolution if $\frac{Q_*}{k_{2,*}} \leq 10^6$ and the planet moves towards the star. At that point, however, the system has lost so much angular momentum that the angular momentum criteria for a double synchronous state are no longer fulfilled and a double synchronous orbit is not possible. Instead, the planet will decay within the remaining lifetime. Therefore, in terms of orbital stability due to stellar and planetary tidal friction, the conclusions here are the same as in Section 5.2: $\frac{Q_*}{k_{2,*}} = 10^7 - 10^8$ is required as a stability limit to guarantee that the planet does not reach the Roche

zone within the remaining lifetime. Double synchronicity can not save the system from the decay because magnetic braking forces the system out of a possible double synchronous state. A transient double synchronicity can force, however, the orbit to become circular much earlier than under tidal evolution without reaching a double synchronous state. See also Chapter F), which confirms this 'duality' of the possible evolution tracks of the CoRoT-20 system.

8.4.2 Limits on $\frac{Q_*}{k_{2,*}}$ to currently maintain a double synchronous rotation state

As was previously shown by modeling the evolution of the CoRoT-3 and CoRoT-15 system, these two systems may already be in a double synchronous state. This depends on $\frac{Q_*}{k_{2,*}}$ and magnetic braking .

It will now be assumed that these systems are currently in the process of being forced into a double synchronous state by tidal friction. Based on this assumption, the upper limit $\frac{Q_*}{k_{2,*}}$ can be derived to achieve a double synchronous state despite magnetic braking using equation (8.2.16) (Table 8.1).

This constraint is not applicable to systems currently not affected by magnetic

System	$\frac{Q_*}{k_{2,* \; upper \; limit, rot}}$	magnetic braking
CoRoT-3	4.5×10^6	$K = 2.7 \times 10^{40}$ Nms
CoRoT-3	4.5×10^7	$K = 2.7 \times 10^{39}$ Nms
CoRoT-15	4×10^7	$K = 2.7 \times 10^{40}$ Nms
CoRoT-15	4×10^8	$K = 2.7 \times 10^{39}$ Nms
CoRoT-20[a]	8.5×10^4	$K = 2.7 \times 10^{40}$ Nms

a) applying $a_{equiv} = 0.063$ AU to Eq. 8.2.16.

Table 8.1: Required $\frac{Q_*}{k_{2,*}}$ for tidal friction to compensate magnetic braking at the planet's current position.

braking. Furthermore, it doesn't necessarily require that the system evolves into a double synchronous state within the remaining stellar lifetime. This yields $\frac{Q_*}{k_{2,*}} \leq$ 4.5×10^7 for CoRoT-3 and reduced magnetic braking and $\frac{Q_*}{k_{2,*}} \leq 4 \times 10^8$ for CoRoT-15 and reduced magnetic braking. After all, for CoRoT exoplanet host stars of spectral type F, reduced magnetic braking appears to be a reasonable assumption (Sections 6.1.2, and Chapter 7).

If it is further assumed that the orbits of CoRoT-3b and CoRoT-15b have evolved into this approximately double synchronous state by tidal friction, another much stronger constraint on $\frac{Q_*}{k_{2,*}}$ can be put that does not depend on magnetic braking. For this purpose, a minimal orbit variation in the past into the double synchronous state is assumed. This approach is similar to the work done by *Dermott* (1979*b*) who derived a constant on $\frac{Q_{Jup}}{k_{2,Jup}}$ of Jupiter by requiring that the orbits of the Galilean moons evolved into the Laplace resonances by tidal migration (See Section 2.8.1).

Using equation 2.6.21 and solving for $\frac{Q_*}{k_{2,*}}$ yields the following upper limit that needs to be fulfilled to allow for orbital migration:

$$\frac{Q_*}{k_{2,*}} = \frac{\frac{39}{2} \left(\frac{G}{M_*}\right)^{1/2} R_*^5 M_{Pl}}{a_0^{13/2} \left[\left| 1 - \left(\frac{a_i}{a_0}\right)^{13/2} \right| \right]} \Delta t. \tag{8.4.5}$$

Here, a_0 is the current semi major axis and a_i is the primordial semi major axis from which the planet originated. The upper limit is derived by setting $a_i = a_0 \pm \Delta a$, where Δa is set to $5\% \, a_0$ and $10\% \, a_0$, respectively, to allow for at least small variation of the semi major axis in the past. The results are listed in Table 8.2. $\frac{Q_*}{k_{2,*}} \leq 1 \times 10^7$ is required for CoRoT-3, and $\frac{Q_*}{k_{2,*}} \leq 1 \times 10^8$ is required for CoRoT-15 to allow for tidal evolution.

System	$\frac{Q_*}{k_{2,*}}$ upper limit,a	a_i/a_0
CoRoT-3	$4 \pm 1 \times 10^7$	0.95
CoRoT-3	$3.1 \pm 0.8 \times 10^7$	1.05
CoRoT-3	$2.3 \pm 0.7 \times 10^7$	0.9
CoRoT-3	$1.4^{+0.3}_{-0.5} \times 10^7$	1.1
CoRoT-15	$4.2 \pm 2.0 \times 10^8$	0.95
CoRoT-15	$3.2 \pm 1.6 \times 10^8$	1.05
CoRoT-15	$2.4 \pm 1.2 \times 10^8$	0.9
CoRoT-15	$1.4^{+0.7}_{-4.4} \times 10^8$	1.1

Table 8.2: Required $\frac{Q_*}{k_{2,*}}$ for tidal friction to allow for minimal migration in the past.

As can be seen, when comparing results from Tables 8.2 and 8.1, the same upper limit of $\frac{Q_*}{k_{2,*}}$ is derived from requiring stellar spin-up in the presence of reduced magnetic braking and from requiring orbital migration into a double synchronous state: $\frac{Q_*}{k_{2,*}}$ in the order of 10^7 for CoRoT-3 and $\frac{Q_*}{k_{2,*}}$ in the order of 10^8 for CoRoT-15. When excluding full magnetic braking for the stars CoRoT-3 and CoRoT-15 and favoring $\frac{Q_*}{k_{2,*}} \leq 10^7$, the double synchronous orbit further remains stable in the remaining stellar lifetime. The possible decay outlined in the previous section only takes place after several billion years and takes much longer than the remaining lifetime.

It is interesting to note that to establish double synchronicity relatively small $\frac{Q_*}{k_{2,*}} \leq 10^7 - 10^8$ are favored, whereas the orbital stability limit and tidal spin up limit from Sections 5 and 6 require $\frac{Q_*}{k_{2,*}} \geq 10^7 - 10^8$.

As was shown in Section 3.1, when a system approaches a double synchronous state, i.e., if the tidal frequency $\omega = 2|\Omega_* - n| \to 0$, it is expected that $Q_* \to \infty$. Instead, the exact opposite is seen. This may be explained by suggesting that the weak friction case is no longer valid. Instead, dynamical tides are at work because, on its way to synchronicity, the tidal frequency has a higher chance to meet stellar

eigenfrequencies. Dynamical tides dissipate tidal energy more efficiently (*Zahn*, 1977), reducing Q_*. Therefore, dynamical tides can easily and consistently explain why $\frac{Q_*}{k_{2,*}}$ apparently becomes smaller instead of larger when $\omega \to 0$.

Chapter 9

Summary and Discussion

The investigation of tidal friction due to tides raised on the star by the planet (stellar tidal friction) and due to tides raised by the star on the planet (planetary tidal friction), may be used to constrain $\frac{Q_*}{k_{2,*}}$ for main sequence stars and different scenarios. In this work, CoRoT planetary systems with close-in Jupiter-mass planets around slowly rotating and fast rotating stars, short-period Jupiter-mass exoplanets on circular and eccentric orbits, short-period brown dwarfs near double synchronous states and a low-mass Super-Earth planet were investigated.

It was found that the majority of the CoRoT planets may migrate towards the star (because $\Omega_* < n$) and be destroyed within the Roche zone if $\frac{Q_*}{k_{2,*}} \leq 10^6$. For $\frac{Q_*}{k_{2,*}} = 10^5$, many planets - including the Super-Earth CoRoT-7b - would reach the Roche zone even within one hundred million years, which is only circa 1% of the total lifetime of a main sequence star. The planets would be destroyed 'in the blink of an eye' on astronomical time scales, making it statistically improbable to find them.

In contrast to that, such planetary systems are ubiquitous and frequently found, as the distribution of the so far discovered exoplanets' semi major axes shows (Section 1.5). Furthermore, the fact that such systems are frequently discovered by transit

surveys, like the CoRoT space mission, proves that such close-in massive planets are not rare. After all, transiting planets represent only $\approx 5-10\%$ of all planetary systems due to the strong observation bias regarding the orbital plane, limiting the detection to planetary systems whose orbital plane is parallel to the line-of-sight (Section 1.3.2).

The detection of Kepler-10b, the second transiting terrestrial planet after CoRoT-7b, shows that even short-period Super-Earths are probably not rare objects and should survive over timescales of billion years. Kepler-10b (*Batalha et al.*, 2011) and CoRoT-7b (Table A.1) are very similar in planetary parameters, except for the age: Kepler-10b is a ten billion years older version of CoRoT-7b. This suggests that such planets should survive over the timescales of several billion years.

With this reasoning, $\frac{Q_*}{k_{2,*}}_{stable} = 10^7 - 10^8$ can be derived as the common lower orbital stability limit. Indeed, this result is consistent with the $\frac{Q_*}{k_{2,*}}$ constraint derived by *Pätzold and Rauer* (2002) ($\frac{Q_*}{k_{2,*}} \geq 10^8$), *Rasio et al.* (1996) ($\frac{Q_*}{k_{2,*}} = 4 \times 10^8$), and *Carone and Pätzold* (2007) ($\frac{Q_*}{k_{2,*}} \geq 3 \times 10^7$), but contradicts the $\frac{Q_*}{k_{2,*}}$- values favored by *Jackson et al.* (2008) ($\frac{Q_*}{k_{2,*}} = 10^{5.5}$), *Dobbs-Dixon et al.* (2004) ($\frac{Q_*}{k_{2,*}} = 10^5 - 10^6$), and *Lin et al.* (1996)($\frac{Q_*}{k_{2,*}} = 10^5$).

Another, independent argument against $\frac{Q_*}{k_{2,*}} \leq 10^6$ and in favor of $\frac{Q_*}{k_{2,*}} \geq 10^7 - 10^8$ can be derived from the stellar rotation evolution. If a planet migrates towards the Roche zone, conservation of angular momentum leads to efficient stellar spin-up compensating even strong magnetic braking in low-mass main sequence stars. The stellar rotation period versus age distribution of the CoRoT planet host stars (Figures 6.8 and 6.9) shows the expected behavior for stars whose rotation is decelerated by magnetic braking with increasing age, except for CoRoT-17. **Therefore, a tidal spin-up constraint for $\frac{Q_*}{k_{2,*}}$ is derived by requiring tidal friction to be weaker than**

magnetic braking at the current position, which yields $\frac{Q_*}{k_{2,*}}$ₛₚᵢₙ₋ᵤₚ $> 10^6$, and agrees nicely with the orbital stability limit.

CoRoT-17, on the other hand, is the one star that seems to be rotating faster than its age suggests (Figure 6.8, $P_* = 18 \pm 2$ days at an age of 10.7 billion years). The star does not show, however, the fast tidal spin-up expected for stars whose planets enter the Roche zone. This would require rotation periods in the order of $1 - 10$ days (Section 6). The star appears rather to be moderately spun-up at the end of its lifetime. It was shown in Section 6 that old stars are susceptible to being spun up by comparatively large $\frac{Q_*}{k_{2,*}} = 10^7$. **Indeed, the tidal $\frac{Q_*}{k_{2,*}\,\text{spin-up}}$ limit at the position of CoRoT-17b requires $\frac{Q_*}{k_{2,*}} \approx 4 \times 10^7$ to account for the current moderate spin-up despite magnetic braking.** This still agrees with the previously derived orbital stability and stellar spin up limit on $\frac{Q_*}{k_{2,*}}$ by excluding $\frac{Q_*}{k_{2,*}} = 10^5 - 10^6$. **But to allow for tidal spin-up, $\frac{Q_*}{k_{2,*}}$ has to be smaller than 10^9 for CoRoT-17. Otherwise no tidal evolution would occur.**

$\frac{Q_*}{k_{2,*}} \approx 10^7$ would allow for long-term stability of short-period Jupiter mass planets, allow for moderate tidal spin-up of old stars, but would not allow for long-term stability of short-period brown dwarfs as can be seen by inspecting Eq. 5.1.2. This stability threshold is proportional to M_{Pl}. If Jupiter mass planets require $\frac{Q_*}{k_{2,*}} \geq 10^7$ for long-term stability, brown dwarfs with masses $M_{Pl} \geq 10 M_{Jup}$ require $\frac{Q_*}{k_{2,*}} \geq 10^8$ on similar orbits. Indeed, in Section 1.5 an erosional feature may be present, which warrants additional investigation. This is, however, not within the scope of this work.

The possible erosion of short-period brown dwarfs and Jupiter mass planets and the corresponding possible tidal spin-up of stars should be taken into account before

trying to derive the age of a star by Gyrochronology. Otherwise, this age determination method may yield an age too small. Old stars towards the end of their lifetime, like CoRoT-17, are particularly susceptible for tidal spin-up. Even stars that don't currently have a close-in companion may have been tidally spun-up in the past when the corresponding companion has migrated towards the Roche zone and has been destroyed there. Interestingly, abnormally fast rotating stars are not unknown. So-called 'blue stragglers' are reported, for example, by *Fuhrmann et al.* (2011) who identified a F6V star whose rotation is spun-up through interaction with an unseen $0.42\,M_{Sun}$ companion.

Another interesting scenario in terms of tidal interactions are presented by CoRoT planets on eccentric orbits. It was shown that for moderate to small orbital eccentricity $e \leq 0.3$, represented by CoRoT-16b, planetary tidal friction with $\frac{Q_{Pl}}{k_{2,Pl}} = 10^4 - 10^6$ (taken from the gas giants in our Solar System), acts on much shorter timescales than stellar tidal friction. Planetary tidal friction, in this case, leads to eccentricity dampening within one billion years conserving the orbital angular momentum. **Therefore, the secular stability of short-period planets with $e \leq 0.3$ can be evaluated with the same equations derived for circular orbits but using $a_{equiv} = a(1 - e^2)$, assuming $\frac{Q_{Pl}}{k_{2,Pl}} \leq 10^6$.** The efficient eccentricity dampening by planetary tidal friction explains the fact that most close-in extrasolar planets have circular orbits. That the orbit of CoRoT-16b, with an age of about six billion years, is still quite eccentric suggests that the orbit was even more eccentric in the past. This warrants additional investigation that is, however, not within the scope of this work.

It was found that a_{equiv} can not be used for planets like CoRoT-10b and CoRoT-20b. **For $e \geq 0.5$, planetary and stellar tidal friction may act on the same time scales, if $\frac{Q_*}{k_{2,*}} = 10^5 - 10^6$ and $\frac{Q_{Pl}}{k_{2,Pl}} = 10^4 - 10^6$. This would lead to a positive feedback effect, decreasing the semi major axis/spinning up the star much stronger than stellar and planetary tidal friction would on their own. This feedback effect may even destabilize planets that would otherwise be stable under tidal friction or may force systems into double synchronous rotation that can not be maintained by stellar tidal friction alone. To avoid such effects, $\frac{Q_*}{k_{2,*}}$ has to be again larger than 10^6.**

Another interesting tidal interaction scenario is presented by the CoRoT-11 system: A short-period Jupiter-mass planet around a fast-spinning F-star. Here, the tidal evolution depends not only on $\frac{Q_*}{k_{2,*}}$ but also on magnetic braking efficiency.

- Scenario 1: The star is braked down efficiently by magnetic braking similar in strength than for lower mass stars $M_* < 1.1 M_{Sun}$.

  Regardless of the strength of stellar tidal friction, the planetary system CoRoT-11 will become within a few hundred million years a 'normal' planetary system with a close-in exoplanet around a slowly rotating star. In this case, the orbital stability limit $\frac{Q_*}{k_{2,*}} = 10^7 - 10^8$ is again required to keep the planet CoRoT-11b from reaching the Roche zone within the remaining lifetime.

- Scenario 2: The star is braked down by reduced magnetic braking that is ten times less efficient than in scenario 1.

  The rotation of CoRoT-11 is still braked down relatively fast within one billion years, until a state is reached where again $\Omega_* < n$ and the planet may migrate towards the star again. The planet will not reach the Roche zone within the

remaining lifetime if $\frac{Q_*}{k_{2,*}} \geq 10^7$. Interestingly, the same may be true for $\frac{Q_*}{k_{2,*}} = 10^5$ due to a fast initial outward migration phase.

- Scenario 3: The star is not slowed down by magnetic braking.

  CoRoT-11b may migrate away from the star, if $\frac{Q_*}{k_{2,*}} \leq 10^7$. The stellar rotation period of CoRoT-11 is tidally spun-down by less than one day even if $\frac{Q_*}{k_{2,*}} = 10^5$ which is negligible.

Only in the absence of magnetic braking can stars like CoRoT-11 maintain their fast rotation over secular timescales. CoRoT-11 itself, however, is relatively young (age=2 ± 1 billion years). The distribution of stellar rotation period versus age for CoRoT stars of spectral type F(Figure 6.9) seems to indicate a reduced magnetic braking mechanism. **If spectral type F-stars are indeed subjected to at least moderate magnetic braking, then the following predication can be made: Only young stars can rotate faster than their close-in Jupiter mass planet revolves around it, because magnetic will decelerate the star within one billion years. Therefore, the fast stellar rotation is only a transient state. In the long run, such systems still require $\frac{Q_*}{k_{2,*}}_{stable} \geq 10^7$ for long-term stability.**

Finally, several possible double synchronous states were identified in the CoRoT subsample and their evolution was investigated:

- Of all investigated CoRoT planetary systems CoRoT-3, CoRoT-6, CoRoT-9, CoRoT-10, CoRoT-15, and CoRoT-20 currently satisfy the angular momenta conditions to achieve a double synchronous state $\Omega_* - n$ described by *Hut* (1980).

- The CoRoT-4 system is a 'false' double synchronous state because it does not

satisfy the angular momentum criteria by *Hut* (1980).

- CoRoT-9b and CoRoT-6b are currently too far away from their stars, however, to establish synchronization within the remaining stellar lifetime.

- Due to the large orbital eccentricity, the CoRoT-20 system can not currently be in double synchronous rotation; even though the limits of uncertainties for the stellar rotation allow in principle $\Omega_* = n$.

- CoRoT-20 may, however, reach a double synchronous state due the positive feedback effect between planetary and tidal friction because the orbital eccentricity is very large. If this happens, then the eccentricity is damped to zero within a few hundred million years. When the eccentricity has become zero and planetary tidal friction seizes to act on the system, stellar tidal friction on its own will not be able to compensate magnetic braking for any $\frac{Q_*}{k_{2,*}} = 10^5 - 10^9$ and the double synchronous orbit can not be maintained.

- In addition, magnetic braking will remove so much angular momentum from the CoRoT-20 system within the next one billion years, that the system will no longer meet all the angular momenta requirements to establish a double synchronous state (*Hut*, 1981).

- CoRoT-3 and CoRoT-15 may be systems that are evolving into 'true' double synchronous states.

- In the presence of magnetic braking, a double synchronous orbit will decay. In other words, the planet may still migrate towards the star and the stellar rotation will be 'dragged' along.

- A mathematical formulation was derived that describes that decay. Once tidal friction has forced the system into corotation, the subsequent decay of the double synchronous orbit does not depend on $\frac{Q_*}{k_{2,*}}$ but on the efficiency of magnetic braking.

- If CoRoT-3 and CoRoT-15 experience efficient magnetic braking like spectral type G-stars, the double synchronous orbit will decay and the brown dwarfs may even reach the Roche limit within the remaining lifetime.

- If CoRoT-3 and CoRoT-15 experience reduced magnetic braking or no magnetic braking at all, the double synchronous states are stable within the remaining lifetime.

This leads to the following prediction: **Only F-stars are capable to maintain a double synchronous state over secular timescales with a close-in massive planetary companion. In addition, it was found that in order to maintain a double synchronous state despite magnetic braking, the following constraints can be derived for $\frac{Q_*}{k_{2,*}}$: $\frac{Q_*}{k_{2,*}} \leq 10^7$ for CoRoT-3, and $\frac{Q_*}{k_{2,*}} \leq 10^8$ for CoRoT-15. If it is further required that CoRoT-3b and CoRoT-15b migrated towards the double synchronous orbit, again, $\frac{Q_*}{k_{2,*}} \leq 10^7$ for CoRoT-3, and $\frac{Q_*}{k_{2,*}} \leq 10^8$ for CoRoT-15 is derived when allowing for a 10% change in the semi major axis.**

The $\frac{Q_*}{k_{2,*}}$-values required to force the CoRoT-3 and CoRoT-15 system into a double synchronous state ($\frac{Q_*}{k_{2,*}} \leq 10^7 - 10^8$) barely overlap with the $\frac{Q_*}{k_{2,*}}$-values required for orbital stability in non-synchronous systems ($\frac{Q_*}{k_{2,*}} \geq 10^7 - 10^8$).

For double synchronous systems, the tidal frequency $\omega = |2\Omega_* - n| \approx 0$ is orders

of magnitude smaller than the tidal frequency in non-synchronous systems where $\omega = 2|\Omega_* - n| \approx 2n$ which is in the order of $10^{-3} - 10^{-5}$ 1/s.

In the weak friction assumption that is used in this work, Q_* is related to the tidal frequency by

$$Q_* = \frac{|\omega_0^2 - \omega^2|}{\omega/\tau_d},\tag{9.0.1}$$

where the resonance frequency ω_0 and the damping timescale τ_d are constants. Therefore, $\frac{Q_*}{k_{2,*}}$ is expected to grow as $\omega \to 0$. This is, however, not the result that is derived here. $\frac{Q_*}{k_{2,*}}$ for double synchronous states ($\omega \to 0$) equals or is even smaller than the values derived for the non-synchronous states.

This contradiction can be solved by suggesting that dynamical tides are at work in double synchronous cases because the tidal frequency meets stellar eigenfrequencies as $2|\Omega_* - n| \to 0$. This leads in turn to an increase in tidal energy dissipation and to a reduction of Q_*. The work by *Penev and Sasselov* (2011) supports this conclusion: *'the time variable tidal perturbation can resonantly excite inertial waves in the star, thus resulting in several orders of magnitude larger shear, and hence dissipation, compared to the static tide'*.

Indeed, this explanation also solves the deviation between the low $\frac{Q_*}{k_{2,*}} = 10^5 - 10^6$ favored by several authors (*Jackson et al.*, 2009; *Lin et al.*, 1996; *Dobbs-Dixon et al.*, 2004) from synchronization time scales of double synchronous binary stars (*Meibom and Mathieu*, 2005), and the relatively high $\frac{Q_*}{k_{2,*}} \geq 10^7 - 10^8$ required for orbital stability as found in this work and supported by *Rasio et al.* (1996); *Pätzold and Rauer* (2002); *Carone and Pätzold* (2007).

As the results in this work and the work of *Penev and Sasselov* (2011) confirm, it is probably not a good idea to apply tidal dissipation factors derived from double

synchronous states to tidal friction cases with $\Omega_* \ll n$. This is a completely different tidal frequency regime with possibly very different tidal dissipation efficiencies. Therefore, one has to take care when applying tidal friction and tidal dissipation models. There are a lot of underlying assumptions that have to be investigated prior to applying them to cases, for which they were not developed. Otherwise the results may be misleading.

Appendix

Appendix A

CoRoT planet references

Table A.1: References for the parameters of the CoRoT planetary systems.

System	References
CoRoT-1	*Barge et al.* (2008)
CoRoT-2	*Bouchy et al.* (2008), *Alonso et al.* (2008)
CoRoT-3	*Deleuil et al.* (2008)
CoRoT-4	*Moutou et al.* (2008)
CoRoT-5	*Rauer et al.* (2009)
CoRoT-6	*Fridlund et al.* (2010)
CoRoT-7	*Léger et al.* (2009), *Queloz et al.* (2009), *Bruntt et al.* (2010), *Hatzes et al.* (2010), *Hatzes et al.* (2011)
CoRoT-8	*Bordé et al.* (2010)
CoRoT-9	*Deeg et al.* (2010)
CoRoT-10	*Bonomo et al.* (2010)
CoRoT-11	*Gandolfi et al.* (2010)
CoRoT-12	*Gillon et al.* (2010)
CoRoT-13	*Cabrera et al.* (2010)
CoRoT-14	*Tingley et al.* (2011)
CoRoT-15	*Bouchy et al.* (2011)
CoRoT-16	In Preparation
CoRoT-17	*Csizmadia et al.* (2011)
CoRoT-18	*Hébrard et al.* (2011)
CoRoT-19	*Guenther et al.* (2012)
CoRoT-20	*Deleuil et al.* (2011)
CoRoT-21	Pätzold and the CoRoT-Team, in preparation

Appendix B

Tidal evolution of CoRoT-4 and CoRoT-9
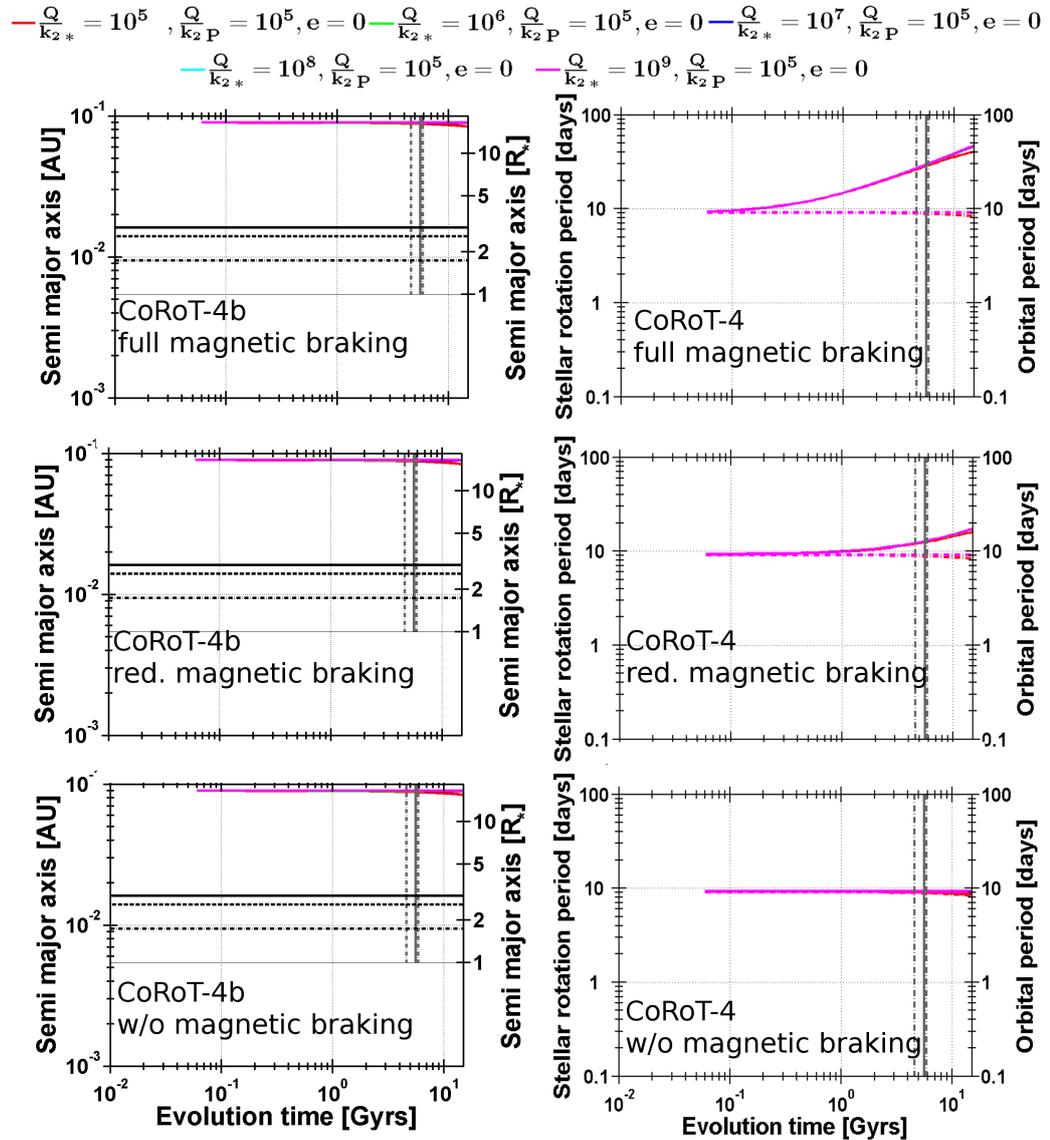
Figure B.1: Tidal evolution of the of the CoRoT-4 system for for $\frac{Q_*}{k_{2,*}} = 10^5 - 10^9$, $\frac{Q_{Pl}}{k_{2,Pl}} = 10^5$, and full, reduced and without magnetic braking. The vertical lines show the remaining stellar lifetime with limits of uncertainty.
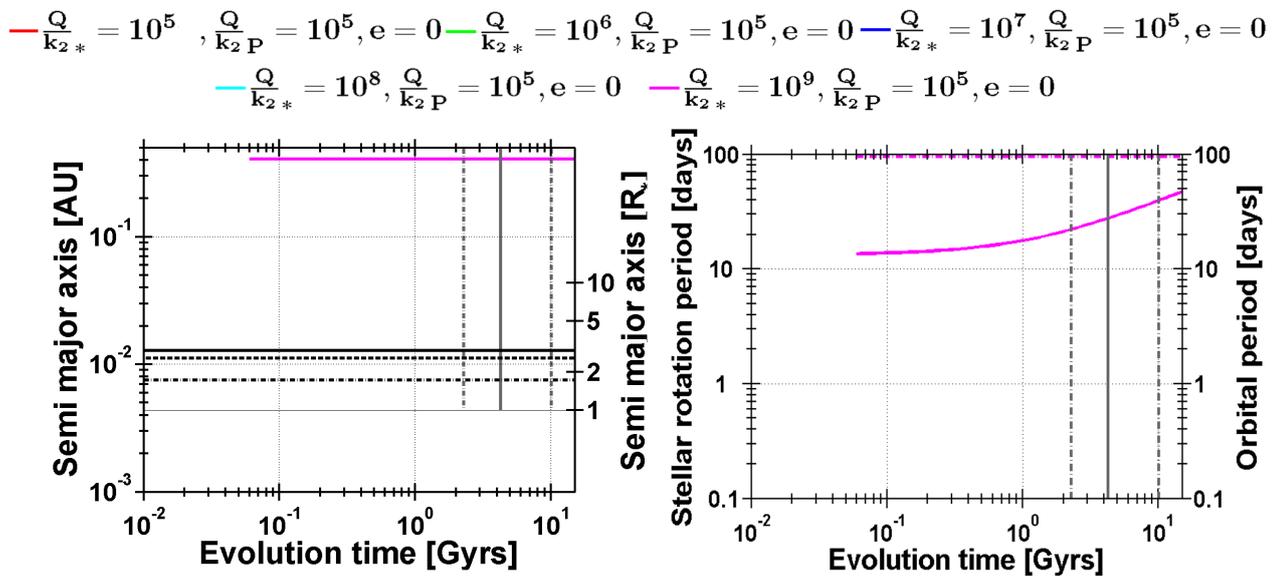
Figure B.2: Tidal evolution of the of the CoRoT-9 system for for $\frac{Q_*}{k_{2,*}} = 10^5 - 10^9$, $\frac{Q_{Pl}}{k_{2,Pl}} = 10^5$ and full magnetic braking. The vertical lines show the remaining stellar lifetime with limits of uncertainty.

Appendix C

# $|\Omega_* - n|$ evolution for close-in CoRoT-planets
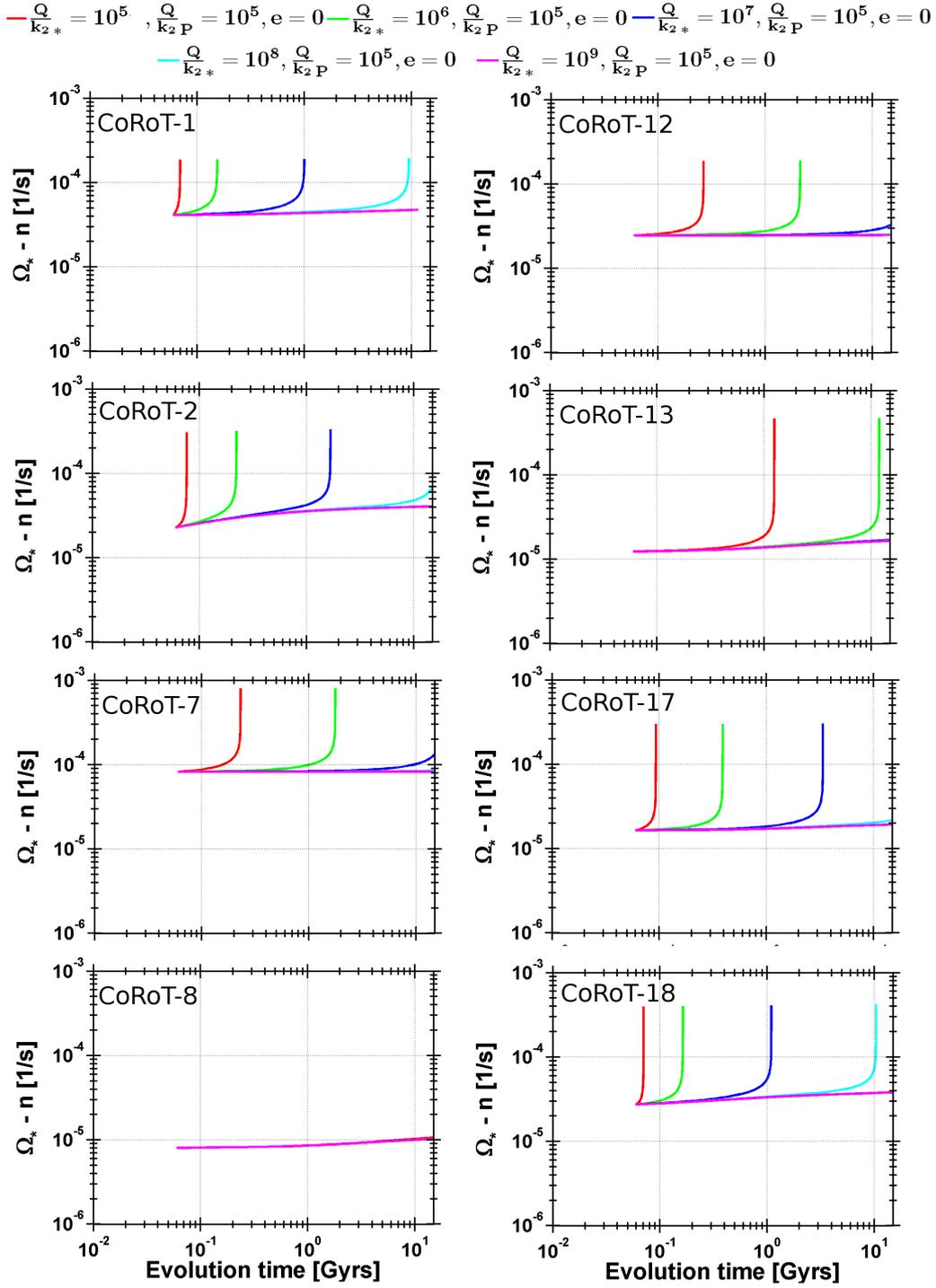
Figure C.1: The evolution of $|\Omega_* - n|$ for the planetary systems CoRoT-1,-2,-7,-8,-12,-13,-17,-18 for the next 1.5×10^{10} years, $\frac{Q_*}{k_{2,*}} = 10^5 - 10^9$.
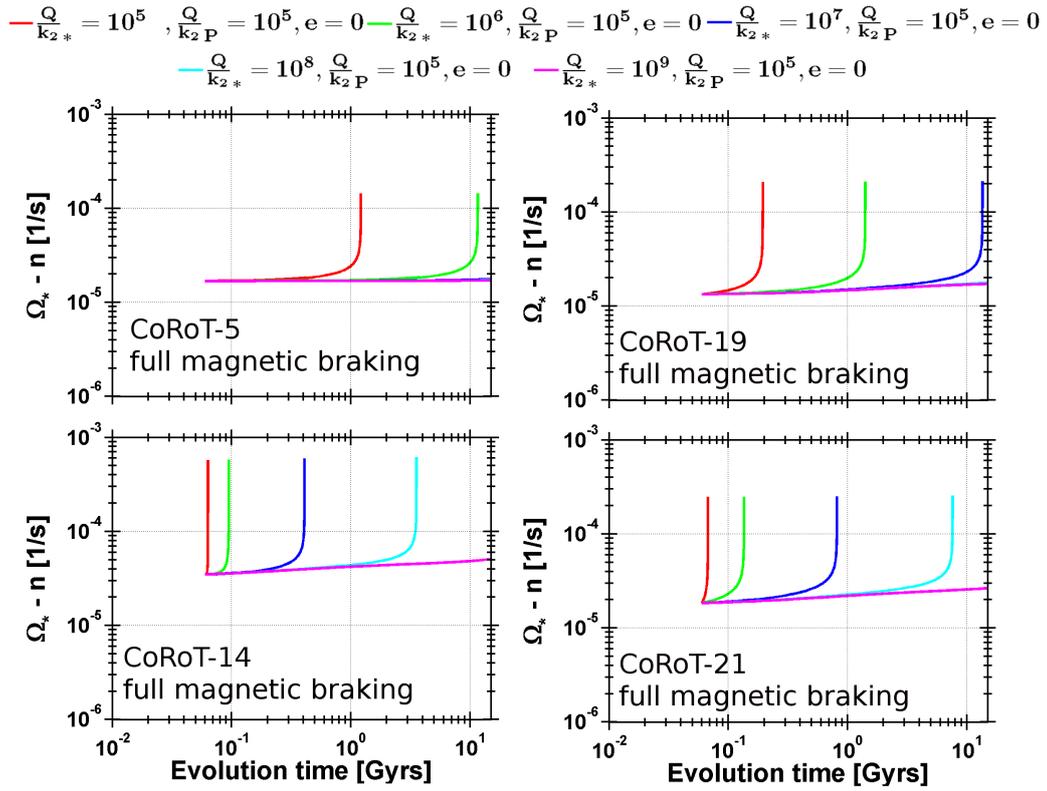
Figure C.2: The evolution of $|\Omega_* - n|$ for the planetary systems CoRoT-5,-14,-19 and full magnetic braking for the next 1.5×10^{10} years, $\frac{Q_*}{k_{2,*}} = 10^5 - 10^9$.
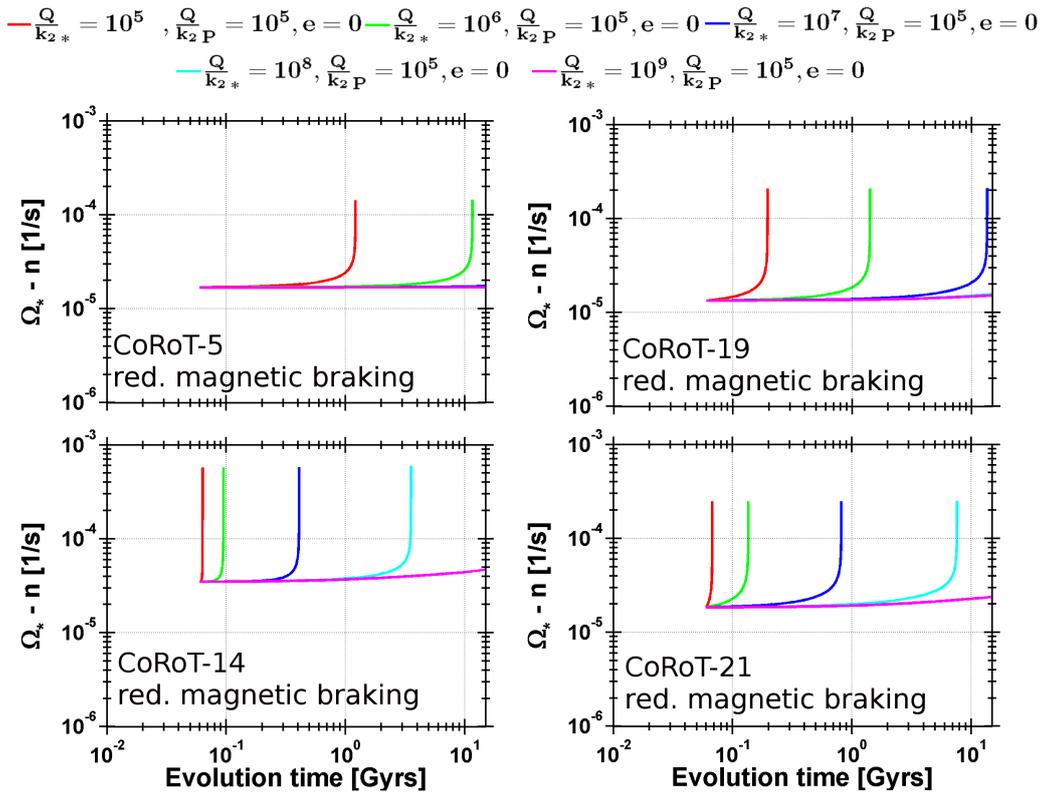
Figure C.3: The evolution of $|\Omega_* - n|$ for the planetary systems CoRoT-5,-14,-19 and reduced magnetic braking for the next 1.5×10^{10} years, $\frac{Q_*}{k_{2,*}} = 10^5 - 10^9$.
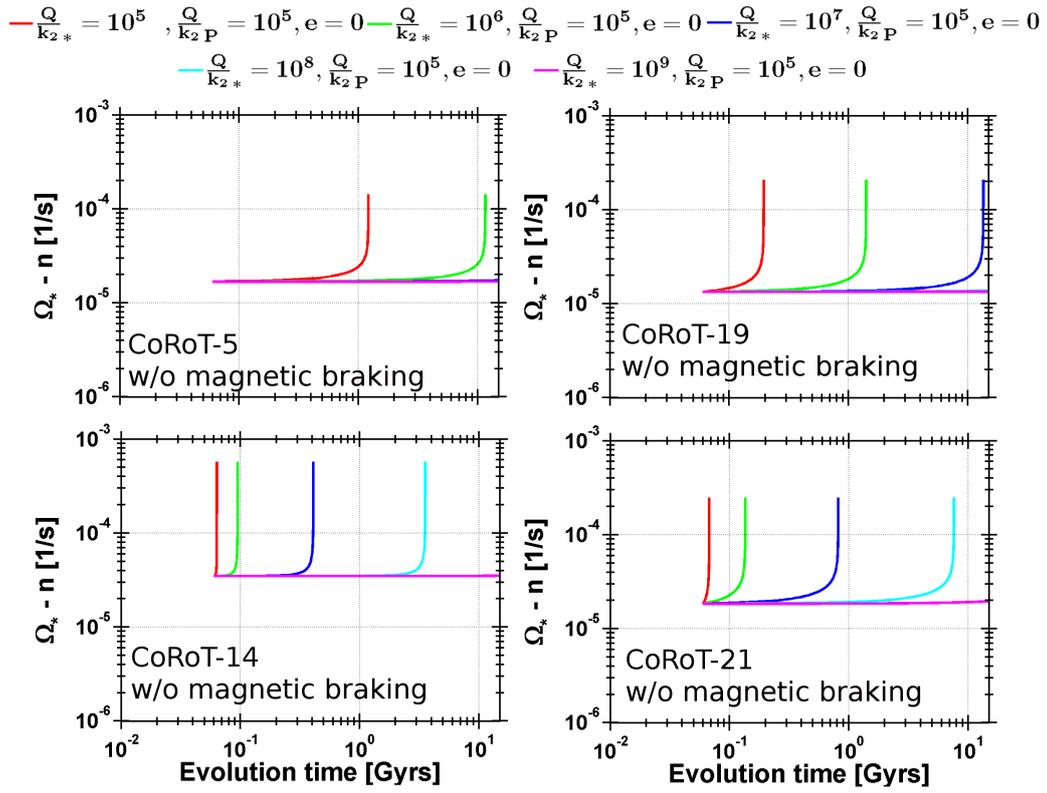
Figure C.4: The evolution of $|\Omega_* - n|$ for the planetary systems CoRoT-5,-14,-19 and without magnetic braking for the next 1.5×10^{10} years, $\frac{Q_*}{k_{2,*}} = 10^5 - 10^9$.
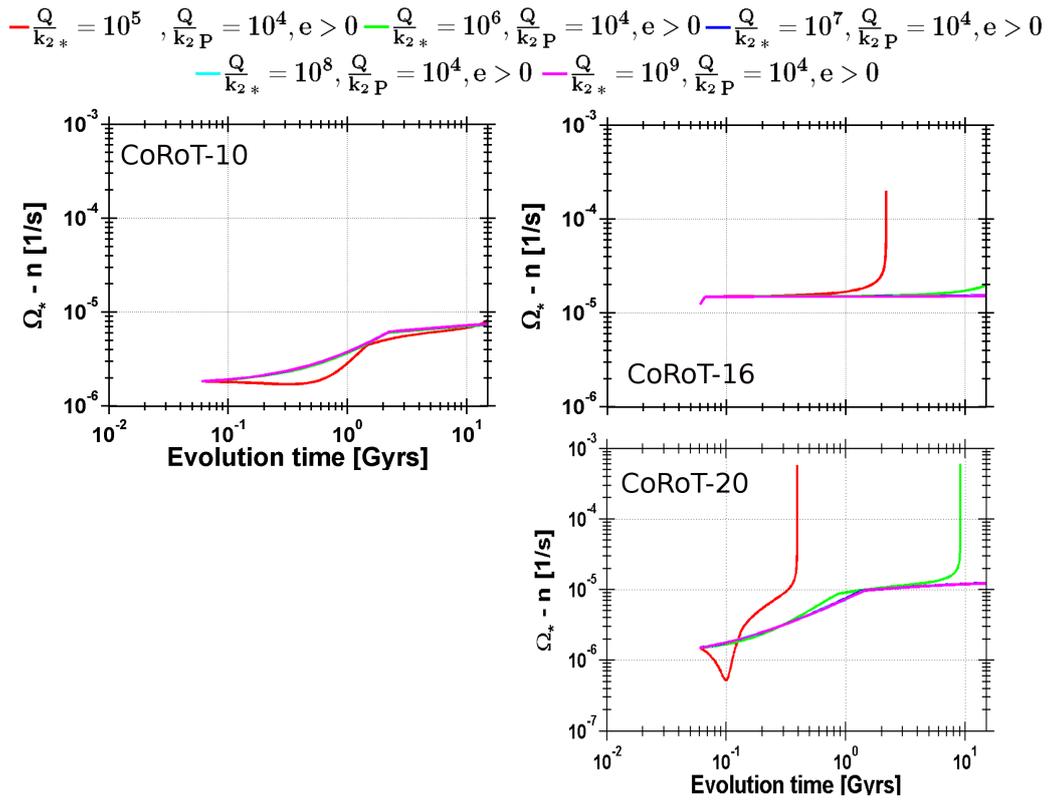
Figure C.5: The evolution of $|\Omega_* - n|$ for the planetary systems CoRoT-10,-16,-20 for the next 1.5×10^{10} years, $\frac{Q_*}{k_{2,*}} = 10^5 - 10^9$ and $\frac{Q_P}{k_{2,P}} = 10^4$.
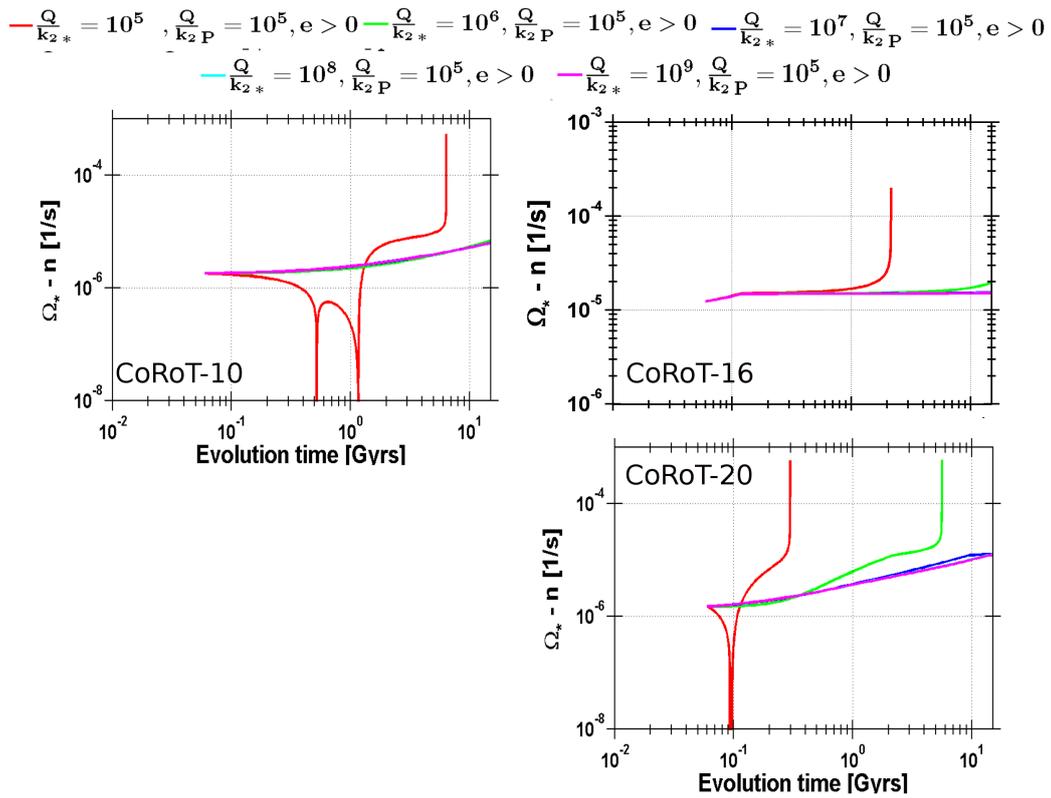
Figure C.6: The evolution of $|\Omega_* - n|$ for the planetary systems CoRoT-10,-16,-20 for the next 1.5×10^{10} years, $\frac{Q_*}{k_{2,*}} = 10^5 - 10^9$ and $\frac{Q_P}{k_{2,P}} = 10^5$.
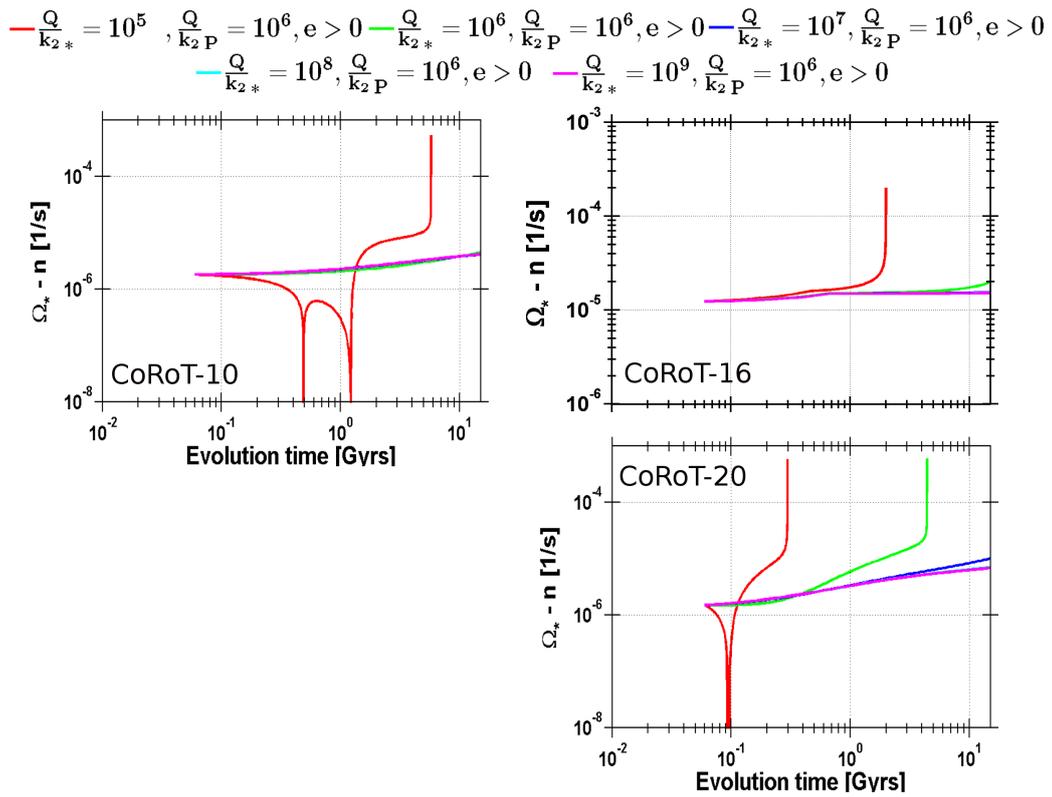
Figure C.7: The evolution of $|\Omega_* - n|$ for the planetary systems CoRoT-10,-16,-20 for the next 1.5×10^{10} years, $\frac{Q_*}{k_{2,*}} = 10^5 - 10^9$ and $\frac{Q_P}{k_{2,P}} = 10^6$.
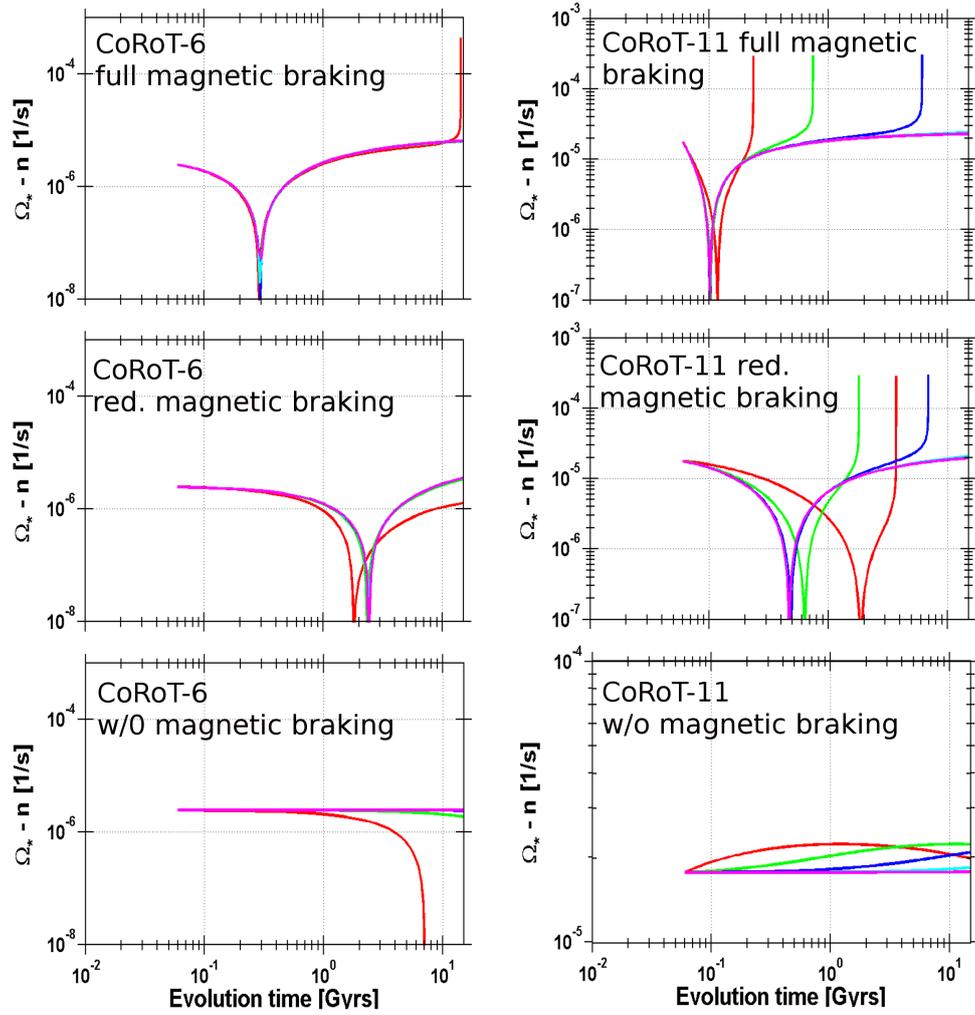
Figure C.8: The evolution of $|\Omega_* - n|$ for the planetary systems CoRoT-6, and CoRoT-11 for the next 1.5×10^{10} years, $\frac{Q_*}{k_{2,*}} = 10^5 - 10^9$.
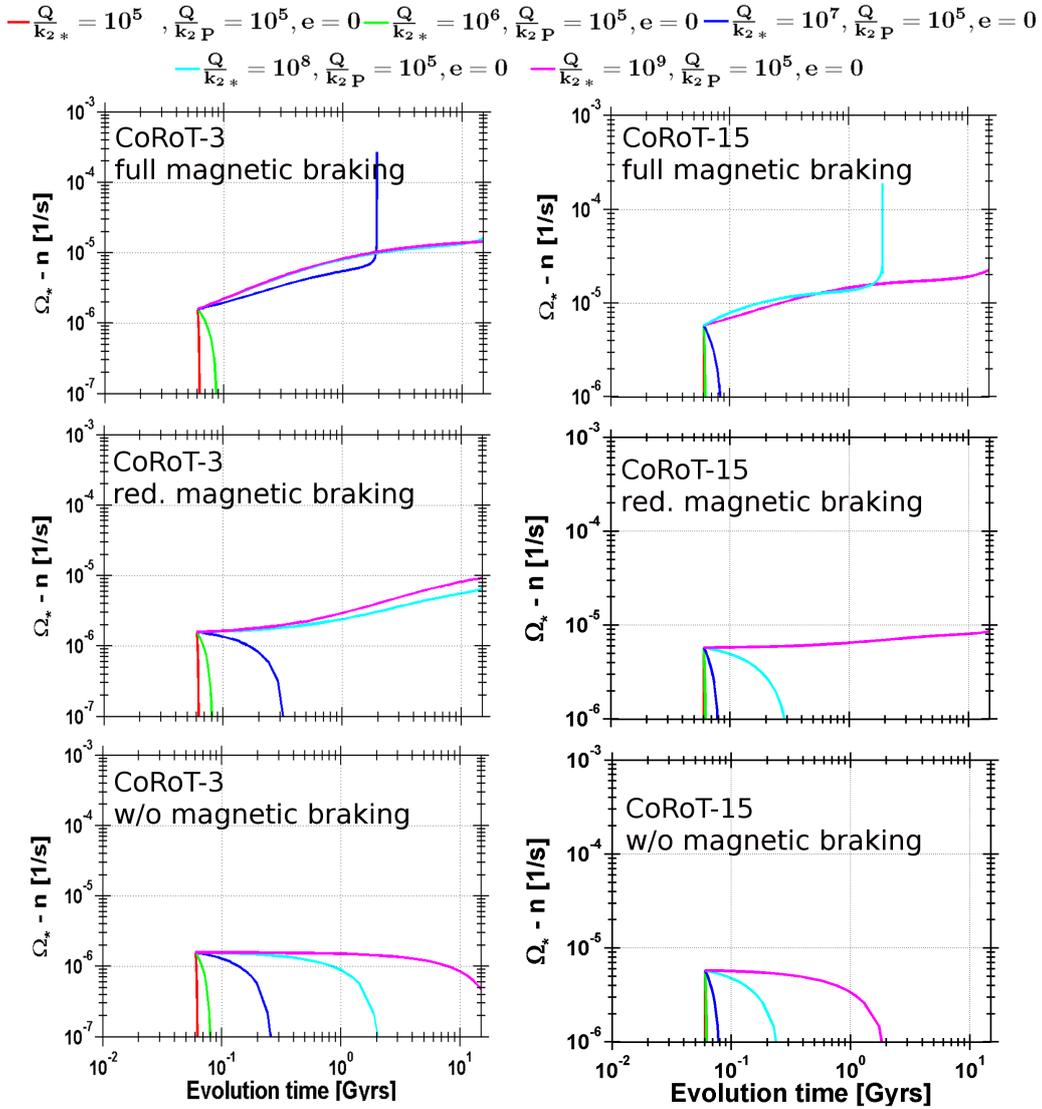
Figure C.9: The evolution of $|\Omega_* - n|$ for the planetary systems CoRoT-3, and CoRoT-15 for the next 1.5×10^{10} years, $\frac{Q_*}{k_{2,*}} = 10^5 - 10^9$.

Appendix D

Evolution of the rotation of CoRoT planets on eccentric orbits

Figures D.1, D.2, and D.3 show the tidal evolution of the planet's rotation period starting with $P_{Pl}(\text{initial}) = 2.5$ days[1]. The planetary rotation of CoRoT-10b, -16b, and -20b is quickly forced into a synchronized state. This happens before the orbit becomes circular. Therefore, the planetary rotation rate Ω_{Pl} is not synchronized with the mean orbital revolution rate n but rather pseudo-synchronized with (*Hut*, 1981)

$$n_{pseudo} = n \left(1 + 6e^2 + \frac{3}{8}e^4 + \frac{223}{8}e^6 \right).$$ (D.0.1)

Therefore, the tidal planetary frequency $2|\Omega_{Pl} - n|$ evolves with

$$2|\Omega_{Pl} - n| = 2n \left(6e^2 + \frac{3}{8}e^4 + \frac{223}{8}e^6 \right),$$ (D.0.2)

starting for the planets CoRoT-10b,-16b, and 20b with

Planet	$2|\Omega_{Pl} - n|_{start}$
CoRoT-10b	$4.66n$
CoRoT-16b	$1.12n$
CoRoT-20b	$5.6n$

---

[1]This value was chosen as a medium value between the fast rotation of 10 hours and 10 days selected in Section 3.2.

and approaching zero, as the eccentricity is damped to zero as well.

The planetary rotation of CoRoT-9b on the other hand may, depending on $\frac{Q_{Pl}}{k_{2,Pl}}$, never become synchronized or take several hundred million years to several billion years to evolve into a pseudo-synchronized state.
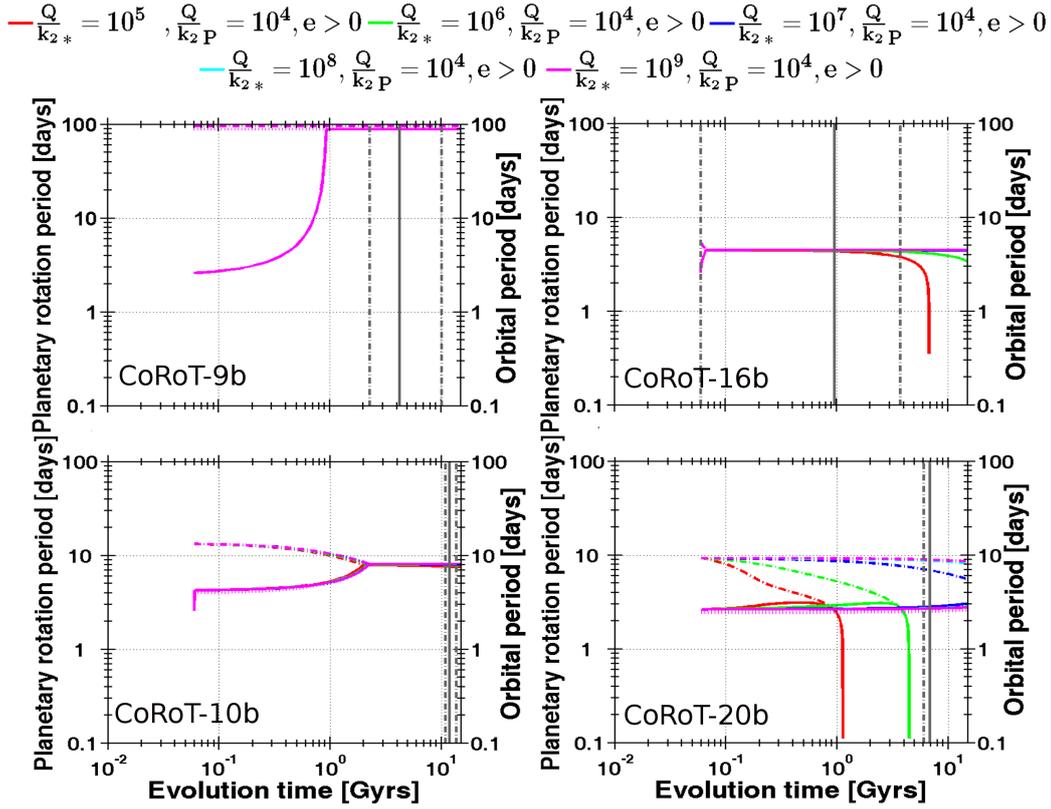
Figure D.1: The tidal evolution of the rotation period of the planets CoRoT-9b,-10b, -16b, and CoRoT-20b for the next 1.5×10^{10} years, for $\frac{Q_*}{k_{2,*}} = 10^{5.5}, 10^6, 10^7, 10^8, 10^9$ (solid lines) and $\frac{Q_{Pl}}{k_{2,Pl}} = 10^4$. The vertical lines show the remaining lifetime of the system. The dashed-dotted lines show the evolution of the mean orbital revolution period for comparison. n_{pseudo} is depicted by a dotted line which is for CoRoT-10b, -16b, 20b hidden by the planetary rotation evolution because – apart from a very brief initial phase – $\Omega_{Pl} = n_{pseudo}$.
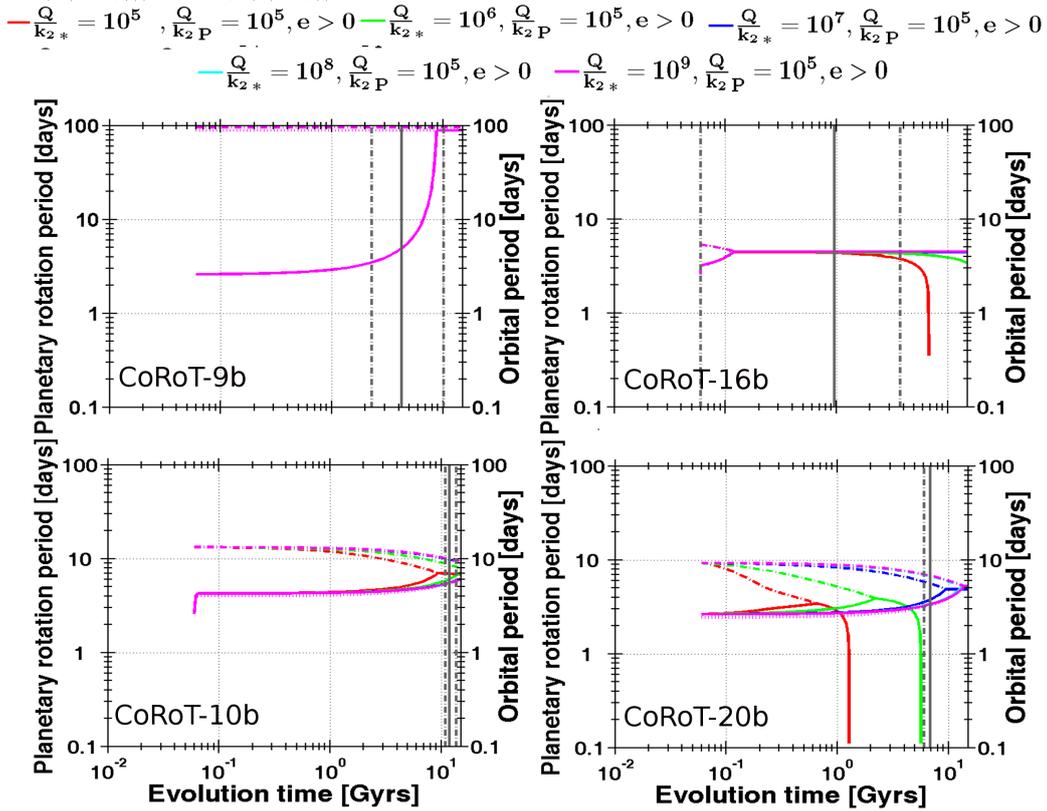
Figure D.2: The tidal evolution of the rotation period of the planets CoRoT-9b,-10b, -16b, and CoRoT-20b for the next 1.5×10^{10} years, for $\frac{Q_*}{k_{2,*}} = 10^{5.5}, 10^6, 10^7, 10^8, 10^9$ (solid lines) and $\frac{Q_{Pl}}{k_{2,Pl}} = 10^5$. The vertical lines show the remaining lifetime of the system. The dashed-dotted lines show the evolution of the mean orbital revolution period for comparison. n_{pseudo} is depicted by a dotted line which is for CoRoT-10b, -16b, 20b hidden by the planetary rotation evolution because – apart from a very brief initial phase – $\Omega_{Pl} = n_{pseudo}$
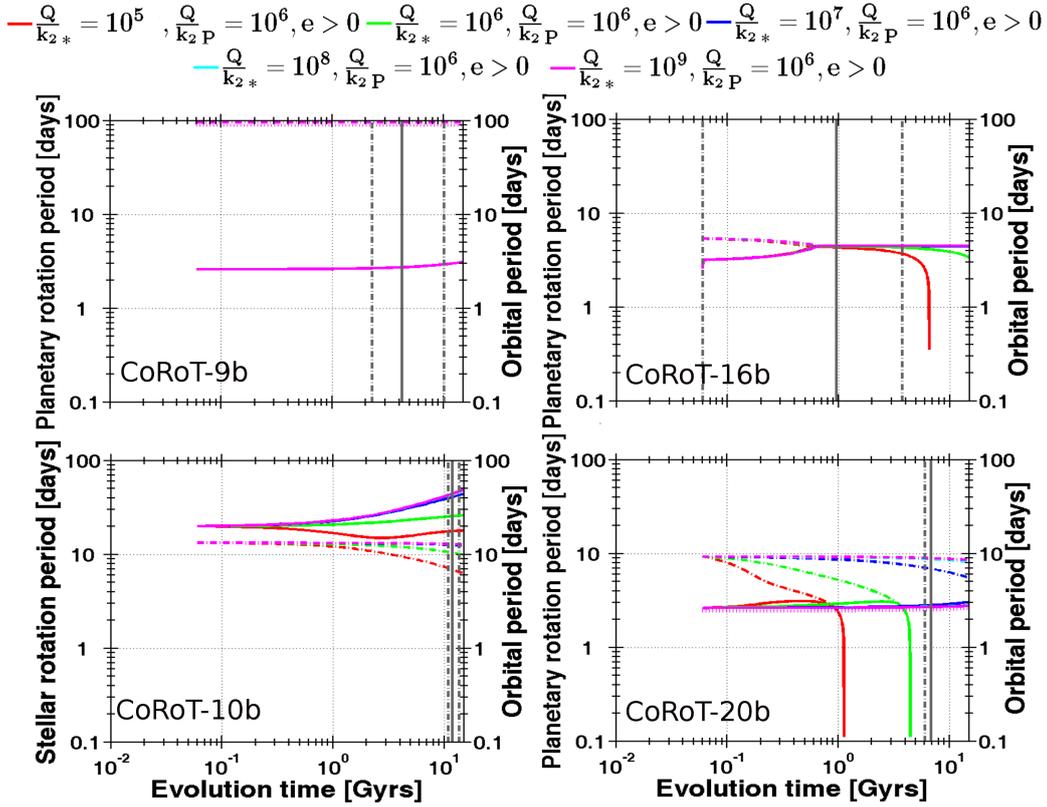
Figure D.3: The tidal evolution of the rotation period of the planets CoRoT-9b,-10b, -16b, and CoRoT-20b for the next 1.5×10^{10} years, for $\frac{Q_*}{k_{2,*}} = 10^{5.5}, 10^6, 10^7, 10^8, 10^9$ (solid lines) and $\frac{Q_{Pl}}{k_{2,Pl}} = 10^6$. The vertical lines show the remaining lifetime of the system. The dashed-dotted lines show the evolution of the mean orbital revolution period for comparison. n_{pseudo} is depicted by a dotted line which is for CoRoT-10b, -16b, 20b hidden by the planetary rotation evolution because – apart from a very brief initial phase – $\Omega_{Pl} = n_{pseudo}$

Appendix E

Integration method

There exists a number of numerical integrators (*Vallado* (2001), and *Gould et al.* (2006)) suitable to solve ordinary differential equations. In this work, the RK4(5) algorithm is used, a special case of the classical Runge-Kutta method (*Gould et al.*, 2006).

The Runga-Kutta method was first formulated in 1895 by Carl Runge and later improved by Heun and Kutta. To explain this method, the following first-order differential equation is considered:

$$f(x,t) = \frac{\mathrm{d}x}{\mathrm{d}t}, \tag{E.0.1}$$

where $f(x,t)$ is the rate of the solution at position x and time t. Let $x_n(t_n)$ be the initial condition. To obtain the solution $x_{n+1}(t_{n+1})$, the rate is evaluated s times in the time interval $[t_n, t_{n+1}]$. Each evaluation yields a slightly different rate $k_i = f(x_i, t_i)$. The solution is derived by using a weighted mean of the intermediate rates for the time step $h = t_{n+1} - t_n$.

The Runga-Kutta algorithm with number of intermediate steps s is described by:

$$x_{n+1}(t_{n+1}) = x_n(t_n) + h \sum_{i=1}^{s} b_i k_i, \tag{E.0.2}$$

where the rates k_i are developed iteratively:

$$k_1 = f(x_n, t_n)$$

$$k_2 = f(x_n + k_1 a_{21} h, t_n + c_2 h)$$

$$k_3 = f(x_n + k_1 a_{31} h + k_2 a_{32} h, t_n + c_3 h)$$

$$\vdots$$

$$k_s = f(x_n + k_1 a_{s1} h + k_2 a_{s2} h + \cdots + k_{s-1} a_{s,s-1} h, t_n + c_s h)$$

The coefficients b_i, c_i with $i = 1, 2, \ldots s$ and a_{ij} with $1 \leq j < i \leq s$ can be derived from the coefficient tableau of the selected Runge-Kutta algorithm:

$$
\begin{array}{c|cccc}
c_1 & 0 & 0 & 0 & 0 \\
c_2 & a_{21} & 0 & 0 & 0 \\
\vdots & \vdots & \ddots & 0 & 0 \\
c_s & a_{s1} & \cdots & a_{s,s-1} & 0 \\
\hline
 & b_1 & b_2 & \cdots & b_s
\end{array}
$$

The coefficients are determined such that

$$\sum_{i=1}^{s} b_i = 1 \quad c_i = \sum_{j=1}^{i-1} a_{ij} \quad \text{and} \quad c_1 = 0. \tag{E.0.3}$$

The accuracy of the numerical integration depends on the step size h. This can be estimated, for example, by applying the method with step size h and $h/2$, and by comparing the solutions with each other. The RK4(5) algorithm uses another method to derive the accuracy at each time step. It simultaneously runs a fourth and fifth order Runge-Kutta method. The difference between the two solutions is the accuracy of the 4th order solution[1]. RK4(5) is an adaptive time step algorithm. The user selects beforehand the relative accuracy required for the integration and the algorithm reduces or increases the step size until the accuracy criterium is met. In this work, the relative accuracy is set to 10^{-8}. The coefficient tableau of the RK4(5) algorithm is:

---

[1]A Runga-Kutta method is of order p if it has the local truncation error $\mathcal{O}(h^{p+1})$.

$$
\begin{array}{c|ccccccc}
0 & 0 & 0 & 0 & 0 & 0 & 0 & 0 \\[4pt]
\frac{1}{5} & \frac{1}{5} & 0 & 0 & 0 & 0 & 0 & 0 \\[4pt]
\frac{3}{10} & \frac{3}{40} & \frac{9}{40} & 0 & 0 & 0 & 0 & 0 \\[4pt]
\frac{4}{5} & \frac{44}{45} & -\frac{56}{15} & \frac{32}{9} & 0 & 0 & 0 & 0 \\[4pt]
\frac{8}{9} & \frac{19372}{6561} & -\frac{25360}{2187} & \frac{64448}{6561} & -\frac{212}{729} & 0 & 0 & 0 \\[4pt]
1 & \frac{9017}{3168} & -\frac{355}{33} & \frac{46732}{5247} & \frac{49}{176} & -\frac{5103}{18656} & 0 & 0 \\[4pt]
1 & \frac{35}{384} & 0 & \frac{500}{1113} & \frac{125}{192} & -\frac{2187}{6784} & \frac{11}{84} & 0 \\[4pt]
\hline
 & \frac{35}{384} & 0 & \frac{500}{1113} & \frac{125}{192} & -\frac{2187}{6784} & \frac{11}{84} & 0 \\[4pt]
 & \frac{5179}{57600} & 0 & \frac{7571}{16695} & \frac{393}{640} & -\frac{92097}{339200} & \frac{187}{2100} & \frac{1}{40}
\end{array}
$$

The validity of the results derived with the RK4(5) algorithm can be tested by computing the tidal evolution of a planetary system without magnetic braking. If the numerical integration is implemented with acceptable accuracy, then the total angular momentum should remain constant during the whole computation[2].

This will be shown for one example: The tidal evolution of the CoRoT-21b system for $\frac{Q_*}{k_{2,*}} = 10^5$ and without magnetic braking is computed. This system is selected because the rate of change $\dot{a}$ is one of the largest: The planet will reach the Roche limit in 7.6 million years for $\frac{Q_*}{k_{2,*}} = 10^5$ (Section 5.1.2, Figure 5.2). Figure E.1 shows the total angular momentum L_{tot}, the orbital angular momentum L_{orb}, the stellar rotational angular momentum $L_{rot,*}$, and the planetary angular momentum $L_{rot,Pl}$ for this evolution track.

L_{tot} appears to be constant over the evolution time. Furthermore, the total angular momentum is $L_{tot}(t_0) = 7.0894 \times 10^{42}$Nms at the start time $t_0 = 60$ million years. At the end time $t_{end} = 67$ million years, the total angular momentum is $L_{tot}(t_{end}) = 7.0900 \times 10^{42}$Nms. This corresponds to a relative change of 0.0085%.

As a control, the tidal evolution of the CoRoT-21b system for $\frac{Q_*}{k_{2,*}} = 10^9$ and without magnetic braking is computed and the angular momenta are compared (Figure E.2). L_{tot} appears to be constant over the evolution time. Furthermore, the total angular momentum is $L_{tot}(t_0) = 7.0894 \times 10^{42}$Nms at the start time $t_0 = 60$ million years. At $t_{end} = 15$ billion years, the total angular momentum is $L_{tot}(t_{end}) = 7.0884 \times 10^{42}$Nms. This corresponds to a relative change of 0.0141%.

These results support the conclusion that the RK4(5) algorithm yields indeed

---

[2]Magnetic braking has to be switched off for this accuracy test, because otherwise the stellar wind would remove angular momentum from the planetary system.
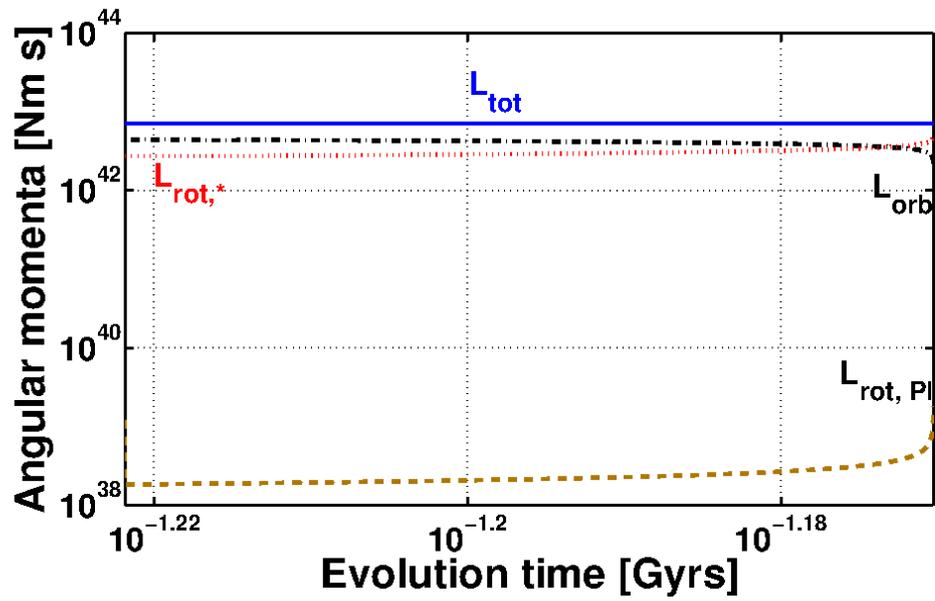
Figure E.1: The evolution of the total angular momentum L_{tot}, the orbital angular momentum L_{orb}, the stellar rotational angular momentum $L_{rot,*}$, and the planetary angular momentum $L_{rot,Pl}$ during the tidal evolution of the CoRoT-21 system for $\frac{Q_*}{k_{2,*}} = 10^5$. The rotation of the planet was initialized with a rotation period $P_{rot,Pl} = 10$ hours which is rapidly synchronized with the revolution period $P_{orb} = 2.72$ days.
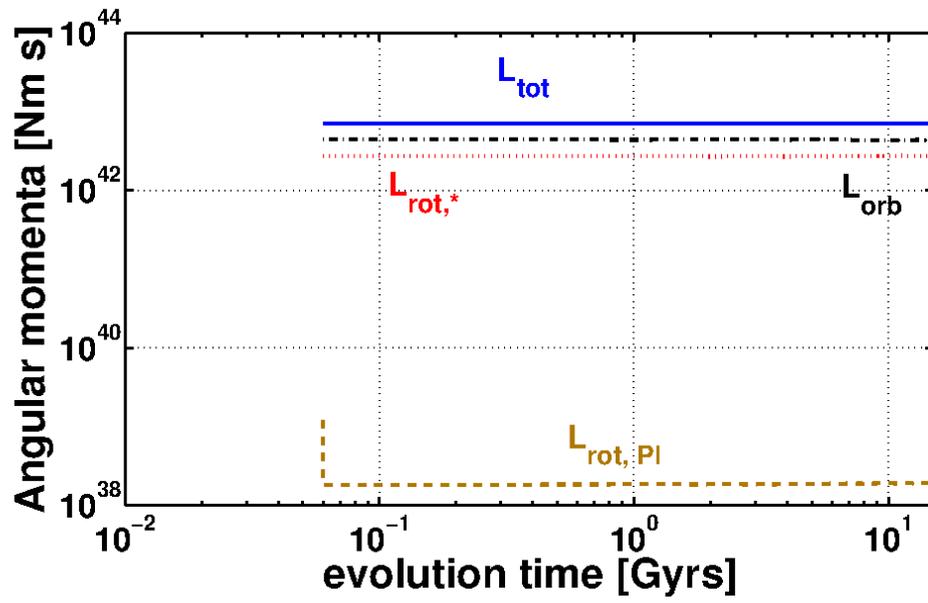
Figure E.2: The evolution of the total angular momentum L_{tot}, the orbital angular momentum L_{orb}, the stellar rotational angular momentum $L_{rot,*}$, and the planetary angular momentum $L_{rot,Pl}$ during the tidal evolution of the CoRoT-21 system for $\frac{Q_*}{k_{2,*}} = 10^9$. The rotation of the planet was initialized with a rotation period $P_{rot,Pl} = 10$ hours which is rapidly synchronized with the revolution period $P_{orb} = 2.72$ days.

sufficiently accurate results.

Appendix F

Model sensitivity analysis

In this work, the models did not take the uncertainties of the input parameters into account. This will now be investigated in this chapter. A representative planetary system is selected for each subcase discussed in this work and the model input parameters are varied using a Monte-Carlo method. The models investigated in this work start with the following initial conditions:

$$a \pm \Delta a$$

$$P_* \pm \Delta P_*$$

$$e \pm \Delta e$$

$$P_{Pl} \pm P_{Pl} \tag{F.0.1}$$

It was shown that the energy and angular momentum of the planetary rotation is negligible compared to the stellar rotation and planetary orbit (Section 3.3), therefore it can be assumed that the tidal evolution does not depend on P_{Pl}.

To investigate the model sensitivity for the initial conditions a, P_*, and e – the latter is only important for planets on eccentric orbits–, a set of one hundred start parameters are randomly chosen within limits of uncertainty. The tidal evolution is computed for each start condition of this set.

F.1 The CoRoT-12 system

Figures F.1 and F.2 show the tidal evolution of the CoRoT-12 system for randomly chosen initial conditions $a = 0.04016 \pm 0.0009$ AU and $P_* = 57^{+43}_{-28}$ days[1] ($e = 0$). For this system, $\Omega_* \ll n$ at all times.
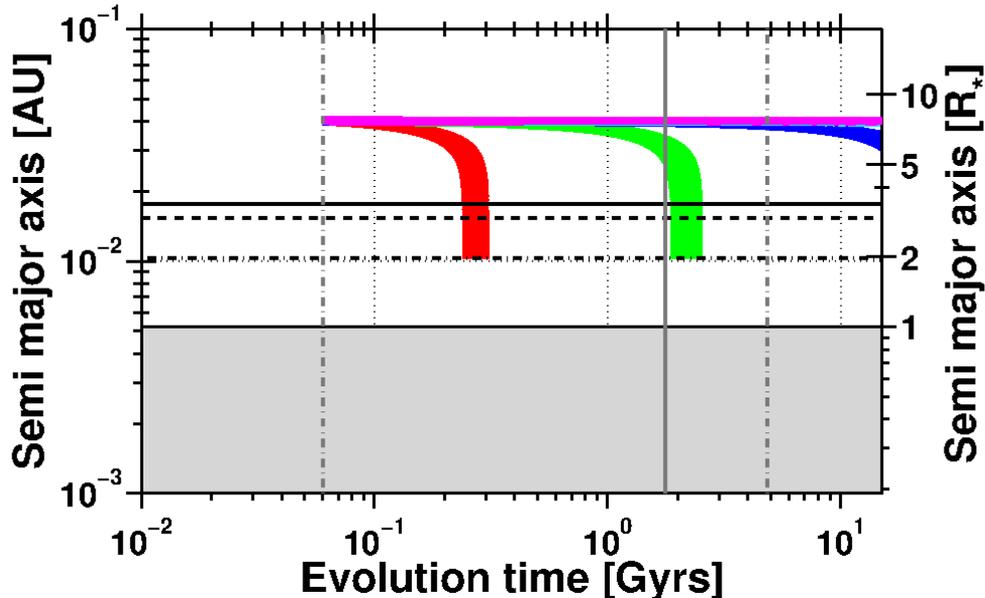
Figure F.1: Tidal evolution of the semi major axis of CoRoT-12b for randomly chosen initial conditions a, P_* within limits of uncertainty for $\frac{Q_*}{k_{2,*}} = 10^5 - 10^9$ and $\frac{Q_{Pl}}{k_{2,Pl}} = 10^5$. The vertical lines show the remaining stellar lifetime with limits of uncertainty.

Apparently, the qualitative evolution of the system, and therefore the derived orbital stability and tidal spin-up limit, remains unchanged when the initial conditions are varied. Interestingly, the stellar rotation evolution does not depend on the initial condition P_* in the presence of tidal spin-up. As the planet moves towards the star, the amount of angular momentum transferred to the star exceeds the initial stellar angular momentum. The transferred orbital angular momentum determines the final stellar spin state as the planet reaches the Roche zone.

[1]An upper limit of $P_* = 100$ days was selected. This choice appears reasonable according to *Barnes* (2003), and Section 2.10.
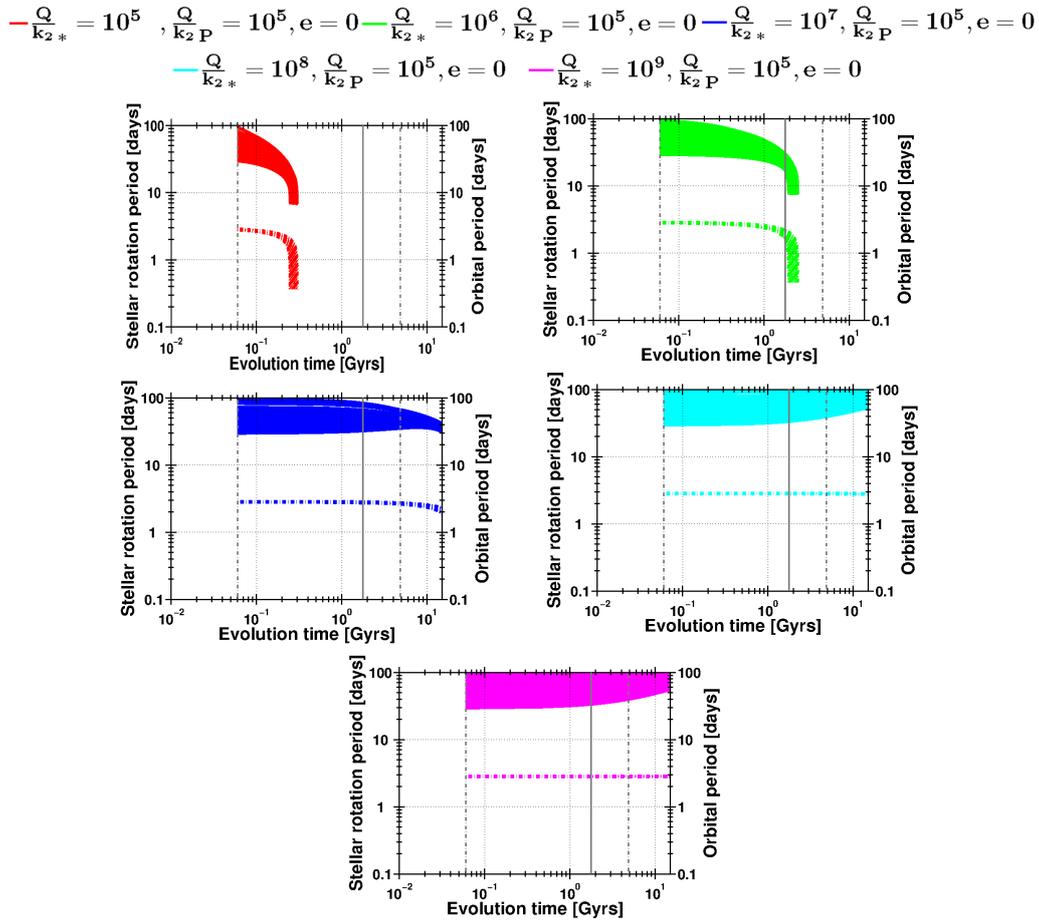
Figure F.2: Tidal evolution of the stellar rotation of CoRoT-12 for randomly chosen initial conditions a and P_* within limits of uncertainty for $\frac{Q_*}{k_{2,*}} = 10^5 - 10^9$ and $\frac{Q_{Pl}}{k_{2,Pl}} = 10^5$. The vertical lines show the remaining stellar lifetime with limits of uncertainty.

F.2 The CoRoT-16 system

Figures F.3, F.4, and F.5 show the tidal evolution of the CoRoT-16 system for randomly chosen initial conditions $a = 0.0618 \pm 0.0015$ AU , $P_* = 60 - 100$ days[2], and $e = 0.3 \pm 0.1$. For this system, $\Omega_* \ll n$ at all times.
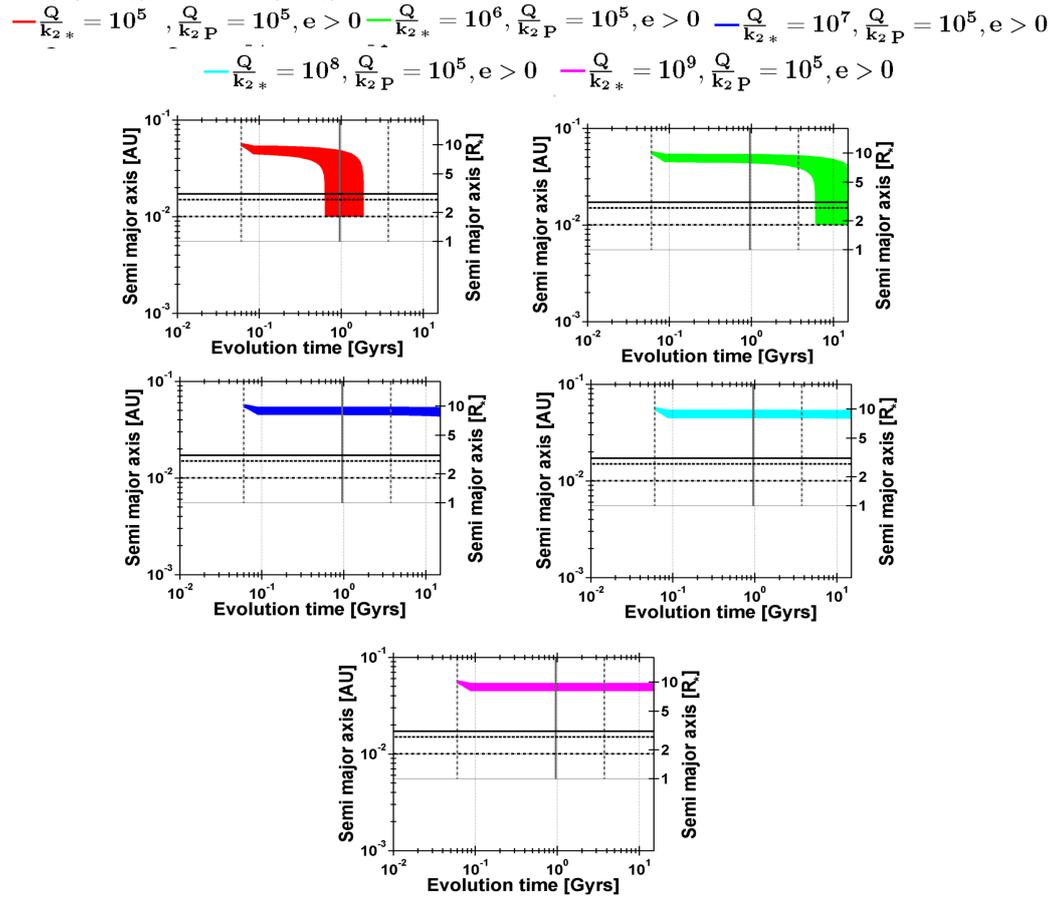

Figure F.3: Tidal evolution of the semi major axis of CoRoT-16b for randomly chosen initial conditions a and P_* within limits of uncertainty for $\frac{Q_*}{k_{2,*}} = 10^5 - 10^9$ and $\frac{Q_{Pl}}{k_{2,Pl}} = 10^5$. The vertical lines show the remaining stellar lifetime with limits of uncertainty.

---

[2]An upper limit of $P_* = 100$ days was selected. This choice appears reasonable according to *Barnes* (2003), and Section 2.10.
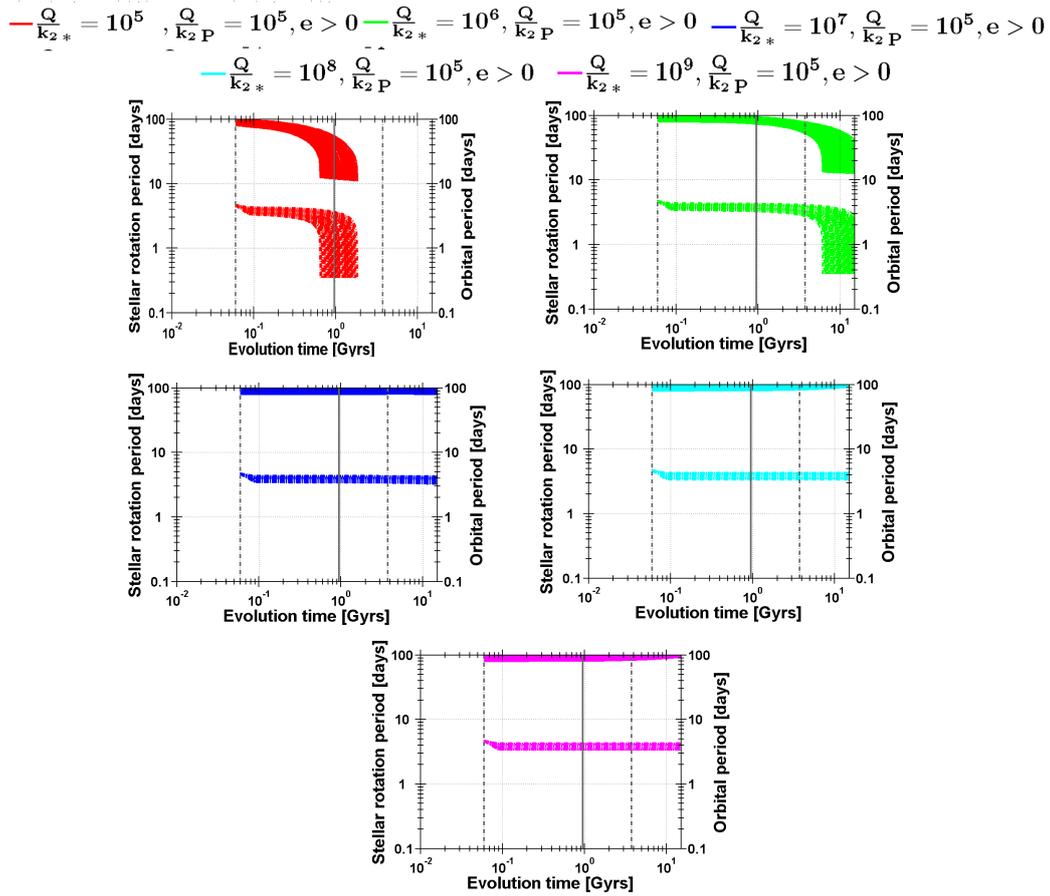
Figure F.4: Tidal evolution of the stellar rotation of CoRoT-16 for randomly chosen initial conditions a and P_* within limits of uncertainty for $\frac{Q_*}{k_{2,*}} = 10^5 - 10^9$ and $\frac{Q_{Pl}}{k_{2,Pl}} = 10^5$. The vertical lines show the remaining stellar lifetime with limits of uncertainty.
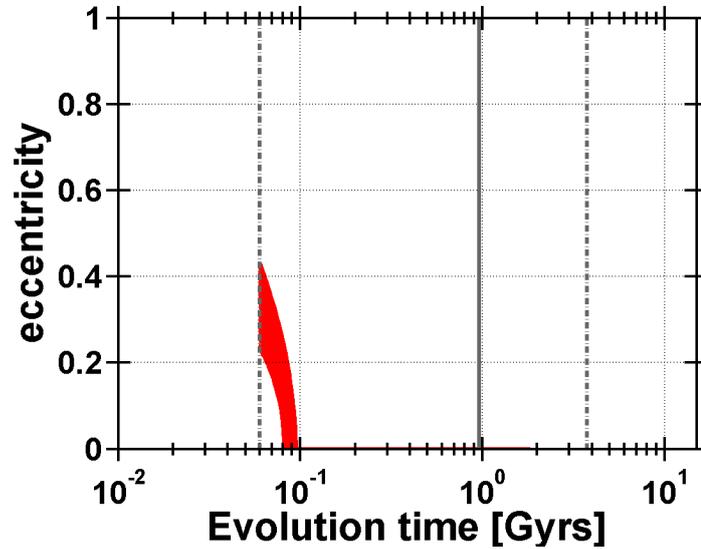
Figure F.5: Tidal evolution of the orbital eccentricity of CoRoT-16b for randomly chosen initial conditions a and P_* within limits of uncertainty for $\frac{Q_*}{k_{2,*}} = 10^5 - 10^9$ and $\frac{Q_{Pl}}{k_{2,Pl}} = 10^5$. The eccentricity evolution does not depend on $\frac{Q_*}{k_{2,*}}$. The vertical lines show the remaining stellar lifetime with limits of uncertainty.

Evidently, the tidal evolution of the semi major axis of CoRoT-16b and the stellar rotation period of CoRoT-16 system varies more strongly with initial conditions for $\frac{Q_*}{k_{2,*}} \leq 10^6$ than the tidal evolution of the semi major axis of CoRoT-12b and the stellar rotation of CoRoT-12. The eccentricity evolution, on the other hand, does not very strongly with initial conditions. The strong variation of the a and P_*-evolution is not surprising because for the evaluation of the CoRoT-16-system an additional parameter, the orbital eccentricity, is introduced. The tidal model of the CoRoT-16 system is sensitive to three input parameters and not to two input parameters like the tidal model of the CoRoT-12 system. Still, the qualitative results with respect to $\frac{Q_*}{k_{2,*}}$ remain valid for this system as well because the tidal models yield qualitatively similar results and depend more strongly on $\frac{Q_*}{k_{2,*}}$ than on the initial conditions.

F.3 The CoRoT-20 system

Figures F.6, F.7, and F.8 show the tidal evolution of the CoRoT-20 system for randomly chosen initial conditions $a = 0.0618 \pm 0.0015$ AU , $P_* = 11.5 \pm 2.6$ days,

and $e = 0.53 \pm 0.1$.
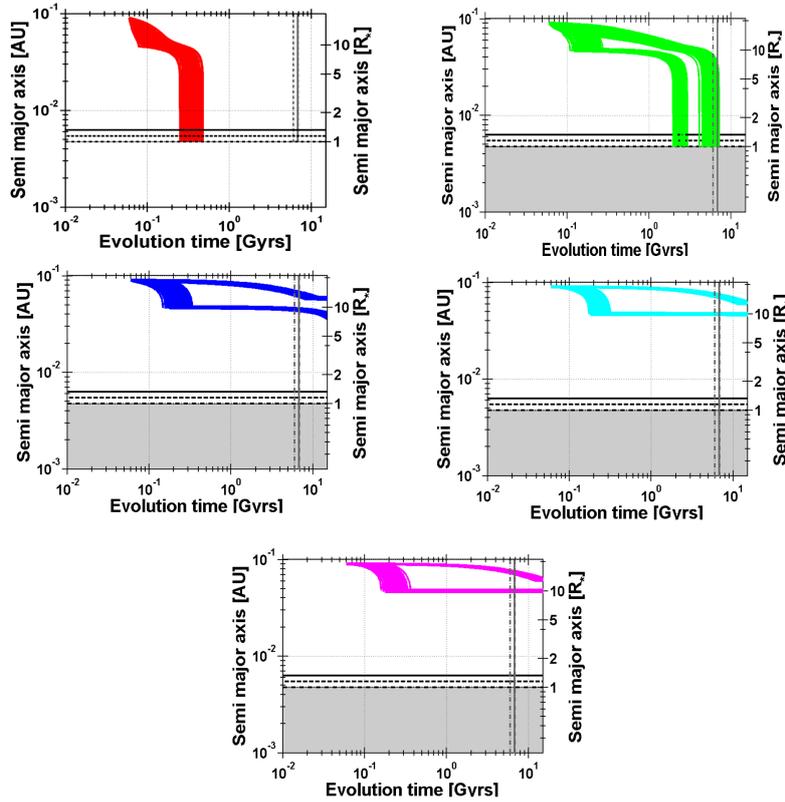
Figure F.6: Tidal evolution of the semi major axis of CoRoT-20b for randomly chosen initial conditions a and P_* within limits of uncertainty for $\frac{Q_*}{k_{2,*}} = 10^5 - 10^9$ and $\frac{Q_{Pl}}{k_{2,Pl}} = 10^5$. The vertical lines show the remaining stellar lifetime with limits of uncertainty.

As was already discussed in Sections 5.2, 6.2 and 8.4.1, depending on the stellar rotation if $\Omega_* \geq n$, the system goes to a transient double synchronous state upheld by the positive feedback between planetary and stellar tidal friction. This double synchronous state is broken down by magnetic braking as soon as the eccentricity is damped to zero and planetary tidal friction seizes to act on the system. Stellar tidal friction on its own is not sufficient to counter-act magnetic braking. If $\Omega_* < n$, the system goes trough a transient double synchronous state only for $\frac{Q_*}{k_{2,*}} = 10^5$
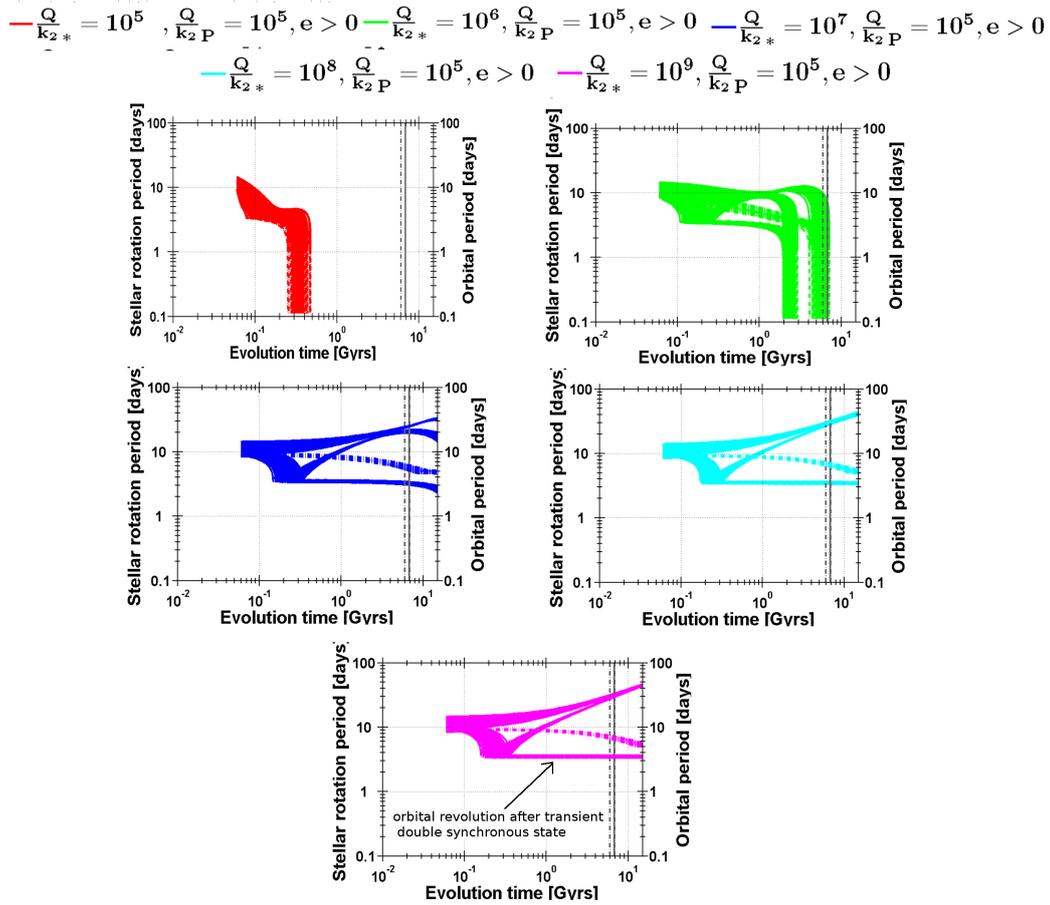
Figure F.7: Tidal evolution of the stellar rotation of CoRoT-20 for randomly chosen initial conditions a and P_* within limits of uncertainty for $\frac{Q_*}{k_{2,*}} = 10^5 - 10^9$ and $\frac{Q_{Pl}}{k_{2,Pl}} = 10^5$. The vertical lines show the remaining stellar lifetime with limits of uncertainty.
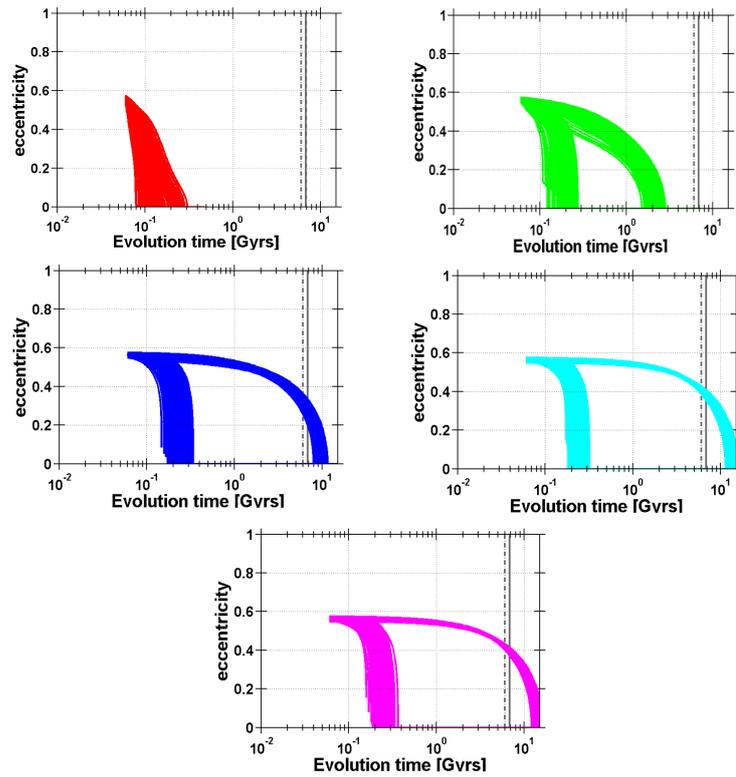
Figure F.8: Tidal evolution of the orbital eccentricity of CoRoT-20b for randomly chosen initial conditions a and P_* within limits of uncertainty for $\frac{Q_*}{k_{2,*}} = 10^5 - 10^9$ and $\frac{Q_{Pl}}{k_{2,Pl}} = 10^5$. The vertical lines show the remaining stellar lifetime with limits of uncertainty.

and $\frac{Q_{Pl}}{k_{2,Pl}} = 10^5 - 10^6$. In any case, the planet will reach the Roche limit within the remaining lifetime if $\frac{Q_*}{k_{2,*}} \leq 10^6$. As a consequence, the star may be spun up. Therefore, the orbital stability limit has to be $\frac{Q_*}{k_{2,*}} > 10^6$. The star may be spun up during the transient double synchronous state. But after the orbit has become circular, the stellar rotation is decelerated by magnetic braking again and 'meets' the stellar rotation evolution tracks that never went trough a double synchronous state. They main difference is the eccentricity evolution. If the system goes though a double synchronous state, the eccentricity is damped to zero within 200 million years. If the system does not go through a double synchronous state, the orbit may never become circular in the remaining lifetime.

F.4 The CoRoT-11 system

Figures F.9 and F.10 show the tidal evolution of the CoRoT-11 system for randomly chosen initial conditions $a = 0.044 \pm 0.005$ AU and $P_* = 1.4 \pm 0.3$ days. The general evolution of the CoRoT-11 system does not change with initial conditions. The results derived in Chapter 7 hold.

F.5 The CoRoT-15 system

Figures F.11 and F.12 show the tidal evolution of the CoRoT-15 system for randomly chosen initial conditions $a = 0.045 \pm 0.01$ AU and $P_* = 3.9 \pm 0.4$ days. Apparently, the semi major axis is not very well constrained for this system. Still, most solutions show that the system will evolve into a double synchronous orbit, depending on $\frac{Q_*}{k_{2,*}}$ and remain there within the remaining stellar lifetime. Therefore, the results derived in Chapter 8 still hold despite the large uncertainty in semi major axis.
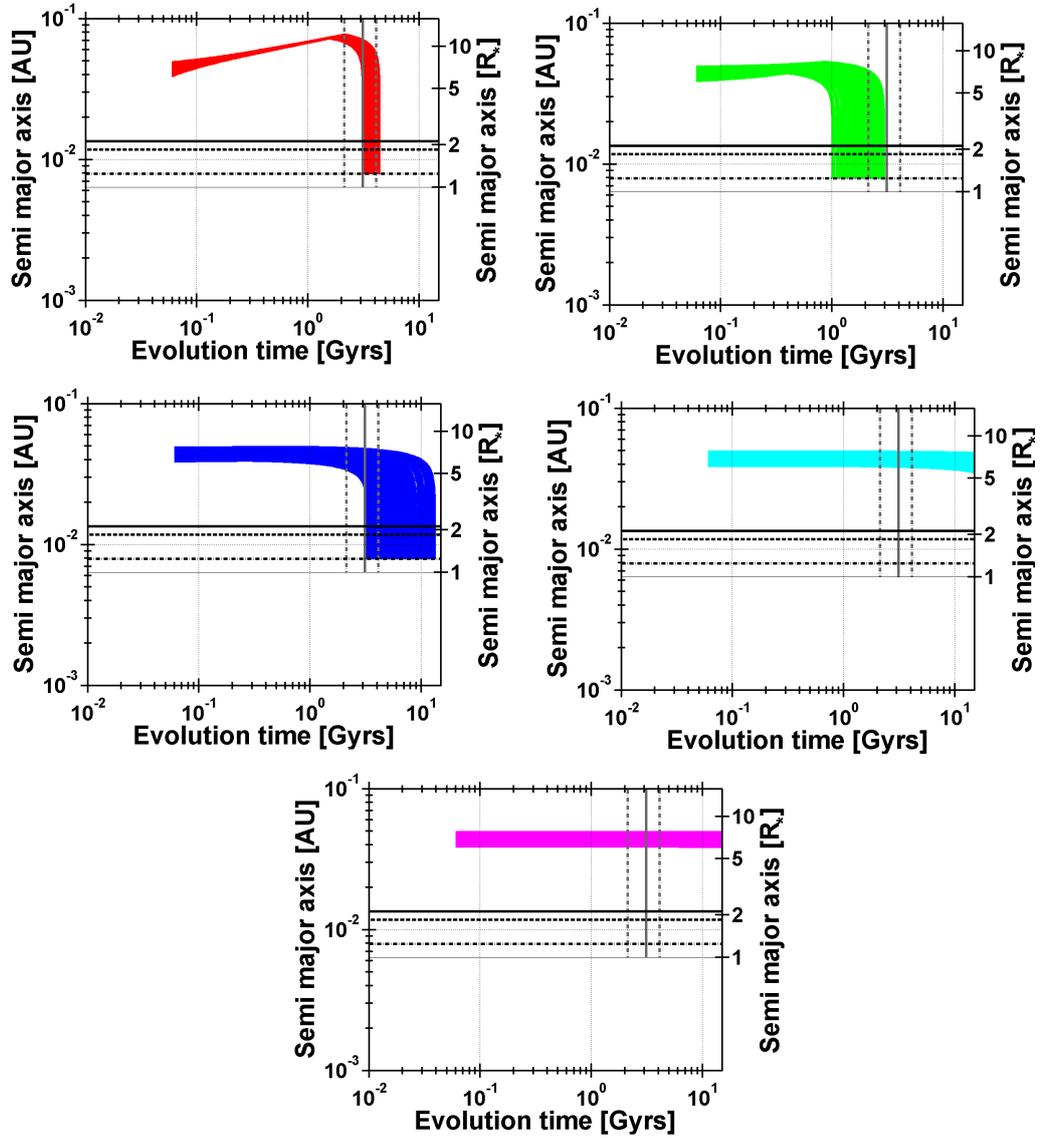
Figure F.9: Tidal evolution of the semi major axis of CoRoT-11b for randomly chosen initial conditions a and P_* within limits of uncertainty for $\frac{Q_*}{k_{2,*}} = 10^5 - 10^9$, $\frac{Q_{Pl}}{k_{2,Pl}} = 10^5$, and reduced magnetic braking. The vertical lines show the remaining stellar lifetime with limits of uncertainty.
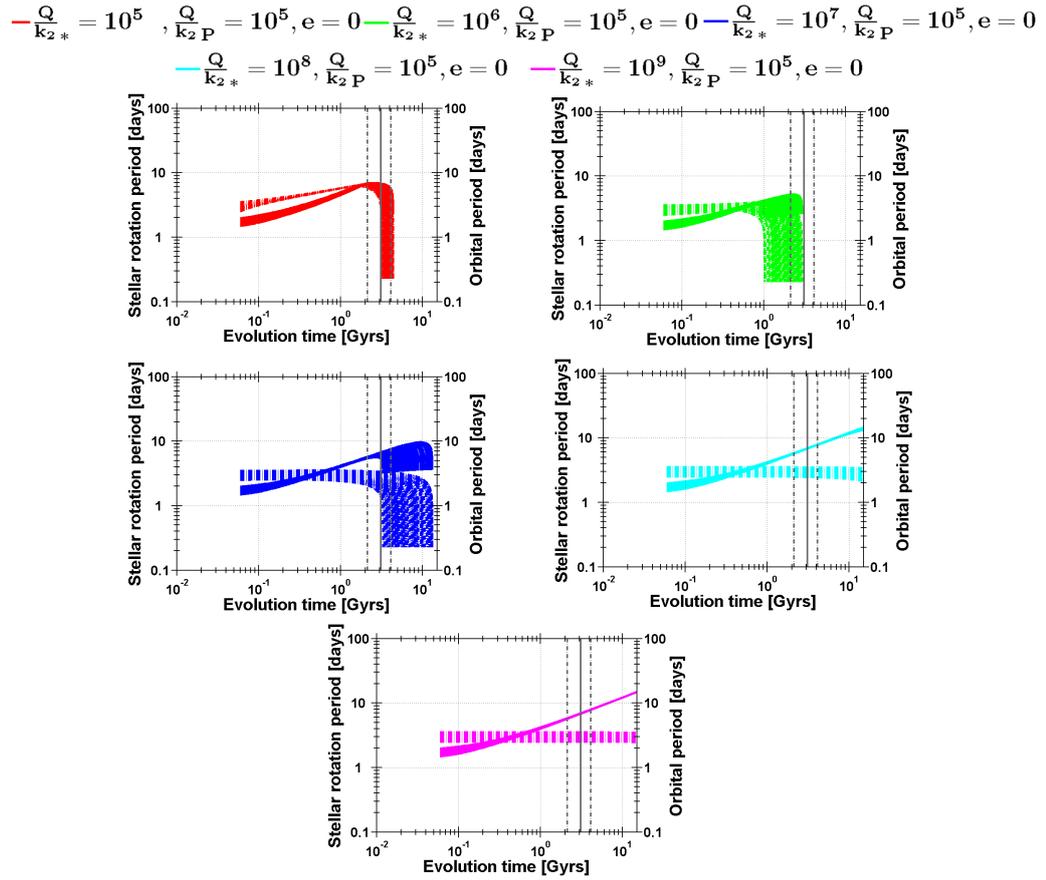
Figure F.10: Tidal evolution of the stellar rotation of CoRoT-11 for randomly chosen initial conditions a and P_* within limits of uncertainty for $\frac{Q_*}{k_{2,*}} = 10^5 - 10^9$, $\frac{Q_{Pl}}{k_{2,Pl}} = 10^5$, and reduced magnetic braking. The vertical lines show the remaining stellar lifetime with limits of uncertainty.
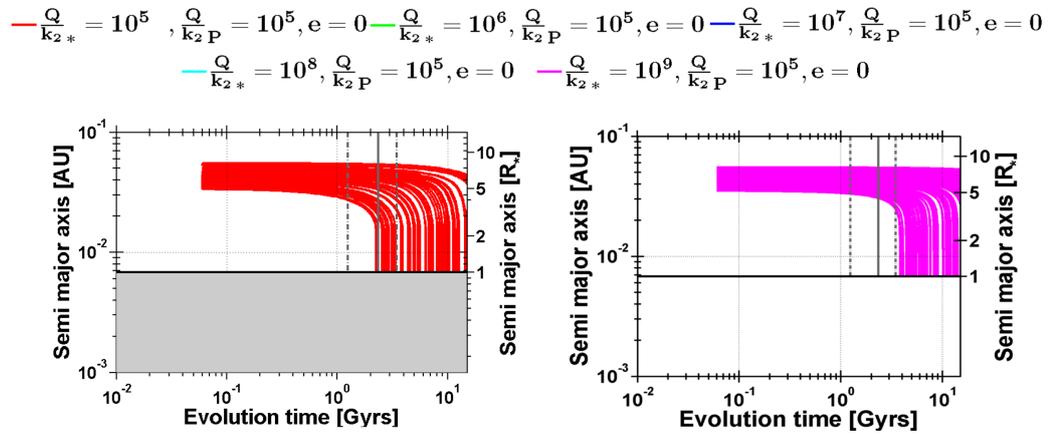
Figure F.11: Tidal evolution of the semi major axis of CoRoT-11b for randomly chosen initial conditions a and P_* within limits of uncertainty for $\frac{Q_*}{k_{2,*}} = 10^5$ and $\frac{Q_*}{k_{2,*}} = 10^9$, $\frac{Q_{Pl}}{k_{2,Pl}} = 10^5$, and reduced magnetic braking. The vertical lines show the remaining stellar lifetime with limits of uncertainty.
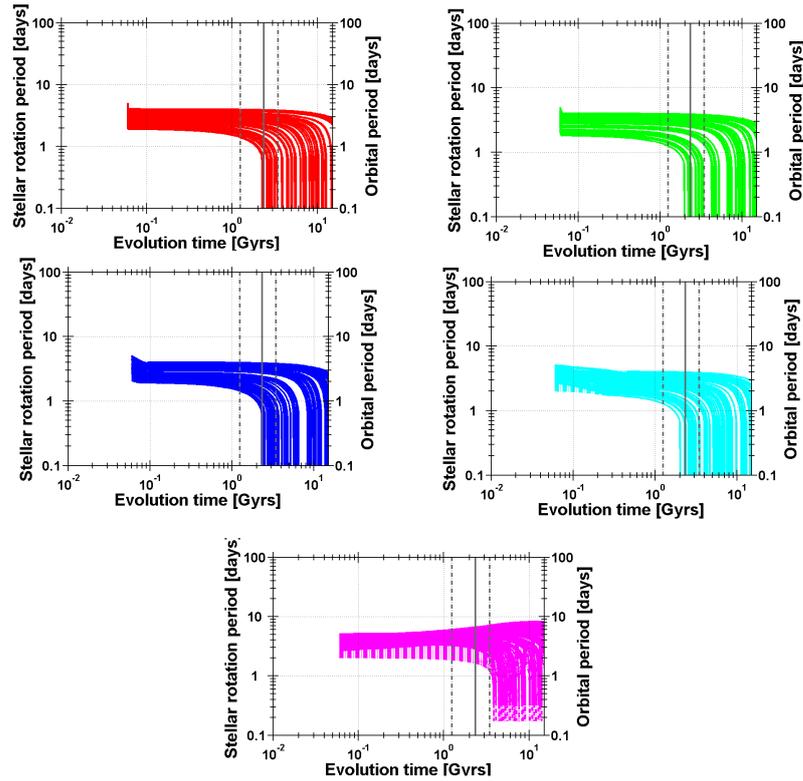
Figure F.12: Tidal evolution of the stellar rotation of CoRoT-11 for randomly chosen initial conditions a and P_* within limits of uncertainty for $\frac{Q_*}{k_{2,*}} = 10^5 - 10^9$, $\frac{Q_{Pl}}{k_{2,Pl}} = 10^5$, and reduced magnetic braking. The vertical lines show the remaining stellar lifetime with limits of uncertainty.

Appendix G

Proof that the double synchronous orbit is always forced into corrotation if $L_{orb} > L_{orb,crit}$

Let's assume that

$$\dot{\Omega}_* > \dot{n}, \tag{G.0.1}$$

where $\Omega_* > n$.

Using Kepler's third law $\dot{n}$ can be derived by

$$\dot{n} = -\frac{3}{2}\frac{\mu}{a^4 n}\dot{a}. \tag{G.0.2}$$

where $\mu = G(M_* + M_{Pl})$.

In the absence of magnetic braking, the condition $\dot{\Omega}_* > \dot{n}$ with $\Omega_* > n$ can be written as

$$\frac{3}{2I_*}\frac{k_{2,*}}{Q_*}\frac{M_{Pl}^2}{M_*(M_* + M_{Pl})}\left(\frac{R_*}{a}\right)^3 n^2 > \frac{9}{2}\mu\frac{k_{2,*}}{Q_*}\frac{M_{Pl}}{M_*}R_*^5 a^{-8}, \tag{G.0.3}$$

which reduces to and can be further rearranged as follows:

$$\frac{M_{Pl}}{I_*(M_* + M_{pl})}\frac{n^2}{a^3} > 3\mu R_*^2 a^{-8}. \tag{G.0.4}$$

In the following, $\mu = G(M_* + M_{Pl})$ is inserted, the relation rearranged, Kepler's third law $n^2 = G(M_* + M_{Pl})/a^3$ is applied and finally the relation is multiplied with

$M_* \cdot n$:

$$\frac{M_{Pl}}{G(M_* + M_{Pl})^2} n^2 a^5 > 3 I_* R_*^2 \tag{G.0.5}$$

$$\frac{M_{Pl}}{M_* + M_{Pl}} a^2 > 3 I_* R_*^2 \tag{G.0.6}$$

$$\frac{M_* M_{Pl}}{M_* + M_{Pl}} a^2 n > 3 I_* R_*^2 M_* n \tag{G.0.7}$$

The left hand side of the relation is L_{orb}, and the right hand side is – assuming that $\Omega_* \approx n$ – approximately $3 \cdot L_{rot,*}$.

Therefore, the relation $\dot{\Omega}_* > \dot{n}$ is automatically fulfilled near double synchronous rotation $\Omega_* \approx n$, if

$$L_{orb} > 3 L_{*,rot}, \tag{G.0.8}$$

which is one of the angular momentum requirements for a stable double synchronous orbit (Section 2.9, *Hut* (1980)). In other words, if the orbital angular momentum exceeds the critical value, the 'fictive' double synchronous orbit decays always faster than the planetary orbit allowing the double synchronous to 'catch up' with the planet.

Appendix H

Centrifugal versus gravitational force

It was shown several times that tidal friction has the potential to spin up the star considerably. It will be investigated if the centrifugal force of a rapidly rotating star may overcome the gravitational force. Following the treatment given in Section 2.12, the gravitational force F_G and centrifugal force F_C acting on a test mass δm on the surface of the star is investigated. In a coordinate system with the center of mass as its origin, the position vector of test mass δm and the axis of rotation shall be perpendicular to each other.

To guarantee stability, the gravitational force has to exceed the centrifugal force

$$F_G > FC \tag{H.0.1}$$

$$\frac{G\delta m M_*}{R_*^2} > \delta m \Omega_*^2 R_*. \tag{H.0.2}$$

This yields the following limit for Ω_*:

$$\Omega_* < \sqrt{\frac{GM_*}{R_*^3}}. \tag{H.0.3}$$

For a solar analogue star $R_* = 1\,R_{Sun}$ and $M_* = 1\,M_{Sun}$ this is:

$$\Omega_{Sun} < 6.273 \times 10^{-4}\mathrm{s}^{-1}, \tag{H.0.4}$$

which corresponds to a rotation period of $P_* = 0.116$ days or 2.78 hours.

This is, of course, only a first order treatment neglecting stellar deformation due to rotation and tides, the structure of the star and other forces. Still, it confirms

that the stars investigated in this work don't run the risk of being disrupted due to centrifugal forces when they are tidally spun up.

Bibliography

Alonso, R., M. Auvergne, A. Baglin, M. Ollivier, C. Moutou, D. Rouan, H. J. Deeg, S. Aigrain, J. M. Almenara, M. Barbieri, P. Barge, W. Benz, P. Bordé, F. Bouchy, R. de La Reza, M. Deleuil, R. Dvorak, A. Erikson, M. Fridlund, M. Gillon, P. Gondoin, T. Guillot, A. Hatzes, G. Hébrard, P. Kabath, L. Jorda, H. Lammer, A. Léger, A. Llebaria, B. Loeillet, P. Magain, M. Mayor, T. Mazeh, M. Pätzold, F. Pepe, F. Pont, D. Queloz, H. Rauer, A. Shporer, J. Schneider, B. Stecklum, S. Udry and G. Wuchterl, Transiting exoplanets from the CoRoT space mission. II. CoRoT-Exo-2b: a transiting planet around an active G star, *Astron. Astrophys.*, *482*, L21–L24, 2008.

Baglin, A., COROT: A minisat for pionnier science, asteroseismology and planets finding, *Advances in Space Research*, *31*, 345–349, 2003.

Baraffe, I., F. Selsis, G. Chabrier, T. S. Barman, F. Allard, P. H. Hauschildt and H. Lammer, The effect of evaporation on the evolution of close-in giant planets, *Astron. Astrophys.*, *419*, L13–L16, 2004.

Barge, P., A. Baglin, M. Auvergne, H. Rauer, A. Léger, J. Schneider, F. Pont, S. Aigrain, J.-M. Almenara, R. Alonso, M. Barbieri, P. Bordé, F. Bouchy, H. J. Deeg, D. La Reza, M. Deleuil, R. Dvorak, A. Erikson, M. Fridlund, M. Gillon, P. Gondoin, T. Guillot, A. Hatzes, G. Hebrard, L. Jorda, P. Kabath, H. Lammer, A. Llebaria, B. Loeillet, P. Magain,

T. Mazeh, C. Moutou, M. Ollivier, M. Pätzold, D. Queloz, D. Rouan, A. Shporer and G. Wuchterl, Transiting exoplanets from the CoRoT space mission. I. CoRoT-Exo-1b: a low-density short-period planet around a G0V star, *Astron. Astrophys.*, *482*, L17–L20, 2008.

Barnes, S. A., An Assessment of the Rotation Rates of the Host Stars of Extrasolar Planets, *Astrophys. J.*, *561*, 1095–1106, 2001.

Barnes, S. A., On the Rotational Evolution of Solar- and Late-Type Stars, Its Magnetic Origins, and the Possibility of Stellar Gyrochronology, *Astrophys. J.*, *586*, 464–479, 2003.

Barnes, S. A., Ages for Illustrative Field Stars Using Gyrochronology: Viability, Limitations, and Errors, *Astrophys. J.*, *669*, 1167–1189, 2007.

Batalha, N. M., W. J. Borucki, S. T. Bryson, L. A. Buchhave, D. A. Caldwell, J. Christensen-Dalsgaard, D. Ciardi, E. W. Dunham, F. Fressin, T. N. Gautier, III, R. L. Gilliland, M. R. Haas, S. B. Howell, J. M. Jenkins, H. Kjeldsen, D. G. Koch, D. W. Latham, J. J. Lissauer, G. W. Marcy, J. F. Rowe, D. D. Sasselov, S. Seager, J. H. Steffen, G. Torres, G. S. Basri, T. M. Brown, D. Charbonneau, J. Christiansen, B. Clarke, W. D. Cochran, A. Dupree, D. C. Fabrycky, D. Fischer, E. B. Ford, J. Fortney, F. R. Girouard, M. J. Holman, J. Johnson, H. Isaacson, T. C. Klaus, P. Machalek, A. V. Moorehead, R. C. Morehead, D. Ragozzine, P. Tenenbaum, J. Twicken, S. Quinn, J. VanCleve, L. M. Walkowicz, W. F. Welsh, E. Devore and A. Gould, Kepler's First Rocky Planet: Kepler-10b, *Astrophys. J.*, *729*, 27–+, 2011.

Bean, J. L., A. Seifahrt, H. Hartman, H. Nilsson, A. Reiners, S. Dreizler, T. J. Henry and G. Wiedemann, The Proposed Giant Planet Orbiting VB 10 Does Not Exist, *Astrophys. J., Lett.*, *711*, L19–L23, 2010.

Bennett, D. P., I. A. Bond, A. Udalski, T. Sumi, F. Abe, A. Fukui, K. Furusawa, J. B. Hearnshaw, S. Holderness, Y. Itow, K. Kamiya, A. V. Korpela, P. M. Kilmartin, W. Lin, C. H. Ling, K. Masuda, Y. Matsubara, N. Miyake, Y. Muraki, M. Nagaya, T. Okumura, K. Ohnishi, Y. C. Perrott, N. J. Rattenbury, T. Sako, T. Saito, S. Sato, L. Skuljan, D. J. Sullivan, W. L. Sweatman, P. J. Tristram, P. C. M. Yock, M. Kubiak, M. K. Szymański, G. Pietrzyński, I. Soszyński, O. Szewczyk, Ł. Wyrzykowski, K. Ulaczyk, V. Batista, J. P. Beaulieu, S. Brillant, A. Cassan, P. Fouqué, P. Kervella, D. Kubas and J. B. Marquette, A Low-Mass Planet with a Possible Sub-Stellar-Mass Host in Microlensing Event MOA-2007-BLG-192, *Astrophys. J.*, *684*, 663–683, 2008.

Bond, I. A., A. Udalski, M. Jaroszyński, N. J. Rattenbury, B. Paczyński, I. Soszyński, L. Wyrzykowski, M. K. Szymański, M. Kubiak, O. Szewczyk, K. Żebruń, G. Pietrzyński, F. Abe, D. P. Bennett, S. Eguchi, Y. Furuta, J. B. Hearnshaw, K. Kamiya, P. M. Kilmartin, Y. Kurata, K. Masuda, Y. Matsubara, Y. Muraki, S. Noda, K. Okajima, T. Sako, T. Sekiguchi, D. J. Sullivan, T. Sumi, P. J. Tristram, T. Yanagisawa and P. C. M. Yock, OGLE 2003-BLG-235/MOA 2003-BLG-53: A Planetary Microlensing Event, *Astrophys. J., Lett.*, *606*, L155–L158, 2004.

Bonfils, X., X. Delfosse, S. Udry, T. Forveille, M. Mayor, C. Perrier, F. Bouchy, M. Gillon, C. Lovis, F. Pepe, D. Queloz, N. C. Santos, D. Ségransan and J.-L. Bertaux, The HARPS search for southern extra-solar planets XXXI. The M-dwarf sample, *ArXiv e-prints*, November 2011.

Bonomo, A. S., A. Santerne, R. Alonso, J. Gazzano, M. Havel, S. Aigrain, M. Auvergne, A. Baglin, M. Barbieri, P. Barge, W. Benz, P. Bordé, F. Bouchy, H. Bruntt, J. Cabrera, A. C. Cameron, L. Carone,

S. Carpano, S. Csizmadia, M. Deleuil, H. J. Deeg, R. Dvorak, A. Erikson, S. Ferraz-Mello, M. Fridlund, D. Gandolfi, M. Gillon, E. Guenther, T. Guillot, A. Hatzes, G. Hébrard, L. Jorda, H. Lammer, A. F. Lanza, A. Léger, A. Llebaria, M. Mayor, T. Mazeh, C. Moutou, M. Ollivier, M. Pätzold, F. Pepe, D. Queloz, H. Rauer, D. Rouan, B. Samuel, J. Schneider, B. Tingley, S. Udry and G. Wuchterl, Transiting exoplanets from the CoRoT space mission. X. CoRoT-10b: a giant planet in a 13.24 day eccentric orbit, *Astron. Astrophys.*, *520*, A65+, 2010.

Bordé, P., F. Bouchy, M. Deleuil, J. Cabrera, L. Jorda, C. Lovis, S. Csizmadia, S. Aigrain, J. M. Almenara, R. Alonso, M. Auvergne, A. Baglin, P. Barge, W. Benz, A. S. Bonomo, H. Bruntt, L. Carone, S. Carpano, H. Deeg, R. Dvorak, A. Erikson, S. Ferraz-Mello, M. Fridlund, D. Gandolfi, J. Gazzano, M. Gillon, E. Guenther, T. Guillot, P. Guterman, A. Hatzes, M. Havel, G. Hébrard, H. Lammer, A. Léger, M. Mayor, T. Mazeh, C. Moutou, M. Pätzold, F. Pepe, M. Ollivier, D. Queloz, H. Rauer, D. Rouan, B. Samuel, A. Santerne, J. Schneider, B. Tingley, S. Udry, J. Weingrill and G. Wuchterl, Transiting exoplanets from the CoRoT space mission. XI. CoRoT-8b: a hot and dense sub-Saturn around a K1 dwarf, *Astron. Astrophys.*, *520*, A66+, 2010.

Born, G. H. and T. C. Duxbury, The motions of PHOBOS and Deimos from Mariner 9 TV data, *Celestial Mechanics*, *12*, 77–88, 1975.

Borucki, W. J., D. G. Koch, G. Basri, N. Batalha, T. M. Brown, S. T. Bryson, D. Caldwell, J. Christensen-Dalsgaard, W. D. Cochran, E. De-Vore, E. W. Dunham, T. N. Gautier, III, J. C. Geary, R. Gilliland, A. Gould, S. B. Howell, J. M. Jenkins, D. W. Latham, J. J. Lissauer, G. W. Marcy, J. Rowe, D. Sasselov, A. Boss, D. Charbonneau, D. Ciardi, L. Doyle, A. K. Dupree, E. B. Ford, J. Fortney, M. J. Holman, S. Seager,

J. H. Steffen, J. Tarter, W. F. Welsh, C. Allen, L. A. Buchhave, J. L. Christiansen, B. D. Clarke, S. Das, J.-M. Désert, M. Endl, D. Fabrycky, F. Fressin, M. Haas, E. Horch, A. Howard, H. Isaacson, H. Kjeldsen, J. Kolodziejczak, C. Kulesa, J. Li, P. W. Lucas, P. Machalek, D. McCarthy, P. MacQueen, S. Meibom, T. Miquel, A. Prsa, S. N. Quinn, E. V. Quintana, D. Ragozzine, W. Sherry, A. Shporer, P. Tenenbaum, G. Torres, J. D. Twicken, J. Van Cleve, L. Walkowicz, F. C. Witteborn **and M. Still**, Characteristics of Planetary Candidates Observed by Kepler. II. Analysis of the First Four Months of Data, *Astrophys. J.*, *736*, 19–+, 2011.

Bouchy, F., D. Queloz, M. Deleuil, B. Loeillet, A. P. Hatzes, S. Aigrain, R. Alonso, M. Auvergne, A. Baglin, P. Barge, W. Benz, P. Bordé, H. J. Deeg, R. de La Reza, R. Dvorak, A. Erikson, M. Fridlund, P. Gondoin, T. Guillot, G. Hébrard, L. Jorda, H. Lammer, A. Léger, A. Llebaria, P. Magain, M. Mayor, C. Moutou, M. Ollivier, M. Pätzold, F. Pepe, F. Pont, H. Rauer, D. Rouan, J. Schneider, A. H. M. J. Triaud, S. Udry and G. Wuchterl, Transiting exoplanets from the CoRoT space mission. III. The spectroscopic transit of CoRoT-Exo-2b with SOPHIE and HARPS, *Astron. Astrophys.*, *482*, L25–L28, 2008.

Bouchy, F., M. Deleuil, T. Guillot, S. Aigrain, L. Carone, W. D. Cochran, J. M. Almenara, R. Alonso, M. Auvergne, A. Baglin, P. Barge, A. S. Bonomo, P. Bordé, S. Csizmadia, K. de Bondt, H. J. Deeg, R. F. Díaz, R. Dvorak, M. Endl, A. Erikson, S. Ferraz-Mello, M. Fridlund, D. Gandolfi, J. C. Gazzano, N. Gibson, M. Gillon, E. Guenther, A. Hatzes, M. Havel, G. Hébrard, L. Jorda, A. Léger, C. Lovis, A. Llebaria, H. Lammer, P. J. MacQueen, T. Mazeh, C. Moutou, A. Ofir, M. Ollivier, H. Parviainen, M. Pätzold, D. Queloz, H. Rauer, D. Rouan, A. Santerne, J. Schneider, B. Tingley and G. Wuchterl, Transiting exoplanets from

the CoRoT space mission. XV. CoRoT-15b: a brown-dwarf transiting companion, *Astron. Astrophys.*, *525*, A68+, 2011.

Bouvier, J., M. Forestini and S. Allain, The angular momentum evolution of low-mass stars., *Astron. Astrophys.*, *326*, 1023–1043, 1997.

Broeg, C. and G. Wuchterl, The formation of HD149026b, *Mon. Not. R. Astron. Soc.*, *376*, L62–L66, 2007.

Brown, R. A. and C. J. Burrows, On the feasibility of detecting extrasolar planets by reflected starlight using the Hubble Space Telescope, *Icarus*, *87*, 484–497, 1990.

Bruntt, H., M. Deleuil, M. Fridlund, R. Alonso, F. Bouchy, A. Hatzes, M. Mayor, C. Moutou and D. Queloz, Improved stellar parameters of CoRoT-7. A star hosting two super Earths, *Astron. Astrophys.*, *519*, A51+, 2010.

Cabrera, J., M. Fridlund, M. Ollivier, D. Gandolfi, S. Csizmadia, R. Alonso, S. Aigrain, A. Alapini, J.-M. Almenara, P. Barge, A. S. Bonomo, P. Bordé, F. Bouchy, H. Bruntt, L. Carone, S. Carpano, H. J. Deeg, R. de La Reza, M. Deleuil, R. Dvorak, A. Erikson, M. Gillon, P. Gondoin, E. W. Guenther, T. Guillot, M. Hartmann, A. Hatzes, G. Hebrard, L. Jorda, H. Lammer, A. Léger, A. Llebaria, C. Lovis, P. Magain, M. Mayor, T. Mazeh, C. Moutou, A. Ofir, M. Pätzold, F. Pepe, F. Pont, D. Queloz, M. Rabus, H. Rauer, C. Régulo, S. Renner, D. Rouan, B. Samuel, A. Santerne, J. Schneider, A. Shporer, B. Stecklum, B. Tingley, S. Udry and G. Wuchterl, Planetary transit candidates in CoRoT-LRc01 field, *Astron. Astrophys.*, *506*, 501–517, 2009.

Cabrera, J., H. Bruntt, M. Ollivier, R. F. Díaz, S. Csizmadia, S. Aigrain, R. Alonso, J. Almenara, M. Auvergne, A. Baglin, P. Barge, A. S. Bonomo, P. Bordé, F. Bouchy, L. Carone, S. Carpano, M. Deleuil, H. J.

Deeg, R. Dvorak, A. Erikson, S. Ferraz-Mello, M. Fridlund, D. Gandolfi, J. Gazzano, M. Gillon, E. W. Guenther, T. Guillot, A. Hatzes, M. Havel, G. Hébrard, L. Jorda, A. Léger, A. Llebaria, H. Lammer, C. Lovis, T. Mazeh, C. Moutou, A. Ofir, P. von Paris, M. Pätzold, D. Queloz, H. Rauer, D. Rouan, A. Santerne, J. Schneider, B. Tingley, R. Titz-Weider and G. Wuchterl, Transiting exoplanets from the CoRoT space mission . XIII. CoRoT-13b: a dense hot Jupiter in transit around a star with solar metallicity and super-solar lithium content, *Astron. Astrophys.*, *522*, A110+, 2010.

Carone, L. and M. Pätzold, Constraints on the tidal dissipation factor of a main sequence star: The case of OGLE-TR-56b, *Planet. Space Sci.*, *55*, 643–650, 2007.

Carone, L., D. Gandolfi, J. Cabrera, A. P. Hatzes, H. J. Deeg, S. Csizmadia, M. Paetzold, J. Weingrill, S. Aigrain, R. Alonso, A. Alapini, J. . Almenara, M. Auvergne, A. Baglin, P. Barge, A. S. Bonomo, P. Bordé, F. Bouchy, H. Bruntt, S. Carpano, W. D. Cochran, M. Deleuil, R. F. Díaz, S. Dreizler, R. Dvorak, J. Eisloeffel, P. Eigmueller, M. Endl, A. Erikson, S. Ferraz-Mello, M. Fridlund, J. . Gazzano, N. Gibson, M. Gillon, P. Gondoin, S. Grziwa, E. W. Guenther, T. Guillot, M. Hartmann, M. Havel, G. Hébrard, L. Jorda, P. Kabath, A. Léger, A. Llebaria, H. Lammer, C. Lovis, P. J. MacQueen, M. Mayor, T. Mazeh, C. Moutou, L. Nortmann, A. Ofir, M. Ollivier, H. Parviainen, F. Pepe, F. Pont, D. Queloz, M. Rabus, H. Rauer, C. Régulo, S. Renner, R. de la Reza, D. Rouan, A. Santerne, B. Samuel, J. Schneider, A. Shporer, B. Stecklum, L. Tal-Or, B. Tingley, S. Udry and G. Wuchterl, Planetary transit candidates in the CoRoT LRa01 field, *ArXiv e-prints*, Oktober 2011.

Carpano, S., J. Cabrera, R. Alonso, P. Barge, S. Aigrain, J.-M. Almenara, P. Bordé, F. Bouchy, L. Carone, H. J. Deeg, R. de La Reza, M. Deleuil,

R. Dvorak, A. Erikson, F. Fressin, M. Fridlund, P. Gondoin, T. Guillot, A. Hatzes, L. Jorda, H. Lammer, A. Léger, A. Llebaria, P. Magain, C. Moutou, A. Ofir, M. Ollivier, E. Janot-Pacheco, M. Pätzold, F. Pont, D. Queloz, H. Rauer, C. Régulo, S. Renner, D. Rouan, B. Samuel, J. Schneider and G. Wuchterl, Planetary transit candidates in Corot-IRa01 field, *Astron. Astrophys., 506*, 491–500, 2009.

Cassan, A., D. Kubas, J.-P. Beaulieu, M. Dominik, K. Horne, J. Greenhill, J. Wambsganss, J. Menzies, A. Williams, U. G. Jørgensen, A. Udalski, D. P. Bennett, M. D. Albrow, V. Batista, S. Brillant, J. A. R. Caldwell, A. Cole, C. Coutures, K. H. Cook, S. Dieters, D. D. Prester, J. Donatowicz, P. Fouqué, K. Hill, N. Kains, S. Kane, J.-B. Marquette, R. Martin, K. R. Pollard, K. C. Sahu, C. Vinter, D. Warren, B. Watson, M. Zub, T. Sumi, M. K. Szymański, M. Kubiak, R. Poleski, I. Soszynski, K. Ulaczyk, G. Pietrzyński and Ł. Wyrzykowski, One or more bound planets per Milky Way star from microlensing observations, *Nature, 481*, 167–169, 2012.

Chandrasekhar, S., *Ellipsoidal figures of equilibrium*, 1987.

Chauvin, G., A.-M. Lagrange, C. Dumas, B. Zuckerman, D. Mouillet, I. Song, J.-L. Beuzit and P. Lowrance, A giant planet candidate near a young brown dwarf. Direct VLT/NACO observations using IR wavefront sensing, *Astron. Astrophys., 425*, L29–L32, 2004.

Csizmadia, S., C. Moutou, M. Deleuil, J. Cabrera, M. Fridlund, D. Gandolfi, S. Aigrain, R. Alonso, J.-M. Almenara, M. Auvergne, A. Baglin, P. Barge, A. S. Bonomo, P. Bordé, F. Bouchy, H. Bruntt, L. Carone, S. Carpano, C. Cavarroc, W. Cochran, H. J. Deeg, R. F. Díaz, R. Dvorak, M. Endl, A. Erikson, S. Ferraz-Mello, T. Fruth, J.-C. Gazzano,

M. Gillon, E. W. Guenther, T. Guillot, A. Hatzes, M. Havel, G. Hébrard, E. Jehin, L. Jorda, A. Léger, A. Llebaria, H. Lammer, C. Lovis, P. J. MacQueen, T. Mazeh, M. Ollivier, M. Pätzold, D. Queloz, H. Rauer, D. Rouan, A. Santerne, J. Schneider, B. Tingley, R. Titz-Weider and G. Wuchterl, Transiting exoplanets from the CoRoT space mission. XVII. The hot Jupiter CoRoT-17b: a very old planet, *Astron. Astrophys.*, *531*, A41, 2011.

Deeg, H. J., C. Moutou, A. Erikson, S. Csizmadia, B. Tingley, P. Barge, H. Bruntt, M. Havel, S. Aigrain, J. M. Almenara, R. Alonso, M. Auvergne, A. Baglin, M. Barbieri, W. Benz, A. S. Bonomo, P. Bordé, F. Bouchy, J. Cabrera, L. Carone, S. Carpano, D. Ciardi, M. Deleuil, R. Dvorak, S. Ferraz-Mello, M. Fridlund, D. Gandolfi, J. Gazzano, M. Gillon, P. Gondoin, E. Guenther, T. Guillot, R. D. Hartog, A. Hatzes, M. Hidas, G. Hébrard, L. Jorda, P. Kabath, H. Lammer, A. Léger, T. Lister, A. Llebaria, C. Lovis, M. Mayor, T. Mazeh, M. Ollivier, M. Pätzold, F. Pepe, F. Pont, D. Queloz, M. Rabus, H. Rauer, D. Rouan, B. Samuel, J. Schneider, A. Shporer, B. Stecklum, R. Street, S. Udry, J. Weingrill and G. Wuchterl, A transiting giant planet with a temperature between 250K and 430K, *Nature*, *464*, 384–387, 2010.

Deleuil, M., H. J. Deeg, R. Alonso, F. Bouchy, D. Rouan, M. Auvergne, A. Baglin, S. Aigrain, J. M. Almenara, M. Barbieri, P. Barge, H. Bruntt, P. Bordé, A. Collier Cameron, S. Csizmadia, R. de La Reza, R. Dvorak, A. Erikson, M. Fridlund, D. Gandolfi, M. Gillon, E. Guenther, T. Guillot, A. Hatzes, G. Hébrard, L. Jorda, H. Lammer, A. Léger, A. Llebaria, B. Loeillet, M. Mayor, T. Mazeh, C. Moutou, M. Ollivier, M. Pätzold, F. Pont, D. Queloz, H. Rauer, J. Schneider, A. Shporer, G. Wuchterl and S. Zucker, Transiting exoplanets from the CoRoT space mission . VI. CoRoT-Exo-3b: the first secure inhabitant of the brown-dwarf desert, *Astron. Astrophys.*,

491, 889–897, 2008.

Deleuil, M., A. S. Bonomo, S. Ferraz-Mello, A. Erikson, F. Bouchy, M. Havel, S. Aigrain, J. . Almenara, R. Alonso, M. Auvergne, A. Baglin, P. Barge, P. Bordé, H. Bruntt, J. Cabrera, S. Carpano, C. Cavarroc, S. Csizmadia, C. Damiani, H. J. Deeg, R. Dvorak, M. Fridlund, G. Hébrard, D. Gandolfi, M. Gillon, E. Guenther, T. Guillot, A. Hatzes, L. Jorda, A. Léger, H. Lammer, T. Mazeh, C. Moutou, M. Ollivier, A. Ofir, H. Parviainen, D. Queloz, H. Rauer, A. Rodríguez, D. Rouan, A. Santerne, J. Schneider, L. Tal-Or, B. Tingley, J. Weingrill and G. Wuchterl, XX. CoRoT-20b: A very high density, high eccentricity transiting giant planet, *ArXiv e-prints*, September 2011.

Delfosse, X., X. Bonfils, T. Forveille, S. Udry, M. Mayor, F. Bouchy, M. Gillon, C. Lovis, V. Neves, F. Pepe, C. Perrier, D. Queloz, N. C. Santos and D. Ségransan, The HARPS search for southern extra-solar planets XXXV. Super-Earths around the M-dwarf neighbors Gl433 and Gl667C, *ArXiv e-prints*, Februar 2012.

Dermott, S. F., Shapes and gravitational moments of satellites and asteroids, *Icarus*, *37*, 575–586, 1979*a*.

Dermott, S. F., Tidal dissipation in the solid cores of the major planets, *Icarus*, *37*, 310–321, 1979*b*.

Dobbs-Dixon, I., D. N. C. Lin and R. A. Mardling, Spin-Orbit Evolution of Short-Period Planets, *Astrophys. J.*, *610*, 464–476, 2004.

Doodson, A. T., The Harmonic Development of the Tide-Generating Potential, *Royal Society of London Proceedings Series A*, *100*, 305–329, 1921.

Dziembowski, W. A., P. R. Goode, A. A. Pamyatnykh and R. Sienkiewicz, A seismic model of the Sun's interior, *Astrophys. J.*, *432*, 417–426, 1994.

Efroimsky, M. and J. G. Williams, Tidal torques: a critical review of some techniques, *Celestial Mechanics and Dynamical Astronomy*, *104*, 257–289, 2009.

Fridlund, M., G. Hébrard, R. Alonso, M. Deleuil, D. Gandolfi, M. Gillon, H. Bruntt, A. Alapini, S. Csizmadia, T. Guillot, H. Lammer, S. Aigrain, J. M. Almenara, M. Auvergne, A. Baglin, P. Barge, P. Bordé, F. Bouchy, J. Cabrera, L. Carone, S. Carpano, H. J. Deeg, R. de La Reza, R. Dvorak, A. Erikson, S. Ferraz-Mello, E. Guenther, P. Gondoin, R. den Hartog, A. Hatzes, L. Jorda, A. Léger, A. Llebaria, P. Magain, T. Mazeh, C. Moutou, M. Ollivier, M. Pätzold, D. Queloz, H. Rauer, D. Rouan, B. Samuel, J. Schneider, A. Shporer, B. Stecklum, B. Tingley, J. Weingrill and G. Wuchterl, Transiting exoplanets from the CoRoT space mission. IX. CoRoT-6b: a transiting "hot Jupiter" planet in an 8.9d orbit around a low-metallicity star, *Astron. Astrophys.*, *512*, A14, 2010.

Fuhrmann, K., R. Chini, V. H. Hoffmeister and O. Stahl, Discovery of the nearby F6V star HR 3220 as a field blue straggler, *Mon. Not. R. Astron. Soc.*, *416*, 391–392, 2011.

Gandolfi, D., G. Hébrard, R. Alonso, M. Deleuil, E. W. Guenther, M. Fridlund, M. Endl, P. Eigmüller, S. Csizmadia, M. Havel, S. Aigrain, M. Auvergne, A. Baglin, P. Barge, A. S. Bonomo, P. Bordé, F. Bouchy, H. Bruntt, J. Cabrera, S. Carpano, L. Carone, W. D. Cochran, H. J. Deeg, R. Dvorak, J. Eislöffel, A. Erikson, S. Ferraz-Mello, J. Gazzano, N. B. Gibson, M. Gillon, P. Gondoin, T. Guillot, M. Hartmann, A. Hatzes, L. Jorda, P. Kabath, A. Léger, A. Llebaria, H. Lammer, P. J. MacQueen, M. Mayor, T. Mazeh, C. Moutou, M. Ollivier, M. Pätzold,

F. Pepe, D. Queloz, H. Rauer, D. Rouan, B. Samuel, J. Schneider, B. Stecklum, B. Tingley, S. Udry and G. Wuchterl, Transiting exoplanets from the CoRoT space mission. XIV. CoRoT-11b: a transiting massive "hot-Jupiter" in a prograde orbit around a rapidly rotating F-type star, *Astron. Astrophys.*, *524*, A55+, 2010.

Gatewood, G. and H. Eichhorn, An unsuccessful search for a planetary companion of Barnard's star BD +4 3561., *Astrophys. J.*, *78*, 769–776, 1973.

Gillon, M., A. Hatzes, S. Csizmadia, M. Fridlund, M. Deleuil, S. Aigrain, R. Alonso, M. Auvergne, A. Baglin, P. Barge, S. I. Barnes, A. S. Bonomo, P. Bordé, F. Bouchy, H. Bruntt, J. Cabrera, L. Carone, S. Carpano, W. D. Cochran, H. J. Deeg, R. Dvorak, M. Endl, A. Erikson, S. Ferraz-Mello, D. Gandolfi, J. C. Gazzano, E. Guenther, T. Guillot, M. Havel, G. Hébrard, L. Jorda, A. Léger, A. Llebaria, H. Lammer, C. Lovis, M. Mayor, T. Mazeh, J. Montalbán, C. Moutou, A. Ofir, M. Ollivier, M. Pätzold, F. Pepe, D. Queloz, H. Rauer, D. Rouan, B. Samuel, A. Santerne, J. Schneider, B. Tingley, S. Udry, J. Weingrill and G. Wuchterl, Transiting exoplanets from the CoRoT space mission. XII. CoRoT-12b: a short-period low-density planet transiting a solar analog star, *Astron. Astrophys.*, *520*, A97+, 2010.

Goldreich, P., An explanation of the frequent occurrence of commensurable mean motions in the solar system, *Mon. Not. R. Astron. Soc.*, *130*, 159–+, 1965.

Goldreich, P. and P. D. Nicholson, Turbulent viscosity and Jupiter's tidal Q, *Icarus*, *30*, 301–304, 1977.

Goldreich, P. and S. Soter, Q in the Solar System, *Icarus*, *5*, 375–389, 1966.

Gould, H., J. Tobochnik and W. Christian, *An introduction to computer simulation methods*, 2006.

Grziwa, S., M. Pätzold and L. Carone, The needle in the haystack: searching for transiting extrasolar planets in CoRoT stellar light curves, *Mon. Not. R. Astron. Soc.*, *420*, 1045–1052, 2012.

Guenther, E. W., R. F. Díaz, J.-C. Gazzano, T. Mazeh, D. Rouan, N. Gibson, S. Csizmadia, S. Aigrain, R. Alonso, J. M. Almenara, M. Auvergne, A. Baglin, P. Barge, A. S. Bonomo, P. Bordé, F. Bouchy, H. Bruntt, J. Cabrera, L. Carone, S. Carpano, C. Cavarroc, H. J. Deeg, M. Deleuil, S. Dreizler, R. Dvorak, A. Erikson, S. Ferraz-Mello, M. Fridlund, D. Gandolfi, M. Gillon, T. Guillot, A. Hatzes, M. Havel, G. Hébrard, E. Jehin, L. Jorda, H. Lammer, A. Léger, C. Moutou, L. Nortmann, M. Ollivier, A. Ofir, T. Pasternacki, M. Pätzold, H. Parviainen, D. Queloz, H. Rauer, B. Samuel, A. Santerne, J. Schneider, L. Tal-Or, B. Tingley, J. Weingrill and G. Wuchterl, Transiting exoplanets from the CoRoT space mission. XXI. CoRoT-19b: a low density planet orbiting an old inactive F9V-star, *Astron. Astrophys.*, *537*, A136, 2012.

Halbwachs, J. L., F. Arenou, M. Mayor, S. Udry and D. Queloz, Exploring the brown dwarf desert with Hipparcos, *Astron. Astrophys.*, *355*, 581–594, 2000.

Harrington, J., B. M. Hansen, S. H. Luszcz, S. Seager, D. Deming, K. Menou, J. Y.-K. Cho and L. J. Richardson, The Phase-Dependent Infrared Brightness of the Extrasolar Planet υ Andromedae b, *Science*, *314*, 623–626, 2006.

Hatzes, A. P., R. Dvorak, G. Wuchterl, P. Guterman, M. Hartmann, M. Fridlund, D. Gandolfi, E. Guenther and M. Pätzold, An investigation into the radial velocity variations of CoRoT-7, *Astron. Astrophys.*, *520*, A93+, 2010.

Hatzes, A. P., M. Fridlund, G. Nachmani, T. Mazeh, D. Valencia, G. Hebrard, L. Carone, M. Paetzold, S. Udry, F. Bouchy, P. Borde, H. Deeg, B. Tingley, R. Dvorak, D. Gandolfi, S. Ferraz-Mello, G. Wuchterl, E. Guenther, H. Rauer, A. Erikson, J. Cabrera, S. Csizmadia, A. Leger, H. Lammer, J. Weingrill, D. Queloz, R. Alonso and J. Schneider, On the Mass of CoRoT-7b, *ArXiv e-prints*, Mai 2011.

Hayashi, C., Structure of the Solar Nebula, Growth and Decay of Magnetic Fields and Effects of Magnetic and Turbulent Viscosities on the Nebula, *Progress of Theoretical Physics Supplement*, *70*, 35–53, 1981.

Hébrard, G., T. M. Evans, R. Alonso, M. Fridlund, A. Ofir, S. Aigrain, T. Guillot, J. M. Almenara, M. Auvergne, A. Baglin, P. Barge, A. S. Bonomo, P. Bordé, F. Bouchy, J. Cabrera, L. Carone, S. Carpano, C. Cavarroc, S. Csizmadia, H. J. Deeg, M. Deleuil, R. F. Díaz, R. Dvorak, A. Erikson, S. Ferraz-Mello, D. Gandolfi, N. Gibson, M. Gillon, E. Guenther, A. Hatzes, M. Havel, L. Jorda, H. Lammer, A. Léger, A. Llebaria, T. Mazeh, C. Moutou, M. Ollivier, H. Parviainen, M. Pätzold, D. Queloz, H. Rauer, D. Rouan, A. Santerne, J. Schneider, B. Tingley and G. Wuchterl, Transiting exoplanets from the CoRoT space mission. XVIII. CoRoT-18b: a massive hot Jupiter on a prograde, nearly aligned orbit, *Astron. Astrophys.*, *533*, A130, 2011.

Heintz, W. D., Reexamination of suspected unresolved binaries, *Astrophys. J.*, *220*, 931–934, 1978.

Heller, R., B. Jackson, R. Barnes, R. Greenberg and D. Homeier, Tidal effects on brown dwarfs: application to the eclipsing binary 2MASS J05352184-0546085. The anomalous temperature reversal in the context of tidal heating, *Astron. Astrophys.*, *514*, A22, 2010.

Hershey, J. L., Astrometric analysis of the field of AC +65 6955 from plates taken with the Sproul 24-inch refractor., *Astronomical Journal*, *78*, 421–425, 1973.

Holman, M. J., D. C. Fabrycky, D. Ragozzine, E. B. Ford, J. H. Steffen, W. F. Welsh, J. J. Lissauer, D. W. Latham, G. W. Marcy, L. M. Walkowicz, N. M. Batalha, J. M. Jenkins, J. F. Rowe, W. D. Cochran, F. Fressin, G. Torres, L. A. Buchhave, D. D. Sasselov, W. J. Borucki, D. G. Koch, G. Basri, T. M. Brown, D. A. Caldwell, D. Charbonneau, E. W. Dunham, T. N. Gautier, J. C. Geary, R. L. Gilliland, M. R. Haas, S. B. Howell, D. R. Ciardi, M. Endl, D. Fischer, G. Fürész, J. D. Hartman, H. Isaacson, J. A. Johnson, P. J. MacQueen, A. V. Moorhead, R. C. Morehead and J. A. Orosz, Kepler-9: A System of Multiple Planets Transiting a Sun-Like Star, Confirmed by Timing Variations, *Science*, *330*, 51–, 2010.

Hut, P., Stability of tidal equilibrium, *Astron. Astrophys.*, *92*, 167–170, 1980.

Hut, P., Tidal evolution in close binary systems, *Astron. Astrophys.*, *99*, 126–140, 1981.

Jackson, B., R. Greenberg and R. Barnes, Tidal Evolution of Close-in Extrasolar Planets, *Astrophys. J.*, *678*, 1396–1406, 2008.

Jackson, B., R. Barnes and R. Greenberg, Observational Evidence for Tidal Destruction of Exoplanets, *Astrophys. J.*, *698*, 1357–1366, 2009.

Kertz, W., *Einführung in die Geophysik: Erdkörper*, Bd. 1 in BI-Hochschultaschenbuch, Bibliographisches Institut, 1969.

Knutson, H. A., D. Charbonneau, L. E. Allen, J. J. Fortney, E. Agol, N. B. Cowan, A. P. Showman, C. S. Cooper and S. T. Megeath, A map of

the day-night contrast of the extrasolar planet HD 189733b, *Nature*, *447*, 183–186, 2007.

Lainey, V., V. Dehant and M. Pätzold, First numerical ephemerides of the Martian moons, *Astron. Astrophys.*, *465*, 1075–1084, 2007.

Lainey, V., J.-E. Arlot, Ö. Karatekin and T. van Hoolst, Strong tidal dissipation in Io and Jupiter from astrometric observations, *Nature*, *459*, 957–959, 2009.

Lambeck, K., Tidal Dissipation in the Oceans: Astronomical, Geophysical and Oceanographic Consequences, *Royal Society of London Philosophical Transactions Series A*, *287*, 545–594, 1977.

Lambeck, K., On the orbital evolution of the Martian satellites, *Journal of Geophysical Research*, *84*, 5651–5658, 1979.

Lanza, A. F., Hot Jupiters and the evolution of stellar angular momentum, *Astron. Astrophys.*, *512*, A77, 2010.

Latham, D. W., R. P. Stefanik, T. Mazeh, M. Mayor and G. Burki, The unseen companion of HD114762 - A probable brown dwarf, *Nature*, *339*, 38–40, 1989.

Leconte, J., D. Lai and G. Chabrier, Distorted, nonspherical transiting planets: impact on the transit depth and on the radius determination, *Astron. Astrophys.*, *528*, A41, 2011.

Léger, A., H. Bruntt, T. Guillot, A. Shporer, E. Guenther, S. Aigrain, J. M. Almenara, R. Alonso, M. Auvergne, A. Baglin, M. Barbieri, P. Barge, W. Benz, P. Bordé, F. Bouchy, H. J. Deeg, R. de La Reza, M. Deleuil, R. Dvorak, A. Erikson, M. Fridlund, M. Gillon, P. Gondoin,

A. Hatzes, G. Hébrard, L. Jorda, P. Kabath, H. Lammer, L. Carone, A. Llebaria, B. Loeillet, P. Magain, M. Mayor, T. Mazeh, M. Ollivier, M. Pätzold, F. Pepe, F. Pont, D. Queloz, H. Rauer, M. Rabus, C. Moutou, D. Rouan, J. Schneider, S. Udry and G. Wuchterl, Transiting exoplanets from the CoRoT space mission. VIII. CoRoT-Exo-7b: the first Super-Earth with measured radius, *Astron. Astrophys.*, tbd, 2009.

Levrard, B., C. Winisdoerffer and G. Chabrier, Falling Transiting Extrasolar Giant Planets, *Astrophys. J., Lett.*, *692*, L9–L13, 2009.

Lin, D. N. C., P. Bodenheimer and D. C. Richardson, Orbital migration of the planetary companion of 51 Pegasi to its present location, *Nature*, *380*, 606–607, 1996.

Lippincott, S. L., The Unseen Companion of the Fourth Nearest Star, Lalande 21185., *Astrophys. J.*, *65*, 349–+, 1960.

Marcy, G. W. and R. P. Butler, Planets Orbiting Other Suns, *Publications of the Astronomical Society of the Pacific*, *112*, 137–140, 2000.

Matsumura, S., S. J. Peale and F. A. Rasio, Tidal Evolution of Close-in Planets, *Astrophys. J.*, *725*, 1995–2016, 2010.

Mayor, M. and D. Queloz, A Jupiter-Mass Companion to a Solar-Type Star, *Nature*, *378*, 355–+, 1995.

Mazeh, T., S. Zucker and F. Pont, An intriguing correlation between the masses and periods of the transiting planets, *Mon. Not. R. Astron. Soc.*, *356*, 955–957, 2005.

Meibom, S. and R. D. Mathieu, A Robust Measure of Tidal Circularization in Coeval Binary Populations: The Solar-Type Spectroscopic Binary Population in the Open Cluster M35, *Astrophys. J.*, *620*, 970–983, 2005.

Moutou, C., H. Bruntt, T. Guillot, A. Shporer, E. Guenther, S. Aigrain, J. M. Almenara, R. Alonso, M. Auvergne, A. Baglin, M. Barbieri, P. Barge, W. Benz, P. Bordé, F. Bouchy, H. J. Deeg, R. de La Reza, M. Deleuil, R. Dvorak, A. Erikson, M. Fridlund, M. Gillon, P. Gondoin, A. Hatzes, G. Hébrard, L. Jorda, P. Kabath, H. Lammer, A. Léger, A. Llebaria, B. Loeillet, P. Magain, M. Mayor, T. Mazeh, M. Ollivier, M. Pätzold, F. Pepe, F. Pont, D. Queloz, M. Rabus, H. Rauer, D. Rouan, J. Schneider, S. Udry and G. Wuchterl, Transiting exoplanets from the CoRoT space mission. V. CoRoT-Exo-4b: stellar and planetary parameters, *Astron. Astrophys.*, *488*, L47–L50, 2008.

Murray, C. D. and S. F. Dermott, *Solar system dynamics*, Solar system dynamics by Murray, C. D., 1999, 1999.

Pätzold, M. and H. Rauer, Where Are the Massive Close-in Extrasolar Planets?, *Astrophys. J., Lett.*, *568*, L117–L120, 2002.

Pätzold, M., L. Carone and H. Rauer, Tidal interactions of close-in extrasolar planets: The OGLE cases, *Astron. Astrophys.*, *427*, 1075–1080, 2004.

Penev, K. and D. Sasselov, Tidal Evolution of Close-in Extrasolar Planets: High Stellar Q from New Theoretical Models, *Astrophys. J.*, *731*, 67–+, 2011.

Perryman, M. A. C., GAIA: An Astrometric and Photometric Survey of our Galaxy, *Astrophysics and Space Science*, *280*, 1–10, 2002.

Pollack, J. B., PHOBOS and Deimos, in *IAU Colloq. 28: Planetary Satellites*, herausgegeben von J. A. Burns, 319–344, 1977.

Pollack, J. B., M. Podolak, P. Bodenheimer and B. Christofferson, Planetesimal dissolution in the envelopes of the forming, giant planets, *Icarus*, *67*, 409–443, 1986.

Pravdo, S. H. and S. B. Shaklan, An ultracool Star's Candidate Planet, *Astrophys. J.*, *700*, 623–632, 2009.

Prialnik, D., *An Introduction to the Theory of Stellar Structure and Evolution*, Juli 2000.

Queloz, D., F. Bouchy, C. Moutou, A. Hatzes, G. Hébrard, R. Alonso, M. Auvergne, A. Baglin, M. Barbieri, P. Barge, W. Benz, P. Bordé, H. J. Deeg, M. Deleuil, R. Dvorak, A. Erikson, S. Ferraz Mello, M. Fridlund, D. Gandolfi, M. Gillon, E. Guenther, T. Guillot, L. Jorda, M. Hartmann, H. Lammer, A. Léger, A. Llebaria, C. Lovis, P. Magain, M. Mayor, T. Mazeh, M. Ollivier, M. Pätzold, F. Pepe, H. Rauer, D. Rouan, J. Schneider, D. Segransan, S. Udry and G. Wuchterl, The CoRoT-7netary system: two orbiting super-Earths, *Astron. Astrophys.*, *506*, (1), 303–319, 2009.

Rasio, F. A., C. A. Tout, S. H. Lubow and M. Livio, Tidal Decay of Close Planetary Orbits, *Astrophys. J.*, *470*, 1187–+, 1996.

Rauer, H., D. Queloz, S. Csizmadia, M. Deleuil, R. Alonso, S. Aigrain, J. M. Almenara, M. Auvergne, A. Baglin, P. Barge, P. Bordé, F. Bouchy, H. Bruntt, J. Cabrera, L. Carone, S. Carpano, R. de La Reza, H. J. Deeg, R. Dvorak, A. Erikson, M. Fridlund, D. Gandolfi, M. Gillon, T. Guillot, E. Guenther, A. Hatzes, G. Hébrard, P. Kabath, L. Jorda, H. Lammer, A. Léger, A. Llebaria, P. Magain, T. Mazeh, C. Moutou, M. Ollivier, M. Pätzold, F. Pont, M. Rabus, S. Renner, D. Rouan, A. Shporer, B. Samuel, J. Schneider, A. H. M. J. Triaud and G. Wuchterl, Transiting exoplanets from the CoRoT space mission. VII. The "hot-Jupiter"-type planet CoRoT-5b, *Astron. Astrophys.*, *506*, 281–286, 2009.

Reffert, S. and A. Quirrenbach, Mass constraints on substellar companion candidates from the re-reduced Hipparcos intermediate astrometric data: nine confirmed planets and two confirmed brown dwarfs, *Astron. Astrophys.*, *527*, A140+, 2011.

Saar, S. H., Recent magnetic fields measurements of stellar, in *Stellar Surface Structure*, herausgegeben von K. G. Strassmeier & J. L. Linsky, Bd. 176 von *IAU Symposium*, 237–+, 1996.

Sasselov, D. D. and M. Lecar, On the Snow Line in Dusty Protoplanetary Disks, *Astrophys. J.*, *528*, 995–998, 2000.

Sato, B., D. A. Fischer, G. W. Henry, G. Laughlin, R. P. Butler, G. W. Marcy, S. S. Vogt, P. Bodenheimer, S. Ida, E. Toyota, A. Wolf, J. A. Valenti, L. J. Boyd, J. A. Johnson, J. T. Wright, M. Ammons, S. Robinson, J. Strader, C. McCarthy, K. L. Tah and D. Minniti, The N2K Consortium. II. A Transiting Hot Saturn around HD 149026 with a Large Dense Core, *Astrophys. J.*, *633*, 465–473, 2005.

Saumon, D. and T. Guillot, Shock Compression of Deuterium and the Interiors of Jupiter and Saturn, *Astrophys. J.*, *609*, 1170–1180, 2004.

Schatzman, E., A theory of the role of magnetic activity during star formation, *Annales d'Astrophysique*, *25*, 18–+, 1962.

Shor, V. A., The motion of the Martian satellites, *Celestial Mechanics*, *12*, 61–75, 1975.

Skumanich, A., Time Scales for CA II Emission Decay, Rotational Braking, and Lithium Depletion, *Astrophys. J.*, *171*, 565–+, 1972.

Strand, K. A., 61 Cygni as a Triple System, *Publ. Astron. Soc. Pac.*, *55*, 29–32, 1943.

Thomson, W., Dynamical problems regarding elastic spheroidal shells and spheroids of incompressible liquid, *Philosophical Transactions of the Royal Society of London*, *153*, pp. 583–616, 1863*a*.

Thomson, W., On the rigidity of the earth, *Philosophical Transactions of the Royal Society of London*, *153*, pp. 573–582, 1863*b*.

Tingley, B., M. Endl, J. Gazzano, R. Alonso, T. Mazeh, L. Jorda, S. Aigrain, J. Almenara, M. Auvergne, A. Baglin, P. Barge, A. S. Bonomo, P. Bordé, F. Bouchy, H. Bruntt, J. Cabrera, S. Carpano, L. Carone, W. D. Cochran, S. Csizmadia, M. Deleuil, H. J. Deeg, R. Dvorak, A. Erikson, S. Ferraz-Mello, M. Fridlund, D. Gandolfi, M. Gillon, E. W. Guenther, T. Guillot, A. Hatzes, G. Hébrard, A. Léger, A. Llebaria, H. Lammer, C. Lovis, P. J. MacQueen, C. Moutou, M. Ollivier, A. Ofir, M. Pätzold, F. Pepe, D. Queloz, H. Rauer, D. Rouan, B. Samuel, J. Schneider, A. Shporer and G. Wuchterl, Transiting exoplanets from the CoRoT space mission: XIII. CoRoT-14b: an unusually dense very hot Jupiter, *ArXiv e-prints*, Januar 2011.

Tittemore, W. C. and J. Wisdom, Tidal evolution of the Uranian satellites. III - Evolution through the Miranda-Umbriel 3:1, Miranda-Ariel 5:3, and Ariel-Umbriel 2:1 mean-motion commensurabilities, *Icarus*, *85*, 394–443, 1990.

Unsoeld, A. and B. Baschek, *The new cosmos : an introduction to astronomy and astrophysics*, 2001.

Vallado, D. A., *Fundamentals of astrodynamics and applications*, 2001.

van de Kamp, P., Astrometric study of Barnard's star from plates taken with the 24-inch Sproul refractor., *Astrophys. J.*, *68*, 515–521, 1963.

Weber, E. J. and L. Davis, Jr., The Angular Momentum of the Solar Wind, *Astrophys. J.*, *148*, 217–227, 1967.

Weidenschilling, S. J. and F. Marzari, Gravitational scattering as a possible origin for giant planets at small stellar distances, *Nature*, *384*, 619–621, 1996.

Weissman, P. R., L.-A. McFadden and T. V. Johnson, *Encyclopedia of the solar system*, 1999.

Wolszczan, A., Confirmation of Earth Mass Planets Orbiting the Millisecond Pulsar PSR:B1257+12, *Science*, *264*, 538–+, 1994.

Wolszczan, A. and D. A. Frail, A planetary system around the millisecond pulsar PSR1257 + 12, *Nature*, *355*, 145–147, 1992.

Wuchterl, G., The critical mass for protoplanets revisited - Massive envelopes through convection, *Icarus*, *106*, 323, 1993.

Wuchterl, G., Extrasolar Giant Planets: Masses and Luminosities from In-situ Formation Theories, in *AAS/Division for Planetary Sciences Meeting Abstracts #31*, Bd. 31 von *AAS/Division for Planetary Sciences Meeting Abstracts*, 36.07, 1999.

Yoder, C. F., Astrometric and Geodetic Properties of Earth and the Solar System, in *Global Earth Physics: A Handbook of Physical Constants*, herausgegeben von T. J. Ahrens, 1–+, 1995.

Zahn, J.-P., Tidal friction in close binary stars, *Astron. Astrophys.*, *57*, 383–394, 1977.

Zapatero Osorio, M. R., V. J. S. Béjar, E. L. Martín, R. Rebolo, D. Barrado y Navascués, R. Mundt, J. Eislöffel and J. A. Caballero, A Methane, Isolated, Planetary-Mass Object in Orion, *Astrophys. J.*, *578*, 536–542, 2002.

Acknowledgements

Erklärung

Ich versichere, dass ich die von mir vorgelegte Dissertation selbständig angefertigt, die benutzten Quellen und Hilfsmittel vollständig angegeben und die Stellen der Arbeit - einschließlich Tabellen, Karten und Abbildungen -, die anderen Werken im Wortlaut oder dem Sinn nach entnommen sind, in jedem Einzelfall als Entlehnung kenntlich gemacht habe; dass diese Dissertation noch keiner anderen Fakultät oder Universität zur Prüfung vorgelegen hat; dass sie - abgesehen von unten angegebenen Teilpublikationen - noch nicht veröffentlicht worden ist sowie, dass ich eine solche Veröffentlichung vor Abschluss des Promotionsverfahrens nicht vornehmen werde. Die Bestimmungen der Promotionsordnung sind mir bekannt. Die von mir vorgelegte Dissertation ist von Priv. Doz. Dr. Martin Pätzold betreut worden.

Köln, den 13.2.2012:   ....

Ludmila Carone

Lebenslauf

	Ludmila Carone
	Kerpstr. 20
	53844 Troisdorf
	geb. am 14.4.1976 in Bukarest
	Staatsangehörigkeit: Italienisch
	Schulausbildung
10.6.1996	Abitur am Bodelschwingh-Gymnasium, Windeck-Herchen
	Studium
1996-2002	Studium der Physik an der Rheinischen Friedrich-Wilhelm-Universität, Bonn
9.1.2002	Erlangung des Physik-Diploms mit der Arbeit: 'Impulsrekonstruktion mithilfe der Vorwärtsdriftkammern des ZEUS-Detektors'
3/2003-12/2010	Promotionsstudium Geophysik an der Universität zu Köln
	Berufliche Tätigkeit
3/2003-12/2011	wissenschaftliche Angestellte an der Universität zu Köln am Institut für Geophysik der Universität zu Köln und am RIU-Planetenforschung